NASA CONTRACTOR REPORT 166365

Axisymmetric & Non-Axisymmetric Exhaust Jet Induced Effects on a V/STOL Vehicle Design (Part II: Analysis of results)

W. C. Schnell

CONTRACT NAS2-9887
January 1982

NASA

NASA CONTRACTOR REPORT 166365

Axisymmetric & Non-Axisymmetric Exhaust Jet Induced Effects on a V/STOL Vehicle Design (Part II: Analysis of results)

W. C. Schnell
Grumman Aerospace Corp.
Bethpage, NY

Prepared for
Ames Research Center
under Contract NAS2-9887

National Aeronautics and
Space Administration

Ames Research Center
Moffett Field, California 94035

Intentionally Left Blank

CONTENTS

CONTENTS (Contd)

ILLUSTRATIONS

ILLUSTRATIONS (contd)

ILLUSTRATIONS (contd)

ILLUSTRATIONS

SYMBOLS & ABBREVIATIONS

ADEN	Augmented Deflector Exhaust Nozzle
AF	Axial force of main balance
AF2	Axial force of nacelle balance
A/B	Afterburning
A_j	Nozzle jet (throat) area
ALBEN	Asymmetric Load Balanced Exhaust Nozzle
A9	Area-ratio-setting flap of ADEN
AOA	Angle-of-attack (also α)
Aw	Wing reference area (6.016 ft^2, 0.559 m^2)
$\bar{c}$	Mean aerodynamic chord (1.787 ft., 0.545 m.)
C	Constant
C_D	Drag coefficient (general application); $Drag/qA_W$
CD1	Total drag minus thrust coefficient
C_{dis}	Nozzle discharge coefficient
CDTR	Thrust- removed drag coefficient
c.g.	center of gravity
C_L	Lift coefficient (general application); $Lift/qA_W$
CL1	Total lift coefficient
CLTR	Thrust-removed lift coefficient
C_M	Pitching moment coefficient (general application); (Pitching moment)/ $(qA_W\bar{c})$
CMMTR	Thrust-removed pitching moment coefficient
COM	ADEN Combat (Maximum - A/B)
C_p	Pressure coefficient; $(P - P_o)/q$
CR	ADEN Cruise (Non -A/B)
D	Installed drag; $D_{ext} + (\Delta F)_D$
DASH	ADEN Dash (Partial -A/B)
DEG	Degrees
D_{ext}	Total external drag
F_G	Resultant installed internal gross thrust
F_{G_s}	Resultant static gross thrust vector (also T_s)

F_{ip}	Nozzle ideal thrust for complete isentropic expansion of measured mass flow to free stream ambient pressure
F.S.	Fuselage Station
I/F	Inlet Fairing
L	Total lift
M	Free-stream Mach number
MBTP	Data reduction procedure to determine T/R parameters using main balance and P_o-Method (page 36)
NBTF	Data reduction procedure to determine T/R parameters using nacelle balance and Fip-Method (page 36)
NBTP	Data reduction procedure to determine T/R parameters using nacelle balance and P_o-Method (page 36)
NF	Normal force of main balance
NF2	Normal force of nacelle balance
NPR	Nozzle pressure ratio
P	Local surface static pressure
P_o	Free-stream ambient pressure
P_{WALL}	Expansion ramp internal surface pressure
q	Free-stream dynamic pressure
(T-D)	Thrust-minus-drag
T/R	Thrust-removed
T_s	Resultant static gross thrust vector (also F_{G_s})
VEER	Variable external expansion ramp (of ADEN)
W.L.	Water Line
α	Angle-of-Attack (also AOA)
δ_{eff}	Wind-on thrust vector angle relative to model axis
δ_G	Geometric deflection angle
δ_s	Static thrust vector angle relative to model axis (defined positive when NF is positive)
Δ	Denotes an incrementing process
$(\Delta F)_D$	Incremental gross thrust resolved in drag direction; $F_G \cos(\alpha + \delta_s) - F_G \cos(\alpha + \delta_{eff})$

$(\Delta F)_L$	Incremental gross thrust resolved in lift direction; $F_{G_s} \sin(\alpha + \delta_s) - F_G \sin(\alpha + \delta_{eff})$
ΔF	Incremental resultant gross thrust; $\left[(\Delta F)_D 2 + (\Delta F)_L 2\right]^{1/2}$

Subscripts

s	Static conditions (M = 0)

AXISYMMETRIC & NON-AXISYMMETRIC EXHAUST JET INDUCED EFFECTS ON A V/STOL VEHICLE DESIGN (PART II: ANALYSIS OF RESULTS)

W. C. Schnell
Grumman Aerospace Corporation

SUMMARY

A wind tunnel investigation, sponsored by the NASA Ames Research Center, was conducted to determine the jet induced effects of several exhaust nozzle configurations (axisymmetric, non-axisymmetric, and vectoring/modulating variants) on the aeropropulsive performance of a twin-engine V/STOL fighter design. A 1/8 scale model was tested in the NASA Ames 11 ft transonic tunnel at static conditions and over a range of Mach numbers from 0.4 to 1.4. Exhaust flow simulation was obtained by employing compressed air. Angle-of-attack and exhaust nozzle pressure ratio were appropriately scheduled with Mach number.

This report is the second in a series of three reports covering this comprehensive wind tunnel investigation of approximately 2,000 test points. The first report, Part I: Data Presentation (ref. 1) presents the model geometry and the entire set of test data (static and wind-on) in graphical form. This second report thoroughly analyzes and interprets the test results and presents highlights of each major data study. The third report, Part III: Experimental Technique, will discuss the experimental aspects (e.g., test technique, test problems and solutions, etc.) of the static and wind tunnel test programs.

This investigation has contributed to the aeropropulsion V/STOL data base. The force and pressure data presented herein show that significant differences in aeropropulsion performance can be expected by varying the exhaust nozzle type and its geometric parameters on a V/STOL underwing nacelle installation. For example, the unvectored single expansion ramp nozzles tested in this program show large aeropropulsion performance gains, at all flight conditions, relative to a circular nozzle

installation. At Mach 0.9 a typical cruise drag reduction is about 50 counts. Additionally, a 40 count drag reduction is realized when the non-axisymmetric cruise nozzle is vectored through a 10^{o} deflection angle. The combined 90 count drag reduction, which is equivalent to 25 percent of zero lift drag for this V/STOL vehicle, represents the total payoff of the vectored non-axisymmetric nozzle over the baseline circular nozzle installation.

SECTION I

INTRODUCTION AND OBJECTIVES

The potential advantages of non-axisymmetric exhaust nozzles have made these nozzles strong candidates for adaptation to the propulsion systems of future V/STOL aircraft. Non-axisymmetric shapes generally blend better with airframes (in particular with wings) than do state-of-the-art axisymmetric nozzles, and the resulting improvement in nozzle/airframe integration can yield important reductions in vehicle minimum drag as well as induced drag (through lift enhancement derived from thrust vectoring). But before non-axisymmetric nozzles can be seriously considered for use in an actual advanced aircraft design, a significant amount of experimental data on installed aeropropulsion performance and induced aerodynamic effects must be obtained.

To contribute to the developing V/STOL air vehicle/non-axisymmetric nozzle data base, the NASA Ames Research Center has sponsored the subject program. A realistic multimission twin-engine V/STOL fighter scale model was tested (June 1979) in the Ames 11 Ft Transonic Wind Tunnel to investigate non-axisymmetric nozzle installed performance and inflight vectoring performance.

This scale model was previously tested in two other research programs (ref. 2, 3), but hardware failures either prevented acquisition of complete aircraft force data or severely limited the test configuration matrix from which worthwhile data could be salvaged. In the subject program, it was possible to obtain complete aircraft force data on all nozzle configurations over a wide range of test conditions.

The overall objectives of this program are to acquire, in the wind tunnel, complete aircraft longitudinal force data and extensive wing/body surface pressure data on a realistic V/STOL vehicle design in its CTOL mode of operation. These data will be used to evaluate the aeropropulsion installation effects of different axisymmetric and non-axisymmetric nozzle designs as well as the effects of thrust vectoring on the lift enhancement and drag characteristics of a non-axisymmetric underwing nacelle installation.

SECTION II

DESCRIPTION OF NOZZLE DESIGNS

This program emphasized the experimental evaluation of the ADEN (Augmented Deflector Exhaust Nozzle) non-axisymmetric exhaust system installed in an underwing nacelle installation. The ADEN was investigated over a range of jet areas and thrust deflection angles. Additionally, a second non-axisymmetric exhaust system, the ALBEN (Asymmetric Load Balanced Exhaust Nozzle), designed for reduced cruise drag, was tested in the program. These two non-axisymmetric nozzle types, together with a state-of-the-art axisymmetric baseline provided a progression of three distinct variants in nozzle type. All concepts represented workable mechanical designs furnished by the General Electric Company.

2.1 FULL SCALE NOZZLE DESCRIPTION

Augmented Deflector Exhaust Nozzle - The Augmented Deflector Exhaust Nozzle (ADEN) V/STOL exhaust system (Fig. 1) is a variable area, internal/external expansion type, non-axisymmetric nozzle with throat area controlled by a variable geometry convergent-divergent upper flap assembly. The throat "collapses" when modulating from non-afterburning to max-afterburning. The variable position ventral flap located downstream of the throat varies the nozzle internal expansion area ratio as required over a range of operating pressure ratios. The throat itself is located forward of the ventral flap hinge plane so that the nozzle throat area is not affected by the ventral flap position.

The arrangement of the ADEN nozzle flaps, deflector, expansion ramp, actuators, and structural elements have been carefully chosen to allow smooth afterbody contours. The non-axisymmetric nozzle shape blends well with supersonic airframe lines, minimizing drag-producing base regions; the cruise throat aspect ratio (4 X 1), permits the ADEN to be installed without increasing frontal projected area.

For V/STOL operation, a rotating deflector mounted outside the nozzle casing diverts the jet downward. The nozzle upper flap assembly is actuated to the maxi-

tional axisymmetric translating flap C-D nozzle design with a scheduled area ratio control. This axisymmetric nozzle provides a meaningful performance yardstick against which the non-axisymmetric nozzles can be evaluated.

The unvectored circular nozzle installation is compared with the ADEN and ALBEN installation in Fig. 3. This illustration shows the nacelle force balance metric break location (or model nozzle/airframe connect) and compares the amount of afterbody/nozzle length and area required to close out the afterbody and still permit thrust vectoring, if desired, with these three different nozzle types.

Note that the circular nozzle is canted slightly downwards (approximately 4^{o}). In addition to hardware requirements relating to thrust mounts that differed from the non-axisymmetric installations, performance considerations, reflecting optimum interfairing design and minimum subsonic cruise specific fuel consumption, were influential in dictating the slight built-in deflection angle.

2.2 MODEL SCALE NOZZLE CRITERIA

Nozzle throat variation and internal area ratios were selected to be consistent with advanced continuous bleed turbojet engine cycles. Throat area was selected to represent an engine operation range from subsonic dry-power (non-afterburning) to supersonic maximum reheat-power (max-afterburning). This resulted in a "turn-down ratio" (ratio of maximum to minimum throat area) of about 1.75. Internal area ratios were selected to be consistent with typical turbojet engine cycles such as those shown in Fig. 4. This operating schedule is representative of Mach 0.6 loiter power, Mach 0.8 cruise power, and Mach 0.9 to Mach 1.5 at maximum power.

Vectoring capability was established as a design requirement for all three nozzle types for their integration into the model (even though only the ADEN nozzle was vectored in this test program). This provided a consistent groundrule which was responsible for the circular nozzle being located slightly aft of the non-axisymmetric nozzles.

An aspect ratio (nozzle internal width divided by dry-power throat height) of about four was chosen for the non-axisymmetric nozzles. This aspect ratio is consistent with a square transition duct design, and is most representative of first-generation non-axisymmetric full-scale designs.

mum open position during V/STOL operation to substantially reduce the flow Mach number approaching the turn. The ventral flap travel is scheduled so that the throat is established between the tip of the ventral flap and the deflector and rotates with the deflector so that flow turning is accomplished subsonically at all deflector settings; also, the low pressure region at the inside of the turn is freely vented to ambient air to allow free supersonic jet expansion.

Additionally, the ADEN is capable of providing inflight thrust vector control to obtain STOL performance as well as to improve aircraft flight maneuver and cruise capabilities by utilizing a Variable External Expansion Ramp (VEER). The VEER upper surface is designed to blend with the airframe contours, and the inner surface is contoured for effective jet expansion control. Variation of the VEER angle will deliver an upward or downward vertical thrust component as desired.

The ADEN utilized on the model tested in this program had not been optimized when the model design was frozen and, therefore, internal performance levels higher than those presented herein can be attained. Internal performance values from full-scale static test results confirm this (ref. 4).

Asymmetric Load Balanced Exhaust Nozzle - The Asymmetric Load Balanced Exhaust Nozzle (ALBEN), Fig. 2, is a CTOL derivative of the ADEN, and features an elliptical throat and expansion surface contours. Throat area and internal area ratio are set by an adjustable lower surface boattail flap. The rotating lower flap is actually part of a swiveling pressure vessel with a continuous structure that proceeds up the sidewalls and through a pressurized cavity in the fixed geometry upper expansion ramp structure. This design reduces actuation forces and maintains structurally effective hoop stress in the area control flap. Vectoring is accomplished by rotating a second flap forming part of the expansion ramp. This flap also has partial sidewalls to contain the flow. The partial sidewall continues upstream as fixed structure attached to the fixed upper ramp section where it houses the swiveling duct section.

The ALBEN utilized on the model tested in this program had not been optimized when the model design was frozen; therefore, performance levels higher than those presented herein can be attained. Internal performance values from scale model test results confirm this (ref. 5).

Circular Exhaust Nozzle - An axisymmetric convergent-divergent (C-D) nozzle was employed in this test as a baseline configuration. This circular nozzle is a conven-

SECTION III

WINDTUNNEL MODEL DESIGN

3.1 TEST MODEL AND SUPPORT SYSTEM

The model was a 1/8th scale representation of a twin-engine, thrust-vectoring, V/STOL fighter designed for Navy application. The general assembly and nacelle assembly drawings are presented in Fig. 5 and 6. The configuration is designated 623-2004B, and a three-view sketch with overall dimensions is shown in Fig. 7. A photograph of the model installed in the Ames 11 ft tunnel test section is shown in Fig. 8.

The model was modular in design and consisted of four major sections:

- Structural support and air supply system
- Fuselage and lifting surfaces
- Faired-over inlet/nacelles
- Exhaust nozzle configurations.

Fig. 9 provides an overview of the model support and air supply systems. As schematically illustrated, the overall model is supported by a bifurcated, twin-boom system which attaches to the vertical tail assemblies. Air supply for powering the model is delivered through the model support system. A representation of the flow path through the model is illustrated in the figure.

Fig. 10 presents an expanded view of the model support assembly. It consists primarily of an air supply tube, a T-support piece with structural/aerodynamic fairings, two sting booms, two vertical tails, and a support beam.

The air supply tube provides the connection between the AMES 11 ft tunnel air supply source and the air passage entrance in the T-support. The forward end of the tube mates with this support piece and the aft end attaches to the AMES air supply source.

The T-support piece establishes the structural interface between the wind tunnel strut and the model. It also contains the air passageway that accepts the oncoming air from the air supply tube and divides it into two separate channels leading to the two sting booms. Holes exist in this piece for instrumentation lines which are routed from the model to the internal portion of the wind tunnel struts. The structural/aerodynamic fairings provide added overall strength to the T-support. In addition, they provide a smooth circular-arc boundary for the wind tunnel flow to follow after passing over the upstream support hardware. This minimizes any pressure disturbances which may feed upstream.

The two sting booms house the air passageways from the T-support to the vertical tails. In addition, they also provide the structural interface between these two adjoining parts. The two vertical tails form the structural link between the sting booms and the support beam. They also contain five holes for air to be transported from the sting booms to the support beam and also serve as channels for routing instrumentation lines out of the model. The inboard side of the vertical tails conform to the aircraft airfoil shape to attempt to simulate the tail interference on the afterbody. The outboard sides of the vertical tails slightly deviate from the true aircraft airfoil contour to allow material thickness through which the air holes were drilled.

The support beam is the strongback of the model and provides a receptacle at the forward end for the non-metric side of the aircraft force balance. It also houses a plenum chamber to reduce the higher velocities emanating from the vertical tail flow path.

The model hardware described above is all non-metric. Attached to the metric side of the main force balance is the centerbody-core piece that in turn supports all other metric model components: forebody/nose, aft-fuselage shells (upper and lower), wings and tails (not tested in this program), and nacelle/nozzle hardware.

The centerbody is the backbone of the model and therefore was constructed of 17-4 PH stainless steel. It houses the metric side of the aircraft force balance and the two model venturi tubes. Air passing through the aircraft force balance travels forward through a bored passageway to a plenum chamber just forward of the aircraft force balance. Then the air travels aft through another bored passage, through the venturi tubes and then dumps into the faired-over nacelles.

The inlet nose simulated the aircraft inlet shape and attached to the forward end of the faired-over nacelles. This model did not employ the familiar bullet nose inlet fairings (except for one configuration); instead, it featured a flat plate dam arrangement recessed from the inlet leading edge surfaces. This design has been observed to more closely resemble the inlet flow field (unchoked) of aerodynamic flow-through models than the "zero-spillage" bullet fairing (ref. 6). The inlet fairing lip simulated the aircraft inlet lower lip contour.

Right and left nacelle assemblies were different because the left side housed the nacelle balance. The nacelle assembly drawing (Fig. 6) shows the several basic components making up the left assembly. The left nacelle houses the non-metric side of the nacelle force balance and was grooved in the middle to provide a passage-way for high pressure air from the wing/centerbody through the nacelle and into the force balance. The nacelle cover piece attached to the lower aft end of the nacelle and matched the aircraft nacelle skin lines up to the model nozzle metric break station.

The right nacelle hardware is the same as the left with the exception of the nacelle force balance. On the right side, a dummy balance sleeve was installed in place of a force balance.

The exhaust nozzles attach to the aft-ends of the nacelle force balance and/or dummy balance sleeve through an adapter piece. This adapter was common to ADEN configurations and mated to the metric side of the nacelle force balance. Internally, it provided a flowpath transition section which was circular at the entrance and two-dimensional at the exit. The external portion of this piece, from the nozzle metric break to the nozzle exit plane, simulated the actual nozzle external contour lines.

For the ALBEN and circular nozzles correspondingly different adapter pieces were required to accommodate differing internal flowpaths and/or external boattail contours.

3.2 FORCE MEASURING SYSTEM

The model force balance arrangement is illustrated in Fig. 11. With the exception of the vertical tails, the entire model was fully metric to a five component flow-through aircraft main balance. This balance measured total aircraft forces and moments. The main balance metric break was located at the base of the vertical tails. This aircraft force balance was installed near the aircraft c.g. station as

shown in Fig. 12. A flexible metal bellows arrangement was employed as the method for the airflow to bridge the metric break. This balance was instrumented to provide measuring capability for the three major components of normal force, axial force, and pitching moment. The design limits of these components are ±5000 lb, ±800 lb, and ±25000 in.-lb, respectively. Electrical leads from this balance were routed along the bottom center fuselage instrumentation passage to the cavity between the model strongback and lower afterbody shell, then up to the stings and tunnel strut through passageways in the aft portion of the vertical tails.

In addition, a second five-component flow-through balance was employed to measure the forces and moments on the metric section of the left-hand nozzle. This balance attached to the main balance in a "piggy-back" arrangement and was similar to the aircraft force balance in design. Understanding of the flow-through balance concept can be obtained from Fig. 6. The nacelle balance was instrumented to provide ±200 lb of normal force, ±400 lb of axial force and ±1500 in.-lb of pitching moment. Electrical lines for this balance were routed from the nacelle to the fuselage in a passageway in the wing and then followed the aircraft force balance leads to the stings and tunnel strut.

Note that the axial load ranges of the balances are of the same order of magnitude despite the 400lb difference in maximum range. With proper calibration, the observed axial force repeatability error of the main balance is not significantly greater than the nacelle balance. This is not true in the normal direction where balance capacities differ by over an order of magnitude. The nacelle balance can be expected to exhibit a much tighter data scatter band than the main balance. If thrust-removed parameters are desired, therein lies the primary reason for employing the additional complexity of the second (nozzle) balance. Static thrust components are required for the determination of the thrust-removed parameters. Under static conditions (wings unloaded) the main balance normal force gauge, which had to be sized for large transonic wing loads, is much oversized for the measurement of the relatively small normal force component of the thrust vector. Typically, the static normal force data measured by the main balance is characterized by large data scatter. (This will be shown in subsection 6.3.)

(It is noted, however, that if great care and time are taken to make the necessary repeat runs to minimize both random and bias errors, then a single balance system may be satisfactory for the measurement of static normal force.)

Another argument for employing the second balance is to determine the wind-on vector angle. However, this requires the additional cost and complexity of the extensive pressure instrumentation to assess tare terms, in both axial and normal directions, on metric surfaces wetted by the external flow. Additionally, friction tare forces must be estimated analytically. Although the wind-on vector angle (if determined with confidence) is an interesting diagnostic, it is not necessary for full-scale aircraft performance to be determined. This is demonstrated in ref. 7 where the (static) thrust-removed model scale results are combined with real engine data using the static vector angle as the interface.

Yet another common argument for utilizing the second balance is to obtain installed nozzle thrust-minus-drag. Since the location of the nozzle metric break is arbitrary and generally not outside the nozzle and/or the jet exhaust sphere of influence, this parameter possess little value from the performance point of view (it is merely a function of the metric break location). On the other hand, if the nozzle metric break somehow could be located so that all jet-effects were included on the nozzle balance metric system — then there would be no need for the main balance, and this particular argument for the two-balance system loses validity.

Thus it is concluded again (unless driven by extraordinary objectives), that the primary reason for employing the nozzle balance is to obtain the static normal force component accurately. Furthermore, because the sphere of influence of nozzle variants and jet-effects is not restricted to the nozzle balance metric system, in this program the main balance is used for all drag/lift comparisons to ensure the accounting of all jet-induced phenomena.

3.3 INSTRUMENTATION

The type and quantity of model-related instrumentation is summarized, according to specific category, below.

Nozzle Total Pressures - Total pressure was measured upstream of the nozzle entrance station. The circular configuration has a constant area-distribution upstream of the nozzle entrance and only five probes per nozzle were needed to properly assess the integrated average total pressure (area-weighted). For the ADEN and ALBEN, characterized by non-constant upstream area distributions, 19 probes per nozzle were utilized. Fig. 13, 14 and 15 illustrate the total pressure

rake design for the circular nozzle, ADEN and ALBEN, respectively. Tubing from these probes was routed to quick-disconnect leads at the aft end of the nacelles; the tubing was then routed through the nacelles to quick-disconnect devices in the wing root before connecting to a 60 psid scanivalve in the model nose.

Flow Path Pressures - A total of eight high pressure measurements were made. Because the pressure levels were in the range of 300-600 psid, individual model-mounted transducers were used instead of a scanivalve.

Two static pressure orifices were located in the flow circuit air plenum in the centerbody section of the fuselage for diagnostic purposes. Four static pressure orifices, two on each side, were located in the model venturi tubes in order to flow-calibrate each nacelle. Each bellows (main balance and nacelle balance) had one pressure orifice which was employed for health-monitoring purposes (so as not to exceed the bellows design pressure level of 900 psid) as well as for calibration purposes (to assess the bellows pressure tare force).

Model Internal Cavity Pressures - Model cavity pressure measurements were required to assess the unbalanced pressure/area tare force for each balance system. Eleven fuselage cavity pressure orifices were located as shown in Fig. 16 and 17. A single orifice was placed in the forward force balance cavity, one on each outboard side of the cavity area, six in the aft fuselage upper and lower shell cavity area (see Fig. 17), and one each at the forward and rearward boundaries of the main balance metric break (base of vertical tail).

Nine nacelle balance pressure tare orifices were located in the left nacelle cavity as shown in Fig. 18. A single tap was placed upstream of the balance, four taps in the downstream cavity region, and four taps along the nozzle metric break. Tubing for all the fuselage and nacelle cavity taps was routed through the nacelle to quick-disconnect devices in the left wing root area and then to a 15 psid scanivalve in the model nose. No metric breaks had to be crossed in the process because the instrumentation was not located within the nacelle balance metric system.

External Surface Pressures - External surface statics located on the wing-body and nacelle/nozzle were employed as diagnostics to study the flowfield changes that occur by varying nozzle type or vectoring angle for example. Up to 37 static taps

(depending on configuration) were located on the nacelle centerline. Twenty-three of these were placed along the nacelle upper surface spaced from the upper inlet lip to the end of the nozzle/wing flap, and up to 12 along the nacelle lower surface spaced from the lower inlet lip to the end of the ADEN/ALBEN lower boattail. Figure 19 shows a representative layout of these surface statics which were measured on a 25 psid scanivalve.

Additionally, on select configurations, limited surface pressure instrumentation was located on either the ADEN sidewalls or the ADEN VEER at off-centerline butt-lines to study the effect of span.

On the wing and body, extensive pressure instrumentation was located such that upper and lower surfaces possess a symmetrical orifice-distribution. Figure 20 shows three rows on the outer wing and three on the inner wing/body. Also the nacelle/nozzle upper surface orifice locations of Fig. 19 have been repeated for reference.

Nozzle Internal Pressures - To assess the effect of external flow on nozzle internal thrust, wall surface taps were located between the nozzle throat and exit planes of the ADEN and ALBEN configurations.

The ADEN Cruise 0^{o} and combat 0^{o} nozzles were outfitted with nine VEER and four ventral flap orifices. Additionally, a limited number of off-centerline orifices were added to the VEER. Due to plumbing constraints, two of the VEER orifices and the off-centerline orifices were located on physically different configurations referred to as alternate (ALT.) that were tested at different times.

The ADEN Combat 10^{o}, 20^{o}, DASH, and ALBEN configurations all were outfitted with seven VEER centerline orifices.

Figure 21 illustrates the pressure orifice layout (centerline) for the ADEN Cruise 0^{o} configuration; the orifice layouts for the other nozzles are conceptually similar. All internal pressure lines were routed to a 60 psid scanivalve.

Model Temperature Instrumentation - Air total temperature in the model was measured at the entrance to the model venturi tubes by two iron-constantan thermocouples. Nozzle exit flow temperatures were measured with iron-constantan thermocouples located at the total pressure rake station. A Joule-Thompson throttling correlation was found to provide data consistency and was favored in lieu of the nozzle exit total temperature measurements.

Facility Instrumentation - Standard facility instrumentation upstream of the model support system was used to measure nozzle flow rate. A calibrated turbine flow meter and associated pressure and temperature measurements were employed for this purpose.

Standard Ames 11 ft tunnel instrumentation was provided to determine tunnel operating conditions (static and total pressures, Mach number, total temperature, and Reynolds number) and model attitude. The angle-of-attack was measured directly with a dangleometer mounted in the model.

SECTION IV

TEST OPERATION AND DESCRIPTION

4.1 FACILITY

This test program was conducted in the NASA Ames Research Center 11 ft Transonic Wind Tunnel. This is a closed circuit, variable-pressure, continuous-flow wind tunnel normally operated from Mach 0.4 to Mach 1.4. Stagnation pressure can be varied over a wide range. The test section is 11 X 11 ft in cross-section, and slotted walls provide for continuous operation throughout the complete Mach range. A facility description is contained in Ref. 8.

Figure 22 shows a sketch of a typical tail-support installation in the AMES 11 ft tunnel facility. A photograph of the Design 623-2004B model installed in the tunnel test section appears in Fig. 23.

4.2 TEST CONFIGURATION MATRIX

Nine different nozzle configurations were evaluated. Figure 24 shows that the circular nozzle and the ALBEN were tested in their unvectored subsonic cruise modes while the ADEN was tested over a range of throat area and deflection angle (geometric) settings. Figures 25, 26 and 27 present representative sketches of the actual nozzle hardware tested for the circular nozzle, ALBEN, and ADEN configurations, respectively. A comparison of the ADEN Cruise and ADEN Combat deflection angle variations is shown in Figs. 28 and 29 respectively.

Photographs of the nozzle/airframe installations are shown in Fig. 30, 31, 32 and 33. The non-afterburning (cruise) unvectored configurations are to be compared by studying Fig. 30, 31 and 32; while the extremes in ADEN VEER vectoring capability can be observed from Fig. 32 and 33.

Utilizing the nine nozzle variants noted above, a total of 13 nozzle/airframe configurations were tested. They are listed in Fig. 34 along with the corresponding average jet (throat) area per nozzle.

The three alternate (ALT.) nozzle configurations denote different nozzle hardware pieces dedicated to pressure measurements on the VEER and the ventral flap.

Additionally, the ADEN Combat 0° nozzle was retested in the presence of an ogive inlet fairing (I/F) as shown in Fig. 35. By comparing configurations ten and eight, the effect of two extremes in inlet fairing type on nozzle jet-effect increments can be studied.

All configurations were tested without horizontal tails so that any control effects unique to this airplane concept would not compromise the generalization of these test data. For example, a user would most probably apply the thrust vectoring results to a canard-type fighter; therefore, testing without horizontal tails facilitates an analytical canard-correction to these test data.

4.3 MODEL CALIBRATIONS

Prior to the wind-on operational test phase, the test program included five calibration tasks that were necessary prior to conducting wind-on runs.

(1) Model venturi mass flow calibration

(2) Nacelle and main balance calibrations (bare and installed)

(3) Assessment of nacelle and main balance bellows interactions

(4) Assessment of nacelle and main balance crossover momentum tares

(5) Asessment of nacelle and main balance static force components.

These calibration activities will be discussed briefly below.

The mass flow measuring system consisted of the facility flowmeter in conjunction with the model left and right nacelle venturi tubes. The total model mass flow was determined from total pressure and temperature measurements at the facility metering section located in the high pressure air supply line. The model venturi tubes were installed in the wing section between the fuselage and nacelle as shown in Fig. 36.

Due to manufacturing tolerances the model venturi tubes could not be expected to pass equal mass flows. Pre-test venturi calibrations, using an ASME standard

nozzle, were necessary to determine the flow-split. This split was approximately 51% and 49% for left and right hand nacelles, respectively. Knowing the split ratio and the facility total mass flow, the flow to each nacelle was then determined.

The individual right and left hand nozzle mass flows, in conjunction with the nozzle average total pressure and temperature measured at each nozzle entrance, were employed in the calculation of ideal thrust for each nozzle.

Task two is noteworthy because the importance of calibrating flowthrough balances with a simulated load point-of-application was recognized. The bellows tare force (and, therefore, balance sensitivity) is not only a function of pressure, but also is dependent upon load location (ref. 9). From the viewpoint of test technique, task three is also noteworthy because each bellows force component correction is a function of applied force, in addition to being a function of pressure level. That is:

$$\text{Bellows Axial Force} = f\,(\text{Axial Force, Bellows Pressure}).$$

Inherent in most thrust measuring systems are crossover momentum tare forces generated by an incoming momentum vector (at the metric/nonmetric interface) that is not perpendicular to axial and/or normal force directions. In this experiment, a standard ASME nozzle, whose thrust characteristics were known, was employed to obtain momentum tare corrections for the axial force, normal force, and pitching moment components of both balances.

The test technique utilized thrust measuring devices; however, the main objective of the program was to obtain thrust-removed parameters (i.e., drag, lift). It was therefore necessary to measure the static (wind-off) internal thrust components of each nozzle so that drag and lift could be determined by the method of differences. In the interest of accuracy, these static force measurements were obtained during the same "model-build" as employed for the wind-on tests. Also, three repeat runs were made over a range of exhaust back pressure levels. Thus, static thrust coefficient measurement precision was enhanced.

4.4 TEST CONDITIONS AND PROCEDURES

The six non-afterburning and the seven afterburning configurations were tested over the range of Mach number, angle-of-attack, and nozzle total pressure ratio shown in the matrices of Fig. 37 and 38 respectively. The nozzle pressure

ratio and angle-of-attack values are representative of nominal target conditions. Actual test values were somewhat different.

The test plan was to obtain data at seven Mach numbers: 0.4, 0.6, 0.8, 0.9, 0.95, 1.2, 1.4 (and/or 1.35). The heaviest emphasis was placed on the three most representative Mach numbers: 0.6, 0.9, 1.4 (1.35). Reynolds number was held constant at 8.2×10^6 per m. NPR ranges were appropriately scheduled with Mach number but always included jet-off and simulated flow-through NPR conditions at each Mach number for diagnostic purposes. A sufficient number of α- conditions were selected so that drag polars could be developed with emphasis on higher lift coefficients at the lower Mach numbers.

Grounding between metric and non-metric portions of the model occurred at certain conditions as angle-of-attack was increased. Instances of grounding were clearly identifiable, and all data contained herein is free from any type of mechanical interference effect.

Further discussion of the test condition matrix and grounding conditions can be found in Ref. 1. Also, Ref. 10 discusses this subject in detail.

The test data were obtained by first selecting the desired Mach number and Reynolds number (which was held constant at 8.2×10^6 per m. for the entire test.) An α- sweep, beginning and returning to $\alpha = 0°$, was made at jet-off conditions (designated as NPR = 1). High pressure air was then turned on and allowed to stabilize at the desired NPR. Angle-of-attack was then varied in discrete increments. After the α- sweep, the model was returned to 0° (a repeat point) and the high pressure air was adjusted to produce another NPR. At the end of each Mach number, a final jet-off data point was taken as a "second-repeat-diagnostic".

In concert with the wind-on test phase, static (M = 0) runs were made "back-to-back" with the wind-on runs. Thus, for each nozzle, static calibration running occurred during the same "model-build" as that employed for the wind-on tests. For each individual nozzle variant three static runs were conducted so that static thrust coefficients could be determined from faired curves as precisely as possible.

SECTION V

DATA REDUCTION METHODOLOGY

This section discusses the fundamentals of the data reduction methodology employed in the subject test program. The data reduction equations themselves have been adapted to the Ames time-sharing system and are available from the facility.

5.1 GENERAL PROCEDURES

The forces and moments directly measured by both the main and nacelle balances (after all component interactions were made) were corrected for: weight tares, bellows tares, momentum tares, and internal cavity pressure/area tares. The resulting net forces and moments were used directly to obtain total lift, powered thrust-minus-drag, and total pitching moment. Total axial force (AF) and total normal force (NF) measurements were used to obtain the total lift (L) and powered thrust-minus-drag (T-D) as follows:

$$L = NF \cos \alpha - AF \sin \alpha$$

$$(T\text{-}D) = AF \cos \alpha + NF \sin \alpha$$

Similarly, the thrust-removed normal and axial force parameters were utilized to obtain thrust-removed lift and drag.

The above wind-on parameters were transferred to coefficient basis by using: free stream dynamic pressure, wing reference area (6.016 ft^2; 0.559 m^2), and mean aerodynamic chord (1.787 ft; 0.545 m). Pitching moments were summed about the aircraft c.g. by effecting a moment transfer operation (Fig. 12).

At wind-off conditions (Mach = 0), force components were non-dimensionalized two ways: (1) tunnel static pressure X unit area, or (2) ideal thrust (defined as measured mass flow expanded isentropically to remote ambient pressure).

At wind-on conditions, only the main balance data was analyzed (as explained in subsection 7.1). On the other hand, at wind-off conditions both main and nacelle balance measurements were used in the analysis of static thrust force

components and moments. However, for determination of the static thrust vector angle only the nacelle balance was utilized as follows:

$$\delta_S = \tan^{-1} (-NF2/AF2)$$

External surface pressures were referenced to remote ambient pressure and non-dimensionalized with free stream dynamic pressure. Nozzle internal pressures on the other hand were ratioed to nozzle exhaust total pressure.

5.2 THRUST-REMOVED PARAMETER BOOKKEEPING

The basic measurement objective of this test was to obtained installed aircraft drag, lift, and pitching moment. These parameters must include the installation effects of the thrust vector but not the magnitude of the uninstalled thrust vector itself.

In order to predict full-scale aircraft performance, the scale model data is combined with real engine data. Real engine data is always provided in terms of static uninstalled thrust at the static uninstalled vector angle. Therefore, as a matter of practicality, the scale model installed lift and drag data must be presented in the same format - based on the removal of static thrust at the static vector angle (as opposed to wind-on thrust at the wind-on vector angle) from the wind-on thrust-minus-drag. Hence, the term "thrust-removed parameter" was originated, where it is understood that thrust refers to static thrust.

To illustrate the determination of thrust-removed parameters, the process is descriptively shown below for the drag direction (for simplicity, $P_O = P_{O_S}$):

$$F_{G_S} \cos(\alpha + \delta_S) - \left[F_G \cos(\alpha + \delta_{eff}) - D_{ext}\right]$$
$$= D_{ext} + \left[F_{G_S} \cos(\alpha + \delta_S) - F_G \cos(\alpha + \delta_{eff})\right]$$
$$= D_{ext} + (\Delta F)_D.$$

$F_{G_S} \cos(\alpha + \delta_S)$ is the static thrust component resolved in the drag direction. The combined term, $F_G \cos(\alpha + \delta_{eff}) - D_{ext}$, which is obtained directly from aircraft balance measurements, is the overall thrust-minus-drag along the wind axis. The right hand side of the equation is what is generally termed "drag", especially when applied to axisymmetric nozzles. In actuality (even for axisymmetric nozzles at some conditions) the right hand side of the equation is equal to two

terms; the external drag, D_{ext}, existing on all surfaces wetted by the free stream flow plus a thrust decrement (or increment) in the wind direction, $(\Delta F)_D$. This thrust decrement is a result of the external flow interactions with the internal flow, which alter the pressure distributions on the nozzle internal surfaces relative to static conditions (at the same nozzle pressure ratio). The sketch below provides a graphical illustration of the make-up of $(\Delta F)_D$. Note that, in general, the static and wind-on internal gross thrust vectors are characterized by different: (1) magnitudes, (2) vector angles, and (3) points of application.

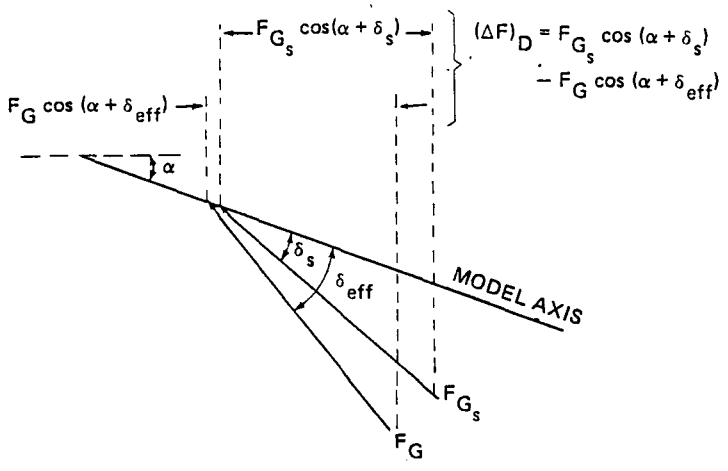

Alternatively, $(\Delta F)_D$ can be considered a nozzle internal drag rather than a thrust decrement. So the thrust-removed parameter commonly referred to as "drag", $\left[D_{ext} + (\Delta F)_D\right]$, is really the sum of both external and internal drags. This parameter includes all installation effects, relative to static conditions, due to the exhaust system and is the key parameter of interest along the wind axis.

Note that this external flow effect on nozzle internal thrust, $(\Delta F)_D$, is not simply the difference between wind-off and wind-on magnitudes resolved along the wind axis (i.e., $(F_{G_s} - F_G) \cos \alpha$). This has generally been considered the case for axisymmetric nozzles. For non-axisymmetric nozzles where, in general:

$$\delta_s - \delta_{eff} \neq 0,$$

the $(\Delta F)_D$ term is much more complex.

This same methodology, as discussed for the drag direction, can be easily applied to the lift direction and pitching moments.

For axisymmetric convergent-divergent nozzles, classified as internal expansion nozzles, ΔF (resultant of $(\Delta F)_D$ and $(\Delta F)_L$) is zero at and above the design pressure ratio. At low pressure ratios, ΔF is a small number which may be positive or negative depending on the pressure-matching boundary condition with the external flow. Generally, ΔF is less than $\pm 1\%$ of ideal thrust, and at conditions at which airplane performance is of prime importance, ΔF is negligible (ref. 6).

For the ADEN/ALBEN nozzle types, classified as internal/external expansion nozzles, ΔF is a parameter of significant magnitude (depending on Mach number and nozzle pressure ratio) that can exceed several percent of ideal thrust. ΔF is very difficult to obtain with sufficient accuracy, from nozzle thrust balance measurements because it requires taking the difference between two large numbers to obtain a small number. On the other hand, for internal expansion nozzles ΔF can be accurately determined by employing adequate pressure instrumentation on the nozzle internal surfaces downstream of the throat (choked at conditions of interest) and using a pressure/area integration technique to obtain forces. For internal/external expansion nozzles, ΔF is difficult to obtain because the internal flow is not totally contained within solid boundaries as it expands. However, substantial insight into the sensitivity of ΔF to Mach number and nozzle pressure ratio can be obtained by studying nozzle internal pressure distributions.

5.3 THRUST-REMOVED PARAMETER CALCULATION PROCEDURES

To implement the philosophy of determining thrust removed parameters, discussed in subsection 5.2, the wind-off and wind-on terms must be properly non-dimensionalized because, in general, each of these terms is measured at different back-pressures (or equivalently, at different ideal thrust levels).

The desire is to remove the exact number of pounds of static thrust that would have existed at the back pressure at which the wind-on thrust-minus-drag was measured. Thus, the static thrust (T_S) must be non-dimensionalized using the static ambient pressure (P_{O_S}) while for the thrust-minus-drag (T-D) the wind-on ambient pressure (P_O) must be used. To be truly non-dimensional, a characteristic area must also be selected. The appropriate area is the nozzle effective throat area

(geometric area multiplied by discharge coefficient; $A_j \cdot C_{dis}$). So, the appropriate determination of the installed drag (D) is as follows (at $\alpha = 0^o$ for simplicity):

$$\frac{D}{P_o A_j C_{dis}} = \frac{T_s}{P_{o_s} A_j (C_{dis})_s} - \frac{(T-D)}{P_o A_j C_{dis}}$$

Also, from one dimensional flow considerations it can be shown that:

$$\frac{P_{o_s}(C_{dis})_s}{P_o\, C_{dis}} = \frac{(F_{ip})_s}{F_{ip}}$$

where Fip is the ideal isentropic thrust. Thus, an alternative method of determining the installed drag could be:

$$\frac{D}{F_{ip}} = \frac{T_s}{(F_{ip})_s} - \frac{(T-D)}{F_{ip}}$$

These two methods are referred to as the "P_o-Method" and the "Fip-Method" respectively.

In practice, the "P_o-Method" is simplified by recognizing that

$$(C_{dis})_s = C_{dis}$$

above nozzle choking conditions (regime of greatest interest) and below choke represents an excellent approximation. Thus the working form of the "P_o-Method" becomes:

$$\frac{D}{P_o} = \frac{T_s}{P_{o_s}} - \frac{(T-D)}{P_o}$$

It is noted that the denominator of the "Fip-Method" is dependent on a larger number of experimental measurements requiring the determination of:

- Mass flow
- Tunnel ambient pressure
- Nozzle total pressure
- Nozzle total temperature.

The repeatability errors inherent in these three parameters can be avoided by selecting the "P_o-Method" in which only tunnel ambient pressure, a quantity very accurately measured, is required.

Relating to the discussion of subsection 5.2, a more general expression for the determination of the installed drag coefficient can now be written as:

$$\frac{D_{ext} + (\Delta F)_D}{q\,Aw} = \left[\left(\frac{F_{G_s} \cos(\alpha + \delta_s)}{P_{o_s}}\right) - \left(\frac{F_G \cos(\alpha + \delta_{eff}) - D_{ext}}{P_o}\right)\right] x \left(\frac{P_o}{q\,Aw}\right)_{NPR = C}$$

Another option existed in the determination of the thrust-removed parameters. Because both balances recorded static thrust components, either one might be used in the determination of thrust-removed parameters. Thus, a total of four alternative calculation methods could be used in the determination of thrust-removed parameters, as summarized in the chart below:

Balance T/R Parameters	Po-Method	Fip-Method
Main Bal. T/R Parameters using Nac. Bal. Static Thrust	1	2
Main Bal. T/R Parameters using Main Bal. Static Thrust	3	4

In this test program, the data reduction program included the capability embodied in methods 1, 2, and 3. These will be discussed in subsection 7.2.

SECTION VI

STATIC TEST RESULTS

Static tests were conducted for three reasons: (1) to obtain static thrust components so that thrust-removed parameters could be determined, (2) to obtain the static vector angle so that the thrust-removed data can be properly mated with real engine data, and (3) to study the uninstalled performance of the nozzle configurations. The model arrangement for the static tests was exactly the same as for wind-on testing. Static runs were conducted either immediately before or after the corresponding wind-on run. High nozzle pressure ratios were obtained by lowering the tunnel ambient pressure and adjusting the jet total pressure to a setting which established the desired pressure ratio level. The static test comparisons discussed herein are highlights based on the complete set of static test data presented in Ref. 1.

6.1 COMPARISON OF DATA PRESENTATION FORMATS

In this test program the static thrust components: axial force, normal force, and pitching moment have been non-dimensionalized two different ways referenced to ideal thrust or referenced to static pressure (times unit area). As explained in subsection 5.3, this provides for the determination of thrust-removed parameters by either the "Fip-Method" or the "P_o-Method".

These two presentation formats are illustrated for the nacelle balance data of the ADEN cruise 0^o configuration in Fig. 39, 40 and 41. Refer to the left vertical axis when referencing to ideal thrust and the right vertical axis for static pressure.

For axial force, the P_o-format is a "linear-type" curve. Comments on the fairing of this curve are noteworthy. It is very easy to fair at low (but greater than choking) pressure ratios where it is practically linear. Below choke it must gently fair to zero which is a straightforward graphical procedure. At high pressure ratios, care must be taken in fairing. Without an abundance of data points, a very slight error in slope is easily made, and because the slope is steep, this can lead to a relatively large error in axial force.

Physical insight can be derived from this format as illustrated by the cross-hatched area. It is determined by taking the difference between the axial force fairing and the extrapolation of the linear low-pressure ratio region of the axial force fairing to high pressure ratios. The lower boundary, the extrapolation, is the thrust of a convergent nozzle which can be shown to be linear:

$$\frac{\text{Thrust}}{P_{o_s}} = (\text{constant})_1 \cdot (\text{NPR}) + (\text{constant})_2$$

Thus, the cross-hatched region represents the "extra" thrust due to the area ratio effect relative to a convergent nozzle.

The Fip-format represents a differently shaped curve. It is very difficult to fair at low pressure ratios because of large scatter in the determination of ideal thrust coupled with an unknown curve shape in the highly overexpand region. On the other hand, at high pressure ratios when ideal thrust is large, the relatively "low-sloped" curve shape is easy to fair. These observations pertaining to fairing ease or difficulty are exactly opposite for each of the two format types. By employing an iterative fairing procedure using both methods as constraints, the optimum fairing providing the best curve fit can simultaneously be generated for each method.

Physical insight can also be gleaned from the Fip-format. For example, the difference between the peak thrust coefficient and unity represents the sum total of model scale losses relative to an ideal nozzle. One minus this loss is a measure of the nozzle efficiency. Thus, use of the Fip-format provides a handy way to evaluate competitive nozzle designs. Another example of physical insight obtained from this format occurs at low pressure ratio when the overexpanded nozzle experiences massive flow separation. This is observed by a change in the sign of the slope of the thrust characteristic notice the "hook" at a pressure ratio below two. Additionally, the Fip-format is useful in discerning the regimes of internal expansion and external expansion which occur below and above the characteristic "cusp" (NPR = 4.8). This will be discussed in subsection 6.4.

Figures 40 and 41 present normal force and pitching moment using the two different formats. The following logic applies to both these parameters. The

change in absolute value of normal force as nozzle pressure ratio is varied is dominant over the change in ideal thrust (e.g., the derivative of the Fip-format numerator, not the denominator, is the driver). Thus, unlike the axial force case, these two formats show the same kinds of shape which reflect the physical phenomena sharp changes in curve shape are perceived in both formats at the same nozzle pressure ratio. Also note that both formats portray changes in pitching moment sense at exactly the same nozzle pressure ratio as expected. Furthermore, because pitching moment is a strong function of normal force and only a weak function of axial force, the major peaks and valleys of the normal force characteristic also are perceived in the pitching moment.

For both normal force and pitching moment the P_0-format is easier to fair at low pressure ratio due to the large scatter that occurs in the ideal thrust of the Fip-format. At high pressure ratios neither format for normal force or pitching moment has any fairing advantage.

6.2 COMPARISON WITH PREDICTIONS

In a previous test (ref. 3) that employed the same model hardware and the same nacelle balance system, static thrust components were measured. Thus, predicted values were available with which the subject program static data could be compared. This will be shown for axial and normal thrust coefficients for the configurations showing the "best" and "worst" agreement.

Figures 42 and 43 present the axial force results for the best and worst agreement cases respectively. The combat 0° faired characteristic is within ±3/4% of the predicted value, while the cruise 10° faired characteristic is typically 1 3/4% to 2 3/4% higher than the predicted value. However, observe that the curves shapes are very similar.

Figures 44 and 45 present the normal force results for the best and worst agreement cases respectively. The cruise 10° fairing is in excellent agreement with the predicted value - generally, within 1%-2% of ideal thrust. The cruise 0° fairing is in good agreement with the predicted value at moderate nozzle pressure ratios; however, at the low and high pressure ratios a disparity of several percent of ideal thrust exists. Upon investigation into the previous test, it was discovered that

a dearth of data characterized these low and high pressure levels thus precluding accurate fairings for these "roller-coaster" type characteristics.

Since true absolute levels are not known, it is impossible to favor either the predicted values or the results from the subject program. Nevertheless, this comparison study did provide a measure of confidence because no gross differences were observed between the results of the two static test programs.

6.3 MAIN VS. NACELLE BALANCE

Under static conditions both main and nacelle balances are capable of measuring static thrust components. The comparison between balances is presented in this subsection and is illustrated with data from the ADEN Combat 0^{o} nozzle for which four static runs existed. Fig. 46 and 47 present axial force coefficient while Fig. 48 and 49 present normal force coefficient for the main and nacelle balances respectively.

First, addressing data scatter (a measure of repeatability) it is generally seen that the main balance axial force exhibits comparable scatter to that of the nacelle balance (both nominally ±1 1/4% or better). On the other hand, the main balance normal force scatter band is more than double that of nacelle balance. The above degrees of scatter are common for thrust-component measuring systems and are to be expected based on the balance capacity discussion of subsection 3.2. But, the importance of repeat runs is obvious, and by utilizing such repeats, the data can be faired reasonably well as shown in the figures.

Occasionally the 5000 lb main balance normal force capacity exhibited unusually large scatter while measuring the relatively small nozzle normal force loads (typically 0 to 100 lb) at static conditions. This is shown in Fig. 50 for the ADEN Dash nozzle. In this instance it would have been desirable to have made additional repeat runs had economic considerations allowed. However, using the more accurately determined nacelle balance normal force trend as a guide, a "best compromise" faired curve was developed by favoring certain data points over others.

It is noted that a probable uncertainty in the "worst-case" main balance normal force of Fig. 50 is ±5% of ideal thrust. This converts to less than a ±.005 uncertainty in lift coefficient at a typical subsonic cruise condition. Since aeropropulsion benefits, in thrust-removed lift coefficient of 0.05, at least, are being sought, the occasional 0.005 uncertainty in main balance static lift coefficient was not as serious as it initially appeared.

Now, using the main balance and nacelle balance faired curves, the absolute values of the balance thrust characteristics can be compared. This is done for the ADEN Combat 0^{o}, 10^{o}, 20^{o} family of nozzles for which the variation in mass flow, axial force and normal force is the largest. Fig. 51 shows that the axial force coefficient levels for each balance are generally within 1% - a very acceptable tolerance. As shown in Fig. 52, the difference between balance normal force levels is larger as expected. However, the normal force trends are very similar, and when these differences are converted to a lift coefficient (as opposed to an ideal thrust) basis the discrepancy is rendered virtually meaningless (as illustrated previously).

The main and nacelle balance differences discussed above for the axial and normal directions will be correspondingly reflected in static pitching moment and vector angle since both of these parameters are a function of axial and normal force.

It is concluded that both balances agree acceptably well in view of: (1) their different full scale capacities, and (2) the reduced sensitivity of the thrust-removed parameters to uncertainties in normal force compared to axial force. The relative behavior of both balance systems was as expected.

6.4 AXIAL FORCE PERFORMANCE COMPARISONS

This subsection presents the results of four static axial force studies:

(1) Effect of unvectored nozzle type

(2) Effect of jet area variation

(3) Effect of cruise nozzle vectoring

(4) Effect of combat nozzle vectoring,

Each will be discussed below. Either balance could have been used for this axial force study since data trends (relative differences among nozzle types) are the same within a ±1% (of ideal thrust) tolerance. However, for this presentation of static axial force, the nacelle balance has been selected because the main balance was subjected to an additional calibration for some configurations as discussed in detail in Ref. 10. Thus, somewhat more confidence is assigned to the nacelle balance static axial force absolute performance levels.

Figure 53 shows the internal performance for the non-afterburning unvectored ADEN Cruise 0°, the ALBEN, and the circular nozzle. As opposed to the circular nozzle, the two non-axisymmetric nozzles exhibit two "peaks", typical of internal/external expansion nozzles. The peaks occur at nozzle pressure ratios associated with the internal and the external area ratios. At a typical cruise pressure ratio of about six, the model ADEN tested shows a 1 1/2% performance decrement relative to the circular nozzle, while for the model ALBEN, it is 4%. It is noted, however, that had the main balance been used for this comparison, the ALBEN penalty would have been 3%. A previous test (ref. 3) of the same model hardware has shown this same penalty to be 2%.

This is a good example to illustrate that a tolerance must be applied to virtually every test result — a simple concept but often ignored.

It is further noted that the ADEN and ALBEN configurations tested in this program represented designs that were on the drawing boards at the time the model lines were frozen. Since then, the ADEN and ALBEN have been optimized, and subsequent static test results (ref. 4 and 5) demonstrate greater than a 1% improvement for the ADEN and greater than a 2% improvement for the ALBEN. It is therefore concluded that the non-axisymmetric ADEN and ALBEN can be designed to exhibit internal performance characteristics that only suffer small penalties relative to the axisymmetric baseline nozzle.

Figure 54 shows the internal performance variation as the ADEN jet area is opened from cruise to dash (partial afterburning) to combat (maximum afterburning) settings. Referring to Fig. 27, note that as jet area is increased, the external area ratio decreases because of the collapsing throat mechanism. This is the opposite of what has traditionally been the case for circular nozzles when the throat opens up the area ratio generally increases accordingly. Therefore, the superior performance, at the higher pressure ratios, of the smaller jet area nozzles relative to the combat can be understood. This is a "first-order" explanation because turning angles and flow path contour vary simultaneously with area ratio as jet area is increased. The main point is that the internal performance trends with jet area for the asymmetric ADEN are much different, and much less amenable to analytical prediction, than those for axisymmetric nozzles.

Figure 55 presents the internal performance variation as the ADEN Cruise configuration is vectored. As expected, the performance decreases as the VEER is rotated downward. This decrease is due to supersonic flow turning, which causes the shock system within the nozzle to change location and strength as the VEER is vectored. Also, note the consistency of the "cusp" movement and the greater prominence of the double-peaks as vector angle increases.

Figure 51 presents the internal performance variation as the ADEN combat configuration is vectored. The combat 10^{o} nozzle shows slightly better high pressure ratio performance than the 0^{o} configuration. This is opposite to the non-afterburning vectoring trend of Fig. 55. However, the flowpaths of the cruise and combat nozzles are very different. Furthermore, the combat 10^{o} nozzle exhibits much less total flow turning (from nozzle entrance to exit) than its cruise 10^{o} counterpart. Thus, it is conceivable that the optimum VEER setting could be closer to 10^{o} for the combat flowpath while for the cruise flowpath it is perhaps closer to 0^{o}. It is noted that the main balance results portray exactly the same trends as those just discussed for the nacelle balance. On the other hand, previous static tests (ref. 3) with the same model hardware show the combat 10^{o} nozzle performance to be about 3/4% lower than the combat 0^{o}. Thus, a small inconsistency has resulted. As discussed earlier in this subsection, we are reminded that a tolerance must exist on any test result; and certainly differences between configurations that approach the 1% level should be labeled "too close to call". It is therefore concluded that the combat 0^{o} and 10^{o} nozzles possess competitive performance while the combat 20^{o} suffers the distinct penalty as expected.

For these relatively low vector angles, the axial force dominates over the normal force in the Theorem of Pythagorus; thus the resultant performance would be very similar to the axial performance trends. This is substantiated in Ref. 3. Hence, the ADEN resultant vector performance is not discussed herein. However, the normal force performance and the static vector angle will be discussed in the ensuing subsections.

6.5 NORMAL FORCE PERFORMANCE COMPARISONS

As with subsection 6.4, this subsection presents the results for four static normal force studies:

(1) Effect of unvectored nozzle type

(2) Effect of jet area variation

(3) Effect of cruise nozzle vectoring

(4) Effect of combat nozzle vectoring.

Based on the accuracy discussion of subsection 6.3, it is clear that the nacelle balance, rather than the main balance, results should be used for the static normal force study.

The normal force coefficient for the unvectored test nozzles is shown in Fig. 56. The circular nozzle positive normal force is a direct result of the nozzle being installed in a canted fashion (trailing edge down $\sim 4^{o}$). The normal force coefficient is relatively constant until the nozzle becomes overexpanded at low pressure ratios and then it gradually decreases. The ADEN and ALBEN show large "roller-coaster" type variations due to an unbalanced downward vertical force resulting from the pressure patterns established on the divergent flap and VEER caused by the asymmetric flowpath. This force varies with nozzle pressure ratio because it governs the shock pattern and expansion characteristics through the supersonic turn.

Figure 57 compares the internal performance for the jet area progression: ADEN Cruise 0^{o}, Dash, Combat 0^{o}. Remember, as stated in subsection 6.4, as jet area increases, area ratio, turning angle and flow path geometry all vary simultaneously. Note that the partial-afterburning dash nozzle, behaves more like the non-afterburning cruise nozzle then the afterburning combat nozzle. As can be observed from Fig. 27, although partially collapsed, the throat geometry of the dash nozzle resembles the cruise nozzle throat and flowpath more closely than it does the combat nozzle. Both the cruise and dash nozzles feature relatively large total turning angles relative to the fully collapsed throat of the combat nozzle. Over the operating range of interest, the ADEN Cruise and Dash nozzles exhibit a negative normal force while the ADEN Combat nozzle is characterized by a positive normal force.

Figure 58 shows the effect of ADEN Cruise nozzle vectoring on normal force. Except at very low pressure ratio, traditionally the region of large data scatter in thrust component coefficients, the data trends are virtually identical for the three different VEER settings. Naturally, the absolute levels vary as expected.

In contrast, the ADEN Combat vectored normal force results of Fig. 52, do not exhibit the marked "roller-coaster" characteristics, of the ADEN Cruise nozzles

because the total flowpath turning angle is much less. It is very significant, for the ADEN Combat family, that for constant VEER deflection angle, the normal force variation is as large as 10% to 20% of ideal thrust over a typical nozzle pressure ratio range of interest. This results from the intentional asymmetric nature of the ADEN coupled with an internal shock system whose strength and location is very sensitive to nozzle pressure ratio (see subsection 7.11).

6.6 STATIC VECTOR ANGLE COMPARISONS

As in the case with the normal force study of subsection 6.5, the nacelle balance is to be used for the vector angle study. Figures 59, 60, 61 and 62 present the same sequence of comparisons as was done in the previous two subsections. Observe that these curves possess exactly the same shapes and relative differences as their normal force counterparts of subsection 6.5. This is as expected because the change in axial force with respect to nozzle pressure ratio is almost constant, while the corresponding variation in normal force can exceed several hundred percent; and clearly, it is the driver (recall the similar logic of subsection 6.1). This can be observed from Fig. 39 and 40. Thus, the complete discussion of subsection 6.5 is also applicable here.

To sum up, the thrust vector angle variations with nozzle pressure ratio are caused by the ADEN asymmetric flowpath. This is manifested by unbalanced pressure forces that vary with nozzle pressure ratio and VEER setting. The measured vector angle is the actual direction of the resultant thrust vector produced by a combination of the momentum efflux and a pressure/area force at the effective exit plane.

The vector angle is only occasionally and coincidently equal to the geometric angle (at select nozzle pressure ratios) for the ADEN and ALBEN. Only for the circular nozzle, as expected, is the vector angle constant (except below choke). For the asymmetric nozzles, the static vector angle can not only vary by, but also differ from the geometric angle by, 5^{o} to 10^{o}. This is very significant and means that the full scale ADEN VEER should be continuously modulating and linked to the flight control system.

Intentionally Left Blank

SECTION VII

WIND TUNNEL RESULTS

This section presents and interprets all major wind-on test results. The philosophy of approach, as outlined below, discusses the rationale underlying the selection of material which properly represents the highlights of this test program.

7.1 PHILOSOPHY OF APPROACH

At least one chart, and usually more, is included to highlight each and every study that can be made with the data. Emphasis is placed on Mach and nozzle pressure conditions that represent major mission points/legs for this typical V/STOL design air vehicle. Additionally, emphasis is placed on presenting data that is new and likely to be of greater interest to the technical community. The following subsections are organized into various categories that represent the major studies of this test program. Force data, external surface pressure data, and nozzle internal pressure data are presented.

All of the force data shown in this Section were measured on the main aircraft force balance. The nacelle balance, which was useful for the static test, as discussed in Section 6.0, cannot be used for the wind-on performance studies. As will be demonstrated in subsection 7.10, nozzle induced disturbances travel much further upstream and spanwise than the limited metric zone of the nacelle balance. Thus this balance, at best, can only be used as a diagnostic tool to support trouble-shooting procedures. On the other hand, the main balance perceives all jet-induced phenomena and is the appropriate instrument to be used for data presentation.

Most force balance results are presented in terms of the thrust-removed parameters discussed in Section 5.0. Thrust-removed parameters are the appropriate data presentation vehicle because they include all basic aerodynamic effects plus all installation (both jet-induced and external-flow-induced) effects. The figure of merit is the thrust-removed polar because both the thrust-removed drag and lift components are nozzle dependent (power sensitive) for this type of underwing/nacelle installation (ref. 3). Therefore greater emphasis will be placed on

presenting the thrust-removed drag polar as opposed to lift and drag separately. A second reason for presenting the thrust-removed parameters (rather than thrust-included parameters) is that they provide the proper format for mating with the real engine data to obtain the total vehicle performance for a given mission.

However, as a point of interest, the thrust-included parameters (total lift and thrust-minus-drag) will be presented occasionally for comparison and academic purposes. The temptation to use these powered polars as the "bottom-line" to rank configurations should be resisted. Scale model static thrust differences between configurations do not necessarily reflect the actual real-engine operation where all candidate nozzles would be sized for a common effective throat area and where such full scale effects as cooling and leakage are properly accounted for.

7.2 COMPARISON OF DATA REDUCTION METHODS

In the data reduction discussion of subsection 5.2, the point was made that the "P_O-method" and the "Fip-method" would be theoretically equivalent if the static and wind-on-discharge coefficients were equal. Figure 63 presents discharge coefficient data for the ADEN combat 0^O nozzle. Note that the typical wind-on (Mach 0.9) data falls within the repeatability bandwidth of the static data. Theoretically, this is to be expected above the choking pressure ratio. At low pressure ratios the discharge coefficient increases to values exceeding unity because the unchoked mass flow equation is intentionally used for NPR < 1.89. Actually, a convergent-divergent nozzle remains choked below this value at which purely convergent nozzles become unchoked. The interesting point, however, is that the static and wind-on data are in accord even at the very lowest pressure ratios where the possibility of unchoking exists. Thus, over the whole pressure ratio range, the theoretical equivalency of the P_O- and Fip-Methods has been demonstrated.

Subsection 5.3 discussed four alternative calculation methods (using either main or nacelle balance static thrust data in conjunction with either the P_O- or Fip-Method). Three of these methods have been included in the data reduction procedure of this program. They are:

(1) NBTP - Nacelle Balance (Static) Thrust; P_O-Method

(2) NBTF - Nacelle Balance (Static) Thrust; Fip-Method

(3) MBTP - Main Balance (Static) Thrust; P_O-Method

These three methods are compared at a subsonic non-afterburning and a supersonic afterburning condition. Figure 64 shows no difference exists among the methods for lift coefficient. Any differences in normal force (~ lift) due to measurement uncertainty or human error (data fairing) are so small that they are imperceptible on this standard lift coefficient scale (0.10 per inch). This was generally true for all nozzles so that lift coefficient need not be considered in the process of selecting a particular data reduction method.

On the other hand the drag coefficient did display significant differences for all nozzles. Figure 65 shows a comparison of the three methods in the drag direction for the ADEN Cruise 0^{o} nozzle. This disparity was typical although some configurations exhibited slightly less and/or somewhat greater differences between methods. Since lift is literally independent of method type, the drag differences are directly reflected in the polar differences of Fig. 66. A typical maximum disparity, depending on lift coefficient (or angle of attack), is 10 to 20 drag counts.

Similarly, at M=1.4 the same presentation is made for the ADEN Dash nozzle for thrust-removed drag (Fig. 67) and the drag polar (Fig. 68). The typical maximum disparity is approximately 15 drag counts over the angle-of-attack range.

Using this type of polar comparison, many charts for all nozzles were prepared that summarize the differences between the three methods for various combinations of Mach number, nozzle pressure ratio and lift coefficient. A typical example is shown in Fig. 69 for four configurations at Mach 0.9 and two configurations at M=1.4. This figure represents six of almost 100 combinations that were studied.

One criterion for selecting the favored data reduction method could be based on the percentage of time that this particular method featured drag levels in between the other two methods. The chart below summarizes the statistics.

DRAG POSITION	METHOD		
	NBTP	NBTF	MBTP
Lowest	16%	41%	43%
Middle	32%	22%	46%
Highest	52%	37%	11%

It could be concluded that the single Fip-Method (NBTF) should immediately be discarded because only 22% of the time does its drag appear in the desired middle

position. Of the other two P_0-Methods, the one using the main balance (MBTP) clearly is the winner for it occupies the middle position much more frequently (46% vs 32%) and holds its worst extreme position less frequently (43% vs 52%).

This rudimentary analysis was only one element in the selection process. Other considerations are discussed below.

(1) Method NBTF introduces large error at low nozzle pressure ratios (see Fig. 65) due to the difficulty in fairing the very steep-sloped thrust characteristic (non-dimensionalized with ideal thrust) as nozzle pressure ratio is decreased towards unity.

(2) In addition to the balance measurement, the NBTF method relies on the measurement of jet total pressure, jet total temperature, tunnel static pressure, and most important, mass flow. On the other hand, the two P_0-Methods only require a corresponding single measurement - tunnel static pressure. Thus the NBTF method can suffer from an accuracy problem. For example, Fig. 63 shows that the repeatability error in mass flow, as reflected by the discharge coefficient, is about ±1 1/2%.

(3) Utilization of the single nacelle balance hinges on the implicit assumption, that the non-dimensional thrust characteristic developed by the left nozzle is applicable to the right nozzle. This is a good assumption as long as the nozzle flow paths are fabricated identically. But throat area measurements of some nozzles differed by up to 2 1/2% between left and right hand sides.

(4) Good experimental practice dictates that the thrust which is removed should be measured by the same physical instrument as the thrust-minus-drag from which it is removed. Note that the NBTP and NBTF methods remove a static thrust that is based on nacelle balance measurements from the thrust-minus-drag measurement of the main aircraft balance. This allows for the possible existence of bias errors. Furthermore, as explained in detail in ref. 10, the main balance axial measurements required a post test correction for some configurations. Since this correction affected both static and wind-on runs, its effect tends to cancel in the MBTP method of calculating the thrust-removed parameters. Thus less

risk is associated with the selection of the main balance static thrust rather than the nacelle balance thrust.

(5) For a limited number of configurations (ADEN Combat 0^{o} and ALBEN), a possibility of mechanical restraint, resulting from plastic pressure tubing, could have affected the nacelle balance slightly.

Based on the above observations in conjunction with the statistical study described previously it was concluded to utilize the MBTP method for final data reduction. All of the data presented hereafter in this report are based on main aircraft balance measurements using the P_{o}-Method.

7.3 ANALYSIS OF AEROPROPULSION PARAMETERS

A complete set of the important aeropropulsion parameters is presented in this subsection for the primary ADEN Cruise 0^{o} configuration at a typical subsonic cruise Mach number for this V/STOL air vehicle.

Figures 70 and 71 show basic thrust-removed lift and drag data plotted and faired versus angle-of-attack for families of nozzle pressure ratio. (This was done for all pressure ratios - only three are shown herein for clarity.) In this relatively low range of angle-of-attack, where vortex lift effects are negligible, all the lift characteristics are virtually linear; thus, the data is easy to fair. Also note that drag characteristics have the familiar "parabolic shape" showing that minimum drag occurs at about 1^{o} for subsonic speeds. At supersonic speeds this critical angle-of-attack is negative for this aircraft design.

Using these two fundamental formats, crossplots of thrust-removed lift and drag were created against nozzle pressure ratio for families of constant angle-of-attack. These are shown in Figs. 72 and 73. Note for this underwing ADEN installation that lift is sensitive to power. This is in contrast to aft-mounted axisymmetric installations where lift is insensitive to power. Also observe that the jet-on lift levels are all higher and the jet-on drag levels are all lower than that jet-off counterparts as expected.

From these faired crossplot formats versus nozzle pressure ratio, the thrust-removed polars, at constant power setting, could be developed as shown in Fig. 74. The reasons for undertaking this fairing/crossplotting procedure in order to develop

the thrust-removed polars (as opposed to plotting them directly from unfaired data) are three-fold:

(1) Data scatter is reduced

(2) Component plots are useful for trouble-shooting purposes and also aid in understanding the physical phenomena

(3) Test data were often taken at non-constant angles-of-attack and nozzle pressure ratio. To facilitate configuration comparisons at constant conditions the above crossplotting procedures were necessary.

Note that the untrimmed polars of Fig. 74 demonstrate that the ADEN underwing installation possesses very significant power effects. At zero lift the jet-off to jet-on (NPR=6) drag reduction is about 40 drag counts and at lifting conditions becomes somewhat greater.

Observe that the power effects are different when interpreted at constant lift coefficient as opposed to constant angle-of-attack (the traditional manner of assessing jet-effect increments). This is especially important at higher attitudes; for example, from Fig. 73 at 6^{o} the maximum jet-off/on increment is about 20 counts, while at a 0.27 lift coefficient (corresponds to 6^{o} angle-of-attack for jet-off conditions) the maximum spread is 55 counts as shown in Fig. 74. This is a good example of aeropropulsion interaction which exists because this V/STOL configuration is lift sensitive to power.

A vehicle performance analysis requires that pitching moment characteristics be developed in addition to the untrimmed polars. A typical set of thrust-removed pitching moment characteristics appears in Fig. 75. At subsonic speeds pitching moment becomes more positive (nose-up) as lift is increased, and this requires increased trim as expected. All jet-on characteristics generally follow the same trend which is somewhat different from the jet-off characteristic. This results in a pitching moment jet-effects increment that becomes either more favorable or less unfavorable in magnitude as angle-of-attack is increased.

Figure 76 presents a sample set of thrust-included or powered polars. Naturally, as nozzle pressure ratio is increased the drag-minus-thrust coefficient rapidly transists from positive to large negative numbers. As pointed out in subsection 7.1, care must be used when comparing different scale model nozzles on a powered polar basis.

Both the thrust-removed pitching moment characteristics and the powered polars were generated by first plotting versus angle-of-attack and then crossplotting versus nozzle pressure ratio as discussed above for the thrust-removed polars.

7.4 COMPARISON OF NON-AFTERBURNING NOZZLE TYPE

This subsection is aimed at studying the integration differences and performance of non-axisymmetric nozzles in the unvectored mode, compared to an axisymmetric baseline nozzle. Even without considering adding thrust vectoring capability to non-axisymmetric nozzles, substantial improvements are realized because of improved nozzle/airframe integration relative to an axisymmetric installation. This will be discussed below for non-afterburning nozzles at subsonic and supersonic speeds.

Figure 77 shows a typical jet-effect increment for the circular nozzle installation. Observe that the jet-off/on drag increment is favorable, as it was for the ADEN Cruise 0^{o} (Fig. 74), but is much smaller in magnitude (about 20 drag counts compared to 40 drag counts for the ADEN Cruise 0^{o} at zero lift conditions). Furthermore as discussed in subsection 7.3 the jet-effects increment for the ADEN improves with lift while for the circular, the increment is relatively insensitive to lift.

Other fundamental differences between the ADEN and circular installations are clear from Fig. 78. The circular configuration lift characteristic is constant with power except that when the jet is first turned on some initial drag clean-up, due to blockage effects, occurs. On the other hand, the ADEN exhibits a lift sensitivity to power over the complete nozzle pressure ratio range in addition to a significant drag clean-up effect from jet-off to jet-on. This is an example of aeropropulsion coupling for the highly integrated ADEN underwing nacelle installation.

Figure 79 compares the thrust-removed polars for the ADEN and circular nozzle at Mach 0.6 (the ALBEN was not tested at this condition). The ADEN polar not only exhibits a lower (32 counts) zero lift drag but also is characterized by an improved polar shape compared to the circular installation; the ADEN drag reduction at a 0.25 lift coefficient increases to 48 counts. It is concluded that the ADEN integrates better with the wing than does the circular nozzle.

The projected nacelle/nozzle area distributions of Fig. 80 provide insight into the drag differences between the ADEN and circular nozzle installations. The curves represent the cumulative total of all projected area that is wetted by the

external flow aft of the nacelle maximum area station. As noted in the figure, the circular nacelle/nozzle assembly possesses about 20% more total projected area and 14% more overall length. Since both nozzles are nominally sized to the same throat area, this 20% is essentially equivalent to the ADEN's internal ramp axial projected area that is wetted by the internal flow. In progressing from the circular to the ADEN, the external boattail area of the former has been traded for internal projected area of the latter. The hope is that external drag will be reduced without attendant decreases in internal thrust (or with possible increases in internal thrust).

Due to the greater projected area of the circular nacelle and its larger slope over the nozzle boattail region, it is not surprising that the measured drag levels exceed the ADEN's. These differences, coupled with a small additional friction drag penalty (5 counts) due to more surface area (126 sq in. model scale) for the circular installation, are largely responsible for the drag deltas at zero lift. As explained above for Mach 0.6, the zero lift drag increment is then increased at lifting conditions because the ADEN/wing combination is more efficient than the circular nozzle/wing combination.

At Mach 0.8, the ADEN and ALBEN are compared (the circular nozzle was not tested at this condition) in Fig. 81. The ALBEN polar shows a slight improvement over the ADEN. This was as expected because the anticipated large drag clean-up effect is realized when the ADEN replaces the circular nozzle; but the ALBEN which is only a refinement (note rounded corners for example by comparing Fig. 31 and 32) over the unvectored ADEN was expected to yield a correspondingly smaller drag reduction.

At Mach 0.9, all three non-afterburning nozzles were tested and are compared in Fig. 82. The same general trend is observed again - large differences ($\sim$ 50 drag counts) between the non-axisymmetric and axisymmetric installations while only a small difference exists between the two non-axisymmetric nozzles. Note however that the ADEN and ALBEN have reversed relative positions compared to Mach 0.8; this was not anticipated. It is concluded, however, that this test could not discriminate between the ADEN and ALBEN drag differences which were generally under 10 counts (see accuracy discussion of Section 8.0). It is concluded

that the ADEN/wing and ALBEN/wing combinations achieve a better integration of lifting and propulsive elements than the circular nozzle/wing combination due to the more favorable interactions of the two-dimensional geometry with the wing.

Insight into the significant performance differences between the ADEN and circular nozzle installations is obtained by studying surface pressures. Representative pressure distributions acting on the projected area for the ADEN and circular configurations appear in Fig. 83. Upper and lower nacelle centerline distributions are compared. On the upper surface the nacelle does not sense the presence of nozzle type until after the flow expansion that occurs in the vicinity of the upper surface metric break station. The trailing edge of the wing flap experiences a more favorable recompression for the ADEN. The circular nozzle extends downstream of the wing trailing edge; its maximum recompression level must necessarily occur at the boattail terminus where it is equivalent to the ADEN maximum recompression level. It is concluded that dramatic differences are not observed on the upper surface.

On the lower surface, under the wing where the differences between the 2-D and axisymmetric geometries are particularly obvious, the pressure characteristics exhibit significantly different trends as far upstream as the maximum nacelle area station. The peak flow expansion is much more negative for the circular than the ADEN (about $-.50\ C_p$ compared to a $-.30C_p$). This is also true for inboard and outboard ($\pm 90^o$) meridians of the circular nozzle, which exhibit almost identical expansion/recompression characteristics as the bottom centerline (180^o) meridian. Note that the critical pressure coefficient is -0.19, so that the recompression characteristics for both nozzles are initiated by a shock system, which by necessity is much stronger for the circular installation.

On the lower nacelle surface the pressure characteristic at an operating nozzle pressure ratio is compared with one at jet-off conditions. As can be seen, the power effect is felt far upstream of the nacelle balance metric system, especially for the ADEN. It is therefore clear, as stated in subsection 7.1, that even for the unvectored nozzles the main aircraft balance must be used to account for all power effects. Note that the distribution at a nozzle pressure ratio of six is significantly less negative than the jet-off distribution. This is in accord with the force balance data which show the jet-on polar to be more favorable than its jet-off counterpart.

Figure 84 presents the powered (thrust-included) polars which are the counterparts of the thrust-removed polars of Fig. 82. Note that the relative positions of the nozzles are very much different. The discussion of subsection 7.1 indicated that caution must be exercised when interpreting the powered polar results. The most apparent anomaly between Fig. 84 and 82 is that the ADEN shows much more drag (less thrust-minus-drag) than the circular nozzle. The explanation is, at the same nozzle pressure ratio, that the circular nozzle is passing much more mass flow for two reasons:

(1) Circular nozzle jet area is 5.2% larger than the ADEN jet area (see Fig. 34)

(2) Circular nozzle discharge coefficient is estimated to be about 2 1/2% greater than the rectangular-throated ADEN Cruise nozzle.

Therefore the circular nozzle is flowing almost 8% more mass, or equivalently, producing 8% more ideal thrust. For this V/STOL vehicle design, 8% of ideal thrust converts to over 70 counts of drag (at Mach 0.9 and a nozzle pressure ratio of six). Thus, this adjustment for effective throat area mismatch shifts the ADEN powered polar to the left of circular nozzle now demonstrating the same trend as the thrust-removed polars of Fig. 82.

The same logic can be applied to the ALBEN but to a lesser degree because the ALBEN jet area was only 1.3% smaller than the circular nozzle, and the discharge coefficient of the elliptical-throated ALBEN would not suffer the same penalty that the ADEN does relative to the circular nozzle.

The important point is that if powered polars are to have any meaning, all thrust-minus-drag and total lift data must be adjusted to reflect the same engine operating condition for each nozzle (e.g. same geometric throat area multiplied by discharge coefficient). Nonetheless, as discussed in subsection 7.1, the proper procedure for ranking nozzles is not with the powered polars (even if adjusted), but instead by mating the thrust-removed polars to the real engine data for a given mission.

It was noted in subsection 6.4 that the ADEN and ALBEN tested in this program represent early vintage single expansion ramp nozzle designs. Reference 4 and 5 have reported substantial internal performance improvements for both the ADEN and

ALBEN. Assuming the integration aspects of the newer designs are at least as good, then it is concluded that powered polar benefits (after the necessary effective flow area adjustment to Fig. 84 are completed) of the ADEN and ALBEN are in excess of those suggested above.

The ADEN, ALBEN, and circular nozzle sequence was also tested supersonically. The two asymmetric nozzles were tested at Mach 1.35 while the circular nozzle was tested at Mach 1.4. Initially, concern was expressed over making any comparison because of the inconsistency in Mach number. An initial attempt was made to adjust the data by making use of the similarity parameter:

$$\left(\frac{C_{D_1}}{C_{D_2}}\right)^2 = \frac{M_1^2 - 1}{M_2^2 - 1} \quad ; \text{ for } M > 1.0$$

However this proved unsatisfactory because it over-predicted the drag differences (between Mach 1.35 and 1.4), and of course could provide no adjustment for the lift direction. This confusion was circumvented by observing the following. Figure 85 shows a single available Mach 1.4 data point ($\alpha = 0^o$) that is consistent with the faired Mach 1.35 polar. Note however that it corresponds to a slightly higher lift and lower drag level (but the lower drag level is not nearly as low as what would be predicted by the similarity parameter). It was therefore concluded that the best approach to be used in comparing the ADEN and ALBEN to the circular nozzle was to utilize the Mach 1.4 data as if it were Mach 1.35.

Figure 86 shows the same general result that was found at subsonic speeds - the axisymmetric nozzle installation is characterized by a higher drag level while the two non-axisymmetric nozzle installations are competitive at a lower drag level. It is to be remembered that these nozzles were compared in their non-afterburning modes, so the result shown in Fig. 86 would be applicable to a dry supercruise installation.

The performance benefits displayed by the ADEN and ALBEN drag polars compared to the circular nozzle drag polar must be adjusted for pitching moment considerations. For example, it is conceivable for a candidate nozzle to possess integration drag benefits that are cancelled or significantly reduced by an excessive trim drag

penalty. Fig. 87 presents the effect of nozzle type and power on aircraft tail-off pitching moment. The Mach 0.9 results which indicate an unstable situation ($dC_M/dC_L > 0$) are representative of the trends measured over the 0.4 to 0.95 Mach range. The Mach 1.35 slopes, which are indicative of a stable condition ($dC_M/dC_L < 0$) also reflect trends measured at Mach 1.2. It is noted that the airplane was intentionally designed to be statically unstable (with tail-on) at subsonic speeds, because fly-by-wire technology was employed to reduce trim penalties relative to those of a statically stable configuration.

The figure demonstrates the significant effect of nozzle type at subsonic cruise conditions. At a lift coefficient of 0.25 and a nozzle pressure ratio of six the ADEN possesses an improvement in pitching moment coefficient of almost 0.04 relative to the baseline circular nozzle. Thus, it is concluded that the ADEN installation is favorable for trim and the total performance improvement of the ADEN is in excess of the magnitudes presented in Fig. 82. The same conclusion is applied to the ALBEN whose pitching moment characteristics are very similar to those of the ADEN.

The two nozzles portray different subsonic power trends. The ADEN shows decreases in pitching moment as NPR increases progressively from jet-off to 3.0 to 6.0. These decreases are manifested as a zero lift pitching moment shift rather than as a slope/stability change. The circular nozzle shows a small pitching moment increase from jet-off to jet-on conditions.

At supersonic speeds, the ADEN installation is only slightly more favorable for trim than the circular nozzle as shown in the right hand portion of Fig. 87. Note that the supersonic pitching moment characteristics portray a slope change relative to the subsonic characteristics as mentioned above.

In summary, it is reiterated that consideration must also be given to the relative uninstalled full-scale engine thrust levels of the ADEN, ALBEN and circular nozzles in order to complete the total performance evaluation of candidate nozzles. Model scale uninstalled thrust comparisons show that the ADEN and ALBEN can be designed to produce static thrust characteristics that are competitive with circular nozzles. With the latest advanced cooling techniques applicable to non-axisymmetric nozzles, currently being developed under recent studies (ref. 11 and 12), the ADEN and ALBEN gross thrust need not be penalized for nozzle cooling losses and the associated cycle derating. Thus, a 50 count Mach 0.9 ADEN or ALBEN

installation drag reduction, when corrected for full-scale uninstalled thrust differences, remains intact.

7.5 EFFECT OF JET AREA VARIATION

The purpose of this subsection is to study the aerodynamic performance increments caused by the unvectored ADEN modulation from non-afterburning (cruise) to partial-afterburning (dash) to maximum-afterburning (combat). Recall (Fig. 1) that as the ADEN throat opens, the upper boundary collapses while the lower boundary (ventral flap) rotates downward. The former is an internal effect while the latter is an external effect. As opposed to a simple axisymmetric convergent nozzle where the increased throat area is reflected as a corresponding reduction in boattail area, only a portion of the ADEN throat area increase is manifested by reduced external boattail area. Therefore, it might be argued that less dramatic drag changes might be expected; however, the data show significant drag effects due to ADEN jet area variation.

The results in this section will, out of necessity, be presented in terms of the drag polar. The "nozzle open/nozzle closed" increment (jet area drag increment) is a function of lift (or angle-of-attack) for the ADEN, so merely studying the drag component alone, as has been traditionally done for axisymmetric nozzles, is not sufficient.

First, the effect of jet area variation at jet-off conditions will be discussed. Figure 88 shows the jet-off polars for the two subsonic Mach numbers at which all three jet area variation nozzles were tested. At both speed regimes the jet-off polars are all very close - typically within ± 7 counts (at constant lift) of the mean. Based on accuracy considerations (Section 8.0), these differences may be "too close to call", although for both data sets, the combat nozzle generally portrays the highest drag. This can be rationalized by noting that the base drag penalty of the larger base area must exceed the boattail drag reduction benefit of the smaller projected boattail area for the combat nozzle.

The Mach 0.9 data show the expected drag rise phenomenon relative to Mach 0.6. Also the magnitude of this drag increment varies with lift increasing from a nominal 40 counts to as much as 70 counts at the highest lift coefficients tested. This drag rise penalty dependence on attitude is typical and was expected.

Figure 89 shows that the jet-off to jet-on increment for the two extreme cases of jet area variation (the dash nozzle was not tested at M = 0.8) is very significant. Note that at jet-off conditions the cruise and combat nozzles have about the same drag, within repeatability error, as was the case at Mach 0.6 and 0.9. However, at jet-on conditions these two nozzles possess markedly different drag levels because the jet-effect increment for the combat nozzle is roughly twice that of the cruise nozzle. This is to be expected because of the physically larger afterburning plume in conjunction with reducted combat boattail area. The nozzle open/nozzle closed drag increment for these two extremes in ADEN jet area varies from a nominal 25 to 50 drag counts as lift coefficient increases from zero to 0.25. Thus, the ADEN is characterized by a significant jet area drag increment that is attitude dependent.

Figure 90 presents the jet-on jet area variation trends for all three ADEN configurations. The same type of drag reduction trend between the cruise and combat nozzles is observed at Mach 0.9 as was discussed above for Mach 0.8. Additionally note that the intermediate dash nozzle polar lies between the cruise and combat polars as expected.

As shown in Fig. 91 the jet area drag variation trends at supersonic speeds portray the same general gross effect - opening the nozzle throat at jet-on conditions reduces drag. This is clearly shown for the cruise and combat nozzles. But the dash and combat nozzles display the same (within repeatability error as discussed in Section 8.0) drag levels which was not expected. Perhaps, at supersonic speeds, the boattail drag reduction, caused by the rotation of the ventral flap from the cruise to dash position has reached the point of diminishing returns before fully rotating to the combat position (see Fig. 27). Additionally, as was the case at subsonic speeds, the cruise/combat drag delta varies with lift but not quite so dramatically perhaps due to the limited jet flow field influence on the airframe at supersonic speeds.

Conventional aft-mounted axisymmetric nozzle installations can also show large total drag reductions with jet area increases, but these are manifested solely in the drag component and are independent of attitude (over the range of interest). With the ADEN non-axisymmetric wing-mounted installation it is the interplay of lift and drag that accounts for the significant jet area drag reductions that become larger as angle-of-attack increases.

7.6 ADEN NON-AFTERBURNING VECTORING STUDY

Vectoring the ADEN results in significant increases in the thrust-removed lift is shown in Fig. 92. The trends shown at six degrees angle-of-attack typify those at all other attitudes tested. As geometric vector angle increases from 0^{o} to 5^{o} to 10^{o}, three effects are observed:

(1) Absolute values of the thrust-removed lift increase

(2) Jet-on blockage effect (explained in Subsection 7.10), which causes the initial "lift-jump" at low pressure ratio, becomes larger

(3) Sensitivity to nozzle pressure ratio becomes more favorable (at moderate and high pressure ratios).

No conclusions about the beneficial effects of thrust-vectoring on lift enhancement will be made at this point. Studying the individual aircraft lift and/or drag trends with vectoring is for educational purposes only. It is the aircraft drag polar and not the individual components, that is the figure of merit for evaluation of the scale model thrust-removed parameters (which then must be mated to real engine data and flown through a mission as outlined at the end of this subsection). Nevertheless, the individual lift and drag components will be briefly discussed to gain insight into the physical aerodynamic phenomena.

The total aircraft lift is comprised of three basic components:

(1) Jet-off aerodynamic lift

(2) Propulsive jet-induced lift

(3) Direct jet lift.

The relative magnitudes of these three components can be graphically illustrated for the model ADEN cruise vectoring configurations. Fig. 93 presents the lift component build-up for the ADEN cruise configuration at a typical Mach 0.9 operating condition. The jet-off aero lift is the foundation for the build-up and represents only aerodynamic effects without any influences from the propulsion system. The second component in the build-up is the propulsive jet-induced lift which, when added to the basic aero lift, yields the thrust-removed lift. The jet-induced lift includes all installation effects, relative to uninstalled conditions, due to the propulsion system. When the direct jet lift is added to the thrust-removed lift, the

total lift of the scale model is obtained. Note that the direct jet lift is the geometrical component of the resultant uninstalled gross thrust vector and is equal to:

$$\left(\frac{Ts}{qAW}\right) \cdot \text{Sin}\ (\alpha + \delta_s)$$

Lift gain factors, as defined by various experimenters (ref. 13), could be calculated from Fig. 93. However, as pointed out previously, the lift component alone tells nothing about the overall benefits of thrust-vectoring. Therefore, lift gain factors will not be discussed herein.

Figure 94 is the drag build-up counterpart to the lift build-up of Fig. 93. Excluding trim drag and ram drag components (which will be discussed later in this subsection), the build-up of forces in the drag direction is composed of three elements:

(1) Jet-off aerodynamic drag

(2) Propulsion jet-induced drag

(3) Thrust-loss.

The jet-off aerodynamic drag includes no propulsion system effects. The propulsion jet-induced drag is the jet-effect increment caused by the influence of the nozzle efflux. These two components when added together form the total thrust-removed drag which includes all nozzle installation effects. The thrust loss is the geometrical component of the uninstalled gross thrust vector resolved along the wind axis. It is calculated as follows:

$$\left(\frac{Ts}{qAw}\right) \cdot \left[1 - \cos\ (\alpha + \delta_s)\right] \cdot$$

The relative magnitudes of these components for the ADEN cruise vectoring configuration at a typical Mach 0.9 operating condition are shown in Fig. 94.

Observe that this figure presents drag trends at constant angle-of-attack. Alternatively, Fig. 95 provides a comparison for studying drag variations due to vectoring with a constant α or constant C_L format. Major differences exist between

the two formats and these differences are α and/or C_L dependent. At $\alpha = 0^o$, when drag equals axial force, and at $C_L = 0$, when normal force is very small, the two presentation formats are practically equivalent in that drag levels and trends with deflection are roughly the same. At conditions where substantial differences exist between drag and axial force and when normal force is not small, the two formats yield very different results. Furthermore, the disparity increases as α and/or C_L increases.

No conclusions can be made about the aircraft sensitivity to thrust vectoring if one only has the constant α characteristics. But the constant C_L format has more significance because definite conclusions can be made about the aircraft drag polars. For example:

- At low and moderate lifting conditions (CLTR = 0 and 0.115) the drag polars become slightly unfavorable as vector angle increases from 0^o to 10^o deflection angles
- At higher lifting conditions (CLTR = 0.232) the drag polars are always favorable as vector angle is increased from 0^o to 10^o deflection angles.

Before the thrust-removed polars at jet-on conditions are discussed, it is instructive to study the effect of the ADEN VEER rotation at baseline jet-off conditions. Here a purely geometrical wing flap phenomena is anticipated; but, this effect is expected to be small because: (1) the effectivity of the lower VEER surface is at least partially reduced by the presence of the jet-off base region, and (2) the span of the VEER is small compared to the wing span. The results of Fig. 96 generally support this expectation. As VEER angle increases from 0^o to 5^o to 10^o, the characteristic polar rotation due to the familiar flap effect is observed. At zero lift, the maximum effect is ± 12 drag counts about the mean while at a 0.30 lift coefficient, the spread is ± 8 drag counts. These trends at jet-off conditions are considered small (although the spread at zero lift was slightly larger than anticipated). The point of interest is to see how the corresponding effect at jet-on conditions differs from these baseline jet-off polar rotation trends. In particular do the jet-on vectoring drag deltas increase at a 0.30 lift coefficient?

Figures 97, 98 and 99 present the jet-on non-afterburning ADEN vectoring study at Mach 0.6, 0.8 and 0.9, respectively. Note the three distinct regimes for the ADEN cruise configuration. At negative values of lift the best-to-worst trend is

0^o, 5^o, 10^o. In other words, vectoring increases drag at this low angle-of-attack academic condition as expected. At moderate values of lift, the best-to-worst trend is either 5^o, 0^o, 10^o or 5^o, 10^o, 0^o. In either case, an optimum deflection angle somewhere between 0^o and 10^o must exist. At higher values of lift, the best-to-worst trend is 10^o, 5^o, 0^o which is the reverse of the trend at low lift coefficients.

In this case, three vectoring angles were evaluated and three separate regimes for the polars were observed. One can generalize and say that if there were four configurations tested, then four regimes would have been observed. . ., and so on. As higher lift regimes are entered it is always a larger deflection angle that will be the optimum. This should be true up to the point where the supercirculation flow field breaks down (just as a wing flow field breaks down at high angles of attack). An optimum polar locus composed of an envelope of points covering a range of deflection angles can therefore be envisioned. This indicates that deflection angle should be scheduled to angle-of-attack to achieve optimum performance.

The effect of the vectoring phenomenon is to both translate and rotate each polar relative to the unvectored polar. In other words, the complete aerodynamic shape of the drag polar is altered by vectoring the propulsion system. Furthermore, observe that the jet-on polar differences at a 0.30 lift coefficient are much larger than those exhibited by the baseline jet-off polar as expected. This indicates that the jet and external wing flow field are mutually interactive. This will be discussed in terms of surface pressure data in subsection 7.10.

The magnitude of the drag reduction due to vectoring is significant. This can be observed by entering the polar of Fig. 99 at a 0.30 lift coefficient. Vectoring 5^o results in a 27 drag count reduction while vectoring 10^o yields a 40 drag count reduction relative to 0^o. Vectoring the second 5^o, a 100% increase, results in an additional 50% drag improvement. This suggests that large amounts of vectoring may not be necessary to show substantial cruise performance payoffs.

The drag reduction effect due to ADEN jet exhaust vectoring at subsonic speeds is summarized in Fig. 100. The performance benefit of the cruise 10^o nozzle is compared to cruise 0^o nozzle, as an unvectored reference point, according to the following:

$$\Delta C_{D_{TR}} = \left[\left(C_{D_{TR}} \right)_{\delta_G = 0^o} - \left(C_{D_{TR}} \right)_{\delta_G = 10^o} \right]_{C_{L_{TR}} = c}$$

Observe that this benefit increases as lift increases and generally decreases as speed increases (for constant lift). The first effect is due to the rotated polars that diverge as lift increases. The second effect is probably related to the fundamental aerodynamic principal that addresses upstream influence - flow field disturbances resulting from exhaust jet vectoring travel much further upstream as speed decreases (this will be shown in the surface pressure study of subsection 7.10). Thus, more of the lifting surface can theoretically be effected at the lower speeds (other things being equal).

So from a purely external aerodynamic viewpoint, it can be concluded that larger thrust-vectoring payoffs can be expected at lower Mach numbers. Note that the trend at Mach 0.9 appears out of order with respect to the other speeds. The reason for this is unknown; however, based on analysis of pressure data (see subsection 7.10), a beneficial shock-movement phenomenon exists at this transonic Mach number which could be responsible for the observed trend.

In passing, it is noted that the total payoff for the vectored ADEN relative to the circular baseline can now be calculated. As discussed in subsection 7.4 (see Fig. 82), the improvement resulting from the integration advantages of the ADEN relative to the circular nozzle installation was on the order of 50 drag counts. Additionally, Fig. 99 shows that the beneficial vectoring effect of the ADEN is approximately 40 drag counts. So, the 50 count installation payoff due to improved integration when added to the 40 count vectoring payoff yields a total ADEN Cruise nozzle payoff of 90 counts at Mach 0.9 — about 25% of aircraft minimum drag, or alternatively about 15% of cruise drag (at 0.30 lift coefficient).

The above discussion applies to untrimmed thrust-removed polars obtained from the wind tunnel model. From the point of view of external aerodynamics these polars can be very useful in interpreting the relative trends of thrust vectoring. However, to undertake a more complete cruise mission performance analysis for the air vehicle, real engine/nozzle effects (jet-lift, thrust-loss, ram drag, and nozzle weight) must be accounted for in addition to the aircraft trim effects. The following two equilibrium equations for the subsonic cruise mission must be solved:

$$C_{D_{TR}} + C_{D_{RAM}} + C_{D_{TRIM}} = \frac{T_s}{qA_w} \cdot \cos(\alpha + \delta_s) \qquad (1)$$

$$C_{L_{TR}} + \frac{T_s}{qA_w} \cdot \sin(\alpha + \delta_s) = \frac{W}{qA_w} = C_{L_{REQD}} \qquad (2)$$

To find the drag reduction due to thrust vectoring at a specific Mach number and altitude, the following additional equations and/or relationships are requried:

$$C_{D_{TR}} = f(NPR, \alpha) \quad (3)$$

$$C_{L_{TR}} = f(NPR, \alpha) \quad (4)$$

$$C_{D_{TRIM}} = f(NPR, \alpha) \quad (5)$$

$$T_S/qAw = f(NPR) \quad (6)$$

$$C_{D_{RAM}} = f(NPR) \quad (7)$$

$$\delta_S = f(NPR) \quad (8)$$

Relationships (3), (4), (5) and (8) in general represent curves developed from analyses of wind tunnel data. Relationships (6) and (7) are obtained from the results of engine company computer programs.

The powered polar of Fig. 101 is the counterpart of the thrust-removed polar of Fig. 99. Here the effects of scale model thrust have altered the thrust-removed polar trends. At a 0.30 lift coefficient the cruise 5° powered polar is now the most favorable because its thrust loss is not as great as the corresponding penalty for the cruise 10° nozzle. Even so, the cruise 10° powered polar still shows a benefit over the unvectored polar because its drag benefit outweighs the thrust loss. These results suggest that only a small amount of vectoring may be required to show a significant performance payoff at subsonic cruise conditions.

Recall the discussion of subsection 7.4 pertaining to the biasing of powered polars due to different nozzle throat areas. Note from Fig. 34 that the ADEN Cruise 5° and 10° nozzles have slightly less jet area than the cruise 0° nozzle. Thus both the 5° and 10° powered polars should be adjusted to the left thereby creating an improved and truer thrust-vectoring result. Again, another example of interpreting powered polars with caution is apparent.

7.7 ADEN AFTERBURNING VECTORING STUDY

This subsection discusses the effect of ADEN Combat (afterburning) nozzle deflection angle variation at both subsonic and supersonic speeds. In many respects, it parallels and is similar to the ADEN Cruise (non-afterburning) nozzle vectoring study of subsection 7.6.

Figure 102 shows how the aircraft lift component increases as VEER geometric deflection angle is increased. Several points are noteworthy:

(1) For both combat and cruise nozzles the generation of incremental lift due to vectoring is essentially independent of angle of attack

(2) Vectoring the combat nozzle through the maximum tested 20^{o} excursion develops a significant incremental lift coefficient of approximately 0.125

(3) Over the 0^{o} to 10^{o} deflection range the cruise nozzle develops approximately 50% more incremental lift than the combat nozzle despite the fact that the ideal momentum coefficient (Fip */. qAw) of the combat nozzle is about 75% greater. This suggests that the momentum coefficient alone is not sufficient as the single correlating parameter for supercirculation effects. (The pressure distribution studies of subsection 7.10 will relate to this finding.)

Note that the above discussion applies at constant angle-of-attack. In practice, to derive either cruise or maneuver benefits from aeropropulsion lift enhancement phenomena, the aircraft would be changing angle-of-attack as deflection angle is varied. Then the drag would change and so would the thrust required and nozzle pressure ratio, etc. - the familiar iterative problem. The point is that the curves of Fig. 102, as well as all other constant angle-of-attack presentations, are of academic interest only to aid in understanding the mechanism of lift enhancement.

Figure 103 presents the lift component build-up for the ADEN combat nozzle; it is the counterpart of Fig. 94 for the cruise nozzle. Although the general nature of the combat and cruise lift build-ups is similar, basic differences exist:

(1) Jet lift is much larger for the combat nozzle due to a greater mass flow rate and a larger static vector angle at the same nozzle pressure ratio

(2) Jet-induced lifts at the common 10^{o} deflection angle are about equal for both combat and cruise nozzles. This is a coincidence because both the jet-off aerodynamic lift (Figs. 93 and 103) and the thrust-removed lift (Fig. 102) possess measurably different trends for combat and cruise nozzles. Furthermore, as will be shown in the surface pressure study

(subsection 7.10) the aerodynamic mechanisms (flow-blockage, super-circulation, or transonic shock-movement) that are responsible for generating induced-lift are uniquely different for combat and cruise nozzles - thus the above coincidence was a surprise.

Recall that Fig. 102 showed how the lift component was enhanced by thrust vectoring; but, this benefit does not come without a penalty. Figure 104 shows that lift production is accompanied by a sizable drag production. Observe for both combat and cruise nozzles that the rate at which drag increases with jet deflection is strongly dependent on angle-of-attack. In contrast, recall that the lift component trend with deflection was insensitive to angle-of-attack over the tested attitude range. For the combat nozzle observe that the drag penalty for vectoring the second 10^{o} is more severe than the first 10^{o}. Also note that the cruise nozzle possesses a less severe vectoring drag penalty than the combat nozzle.

The ADEN Combat thrust-removed drag polars are presented in Figs. 105 and 106 for Mach 0.9 where maneuvering benefits due to thrust vectoring are desirable. First, at jet-off conditions the differences between the combat 0^{o}, 10^{o}, and 20^{o} polars are relatively small as expected. This was also true for the cruise 0^{o}, 5^{o}, and 10^{o} polars as discussed in subsection 7.6 where it was pointed out that the trend with VEER deflection was due to familiar flap-effect.

Secondly, at jet-on conditions (Fig. 106) significant spreading of the polars occurs relative to jet-off conditions. For example, at low to moderate lift conditions the combat 0^{o} and 10^{o} jet-on polars have become more favorable (moved left) while the combat 20^{o} polar has become more unfavorable (moved right). At higher attitudes, however, the combat 20^{o} jet-on polar does cross-over its jet-off counterpart. This generally unfavorable jet-effects drag increment for the ADEN Combat 20^{o} nozzle was not anticipated and remains unexplained. Since this effect occurs at all operating nozzle pressure ratios at subsonic speeds, it therefore is considered to be valid.

Unfortunately, this experiment was angle-of-attack limited and data could not be obtained in the combat maneuver regime (0.5 to 1.0 in lift coefficient). However, employing mental extrapolation on Fig. 106 the combat 20^{o} polar crossing over the 0^{o} and then the 10^{o} polars can be envisioned at higher values of lift. Thus, the same

three-regime characteristic would be evident here as was observed with the cruise nozzles (Fig. 99).

The ADEN Combat 20° nozzle obviously suffers a very large drag penalty that the more moderately vectored 10° nozzle does not experience. This fact, coupled with the knowledge that the resultant static performance of the combat 10° nozzle is equivalent to that of the combat 0° nozzle while the combat 20° nozzle suffers a turning efficiency as well as cosine loss, suggests that large vector angles at combat maneuvering conditions are not likely to pay-off.

Vectoring at supersonic speeds is not envisioned as a viable technology because vectoring was neither expected to show a payoff nor would V/STOL aircraft be expected to pull high-gs at supersonic speeds. For academic purposes, however, limited data was obtained in this program to confirm that thrust vectoring has little effect on the air vehicle at supersonic speeds. Figure 107 presents the jet-off and jet-on polars at Mach 1.4. The jet-off polars are very close as expected with the ADEN Combat 20° portraying somewhat higher drag levels probably due to the additional supersonic flow expansion on the deflected VEER.

At jet-on conditions, both nozzles exhibit the characteristic large supersonic drag reduction phenomenon as the sensitive nozzle base area region is eliminated and replaced by the jet plume. The main point, however, is that the <u>difference</u> between the combat 0° and combat 20° polars at jet-on conditions compared to jet-off conditions is very small. This is in contrast to the corresponding drag difference at subsonic speeds as exemplified in Figs. 105 and 106. This finding most probably results from the fact that fluid mechanic disturbances do not propagate upstream at supersonic speeds (except through the boundary layer as a second-order effect). Thus it is concluded that the effect of thrust vectoring is not significant at supersonic speeds.

7.8 EFFECT OF VECTORING ON PITCHING MOMENT

The untrimmed polar improvements due to vectoring the ADEN must be adjusted for trim effects. For example, if vectoring resulted in a larger trim drag require ment, then some of the untrimmed polar benefit would be reduced. Conversely, if vectoring reduced the trim penalty, then the untrimmed polar benefit would be further increased. For the specially designed V/STOL configuration tested in this program the latter case is applicable as will be discussed in this section.

Fig. 108 shows the effect of vectoring the ADEN Cruise nozzle on aircraft tail-off pitching moment. These Mach 0.9 results which indicate an unstable situation ($dC_M/dC_L > 0$) are representative of the trends obtained throughout the 0.4 to 0.9 Mach range. It is noted that this airplane configuration was intentionally designed to be statically unstable (with tail-on) at subsonic speeds because fly-by wire technology was employed to minimize trim penalties relative to those of a statically stable configuration.

The figure demonstrates the effect of cruise nozzle vectoring at subsonic conditions. At conditions of interest as geometric deflection angle is increased, the pitching moment needed to be trimmed-out decreases. For example, at a typical cruise 0.30 lift coefficient, the 10^o nozzle produces a 0.04 pitching moment improvement relative to the baseline 0^o nozzle. Thus, it is concluded that vectoring the ADEN, at conditions of interest, is favorable for trim, and total aircraft performance improvements are actually in excess of those indicated by the untrimmed polars of subsection 7.6. Wherewithal did not exist to translate this vectoring trim benefit into drag counts because tail-on (or canard-on) configurations were not tested, but it is estimated to be in the five to ten count range.

Fig. 109 is the counterpart of Fig. 108 and presents similar results for the combat nozzle. Vectoring between 0^o and 10^o produces almost the same 0.04 favorable pitching moment increment as the corresponding cruise vectoring configurations. Vectoring another 10^o doubles this value. These results are representative of the trends obtained throughout the 0.4 to 0.9 Mach range. Thus, it is concluded that vectoring the ADEN, in the combat mode, is also favorable for trim, and the total aircraft performance improvements are actually in excess of those indicated by the untrimmed polars of subsection 7.7.

7.9 EFFECT OF INLET FAIRING VARIANT

Traditionally, in jet effects testing, the effect of either inlet fairing type or a flow through inlet has been considered to have negligible effect on the jet effect increment (drag difference between jet-on and jet-off). This contention has been demonstrated to be valid for an aft-mounted nozzle installation where the distance between inlet and nozzle was considered large (ref. 6). Even for somewhat shorter inlet/nozzle coupling distances, such as on the subject V/STOL wing-mounted configuration, this contention has still been expected to be true. Only on very obvious closely-coupled configurations has the effect of inlet simulation been questioned. During the subject test program, this assumption was checked on the ADEN Combat 0^{o} configuration, and the result is very surprising, not totally understood, and still under question.

The standard recessed plate inlet fairing (Fig. 8) and the ogive inlet fairing (Fig. 35) were evaluated at a jet-off and a typical jet-on condition over the 0.4 to 1.4 Mach range. The data at Mach 0.4, however, is considered suspect due to data scatter because of the very low tunnel dynamic pressure, so the trends presented herein are from Mach 0.6 to 1.4.

Figure 110 presents a typical subsonic result. The first observation is that the ogive inlet fairing results in substantially reduced total aircraft drag as was expected. The mean pressure coefficient acting on the forward facing area of this aerodynamically designed bullet-nose fairing is close to ambient thereby producing low drag. On the other hand, the mean pressure acting on the recessed plate is very close to tunnel total pressure thereby producing high drag, not to mention the spillage drag associated with the lower lip.

Now, observe the behavior of the jet-effect drag increment from jet-off to jet-on. For both inlet fairing variants this increment is large and favorable as expected. However, the key point is that this jet-effect increment is <u>different</u> for each of the two types of inlet fairings. For example, at zero lift, the ogive fairing yields a 70 count drag increment while the recessed plate fairing produces a smaller 50 count drag increment. Figure 111 presents the same comparisons at a typical supersonic Mach number.

The jet-effect drag increment result for all Mach numbers is presented in Fig. 112 for the zero lift condition which corresponds to the baseline aircraft

minimum drag condition. Note that at supersonic speeds, the effect of inlet fairing variant is negligible. This certainly was anticipated based on the theory that the sphere of nozzle/back-end disturbances can only travel a limited distance upstream at supersonic speeds. At subsonic Mach numbers, there is a very significant effect of inlet fairing on the jet-effect increment; and furthermore this effect is diverging as Mach number decreases. This appears to be consistent with the well known fact that disturbances travel further upstream as flight speed is reduced. Nevertheless, the magnitude of the disparity causes surprise and concern because it suggests that numerous jet-effects test programs may be suspect.

Figure 113 presents the jet-effect drag increment trend at lifting conditions; it is the counterpart to Fig. 112 showing the zero lift result. At subsonic speeds, the same basic trend is observed although somewhat diminished in magnitude. A more dramatic mystery exists at supersonic speeds where these data show a significant difference in the jet-effect increment. This was certainly not expected, again, because of the principal of limited upstream influence. Can it be rationalized that, at angle-of-attack, the inlet fairing/fuselage crotch region is creating strong vortex and/or shock systems that do not dampen out before impinging on the nozzle?

The largest disparity between inlet fairing variants occurred at Mach 0.6 at low angle-of-attack as shown on Fig. 113. Pressure distributions along the upper and lower nacelle surfaces were studied to see if the force balance trends could be supported by observing large differences in the jet-on/jet-off deltas between the two inlet fairing types. Figures 114 and 115 show these pressure data for the recessed plate and ogive fairings respectively. If these data were to corroborate the force data, then the difference between the circle and square symbols would be very much different for each figure. However, the data do not support this hypothesis; thus, a quandry exists.

It may be argued that sufficient pressure instrumentation did not exist to properly document the force balance result. Additionally, it may be argued that the force balance axial force gauge at subsonic jet-off conditions possesses large uncertainty (measuring less than 50 lb on an 800 lb gauge). However, this latter argument, which could explain away the subsonic mystery, certainly could not reconcile the supersonic disparity (Fig. 113), because at these high dynamic pressure conditions the axial force gauge measures large (200-300 lb) jet-off forces. At this point no adequate explanation can be offered for the unexpected inlet fairing variant trends.

The question arises as to which of the two types of inlet fairing designs is the better. The data of Ref. 6, which compare a bullet-type and a recessed plate fairing to a flow through inlet, demonstrate that the recessed plate fairing provides a much better flow field simulation of the flowing (unchoked) inlet. The reason is because the bullet-type fairing is characterized by essentially zero spillage as manifested by lip vicinity pressures that are very close to ambient. On the other hand, the recessed plate fairing, which can be envisioned as characterized by 100% spillage, produces very large negative pressures around the inlet lip. Now, the flowing inlet also produces significant spillage (of course much less than 100%) and is also characterized by very large negative pressures around the inlet lip. Thus, by deduction, in the study of Ref. 6, it was concluded that the recessed plate inlet fairing provided the better simulation.

Relating the above to the subject test program, Fig. 114 and 115 show that the pressure levels in the vicinity of the lower lip are very highly negative for the recessed plate while they are very close to ambient for the ogive fairing. Therefore, applying the result of Ref. 6, discussed above, to interpret the subject test data, it is deduced that the more realistic of the two candidate inlet fairing designs is the recessed plate. Furthermore, it is the one that is characterized by the lower of the two jet effect drag magnitudes which would correspond to the more conservative selection!

In passing, attention is drawn to the pressure orifices that were symmetrically located (same fuselage station, water line, and butt line) on the model. The data from these measurements is noted in Fig. 114 and 115. It is concluded that the model was properly aligned so that the flow field over left and right hand sides of the model was symmetrical.

7.10 ANALYSIS OF EXTERNAL PRESSURE DISTRIBUTIONS

External surface pressure distributions have provided insight into the fluid mechanic flow field phenomena that characterize this V/STOL ADEN underwing installation. Four categories of surface pressures are discussed in this subsection as summarized below:

(1) Nacelle/Nozzle - to study the effect of vectoring on the nozzle surfaces itself (VEER in particular) and the upstream zone of influence along the nacelle centerline

(2) Wing Upper and Lower Surfaces - to study the longitudinal and spanwise effect of vectoring on the lifting planform to add physical insight to the overall integrated effect of thrust vectoring as measured by the force balance

(3) ADEN VEER - to study the localized span effect of thrust vectoring on the ADEN deflecting VEER

(4) ADEN sidewalls - to study nozzle pressure ratio and flight condition effects on inboard and outboard sidewalls.

Effect of Vectoring on Nacelle/Nozzle Pressures

Analysis of the diagnostic pressures measured on the nacelle/nozzle surface aids in the understanding of flow field changes that are responsible for the production of incremental lift due to vectoring. Figure 116 presents the pressure distributions for the vectoring ADEN Combat nozzle at Mach 0.6 at zero angle-ofattack. The trends to be discussed apply equally well to all subsonic Mach numbers and all angles-of-attack tested.

The top of the figure presents pressure data along the wing upper surface at a spanwise location corresponding to the nacelle longitudinal centerline. The bottom of the figure shows the pressure profiles along the centerline of the nacelle lower surface. The approximately-scaled sketch illustrates the geometric variations of the three ADEN Combat vectoring modes tested.

The first observation to make is that the influence of thrust vectoring travels very far upstream to the nacelle maximum area region. However, the most dramatic effect is on the ADEN VEER. Note the huge change in minimum over expansion pressure coefficient at the "shoulder". For the combat 20^{o} nozzle, the flow over expands to a -1.25 pressure coefficient (approximately equal to the critical pressure coefficient) before shocking to a value in excess of ambient pressure. Then a second, but weaker, over expansion occurs before the flow recompresses subsonically. In all cases, the entire upper surface pressure distribution becomes more depressed (more negative) as vector angle increases. This is a result of the jet exhaust pumping-action and is a lift-producing (and drag-producing) mechanism.

The lower surface shows opposite trends; as vector angle increases the entire pressure distribution becomes less depressed (less negative). This is a result of flow blockage due to plume geometry causing the external flow to turn and recompress more abruptly as vector angle increases. It is also a lift-producing (but drag-reducing) mechanism. Thus both upper and lower surface pressure distribuons complement one another in the generation of lift.

Wing Surface Pressure Analysis and a Lift Enhancement Model

The identification and extent of the various phenomena responsible for the lift increments obtained through thrust vectoring can be more readily understood by analyzing the wing surface pressure orifices. The distribution of pressure orifices on both upper and lower wing and nacelle surfaces has been shown in Fig. 20. This information, along with upper wing surface flow visualization patterns, have proven to be invaluable in understanding the role of the aeropropulsion mechanisms responsible for lift enhancement. This information additionally provides a usable set of data to aid the development of theoretical models for these mechanisms.

Three lift mechanisms have been identified from the wing surface pressure studies. It is interesting to note that these three mechanisms are not always present and appear together only during the operation of the ADEN Cruise nozzle configuration during transonic (Mach 0.9) flight conditions. The reasons will be discussed in this subsection.

Pressure distributions over the entire wing planform for such a condition are shown in Fig. 117. The three lift mechanisms are:

1) Lower surface flow blockage by the exhaust plume
2) Supercirculation effects over the entire chord length due to the jet flap effect of the exhaust at the wing trailing edge
3) Aft shock movement on the wing upper surface due to additional wing circulation (only present during transonic conditions).

It is also clear from the lift distribution over the span that these jet induced lift benefits are not localized solely on the wing area directly ahead of the jet exhaust. The data show that the entire wing span lift distribution is affected by placing the exhaust near the wing inboard trailing edge.

The oilflow patterns in Fig. 118 corroborate this outboard effect of the nozzle. The jet-off conditions show separated flow over the trailing edge of the ADEN upper surface (VEER) and a strong spanwise flow gradient at the wing trailing edge along the span. When the jet is flowing at an operating pressure ratio, the flow directly over the nozzle becomes more organized and remains attached to the VEER. In addition, the wing trailing edge flow has become more aligned with the streamwise direction for a large portion of the span. Both conditions are indicative of more negative upper surface pressures which generate increased lift.

As stated earlier, these lift mechanisms do not necessarily all appear for each configuration. For example, Fig. 119 shows major differences in the effect of the ADEN Cruise and Combat nozzles on the wing flow field during transonic flight conditions. The cruise 0^{o} configuration shows minimal lower surface blockage and very little supercirculation lift generated at jet-on conditions. This is to be expected since the jet deflection is probably small (although not necessarily zero as implied by this configuration's zero degree designation). On the other hand, the ADEN Combat 0^{o} nozzle, while also generating minimal supercirculation lift due to the small jet deflection angle, does however generate a larger lower surface blockage lift than its cruise 0^{o} counterpart. This is a result of the much thicker combat exhaust jet providing a larger obstruction to the lower surface flow than the thinner cruise nozzle exhaust jet.

When both of these nozzles are deflected, a further difference arises. The ADEN Cruise 10^{o} configuration, with jet-on, generates not only strong supercirculation lift but also strong lower surface blockage lift (see Fig. 119). Both effects are due to the trailing edge jet deflection. The combat 10^{o} configuration also produces strong lower surface blockage but, surprisingly, only minimal supercirculation lift. This effect is further emphasized by studying the force balance data in Fig. 120. This was not expected since it was theorized that the combat 10^{o} jet deflection at the wing trailing edge should produce a supercirculation lift component comparable to the cruise 10^{o} deflection.

The explanation of this phenomenon, the inability of the combat nozzle to generate the expected levels of supercirculation lift, is open for speculation. The only apparent difference between the two cases is the geometry of the lower portion of the exhaust jets. This immediately suggests the possibility that the vertical

position of the exhaust center of momentum below the wing trailing edge plays an important role in the jet's ability to create wing supercirculation. The proposed analytical model (ref. 14) for jet-wing interaction is the jet flap (i.e., an infinitely thin jet issuing directly from the wing trailing edge). This theory predicts that maximum supercirculation benefits are obtained by control of upper and lower surface wing trailing edge pressures and wake/jet curvature. Any movement of the jet away from the trailing edge weakens both of these effects. If the modeling of the ADEN Cruise or Combat exhaust jets were accomplished by placing an infinitely thin jet sheet under the wing at the center of momentum location for the respective true jet exhausts, the following would result. The thick combat nozzle exhaust, having its momentum center further below the wing trailing edge than the thinner cruise nozzle exhaust, would generate less supercirculation lift. Until further work is undertaken, these thoughts remain purely speculatory.

The third lift enhancement mechanism, shock movement, is purely a transonic effect and can only be seen in these data for the Mach 0.9 condition. Fig. 121 shows this effect on the ADEN Cruise 10^{o} nozzle. At Mach 0.6, the jet effect mechanism is blockage at low pressure ratio followed by supercirculation lift which increases slightly as nozzle pressure ratio increases. For the transonic case (Mach 0.9) with a wing shock present, the same sequence begins but at some point during the pressure ratio excursion the additional circulation causes the shock to jump aft thereby creating a rapid increase in lift. This accounts for the strong non- linear lift increase in the force data after a nozzle pressure ratio of about 4.5 for the cruise 10^{o} nozzle. Again, note that this aft shock movement is caused by the increase in circulation due to the jet flap effect. If this jet flap effect is weak, as is observed for the combat nozzle, then minimal shock movement should be present. Thus, a non-linear lift increase after a pressure ratio of about 4.5 should not occur; in fact as shown in Fig. 120, it does not occur for the combat nozzle during transonic flight conditions.

Figure 122 attempts to sort out each of the mechanisms which might be expected for the listed configurations and flight conditions. Both force measurement data and wing pressure distributions support these contentions.

To summarize, Fig. 123 builds a schematic composite thrust-removed lift curve as a function of nozzle pressure ratio. The effects of each of the three lift mechanisms discussed above are shown. To reiterate, all, some or none of these lift

enhancement mechanisms might be present depending on: the installed nozzle configuration, nozzle pressure ratio, and flight condition.

Effect of Span on ADEN VEER Pressures

The ADEN Combat 20° configuration was selected for the study of VEER span effects because it was the configuration employing the largest deflection angle. Figures 124, 125, and 126 present the pressure distributions for the combat 20° inboard (butt line 8.125 in.), outboard (butt line 10.125 in.), and centerline (butt line 9.125 in.) locations. The off-centerline pressure orifices were positioned only on the VEER while the centerline orifices were located over the complete nacelle/nozzle length. Also shown in the figures, for reference, is the corresponding unvectored combat 0° centerline pressure distribution.

From all three figures, no matter if low speed (Mach 0.4), subsonic/transonic speed (Mach 0.9) or high speed (Mach 1.4), the same conclusion applies - the off-centerline VEER pressure distributions are generally dissimilar from the centerline distribution. For instance, at all three Mach numbers, the centerline flow experiences a double expansion/compression phenomenon while the off-centerline flow is characterized by only a single expansion followed by a single compression (except at the end of the VEER inboard side at Mach 0.9). Furthermore, the off-centerline pressures are generally more negative than the centerline distributions.

When the VEER is deflected 20°, it becomes exposed to the flow on the bottom in addition to the top of the wing (see Fig. 33). Since the pressures under the wing are positive, it could be expected that the off-centerline VEER pressures would reflect this influence and exhibit higher (less negative) values than on the centerline. The data does not support this hypothesis. Another theory, one that fits the observations, reasons that the centerline flow is largely two-dimensional while the off-centerline flow is influenced by a three-dimensional relief mechanism which allows spanwise spilling over the sides of the VEER.

Observe that both inboard and outboard distributions generally exhibit the same characteristics with the outboard profiles tending to portray slightly higher pressure levels.

As a reference, the ADEN unvectored combat 0° data is presented to again show how far the effect of vectoring travels upstream (recall Fig. 116). At the lowest 0.4 Mach number, the effect of vectoring travels much further upstream than the

nacelle maximum area station. At Mach 0.9, the sphere of influence does not extend to this maximum area station, while at Mach 1.4 the effect is restricted to the nozzle itself. These pressure data trends are consistent with the force data trends of subsection 7.6 in which the effect of thrust vectoring was observed to show larger effects at the lowest Mach numbers.

In summary, it is concluded that strong spanwise gradients can exist on deflected two-dimensional nozzle surfaces. Pressure/area integration schemes would require extensive spanwise as well as longitudinal pressure instrumentation in order to accurately assess component lift and drag coefficients.

ADEN Sidewall Pressure Effects

In practice, the sidewalls of two-dimensional nozzles are not flat because mechanical and kinematic considerations demand substantial wall thicknesses that must be ultimately boattailed to minimize drag producing base area. Therefore, it is important to study the ADEN sidewall pressure distributions for this V/STOL underwing nacelle installation. This will be done for the ADEN Cruise 10^{o} configuration.

Figure 127 presents the inboard and outboard sidewall pressures at jet-off and jet-on conditions. The outboard sidewall shows the classical flow recompression phenomenon while the inboard recompression is followed by an expansion to the trailing edge. The reason for the different outboard/inboard trends is because the flow field on the inboard side is shielded by the fuselage which does not allow as natural a "free-compression" as the outboard sidewall. Also, observe that the outboard sidewall is relatively insensitive to jet effects while the inboard side exhibits the classical favorable effect of pressure ratio. At the conditions of Fig. 127, practically the entire sidewall surfaces are bathed by a lower than ambient flow field thereby creating drag.

Figure 128 presents the effect of Mach number on the sidewall pressure distribution. On the outboard side, the effect of an increase in Mach number is unfavorable - exaggerated flow expansion and minimized flow recompression. On the inboard side the integrated effect is also unfavorable. This is the familiar trend with Mach number as expected.

Figure 129 presents the effect of angle-of-attack which is very pronounced for this highly integrated underwing nacelle installation. As attitude increases the com-

plete sidewall pressure level also increases from highly negative to generally positive (or close to ambient) pressure coefficients. These trends were consistently observed regardless of subsonic Mach number or nozzle pressure ratio. This trend with attitude is to be expected because the higher under-wing pressure levels impinge on the nozzle as angle-of-attack is increased.

In summary, the relatively low-boattailed ADEN sidewalls are characterized by significant longitudinal pressure gradients, as a function of Mach number and pressure ratio, which contribute to vehicle drag at low attitudes, but on the other hand can produce thrust at moderate to high attitudes (in excess of about six degrees).

7.11 ANALYSIS OF INTERNAL PRESSURE DISTRIBUTIONS

In subsection 5.2 which discussed aeropropulsion bookkeeping, it was shown that the thrust-removed drag (or lift) included two terms: (1) the external drag (or lift) of all surfaces wetted by the external flow, and (2) on the internal thrust-component decrement (or increment) caused by the effect of the external flow on the internal thrust vector. This second term is negligible for practical internal expansion nozzles (ref. 6) except at very low pressure ratios generally not of interest; however, for asymmetric internal/external expansion nozzles, the effect of external flow on internal thrust may be significant.

Pressure orifices were located on the ADEN and ALBEN internal surfaces, as discussed in subsection 3.3 (Fig. 21). Pressure distributions were studied and integrated over the upper (VEER on the ADEN) and lower (ventral on the ADEN) flaps at wind-on and at static conditions to obtain insight into the effect of external flow on nozzle internal thrust. No attempt is made to precisely quantify this component of lift, $(\Delta F)_L$, and drag $(\Delta F)_D$ because: (1) knowledge of the free pressure boundary (dividing streamline between external and internal flows) is not available, and (2) more pressure instrumentation is required. Nevertheless, the interesting influence of the free stream on the nozzle internal surface pressure distributions is a worthwhile qualitative study.

The analysis presented herein will concentrate most heavily on the ADEN Cruise 0^o because this nozzle, which has the largest internal turning angle, shows the most dramatic effects. Surface pressure distributions will be analyzed and integrated for both the VEER and the ventral flap in both the axial and normal directions. Highlights for the other nozzles in the test matrix will be presented so that conclusions can be developed for three major studies:

(1) Effect of nozzle type (ADEN, ALBEN, and circular nozzle)

(2) Effect of jet area (ADEN: Cruise 0^o, Dash, and Combat 0^o)

(3) Effect of vectoring (ADEN: Combat 0^o, Combat 10^o, and Combat 20^o).

The discussion of this subsection will be presented for zero degrees angle-of-attack; however, the trends are generally applicable to all attitudes tested.

Figure 130 presents the ADEN VEER static (Mach 0.0) pressure distributions for several values of NPR. The wall surface pressure is non-dimensionalized with the area-weighted average exhaust total pressure to form a parameter independent of ambient pressure. Observe that strong shock systems exist inside the ADEN at all pressure ratios between a throat-choked condition and the flowing full condition. For all pressure ratios greater than eleven, the VEER pressure distribution will always lie on the "flow full locus." Below choke (see NPR = 1.26), the nozzle exhaust flow is subsonic throughout and is not characterized by an imbedded shock system. At all intermediate values of NPR, the shock system location is a function of nozzle pressure ratio as shown in the figure. It is noted that at values of NPR larger than about eleven, the shock is "blown-out" of the nozzle and occurs in the plume.

Figure 131 shows how the effect of external flow alters the internal VEER pressure distribution. Furthermore this effect is Mach number dependent. At Mach 0.9, the shock moves upstream while at Mach 1.35 it moves downstream relative to static conditions (Mach 0.0). This is a result of complex local back-pressure effects that "set" the shock system when the nozzle is not flowing full. The same phenomenon occurs at all other values of NPR but at different locations on the VEER surface.

When the pressure distributions are increased relative to static conditions, the effect of the external flow is favorable because an additional thrust increment is provided. This is the case at Mach 0.9 in Fig. 131. The same reasoning applied in reverse shows that at Mach 1.35 the effect is unfavorable because a thrust decrement (or internal drag) occurs.

The pressure/area integral of these VEER pressure distributions, over the range of Mach numbers and nozzle pressure ratios tested, is presented in Fig. 132 to gain insight into the relative magnitude of the VEER axial force as a percent of ideal thrust. All subsonic Mach numbers show increased thrust relative to static conditions while the reverse is true at supersonic speeds - this is in accord with the wall pressure trends of Fig. 131. Observe that as an NPR of eleven is approached, the wind-on/wind-off differences all tend to zero because the nozzle is now flowing full. Most importantly, note the large differences between the wind-on/wind-off VEER axial force, at low and moderate values of NPR, equivalent to several percent of ideal thrust.

Figure 133 presents the integrated axial force on the ADEN ventral; it is the counterpart of Fig. 132 for the ADEN VEER. Observe here that the force is negative because the ventral and VEER area vectors are of opposite sense. Also, note that the magnitude of the ventral axial force is much smaller than that of the VEER largely because its axial projected area is only 15 percent of the VEER area projection. The key point is that the difference between wind-on and wind-off ventral forces is well within one percent of ideal thrust; so, it is concluded that the effect of external flow on the ADEN ventral is negligible with the bulk of the action in the axial direction occurring on the ADEN VEER.

Figures 134 and 135 present the VEER and ventral pressure integrations in the normal (lift, at $\alpha = 0^{o}$) direction. The magnitudes of the normal forces are much greater than their respective axial force counterparts due to the greater magnitudes of the normal area vectors. Also, observe that the magnitude of the VEER normal force is larger, but of opposite sense, than the ventral normal force, but not in proportion to their respective normal projected areas. This is because it is the interplay of both pressure distribution and area distribution in generating the resultant force.

Three similarities are observed between the axial force and the normal force studies:

(1) At subsonic speeds, the effect of the external flow on the VEER is favorable

(2) At supersonic speeds, the effect of the external flow on the VEER is unfavorable

(3) The effect of external flow on the ventral is negligible at all speeds.

The last point is explained by realizing that the short ventral flap experiences flowing full conditions at very low values of NPR compared to the long overhung ADEN VEER.

Another perspective is gained by converting the wind-on/wind-off lift increment to an aerodynamic basis. Figure 134 shows that this increment can be as large as 30-35% of ideal thrust at Mach 0.9. Converting from an ideal thrust basis, this is equivalent to a lift coefficient of almost 0.02. At a typical aircraft lift coefficient of 0.30, the ADEN VEER normal force increment, relative to static conditions, can represent about 7% of total lift.

The thrust of the ADEN Combat configurations is also affected by the external flow although not to such a large degree because of reduced axial projected boattail area. Figure 136, 137, and 138 present typical VEER surface pressure distributions, as a function of Mach number, for the three combat nozzles. The same physical phenomena, exhibited by the wall pressure characteristics, are present that characterized the cruise 0^{o} nozzle (Fig. 131).

Although the combat 0^{o} nozzle shows similar increments between the wind-on and wind-off characteristics as the cruise 0^{o} nozzle, the integrated VEER axial force is much reduced to due less projected boattail area in the axial direction. The vectoring combat nozzles, especially the combat 20^{o}, are characterized by smaller wind-on to wind-off increments which when integrated over the net axial projected boattail area (comprised of partially cancelling forward and rearward facing areas) lead to even smaller axial forces than on the combat 0^{o}. These treneds will be shown later.

Another significant difference between ADEN Combat and Cruise nozzles is the behavior of the flow full locus. Figures 28 and 29 are helpful in understanding this point. The break in the combat 0^{o} flow full locus (F.S. 66.5) corresponds exactly to the location at which the expansion surface changes geometric characteristics. And for the vectored configurations, the flow full locus itself is actually characterized by an imbedded oblique shock whose strength increases with VEER deflection angle. Its location is just upstream of the VEER hinge as would be expected.

The expansion ramp of the ALBEN is significantly shorter and possesses less axial projected area than the ADEN VEER; thus less external flow effects are anticipated. Figure 139 presents the expansion ramp pressure distribution at a nozzle pressure ratio of six for Mach 0, 0.9, 1.35. As with the ADEN VEER, the subsonic pressure distribution is favorable while the supersonic one is unfavorable. It is however interesting to observe that the ALBEN is already flowing full at a nozzle pressure ratio of six while for the ADEN it is about eleven. The reason is because the effective overall area ratio of the ALBEN is smaller than that of the ADEN.

The series of graphical trends in Fig. 140, 141, and 142 crystalize the effect of external flow on the internal thrust produced by the upper external expansion ramps of asymmetric exhaust nozzles. The first of these figures shows the effect of nozzle type as the size of the expansion ramp is physically reduced approaching the

circular nozzle as the limiting case. It is seen that the large influence of external flow for the ADEN rapidly diminishes with expansion ramp size. (As pointed out previously, based on Ref. 6, this effect is zero for circular nozzles at subsonic operating conditions.) In terms of aerodynamic drag, at this Mach 0.9 condition, the five percent thrust increment for the ADEN VEER is equivalent to about 25 drag counts.

Figure 141 presents the trend of the VEER axial force increment as jet area is increased for the unvectored ADEN configuration. The effect of external Mach number on this thrust component reduces rapidly as throat area is opened up. This trend is consistent with the fact that the total flow path turning angle decreases as jet area increases for the ADEN.

Lastly, Fig. 142 shows the effect of ADEN Combat vectoring on the incremental VEER thrust component. For all three combat nozzles, the influence of external flow is small, but a definite trend is apparent. As the VEER is deflected, the initial favorable effect of external Mach number changes to an unfavorable one. This is caused by the axial projected area vector of the VEER which changes sense at deflection conditions.

The above discussion has demonstrated the existence of very interesting fluid mechanic mechanisms that are responsible for the thrust installation effect of asymmetric nozzles. The interplay between external and internal flows can lead to significant lift and drag contributions that are produced on the ADEN internal surfaces.

Intentionally Left Blank

SECTION VIII

ACCURACY AND REPEATABILITY CONSIDERATIONS

The absolute accuracy of this program's test data, as with most wind tunnel programs, cannot be determined. That is because truth or an absolute standard is unknown. However, the related subject of repeatability can be discussed. Good repeatability does not necessarily mean good accuracy because the experiment may be merely repeating the incorrect absolute level; for example, if a constant bias existed in the experiment. However, in this test program, as in most research programs, interest lies in comparing configurations on an incremental basis; thus, for such an experiment, designated a "test of differences", the repeatability becomes the parameter of significance (assuming bias errors are not random).

There are several classifications of repeatability that vary in their respective degrees of stringentness. For example, the most common repeatability categories are listed below in descending order of rigor:

(1) Same model; two different tunnels

(2) Same model and tunnel; different entries

(3) Same model, tunnel, and entry; different tunnel-blows

(4) Same model, tunnel, entry, and tunnel-blow; repeat at different time within the tunnel-blow

(5) Same model, tunnel, entry and tunnel-blow; "back-to-back" repeat.

These thoughts are to be taken into account when the subject of repeatability is presented.

The total uncertainty, a measure of repeatability, in the key output parameters can be predicted analytically provided certain conditions are met. This calculation assumes that all the individual component uncertainties are random, independent, and normally distributed. This is a valid assumption for properly operating wind tunnel measurement systems. For such measurement systems, in

which the magnitude and/or sign of the independent variable contributing uncertainties are not known, the total uncertainty is given by the Root-Sum-Square of these individual contributing uncertainties.

For example, the total uncertainty, E_{TOT}, for a balance component measurement is dependent upon four contributing uncertainties:

- Balance calibration, E_1
- Bellows pressure tare correction, E_2
- Momentum tare correction, E_3
- Cavity tare correction, E_4.

Thus the total uncertainty would be calculated as follows:

$$E_{TOT} = \pm \left[E_1^2 + E_2^2 + E_3^2 + E_4^2 \right]^{1/2}$$

The uncertainties, E_1 through E_4, can be determined by studying the calibration curves of all the particular measurement instruments utilized. This was done for E_1 using balance calibration data. Estimates for E_2 through E_4 were more easily and practically obtained by studying the actual data obtained from numerous identical repeat runs for each correction (E_2 through E_4) and using engineering judgment to define the realistic component uncertainties. Finally, the main balance uncertainty for an empirically estimated 90% confidence level were calculated and are summarized below:

Main Balance Component	Theoretical Uncertainty
Axial Force	± 6 lb
Normal Force	± 15 lb
Pitching Moment	± 60 in.-lb

In terms of lift and drag coefficients at the key Mach 0.9 condition these uncertainties represent ±0.006 and ±0.0025 respectively. For lift coefficient, ±.006 is small compared to the magnitude of lift enhancement increments that characterize the differences between configurations of this test. However, for the drag direction, ±0.0025 is a significant number that must always be kept in mind when analyzing test results and developing conclusions.

Figure 143 shows the variation in theoretical drag coefficient uncertainty over the complete test Mach number range in addition to Mach 0.9. Note that at the higher speeds, the uncertainty decreases to ±20 drag counts, while at Mach 0.4, the uncertainty grows to ±50 counts. Because of this well-known effect (resulting from dynamic pressure variations with speed), the test data at Mach 0.4 many times was characterized by abnormally large scatter.

In general, observation has shown that the bulk of the actual test data does not exhibit the degree of scatter suggested by Fig. 143. It is to be emphasized that this uncertainty represents a worst case situation for any single data point within 90% of the total data population. Any given data point may be in error by as much as ±25 drag counts at Mach 0.9; however, most of the data points will be grouped much closer to the mean of Gaussian distribution.

Notwithstanding, in the data analysis phase of this program, special emphasis was placed on eliminating scatter from the data to attempt to reduce the uncertainty even further. For every configuration, both lift and drag were first faired versus angle-of-attack for consistency. Then, the data was crossplotted and faired versus nozzle pressure ratio. From the latter, smooth drag polars were developed which were employed in the ensuing analyses of comparing nozzle configurations.

The above discussion addressed the uncertainty in a measured force balance component such as total lift, thrust-minus-drag, or jet-off drag. The uncertainty in a thrust-removed parameter will be larger because the uncertainty in static thrust must also be considered. The static thrust uncertainty can either be negligible or significant depending on the number of static runs and the precision with which the static data is faired. For example, if many repeat static runs were conducted, as in the subject program, and the data is very carefully faired (iterating between the Fip- and P_o-formats as explained in subsection 6.1), then the uncertainty in static thrust (axial component) can approach the ±1/2% level (of ideal thrust) which is on the order of ±5 drag counts (at operating pressures at Mach 0.9). Thus, the theoretical uncertainty in the thrust-removed parameter becomes dominated by the wind-on as opposed to the wind-off measurement (e.g., ±25 versus ±5 counts). In such cases, the uncertainty in static thrust is considered relatively negligible.

On the other hand, a lack of repeat runs or imprecise fairings for the static data can lead to large errors, and, in fact, easily double the uncertainty in the thrust-removed drag. It was pointed out in subsection 6.1 that care must be exercised in fairing the static thrust data of the P_o-format at high pressure ratios due to a strong uncertainty sensitivity to slope error. For example, an inaccuracy in the faired static thrust (T_s/P_o) of only 0.005 for each of two nozzles, but in opposite directions, can easily lead to an error, in the difference of their respective thrust-removed drags, of 25 drag counts. This can be serious when comparing the trends of thrust-removed drag for a configuration series such as for the ADEN Combat 0^o, 10^o, 20^o. For the comparison studies presented herein, this knowledge was taken into account by occasional "fine-tuning" of the static thrust fairings.

Reference 10 discusses in detail the additional post-test calibration that was applied to the main balance axial force of several nozzle configurations to account for a balance shift that introduced a constant bias in the data. Therefore the total uncertainty in drag will be somewhat greater than it otherwise would have been as discussed above. It is estimated that this additional tolerance is on the order of ±5 to 10 drag counts.

An actual example of data repeatability, within a tunnel blow, but not obtained "back-to-back", is given in the chart below for the ADEN Cruise 0^o configuration:

Mach Number	Drag Coefficient	Drag Difference
0.40	0.0301	
0.40	0.0272	0.0029
0.60	0.0303	
0.60	0.0286	0.0017
0.80	0.0326	
0.80	0.0326	0.0000
0.90	0.0358	
0.90	0.0352	0.0006
0.95	0.0403	
0.95	0.0399	0.0004
1.35	0.0866	
1.35	0.0875	0.0009

The general trend of the repeatability difference is consistent with both the theoretical discussion above and the trend shown in Fig. 143. Data confidence is greater at the higher Mach numbers and is poorer at the lower Mach numbers. Note, however, that the chart above represents only a sample set of data - some of which, coincidentally, could have been distributed close to the mean of the Gaussian distribution. Thus, for example, it is not necessarily surprising that the Mach 0.8 point repeated exactly.

An example of tunnel-to-tunnel repeatability is shown for the primary ADEN Cruise 0^{o} configuration using the data of Ref. 3. Figure 144 presents the thrust-removed polars at the key Mach 0.9 condition at an operating pressure ratio of 5.0. It is readily observed that very little difference exists between the polars of the two different facilities at low angles-of-attack. At lifting conditions, a slight change in slope is observed showing a typical disparity of 25 drag counts. Realizing the many differences that characterized the two facilities, model-builds, and experimental procedures, this tunnel-to-tunnel repeatability comparison is surprisingly good.

Discussions of accuracy and repeatability should also include considerations based on experience and intuition even though they can't be quantified. In this test program, not unlike many others, certain discrete batches of data exhibited irreconcilable behavior. In such instances, when the preponderance of similar data (at other Mach numbers or nozzle pressure ratios for example) was overwhelming in comparison to the irreconcilable data, the latter was deemed invalid. Accordingly, all the comparisons presented herein were not extracted from the complete data set at random, but instead were extracted only after studies showed the trends to be representative of the majority of the data.

In closing, it is noted that the only data presentation included herein that cannot be confirmed is the study on inlet fairing type (subsection 7.9). Although the force balance trends appear reasonable, they not only defy intuition, but also are not supported by the pressure data. In the spirit of full disclosure, the author desires to present the results, but cannot express a confident opinion on them.

Intentionally Left Blank

SECTION IX
CONCLUSIONS

This wind tunnel jet-effects test program employing a highly integrated underwing nozzle installation on a V/STOL vehicle design produced many significant conclusions that are summarized below:

(1) The ADEN and ALBEN installations are characterized by synergistic jet/wing interactions (jet-effect increments are lift dependent) as angle-of-attack is increased in contrast to the circular nozzle installation which is not lift sensitive to power

(2) The unvectored ADEN and ALBEN configurations, which are competitive on a thrust-removed polar basis, both show large performance gains, at all flight conditions, relative to the circular nozzle. A typical cruise drag reduction is 50 counts at Mach 0.9

(3) Relative to the axisymmetric installation, the ADEN and ALBEN installation exhibit lower trim drag which will further increase the performance benefits noted in (2)

(4) For either vectored or unvectored modes, markedly different drag trends occur when nozzle pressure ratio is varied at constant lift compared to constant angle-of-attack for the ADEN installation

(5) Drag increments due to jet area changes are heavily dependent on angle-of-attack, in addition to nozzle pressure ratio, for the non-axisymmetric ADEN configuration because additional drag reductions occur as lift is increased

(6) The aircraft drag polar, and not the individual drag or lift components, must be used as the figure of merit in evaluating the aeropropulsion performance of highly integrated non-axisymmetric underwing nacelle installations. Total vehicle performance is then obtained by combining the thrust-removed polars with real engine data for a given mission

(7) The influence of thrust-vectoring, for this low aspect ratio ADEN, travels very far upstream and spanwise (almost to the wing tip) as a function of Mach number. This demands that a fully-metric model be utilized when assessing aeropropulsion phenomena

(8) Vectoring the ADEN has a dramatic effect on polar shape. An optimum polar locus is formed by an envelope of points covering a range of deflection angles. This means that deflection angle should be scheduled to angle-of-attack to achieve optimum performance

(9) Drag reductions due to thrust vectoring generally increase as subsonic Mach number is reduced. No vectoring benefits exist at supersonic speeds

(10) At a key Mach 0.9 cruise (non-afterburning) condition, a 40 count drag reduction is realized as the ADEN is vectored from 0^{o} to 10^{o}

(11) When the thrust-vectoring payoff of (10) is combined with the axi-/non-axisymmetric nozzle payoff of (2), a 90 count drag reduction, which represents 25% of zero-lift drag for this V/STOL vehicle, is achieved for the vectored ADEN over the baseline circular nozzle installation

(12) At Mach 0.9 maneuver conditions, only moderate (10^{o}) deflection angles of the ADEN Combat (max-afterburning) nozzle are expected to possess potential payoffs because larger deflections are characterized by severe thrust-loss and induced drag penalties

(13) Relative to undeflected conditions, both ADEN Cruise and Combat vectoring modes exhibit lower trim drag, at conditions of interest, which will further increase the performance benefits noted in (10), (11) and (12)

(14) Extensive wing/body surface pressure instrumentation is invaluable in developing a theoretical understanding of the three lift enhancement mechanisms (plume blockage, supercirculation, and, transonic shock movement) responsible for thrust vectoring benefits

(15) Force data results show that the effect of inlet fairing type can influence the magnitude of the jet-effect drag increment as a function of Mach number and angle-of-attack. Corresponding pressure data results do not support this conclusion so that further investigation is required

(16) Analysis of ADEN internal pressure data show that the upper expansion ramp surface is very sensitive to the effects of external flow. At subsonic speeds, relative to static conditions, the incremental thrust produced by the expansion ramp is favorable; at supersonic speeds this effect is unfavorable. These effects are roughly proportional to ramp size and inversely proportional to both jet area and deflection angle increases

(17) Accuracy demands when employing thrust measuring systems that are used to deduce thrust-removed drag (by employing the method of differences) are severe. Drag data uncertainty can be a strong function of not only the test procedures used to obtain static thrust calibrations but also the techniques employed to fair the static data

(18) The magnitude and shape of the ADEN V/STOL installation drag polar generated in this wind tunnel program is in good agreement with a recent AFFDL sponsored test program (ref. 3).

GRUMMAN AEROSPACE CORPORATION
BETHPAGE, NEW YORK
JUNE 30, 1981

The author wishes to thank Mr. Alan Levin, of NASA Ames, and Mr. Ken Oliver, formerly of the Grumman Aerospace Corporation, for the development of the data reduction computer code and its adaptation to the NASA Ames computer facility. Additionally, special commendation is given to Mr. Warren Davis and Mr. Gianky DaForno, both of the Grumman Aerospace Corporation, who provided technical assistance in the aerodynamic analysis and interpretation of the wing surface pressure data (their efforts were supported through Grumman in-house IR & D funding). Most importantly, the author gratefully thanks Mr. Gus Ordonez, of the Grumman Aerospace Corporation, for preparing the extensive wind-tunnel data comparison graphs which are highlighted in this document.

Intentionally Left Blank

REFERENCES

1. Schnell, W. C., and Ordonez, G. W., "Axisymmetric & Non-Axisymmetric Exhaust Jet Induced-Effects on a V/STOL Vehicle Design" (Part I: Data Presentation), NASA CR 166146, May 1981

2. Hoff, G., "Installed Performance of the 2-D ADEN on an Advanced Multimission V/STOL Fighter Aircraft Model," General Electric Co. Report No. R76AEG468, 1978

3. Schnell, W. C., and Grossman, R. L., "Wind Tunnel Test of a Propulsive Lift Enhancement Model," AFFDL-TR-78-104, August 1978

4. Boardman, W. R., "Augmented Deflector Exhaust Nozzle (ADEN) Demonstrator 1/8 Scale Cold Flow Static Test Results", General Electric Report No. R75AEG301, September 1975

5. Prather, J. G., "ALBEN (Asymmetric Load Balanced Exhaust Nozzle) Static Performance Test", General Electric Memorandum No. 75-281, July 1975

6. Schnell, W. C., "F-14 Installed Nozzle Performance," AIAA Paper No. 74-1099, October 1974

7. Schnell, W. C., and Grossman, R. L., "Vectoring Non-Axisymmetric Nozzle Jet Induced Effects on a V/STOL Fighter Model," AIAA Paper No. 78-1080

8. NASA Ames 11 ft. Tunnel Facility Description, Ames Research Facilities Summary, 1974

9. Toscano, E. J., and McAllister, W. J., "Design Procedure for a Bellows Sealing System," Presented at 44th Semi-Annual Supersonic Tunnel Association Meeting, September 1975

10. Schnell, W. C., "Axisymmetric & Non-Axisymmetric Exhaust Jet Induced-Effects on a V/STOL Vehicle Design" (Part III: Experimental Technique), NASA CR 166147, To Be Published (late 1981)

11. USAF Contract No. F33615-76-C-2036," Installed Turbine Engine Survivability Criteria (ITESC) Program"

12. USAF Contract No. F33615-76-C-3019, "Experimental Evaluation of Non-Axisymmetric Exhaust Nozzles"

13. Capone, F. J., "A Summary of Experimental Research on Propulsive-Lift Concepts in the Langley 16-Foot Transonic Tunnel," AIAA Paper No. 75-1315, 1975

14. Maskell, E. C., and Spence, D. A., "A Theory of the Jet Flap in 3-D," Proceedings of the Royal Society, A251, pages 407-425, 1959

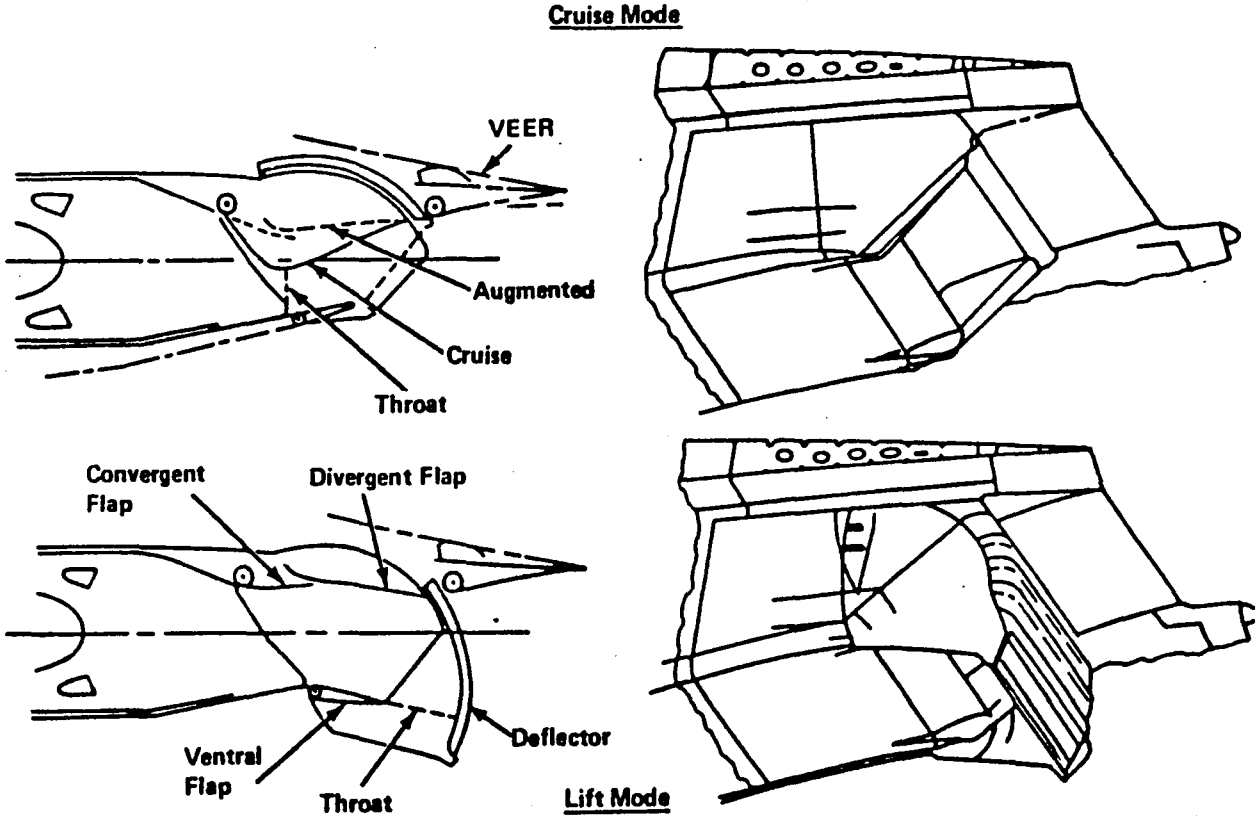

Figure 1 Augmented Deflector Exhaust Nozzle (ADEN)

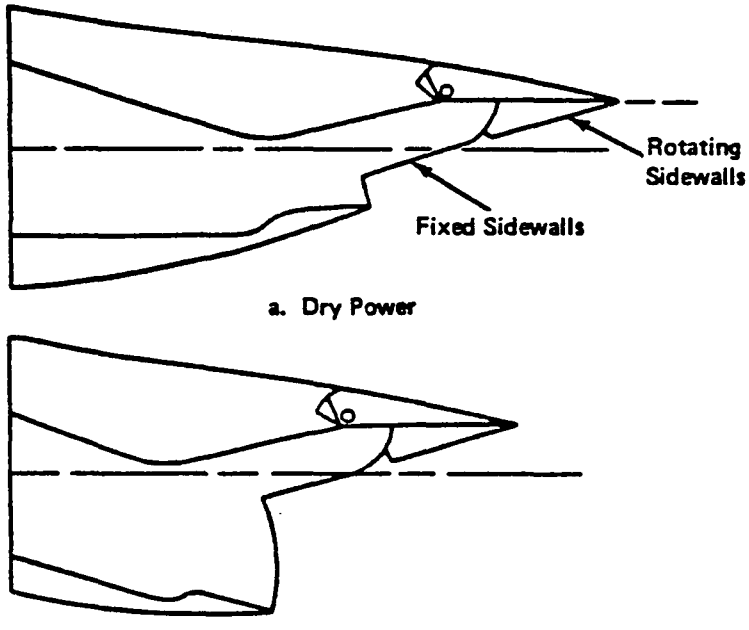

Figure 2. Asymmetric Load Balanced Exhaust Nozzle

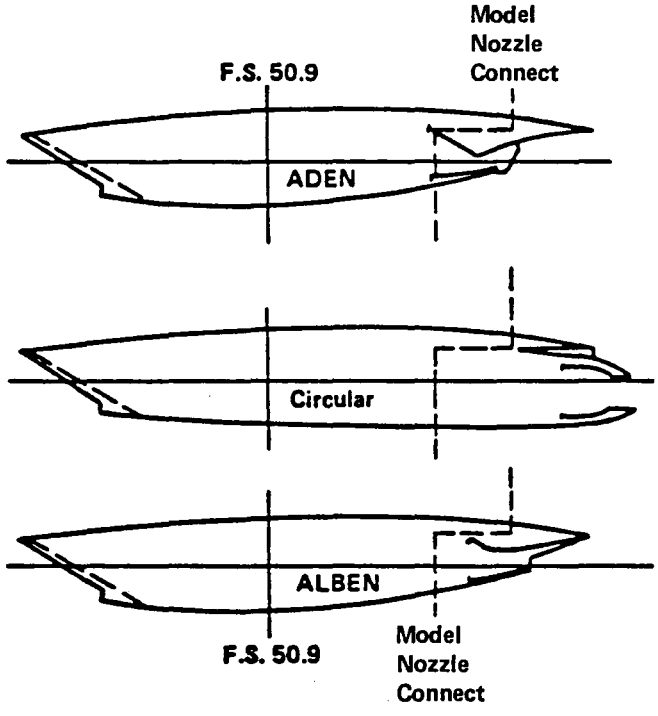

1068-030(T)

Figure 3 Test Nozzle Installations

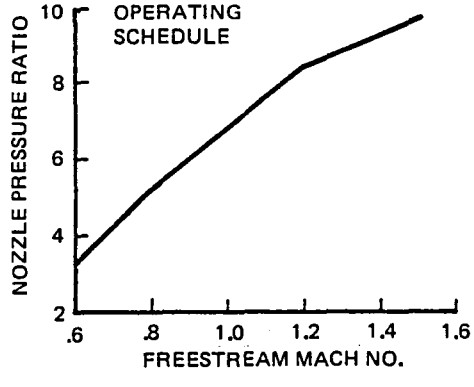

1068-001(T)

Figure 4 Engine Operating Schedule

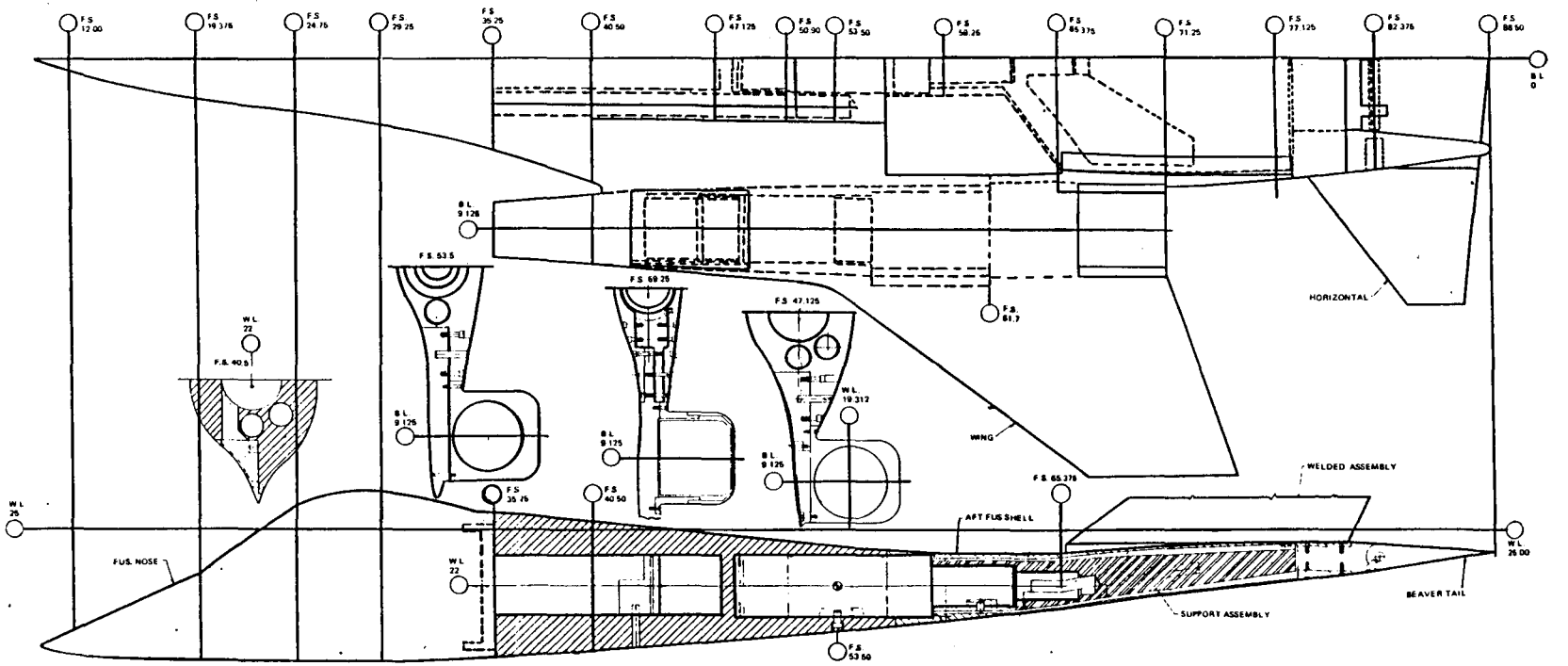

1068-044(T)

Figure 5 General Assembly Drawing

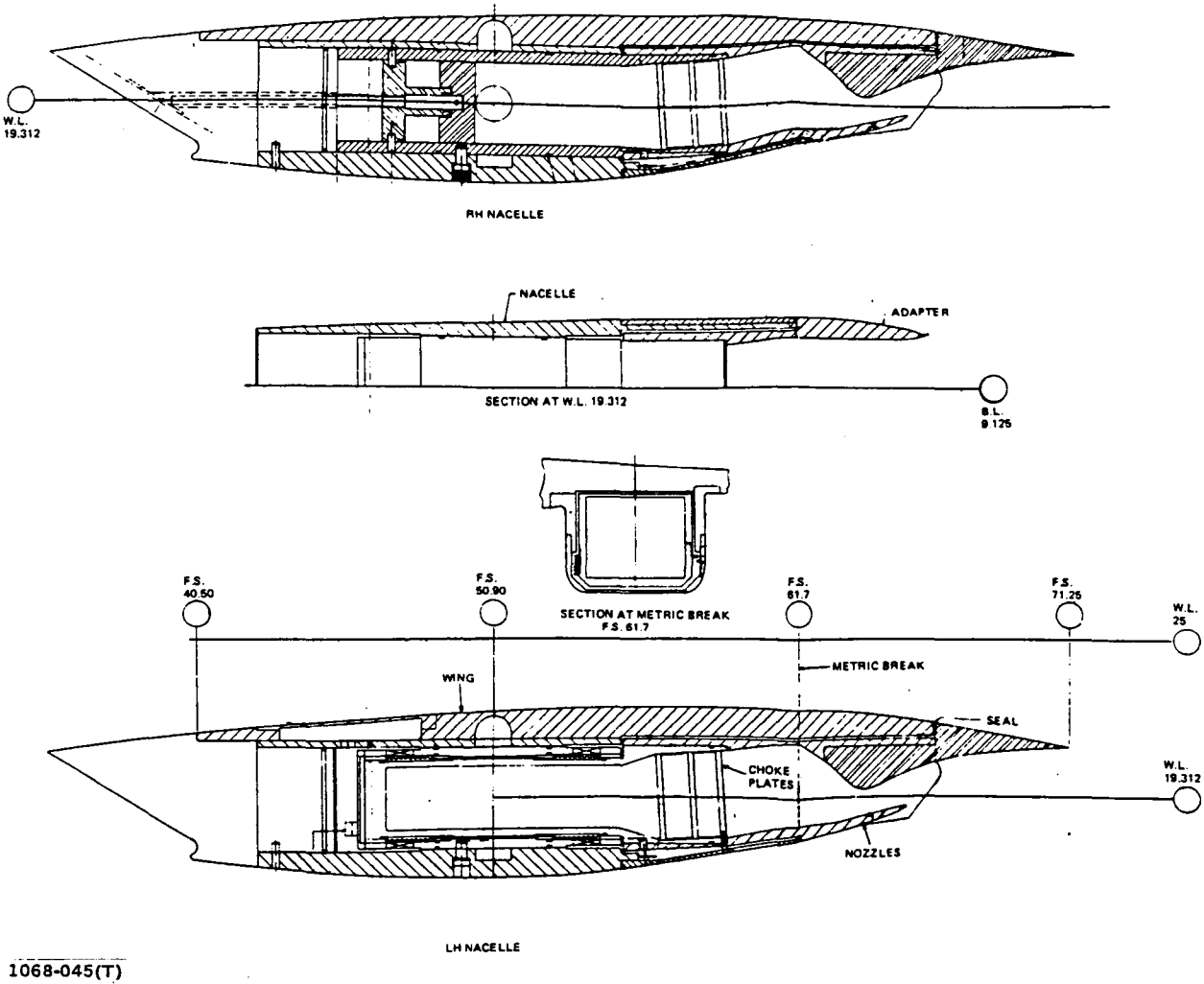

1068-045(T)

Figure 6 Nacelle Assembly Drawing

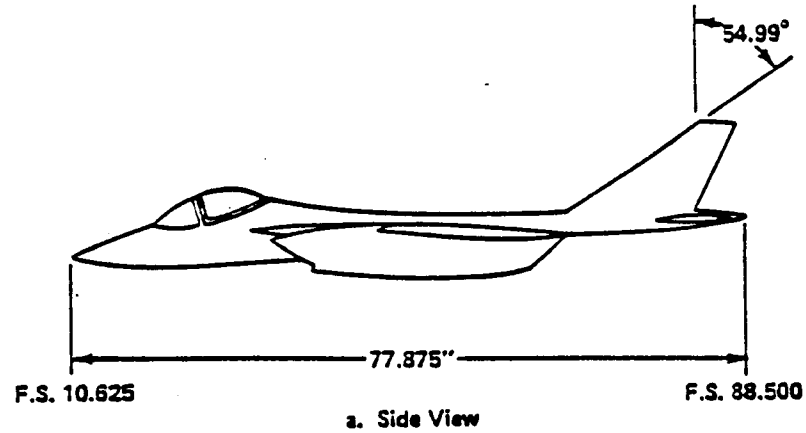

a. Side View

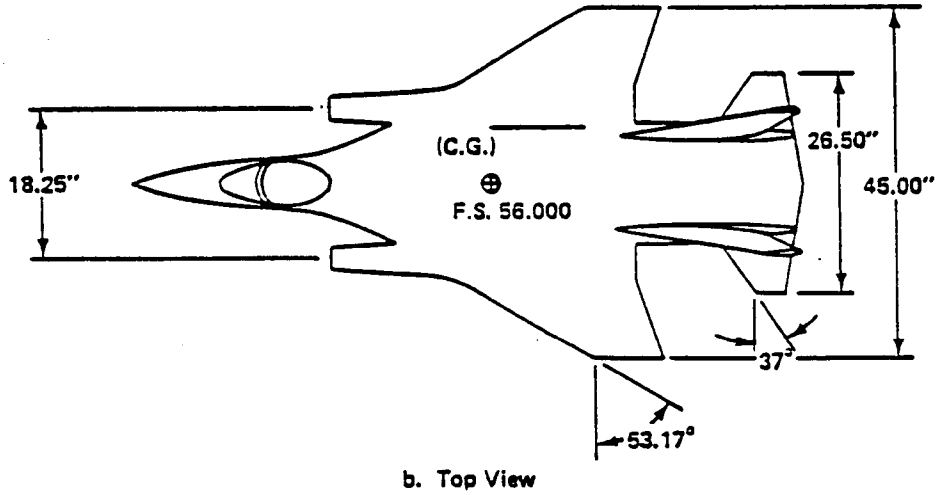

b. Top View

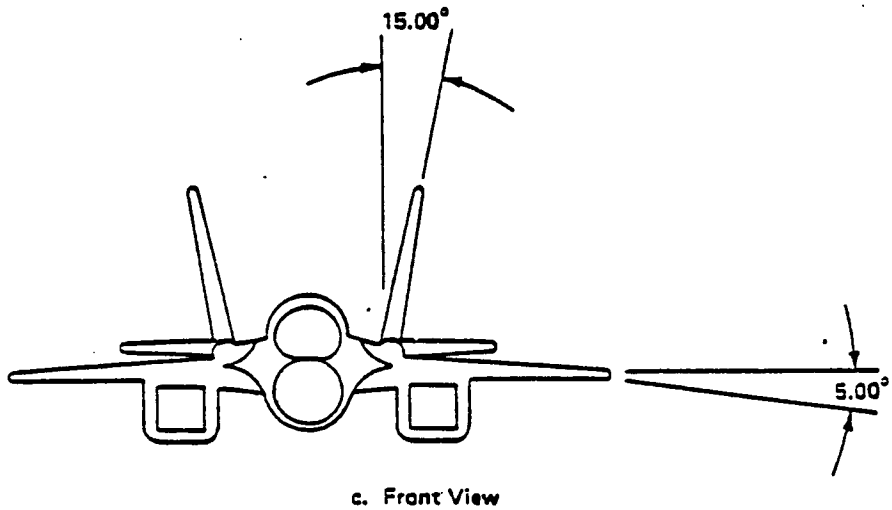

c. Front View

1068-031(T)

Figure 7 Navy V/STOL High-Speed Model 623-2004B

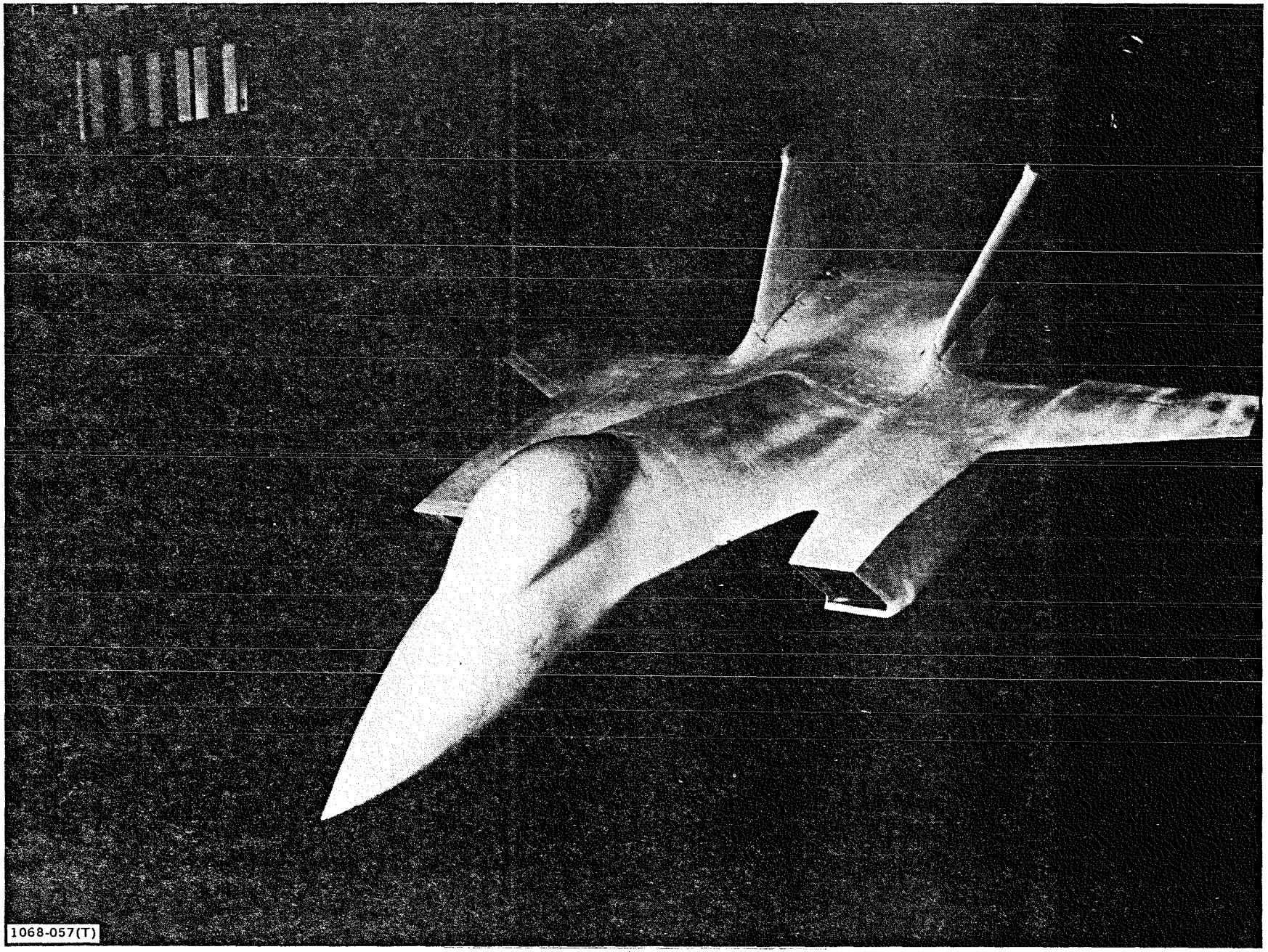

Figure 8 Model Installed in AMES 11 Ft. Tunnel

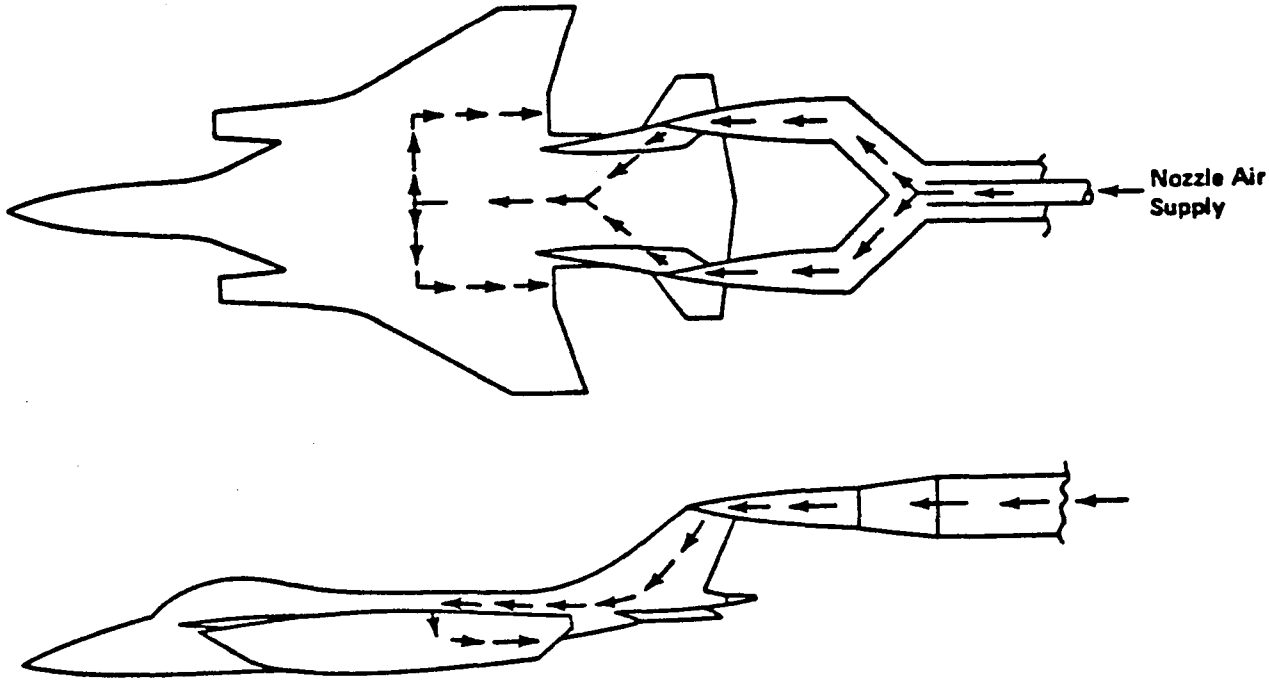

1068-032(T)

Figure 9 Model Support and Flow Systems

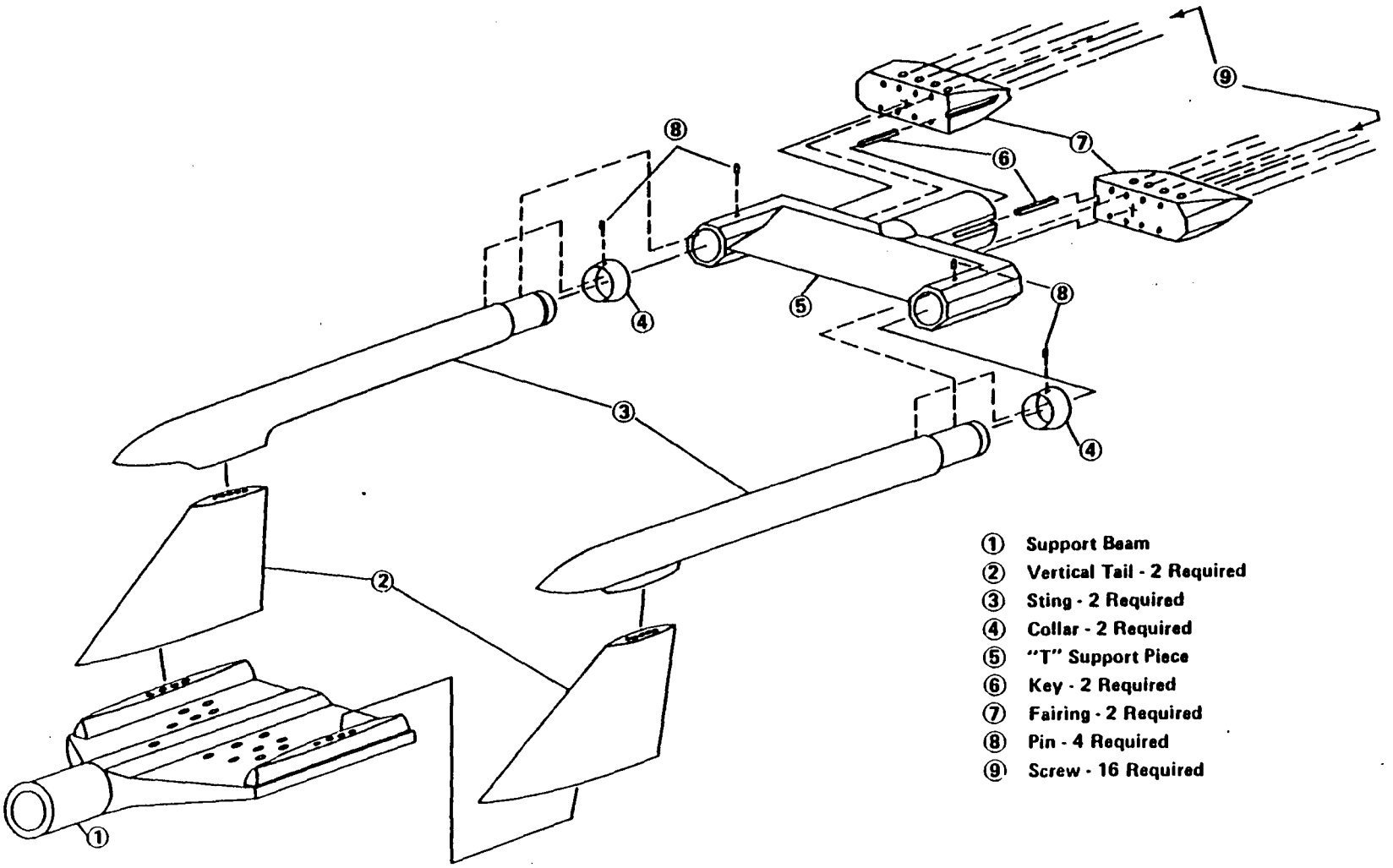

1068-046(T)

Figure 10 Model Support Assembly

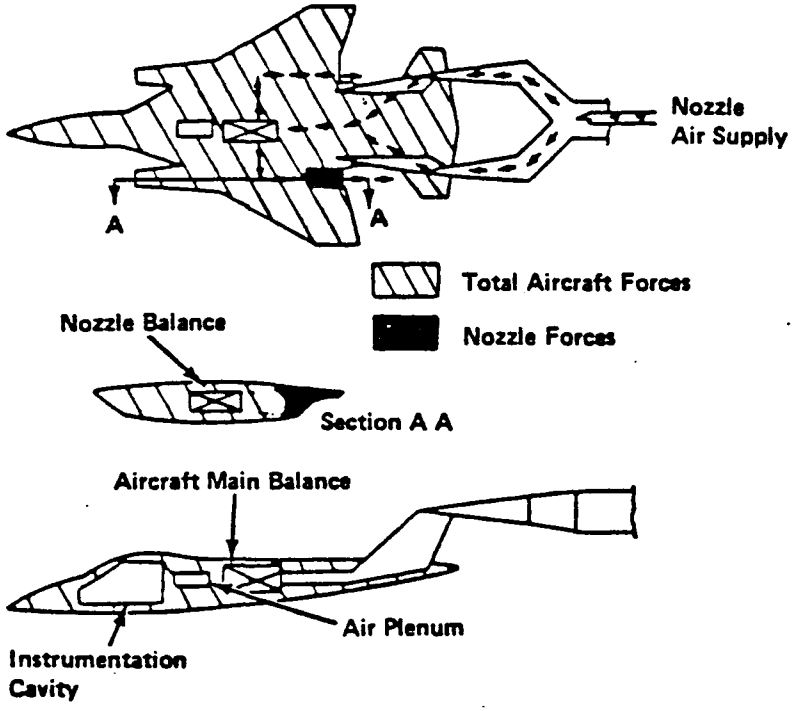

Figure 11 Model Force Balance Systems

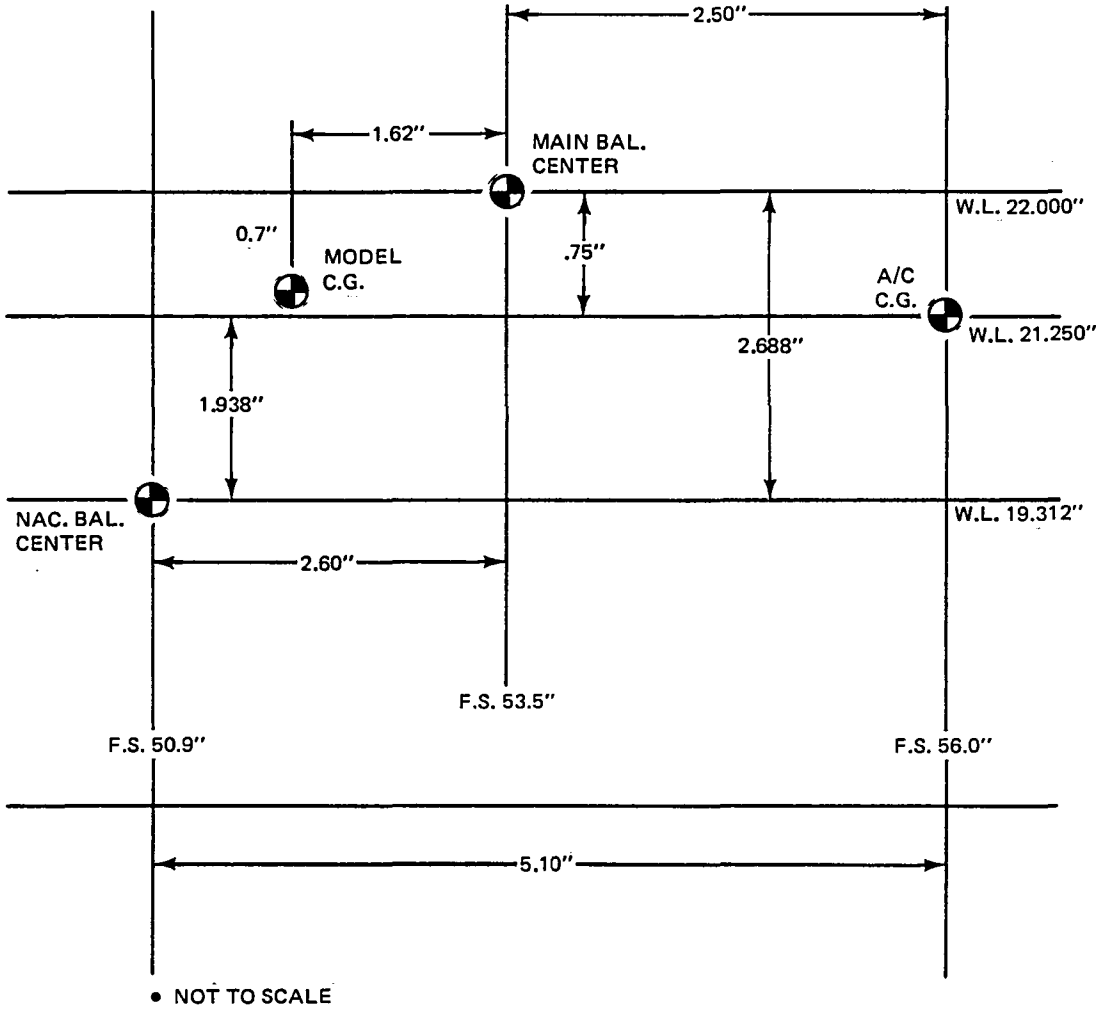

1068-002(T)

Figure 12 Balance Locations Relative to Aircraft C.G.

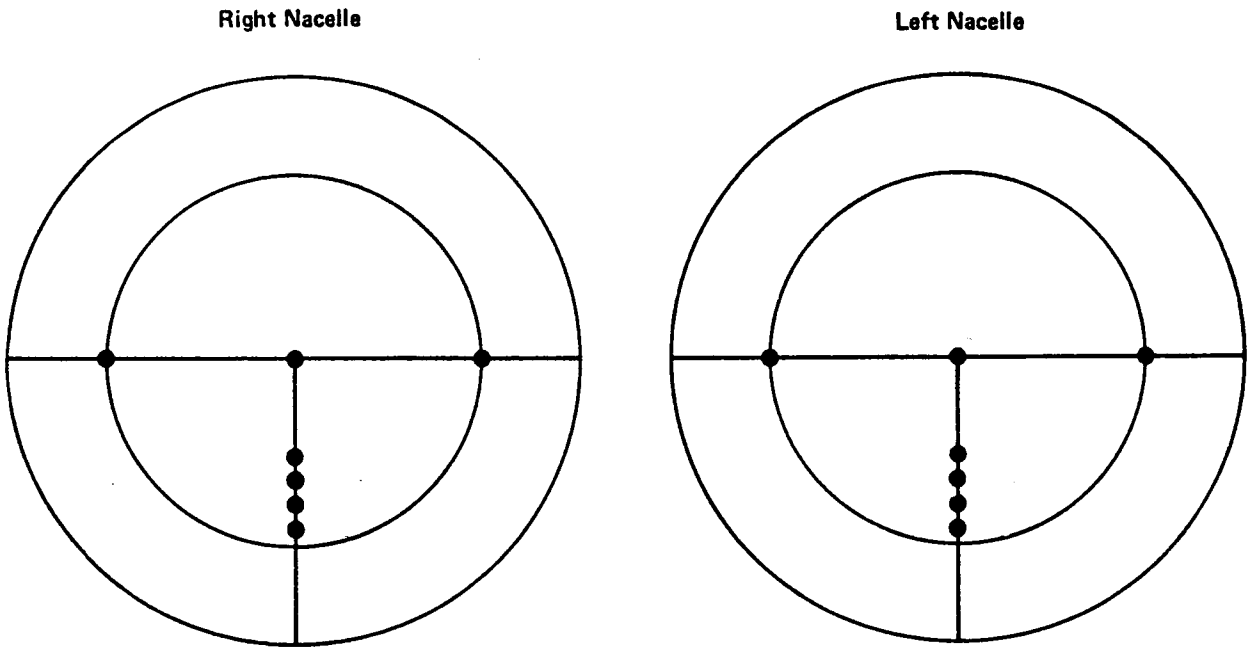

Figure 13 Circular Nozzle Total Pressure Probe Locations

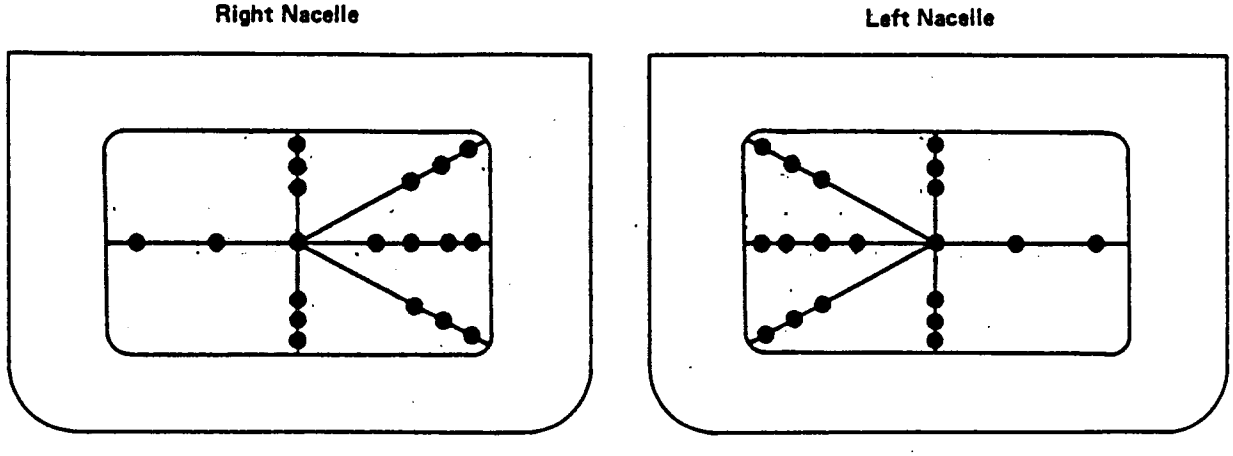

Figure 14 ADEN Total Pressure Probe Locations

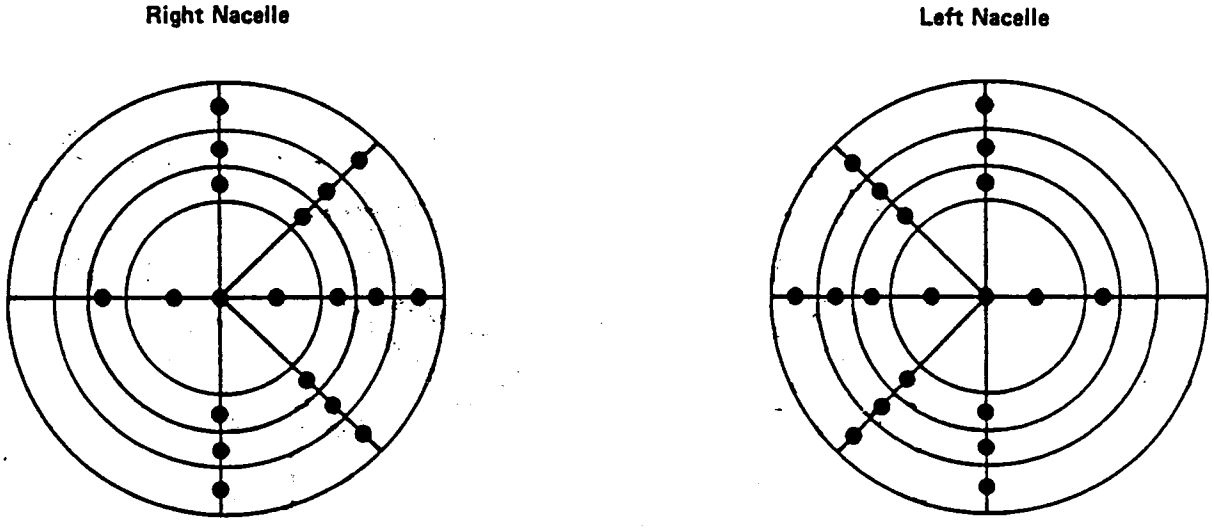

1068-048(T)

Figure 15 ALBEN Total Pressure Probe Locations

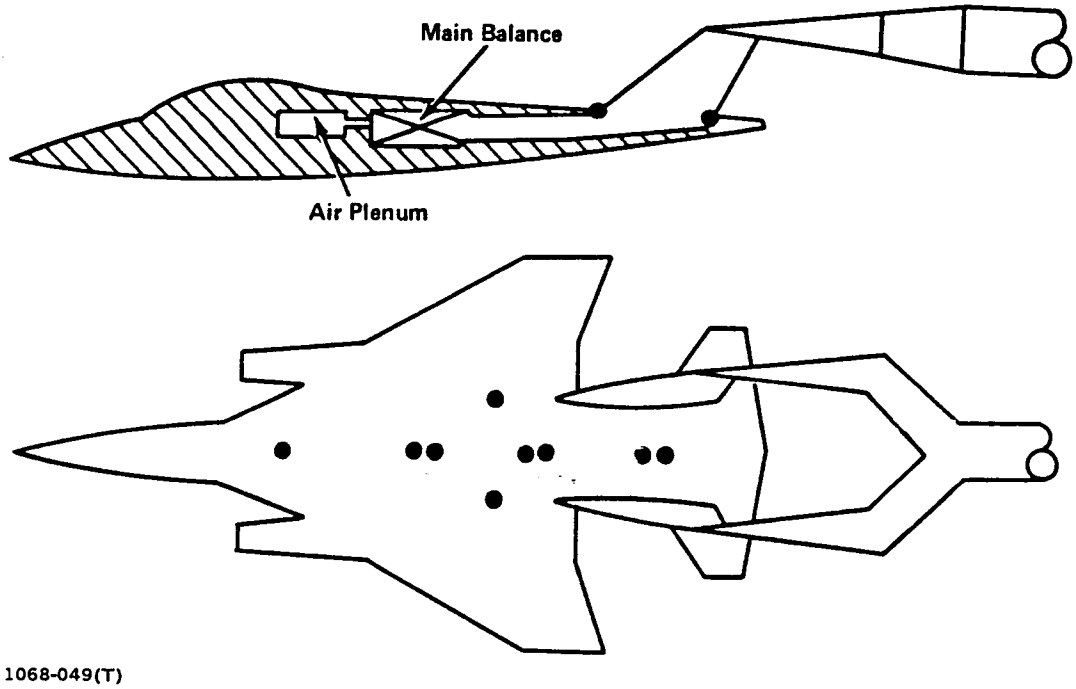

1068-049(T)

Figure 16 Fuselage Cavity Pressure Orifice Locations

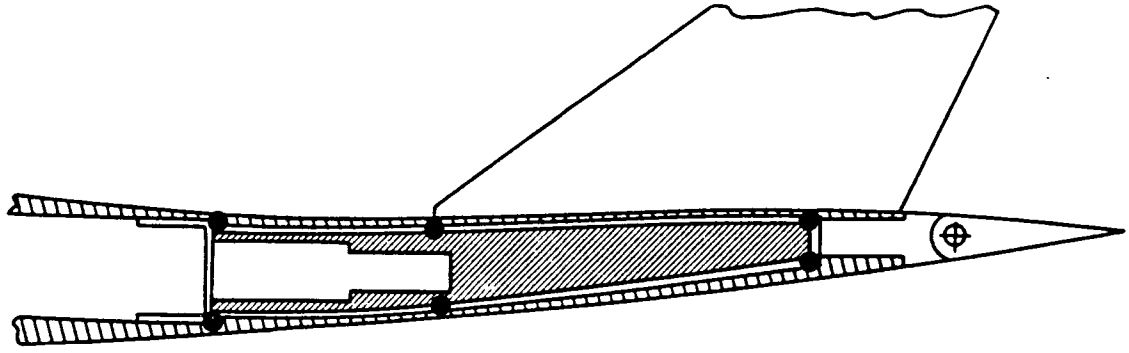

1068-055(T)

Figure 17 Aft Fuselage Cavity Pressure Orifice Locations

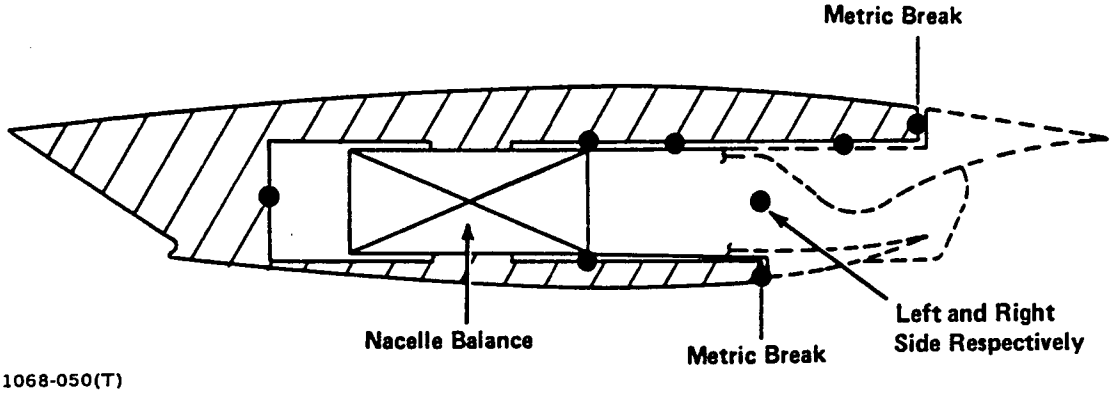

1068-050(T)

Figure 18 Left Nacelle Cavity Pressure Orifice Locations

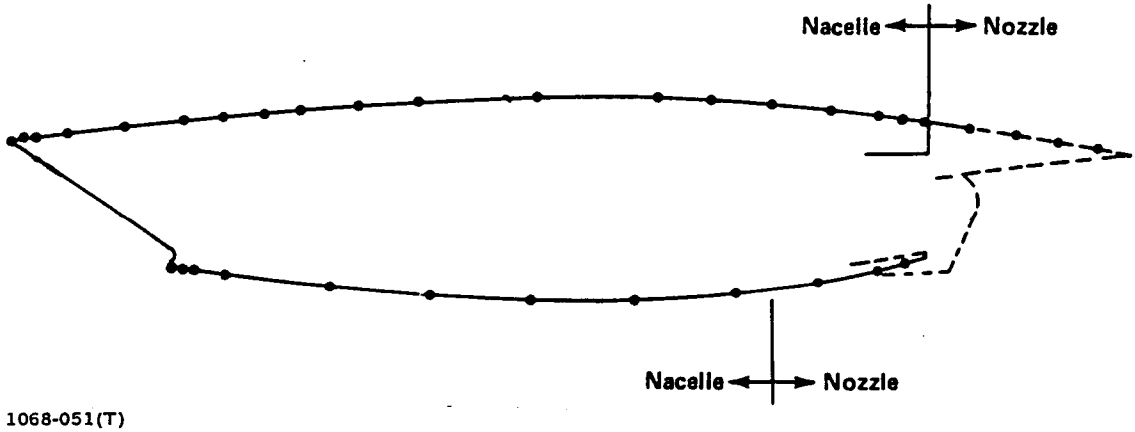

1068-051(T)

Figure 19 Nacelle/Nozzle External Pressure Orifice Locations

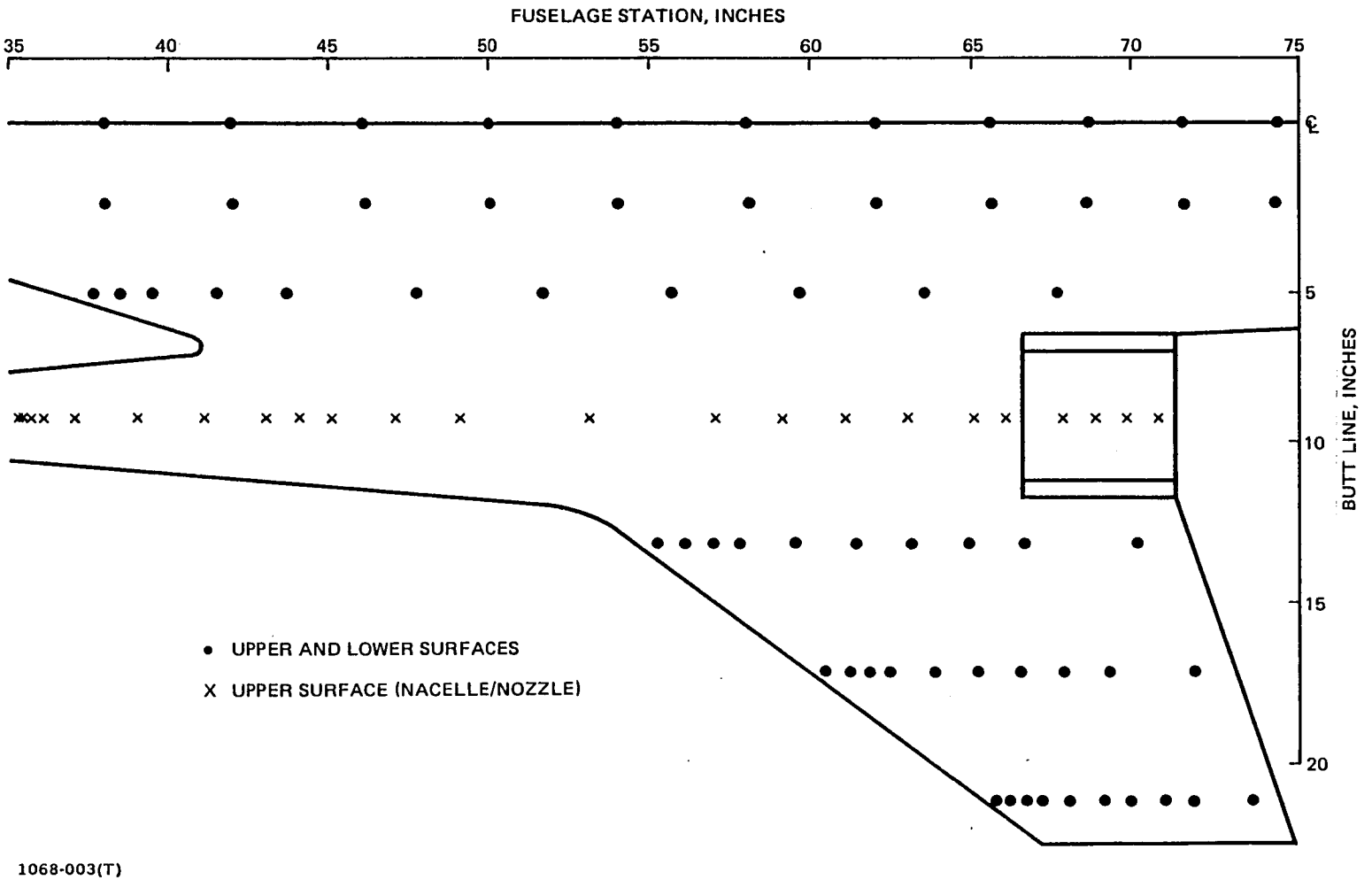

Figure 20. Wing/Body Pressure Orifice Locations

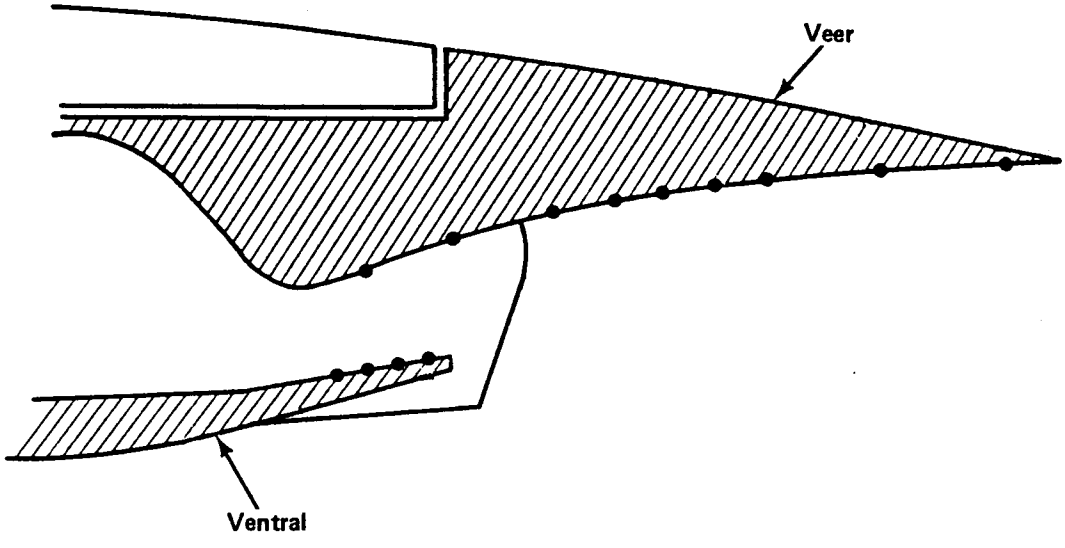

1068-052(T)

Figure 21. ADEN Internal Pressure Orifice Locations

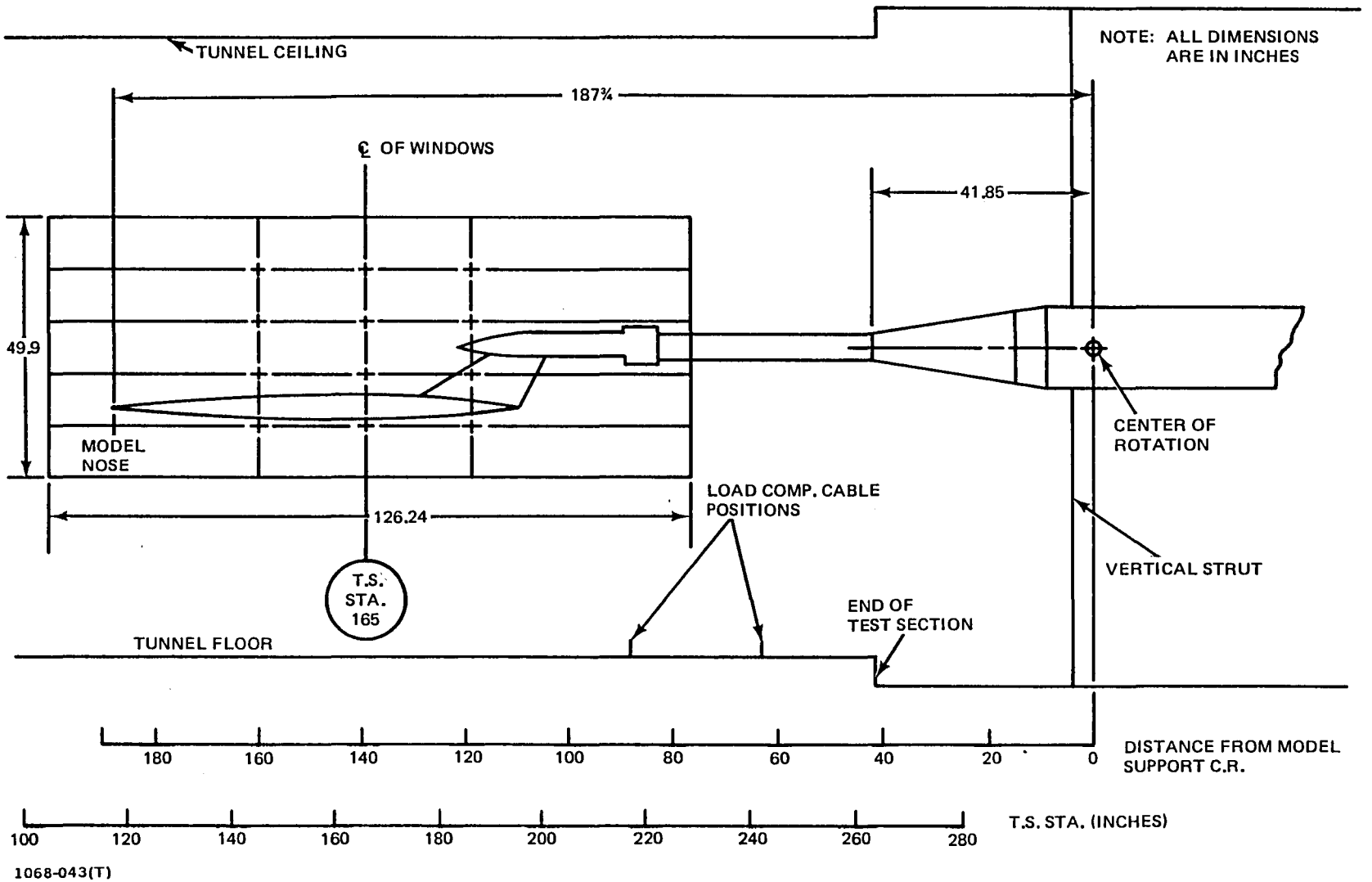

Figure 22 11- By 11-Ft TWT Model Installation Sketch without 40-Inch Extension

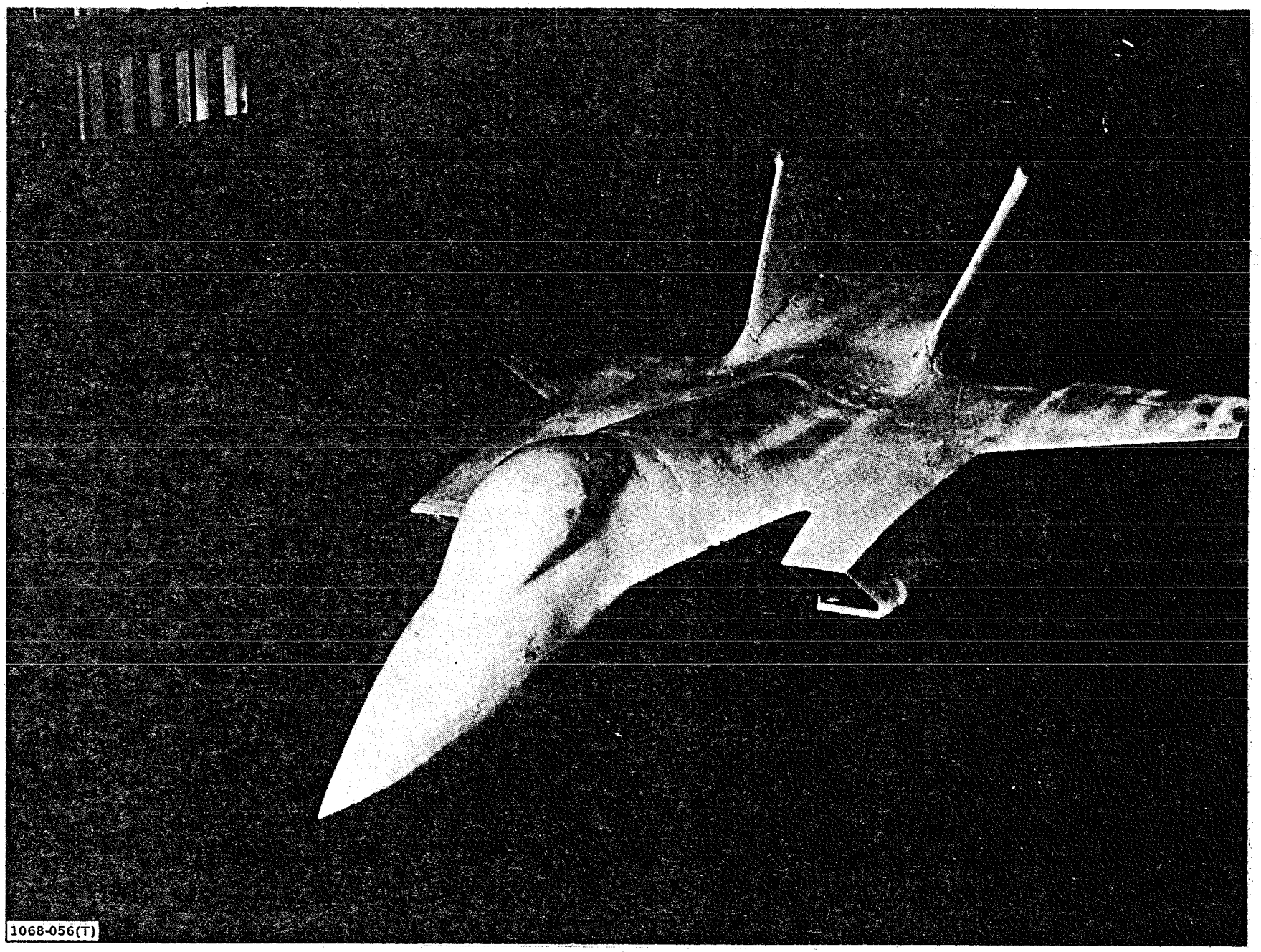

Figure 23 Model Installed in AMES 11 Ft. Tunnel

NOZZLE TYPE	OPERATING MODE	DEFLECTION ANGLE, DEG
CIRCULAR CONVERGENT DIVERGENT REFERENCE NOZZLE	CRUISE (NON A/B)	0
ADEN AUGMENTED DEFLECTOR EXHAUST NOZZLE	CRUISE (NON A/B) CRUISE (NON A/B) CRUISE (NON A/B) DASH (INT A/B) COMBAT (MAX A/B) COMBAT (MAX A/B) COMBAT (MAX A/B)	0 5 10 0 0 10 20
ALBEN ASYMMETRIC LOAD BALANCED EXHAUST NOZZLE	CRUISE (NON-A/B)	0

1068-034(T)

Figure 24 Nozzle Configuration Matrix

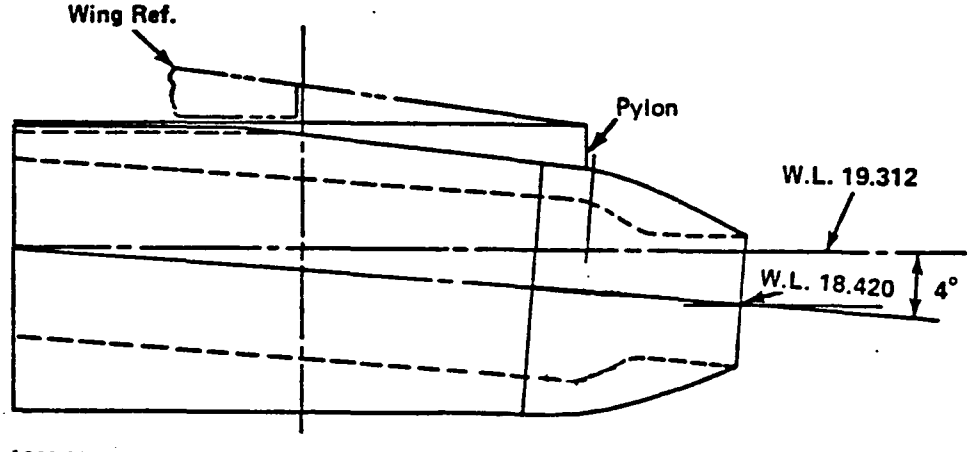

1068-035(T)

Figure 25 Circular Nozzle Model

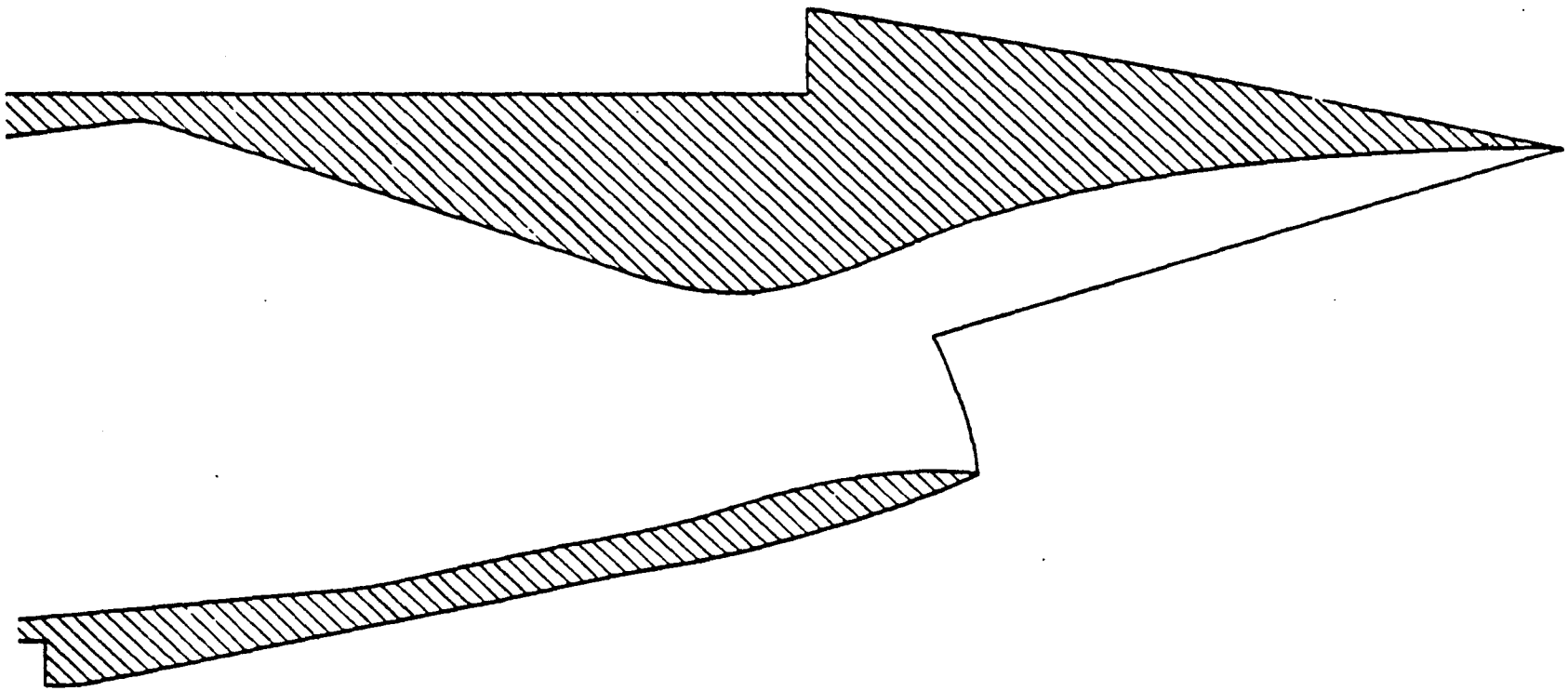

1068-036(T)

Figure 26 ALBEN Configuration

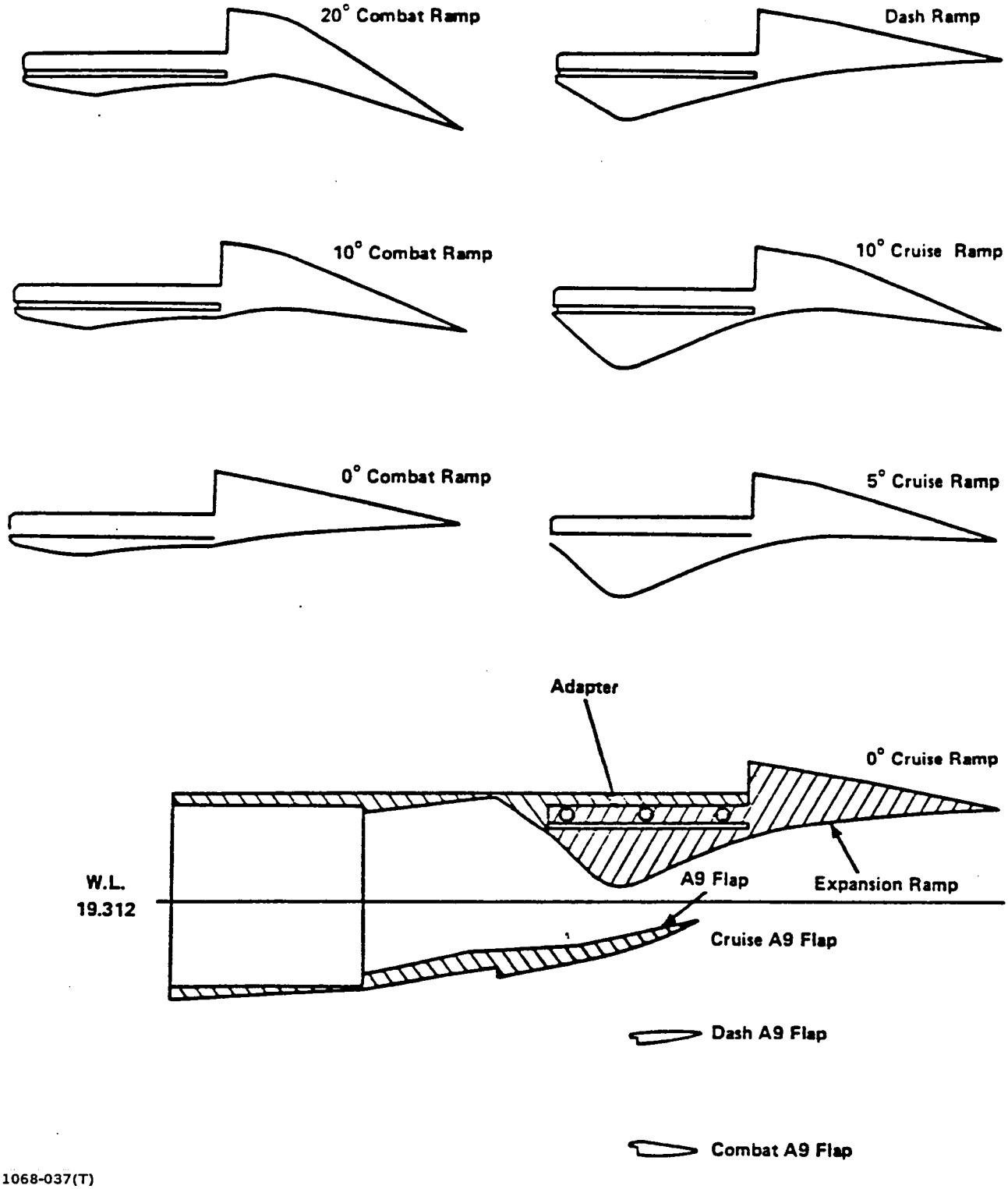

Figure 27 ADEN Configuration Variants

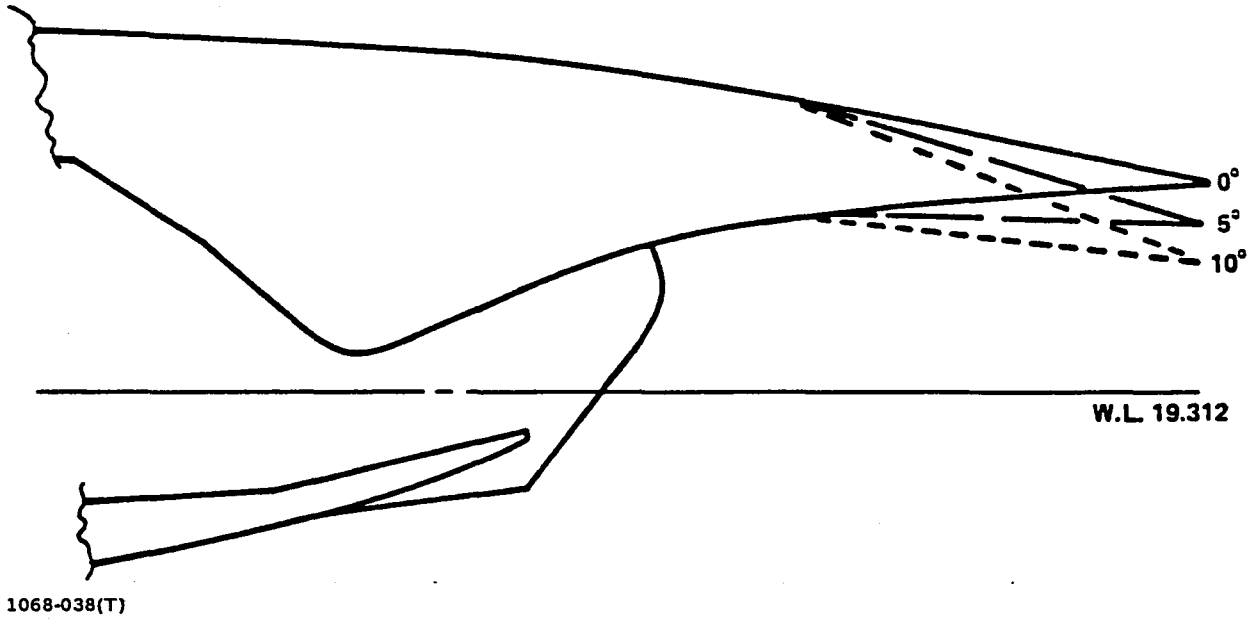

Figure 28 ADEN Cruise Vectoring Comparison

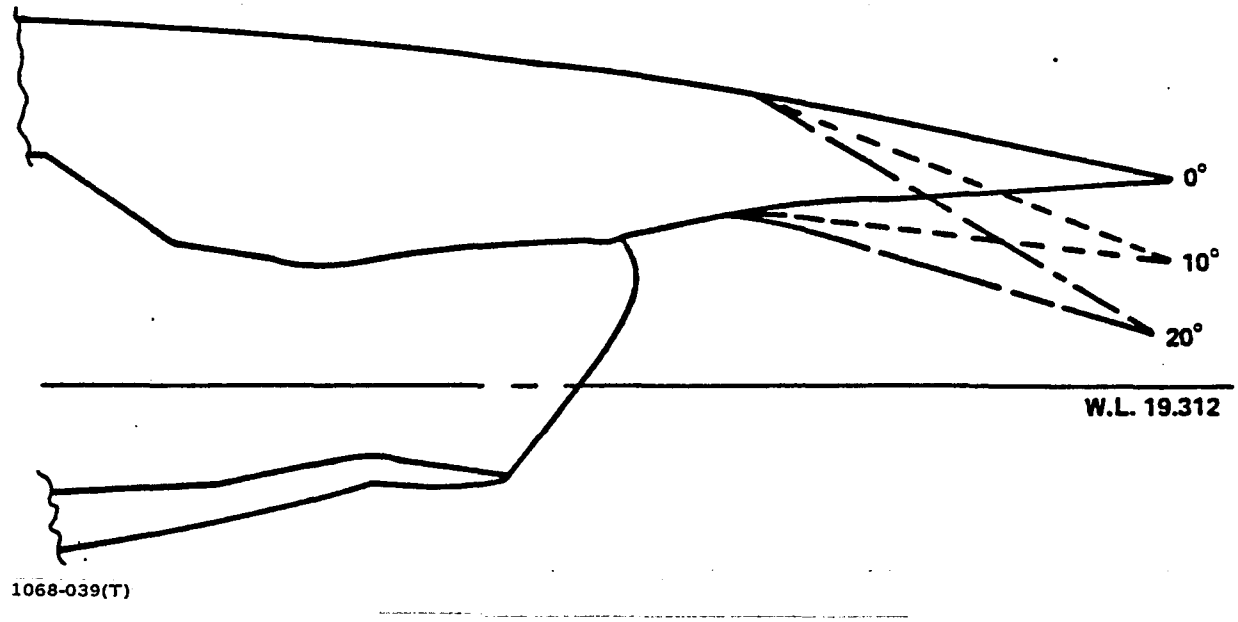

Figure 29 ADEN Combat Vectoring Comparison

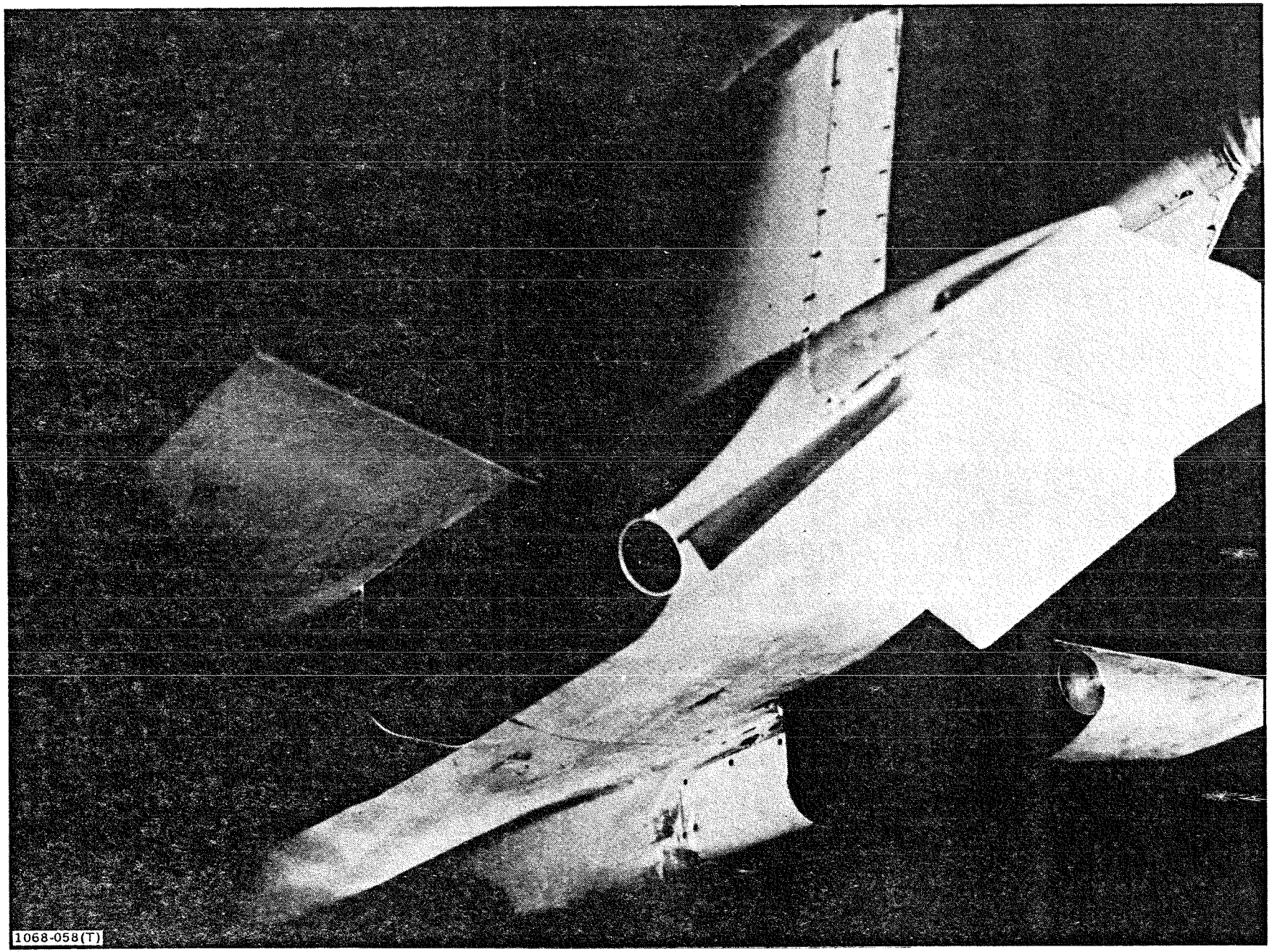

Figure 30 Circular Nozzle/Airframe Configuration Installed in Tunnel

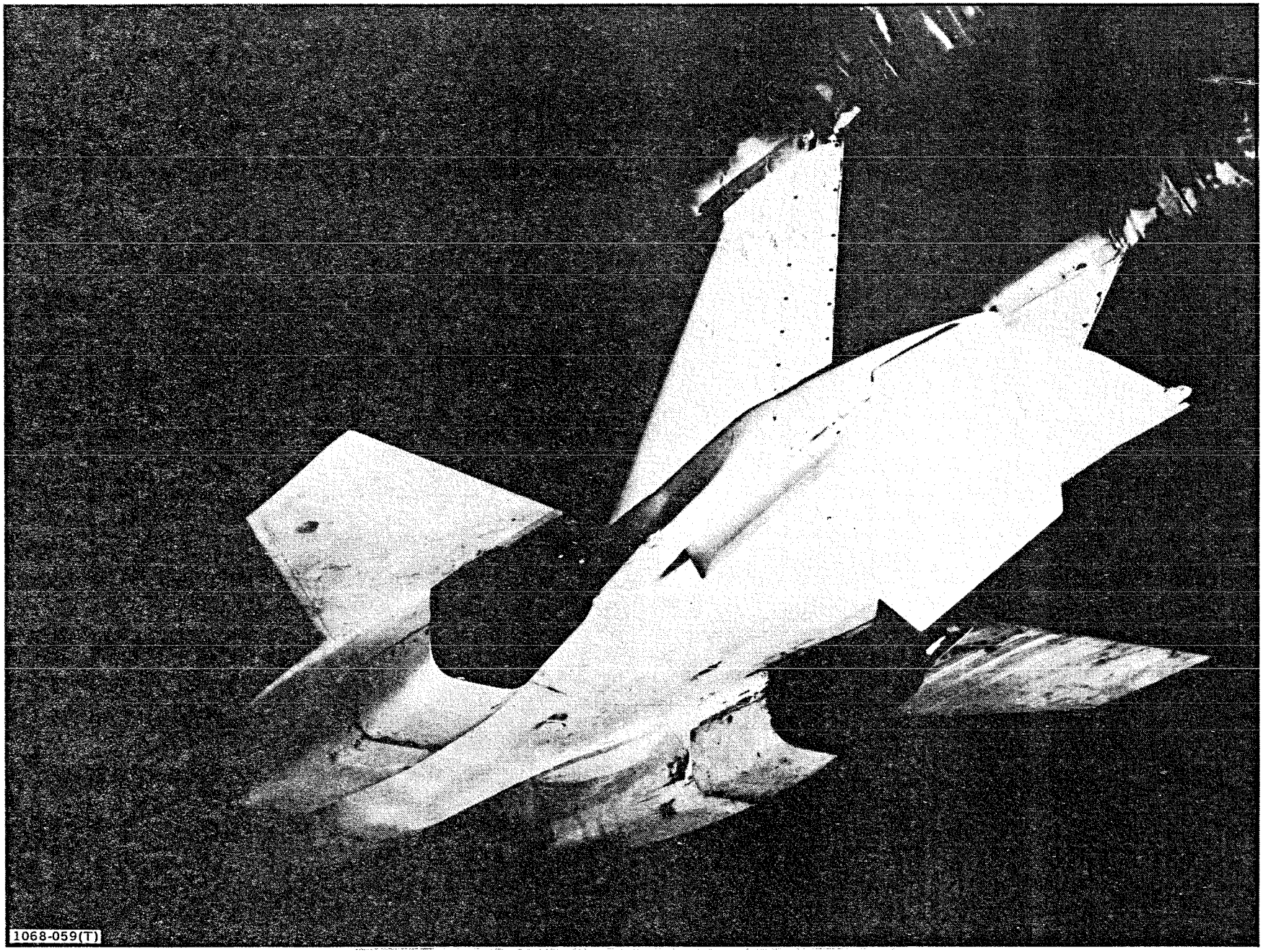

Figure 31 ALBEN Nozzle/Airframe Configuration Installed in Tunnel

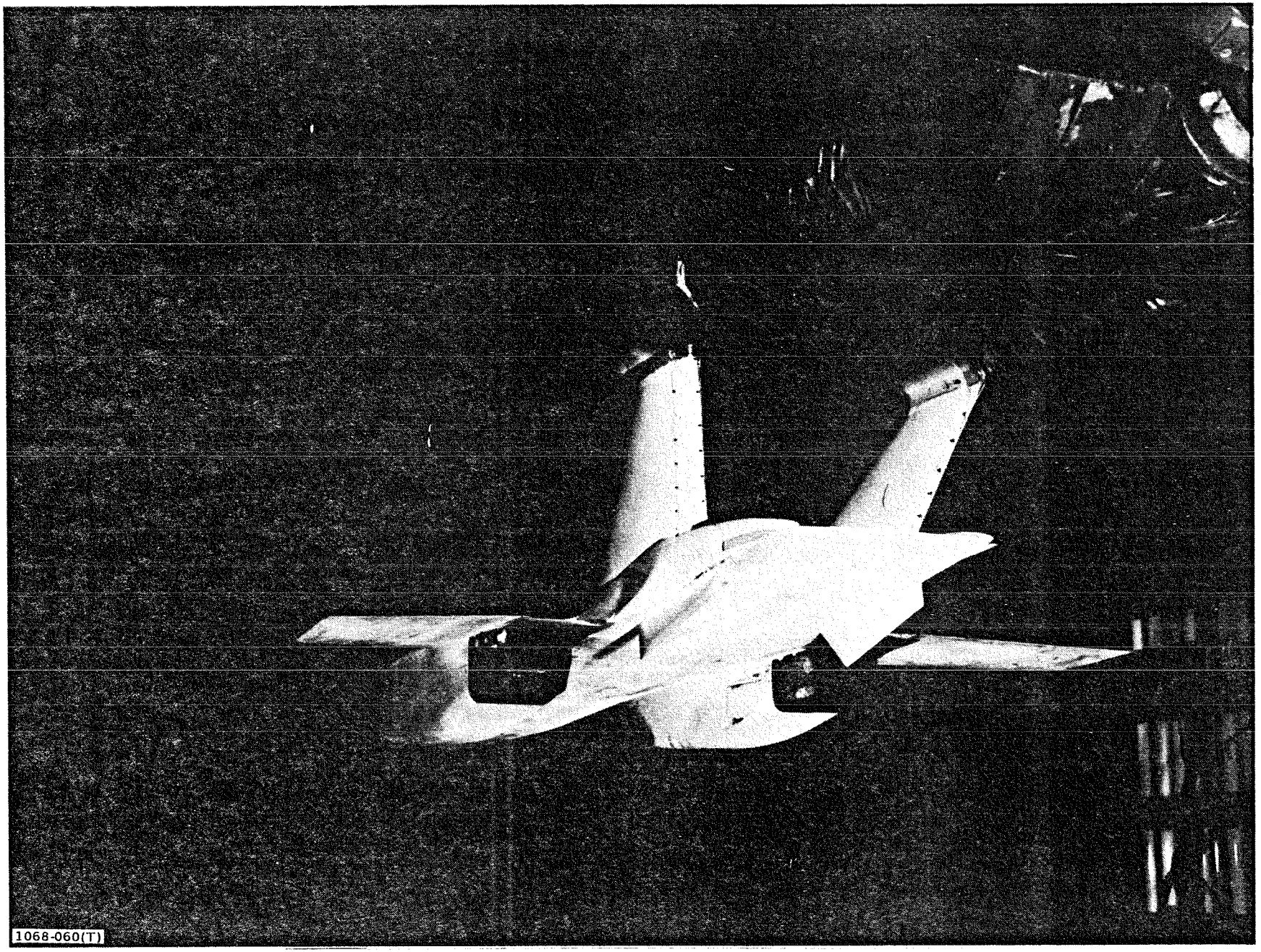

Figure 32 ADEN Cruise, Unvectored Nozzle/Airframe Configuration Installed in Tunnel

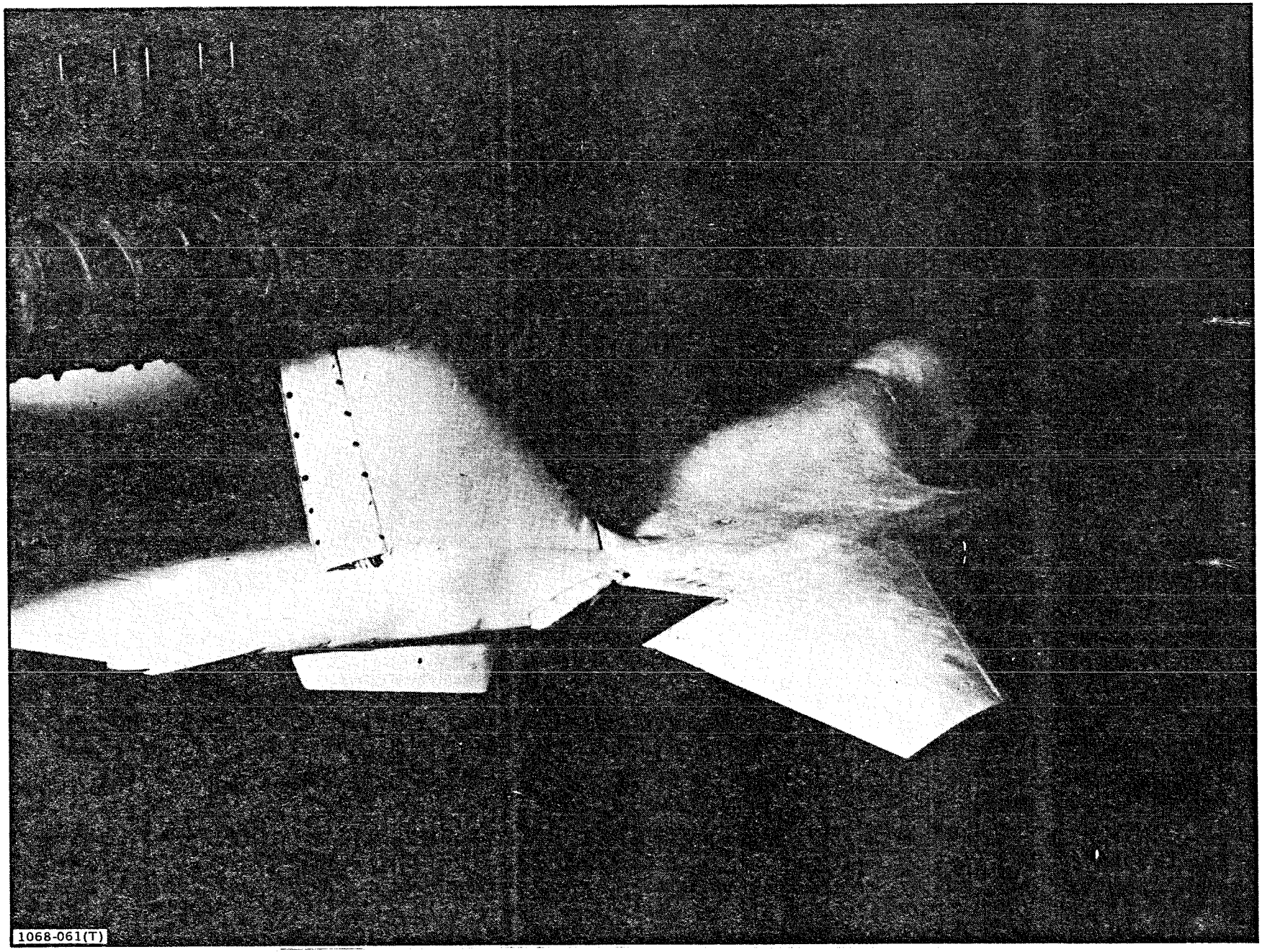

Figure 33 ADEN Combat, Vectored Nozzle/Airframe Configuration Installed in Tunnel

CONFIGURATION	GEOMETRIC JET AREA
1 – CIRCULAR NOZZLE	3.491 IN^2, 22.523 CM^2
2 – ALBEN	3.445 IN^2, 22.226 CM^2
3 – ADEN CR 0°	3.319 IN^2, 21.413 CM^2
4 – ADEN CR 0° ALT.	3.293 IN^2, 21.245 CM^2
5 – ADEN CR 5°	3.249 IN^2, 20.961 CM^2
6 – ADEN CR 10°	3.256 IN^2, 21.006 CM^2
7 – ADEN DASH	4.280 IN^2, 27.613 CM^2
8 – ADEN COM 0°	5.726 IN^2, 36.942 CM^2
9 – ADEN COM 0° ALT.	5.702 IN^2, 36.787 CM^2
10 – ADEN COM 0° + I/F	SAME AS COM 0°
11 – ADEN COM 10°	5.727 IN^2, 36.948 CM^2
12 – ADEN COM 20°	5.698 IN^2, 36.761 CM^2,
13 – ADEN COM 20° ALT.	SAME AS COM 20°

1068-040(T)

Figure 34 Nozzle Jet Area Comparison

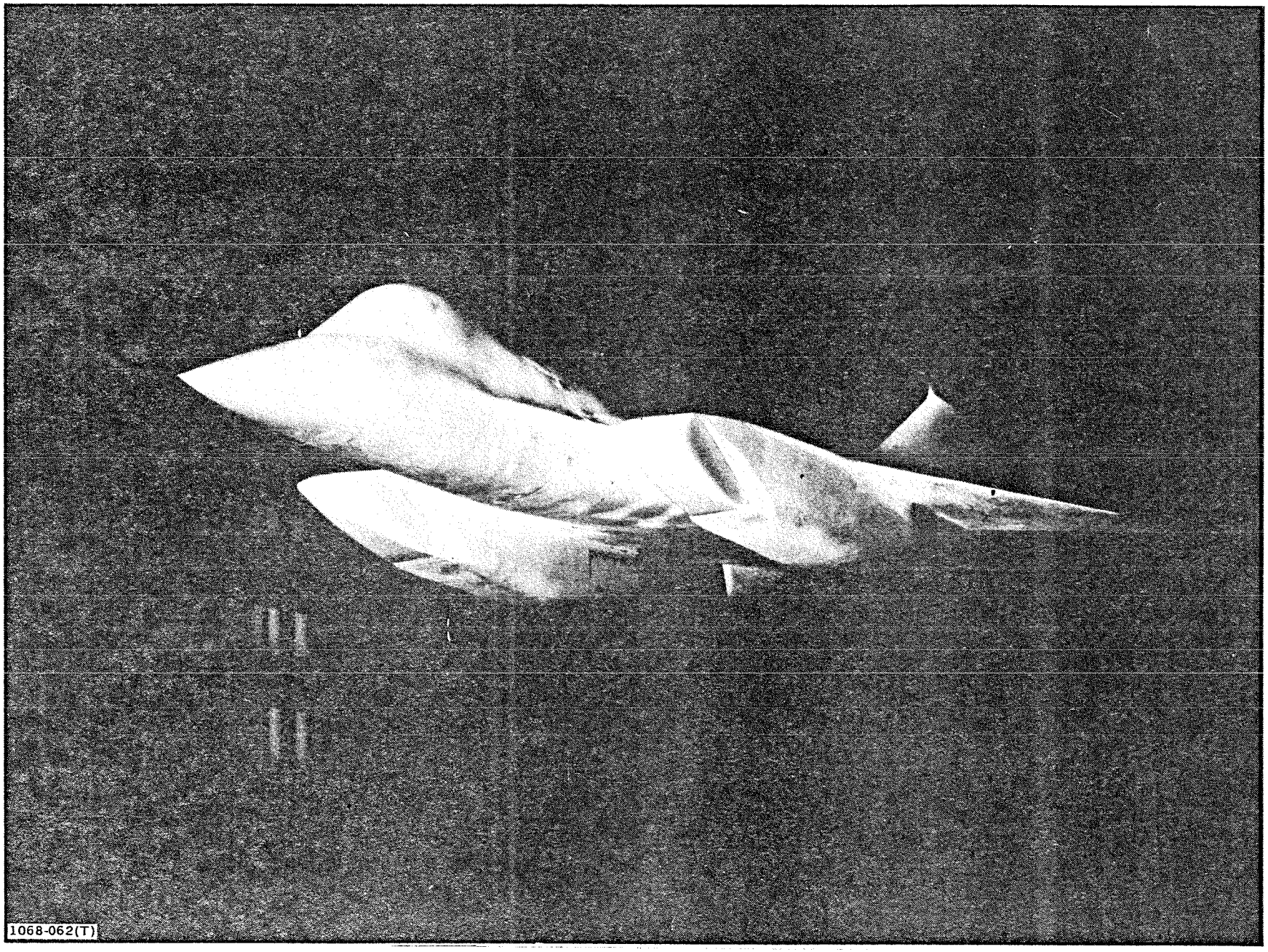

Figure 35 Model with Ogive Inlet Fairings Installed on Model

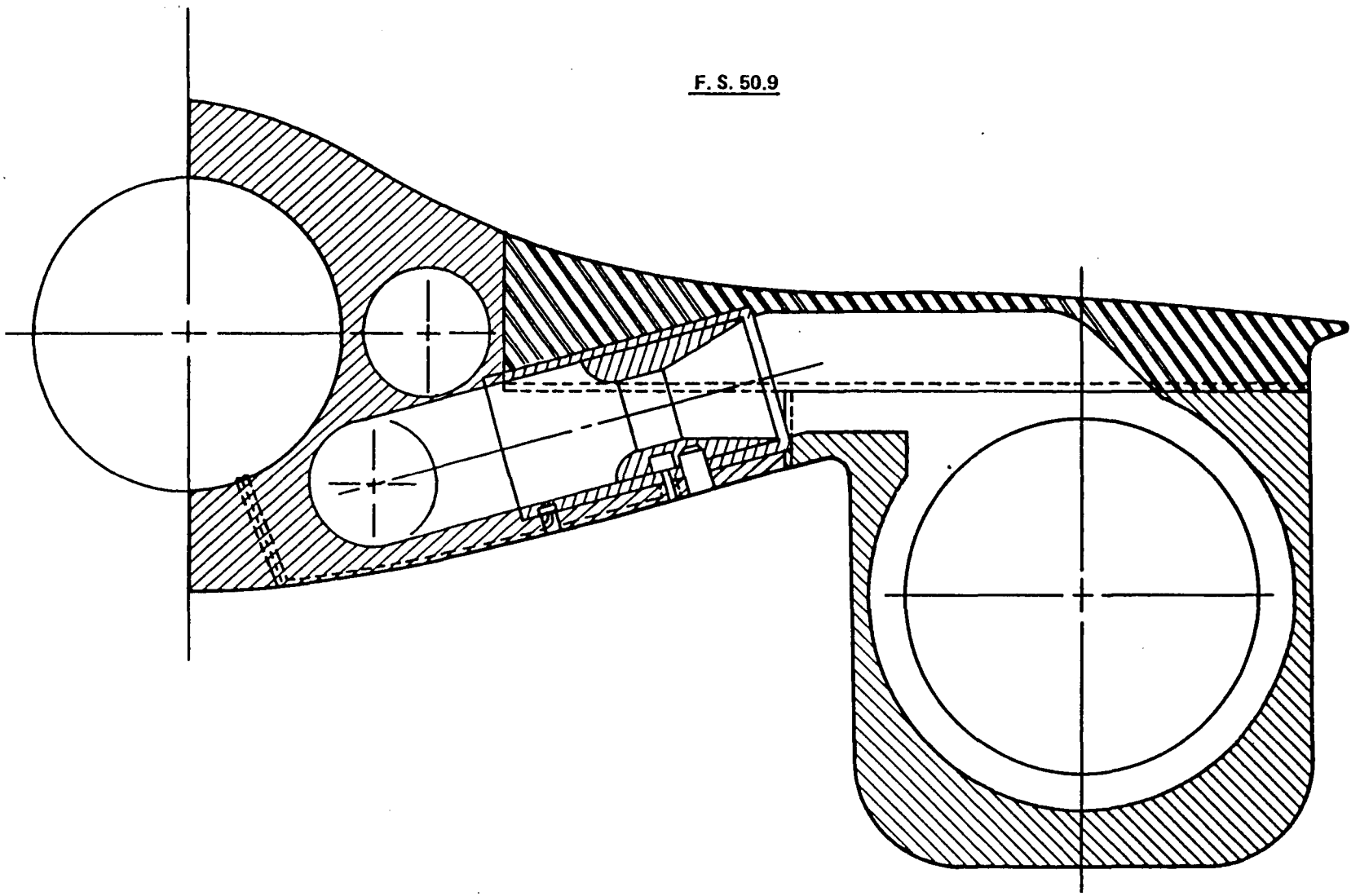

1068-053(T)

Figure 36 Model Venturi Installation

CONFIGURATION & TEST CONDITION MATRIX
(NON–AFTERBURNING)

NOMINAL		ANGLE OF ATTACK PER CONFIGURATION (NOMINAL)					
MACH	NPR	ADEN CR 0°	CR 0° ALT	ADEN CR 5°	ADEN CR 10°	CIRCULAR	ALBEN
0.4	1	0,3,6,9,12			0,3,6,9,12		
	1.15	0,3,6,9,12			0,3,6,9,12		
	2.5	0,3,6,9,12			0,3,6,9,12		
	3.0	0,3,6,9,12			0,3,6,9,12		
	4.0	0,3,6,9,12			0,3,6,9,12		
0.6	1	0,2,4,6,8,10	0,4,8		0,2,4,6,8,10	0,2,4,6,8,10	
	1.25	0,2,3,4,6,8,10,12	–		0,2,4,6,8,10	0,2,4,6,8,10	
	2.5	0,2,3,4,6,8,10,12	0,4,8		0,2,4,6,8,10	0,2,4,6,8,10	
	3.0	0,2,3,4,6,8,10,12	0,4,8		0,2,4,6,8,10	0,2,4,6,8,10	
	4.0	0,2,3,4,6,8,10,12	0,4,8		0,2,4,6,8,10	0,2,4,6,8,10	
0.8	1	0,2,4,6,8		0,2,4,6,8	0,2,4,6,8		0,2,4,6,8
	1.5	0,2,4,6,8		–	0,2,4,6,8		0,2,4,6,8
	3.0	0,2,4,6,8		–	0,2,4,6,8		0,2,4,6,8
	4.0	0,2,4,6,8		0,4,8	0,2,4,6,8		–
	5.0	0,2,4,6,8		0,2,4,6,8	0,2,4,6,8		0,2,4,6,8
	6.0	0,2,4,6,8		0,4,8	0,2,4,6,8		0,2,4,6,8
	7.0	0,2,4,6,8		–	2,4,6,8		–
0.9	1	0,2,4,6,8	0,4,8	0,2,4,6,8	0,2,4,6,8	0,2,4,6,8	0,2,4,6,8
	1.6	0,2,4,6,8	–	–	0,2,4,6,8	0,2,4,6,8	0,2,4,6,8
	3.0	0,2,4,6,8	0,4,8	0,2,4,6,8	0,2,4,6,8	0,2,4,6,8	0,2,4,6,8
	4.0	0,2,4,6,8	0,4,8	0,2,4,8	0,2,4,6,8	0,2,4,6,8	0,2,4,6,8
	5.0	0,2,4,6,8	0,4,8	0,2,4,6,8	0,2,4,6,8	0,2,4,6,8	0,2,4,6,8
	6.0	0,2,4,6,8	0,4,8	0,4,8	1½,2,4,6,8	0,2,4,6,8	0,2,4,6,8
0.95	1	0,2,4,6			4	0,2,4,6	
	1.8	4			4	–	
	3.0	4			4	–	
	4.0	4			4	–	
	5.0	4			4	–	
	6.0	0,2,4,6			4	0,2,4,6	
	7.0	4			4	–	
1.35	1	0,2,4,6	0,4,6				0,2,4,6
	6.0	–	–				0,2,4
	8.0	0,2,4,6	0,4,6				0,2,4
	10.0	0,2,4,6	0,4,6				0,2,4
1.4	1	0				0,2,4,6	
	3.0	–				–	
	5.0	–				–	
	6.0	–				–	
	8.0	–				0,2,4,6	
	10.0	–				0,2,4,6	

1068-041(T)

Figure 37 Test Condition Matrix: Non-Afterburning Configurations

CONFIGURATION & TEST CONDITION MATRIX
(AFTERBURNING)

NOMINAL		ANGLE OF ATTACK PER CONFIGURATION (NOMINAL)						
MACH	NPR	ADEN COM 0°	COM 0° ALT	COM 0° + I/F	ADEN COM 10°	ADEN COM 20°	COM 20° ALT	ADEN DASH
0.4	1	0,3,6,9,12		0,3,6,9,12		0,3,6,9,12	0,3,6,9,12	
	1.15	0,3,6,9,12		–		0,3,6,9,12	–	
	2.5	0,3,6,9,12		0,3,6,9,12		0,3,6,9,12	0,3,6,9,12	
	3.0	0,3,6,9,12		–		0,3,6,9,12	–	
	4.0	0,3,6,9,12		–		0,3,6,9,12	–	
0.6	1	0,2,4,6,8,10	0,4,8	0,2,4,6,8	0,2,4,6,8	0,2,3,4,6,8,10	0,2,4,6,8,10	0,2,4,6,8
	1.25	0,2,4,6,8,10	–	–	0,2,4,6,8	0,2,4,6,8,10	–	0,2,4,6,8
	2.5	0,2,4,6,8,10	0,4,8	–	0,2,4,6,8	0,2,4,6,8,10	–	0,2,4,6,8
	3.0	0,2,4,6,8,10	0,4,8	0,2,4,6,8	0,2,4,6,8	0,2,4,6,8,10	0,2,4,6,8,10	0,2,4,6,8
	4.0	0,2,4,6,8,10	0,4,8	–	0,2,4,6,8	0,2,4,6,8,10	–	0,2,4,6,8
0.8	1	0,2,4,6,8			0,2,4,6,8	0,2,4,6,8		
	1.5	0,2,4,6,8			0,2,4,6,8	0,2,4,6,8		
	3.0	0,2,4,6,8			0,2,4,6,8	0,2,4,6,8		
	4.0	0,2,4,6,8			0,2,4,6,8	0,2,4,6,8		
	5.0	0,2,4,6,8			0,2,4,6,8	0,2,4,6,8		
	6.0	0,2,4,6,8			0,2,4,6,8	0,2,4,6,8		
	7.0	–			–	–		
0.9	1	0,2,4,6,8,10,11	0,4,8	0,2,4,6,8	0,2,4,6,8,10,11	0,2,4,6,8,10,11	0,2,4,6,8,10	0,2,4,6,8
	1.6	0,2,4,6,8,10,11	–	–	0,2,4,6,8,10,11	0,2,4,6,8,10,11	–	0,2,4,6,8
	3.0	0,2,4,6,8,10,11	0,4,8	–	0,2,4,6,8,10,11	0,2,4,6,8,10,11	–	0,2,4,6,8
	4.0	0,2,4,6,8,10,11	0,4,8	–	0,2,4,6,8,10,11	0,2,4,6,8,10,11	–	0,2,4,6,8
	5.0	0,2,4,6,8,10,11	0,4,8	–	0,2,4,6,8,10,11	0,2,4,6,8,10,11	–	0,2,4,6,8
	6.0	0,2,4,6,8,10,11	0,4,8	0,2,4,6,8	0,2,4,6,8,10,11	0,2,4,6,8,10,11	0,2,4,6,8,10	0,2,4,6,8
0.95	1	4			0,4	0,4		
	1.8	4			4	4		
	3.0	4			4	4		
	4.0	4			4	4		
	5.0	4			4	4		
	6.0	4			4	4		
	7.0	4			4	4		
1.2	1	0,2,4,6		0,2,4,6		0,2,4,6	0,2,4,6	0,2,4,6
	3.0	0,2,4,6		–		–	–	0,2,4,6
	5.0	0,2,4,6		–		–	–	0,2,4,6
	6.0	0,2,4,6		–		0,2,4,6	–	0,2,4,6
	8.0	0,2,4,6		0,2,4,6		0,2,4,6	0,2,4,6	0,2,4,6
1.4	1	0,2,4,6,	0,4,6	0,2,4,6		0,2,4,6	0,2,4,6	0,2,4,6
	3.0	0,2,4,6	–	–		–	–	0,2,4,6
	5.0	0,2,4,6	–	–		–	–	0,2,4,6
	6.0	0,2,4,6	0,4,6	–		–	–	0,2,4,6
	8.0	0,2,4,6	–	–		0,2,4,6	–	0,2,4,6
	10.0	0,2,4,6	0,4,6	0,2,4,6		0,2,4,6	0,2,4,6	0,2,4,6

1068-042(T)

Figure 38 Test Condition Matrix: Afterburning Configurations

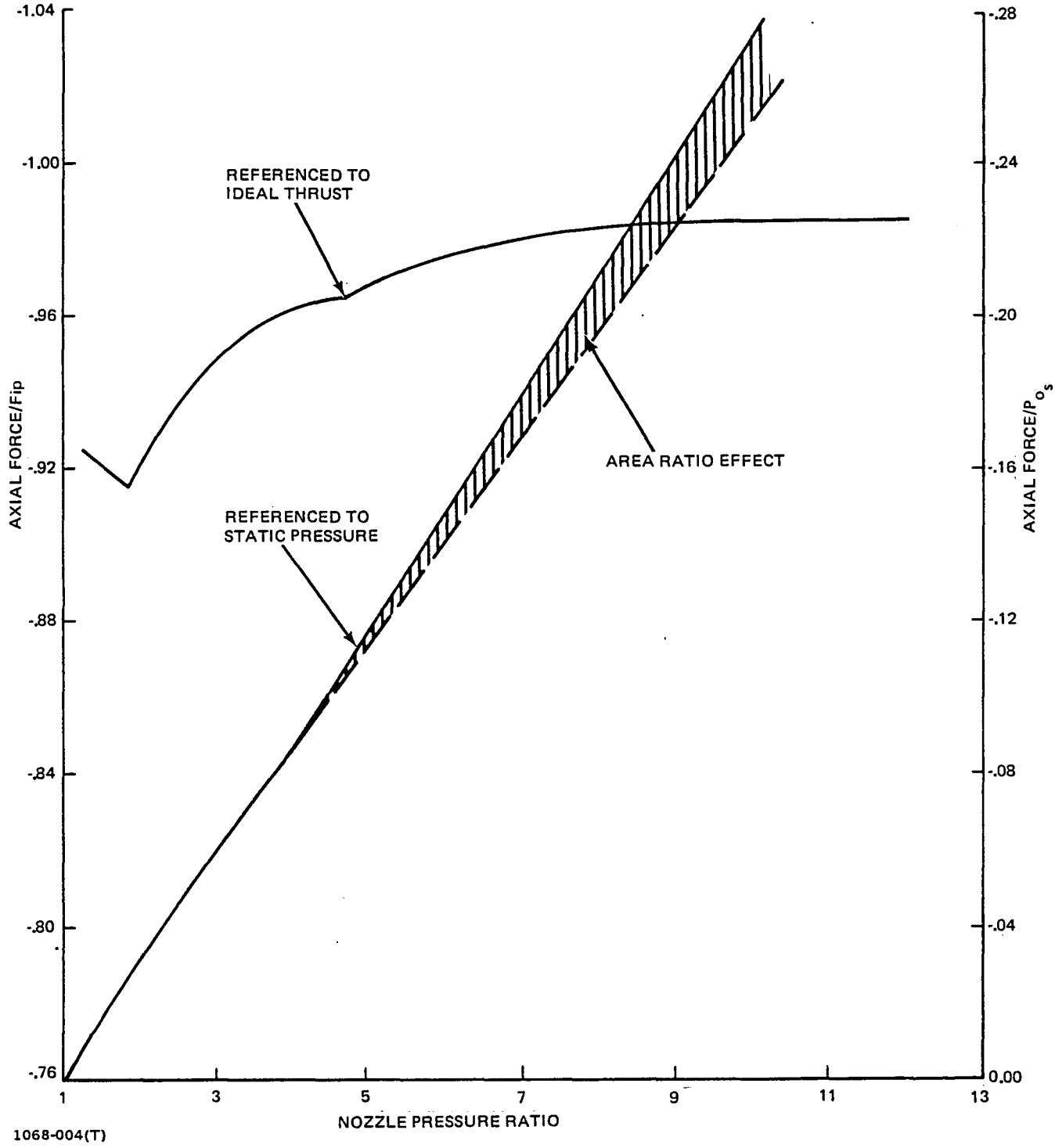

Figure 39 ADEN Cruise 0° Static Axial Force Presentations

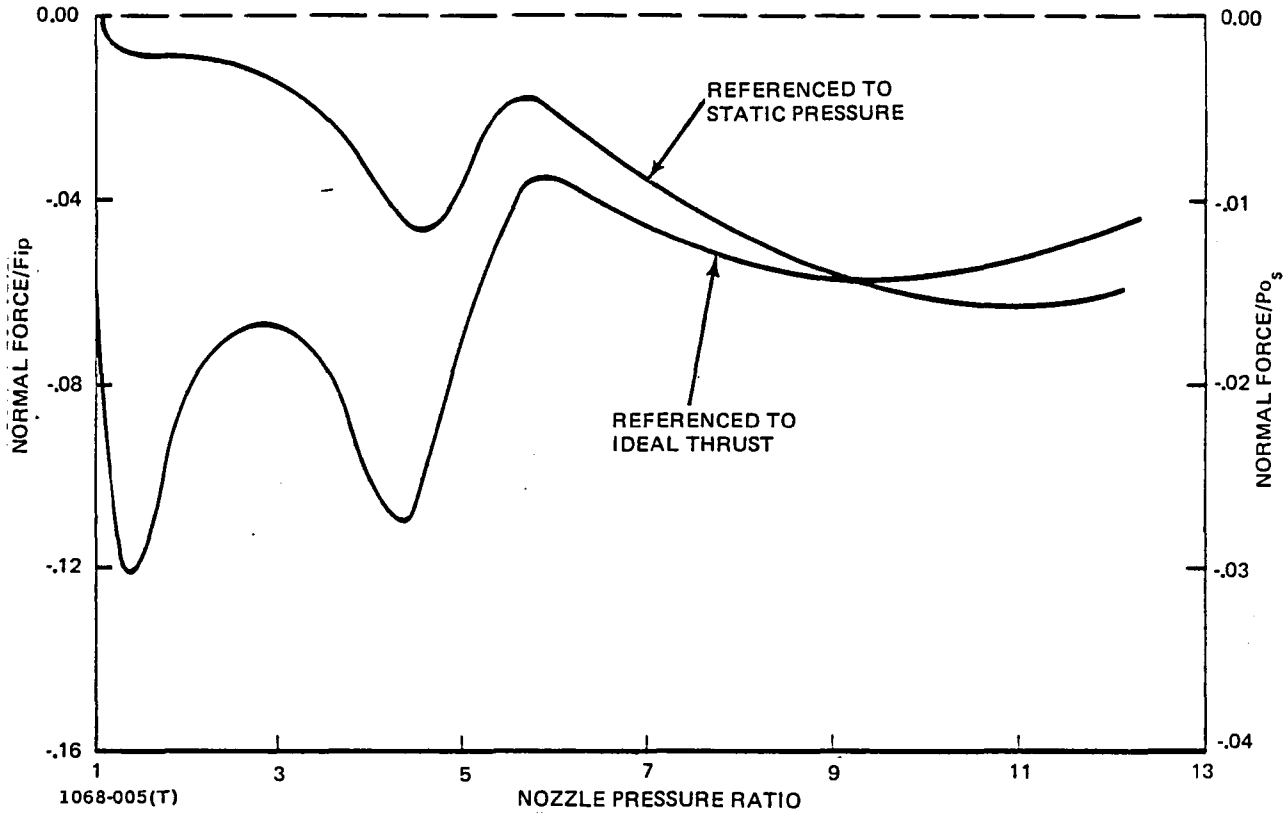

Figure 40 ADEN Cruise 0° Normal Force Presentations

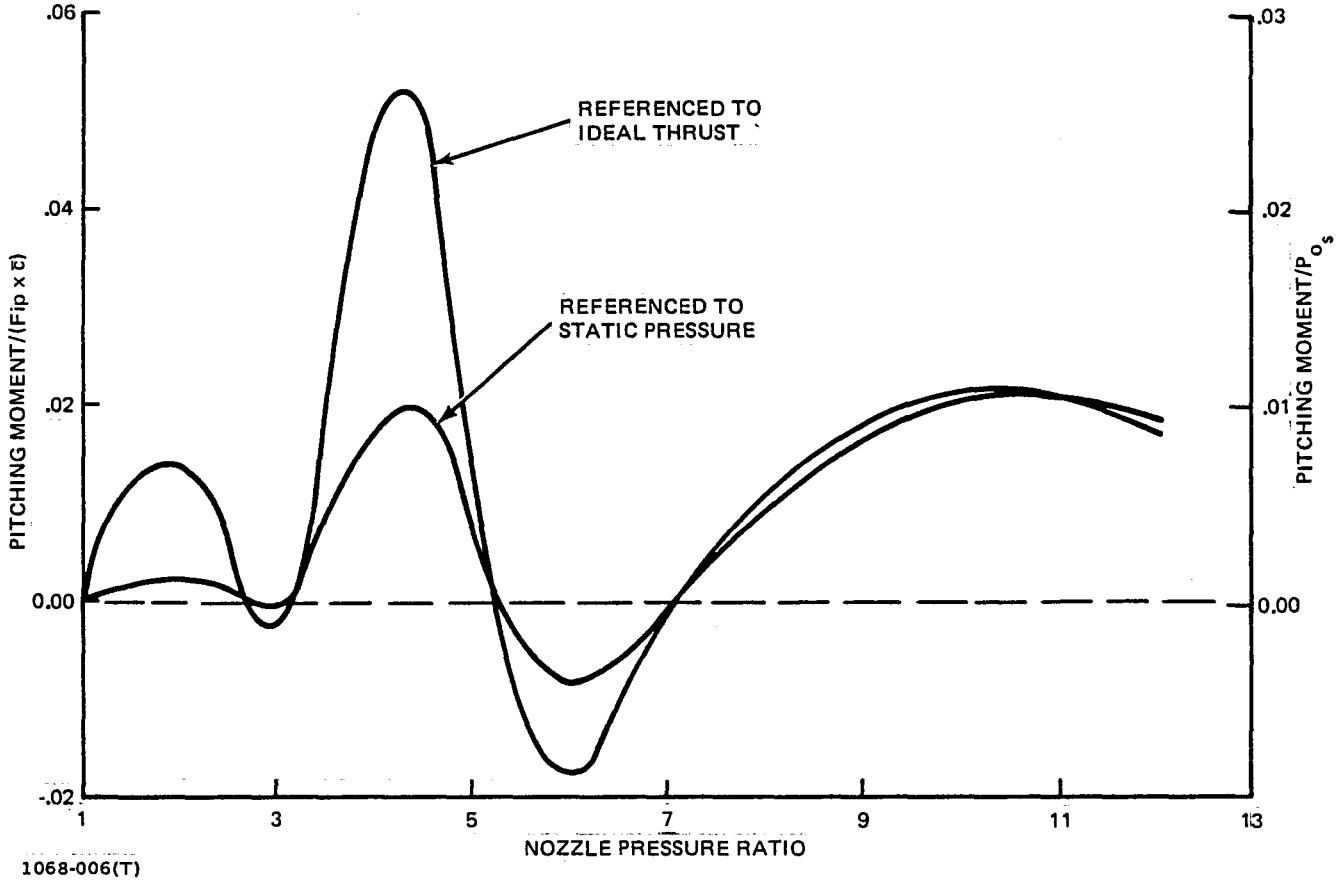

Figure 41 ADEN Cruise 0° Pitching Moment Presentations

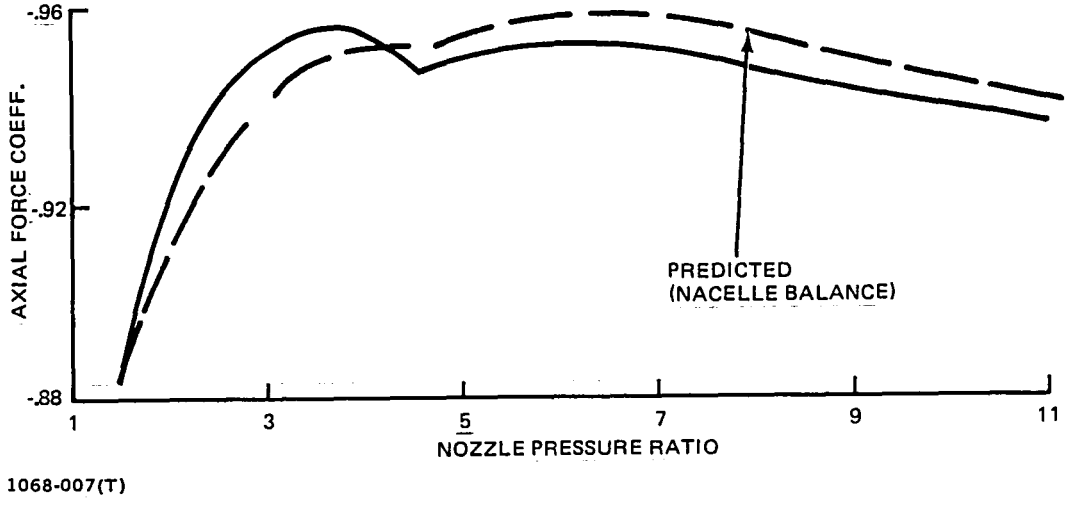

Figure 42 ADEN Combat 0° Static Axial Force: Comparison with Prediction

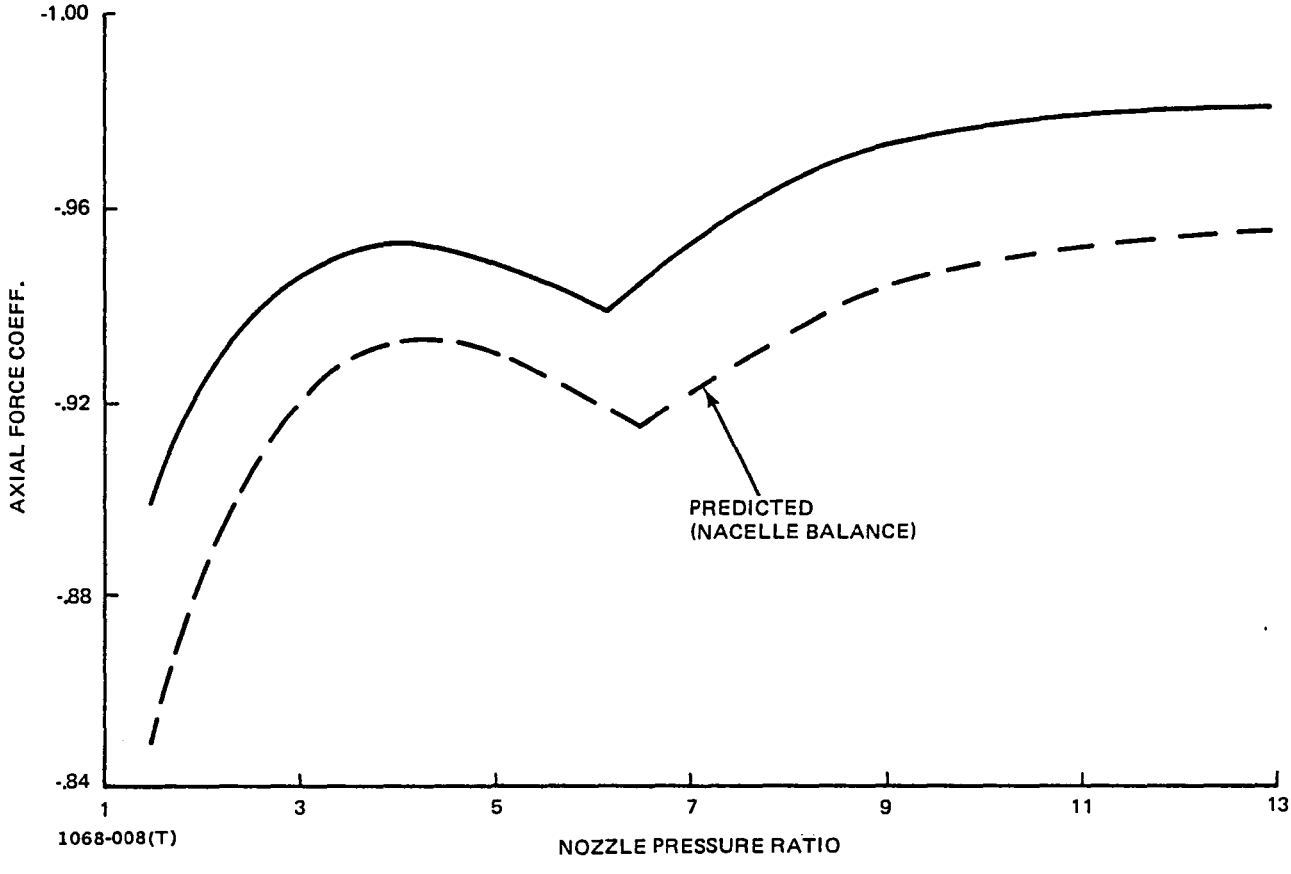

Figure 43 ADEN Cruise 10° Static Axial Force: Comparison with Prediction

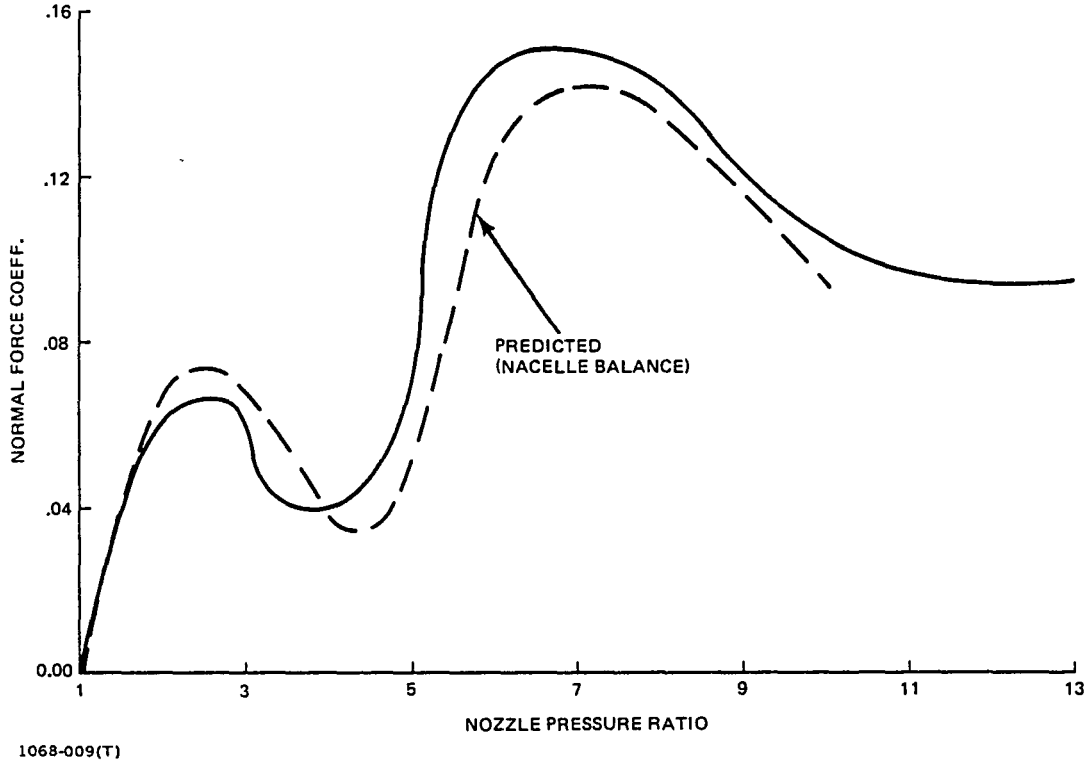

Figure 44 ADEN Cruise 10° Static Normal Force: Comparison with Prediction

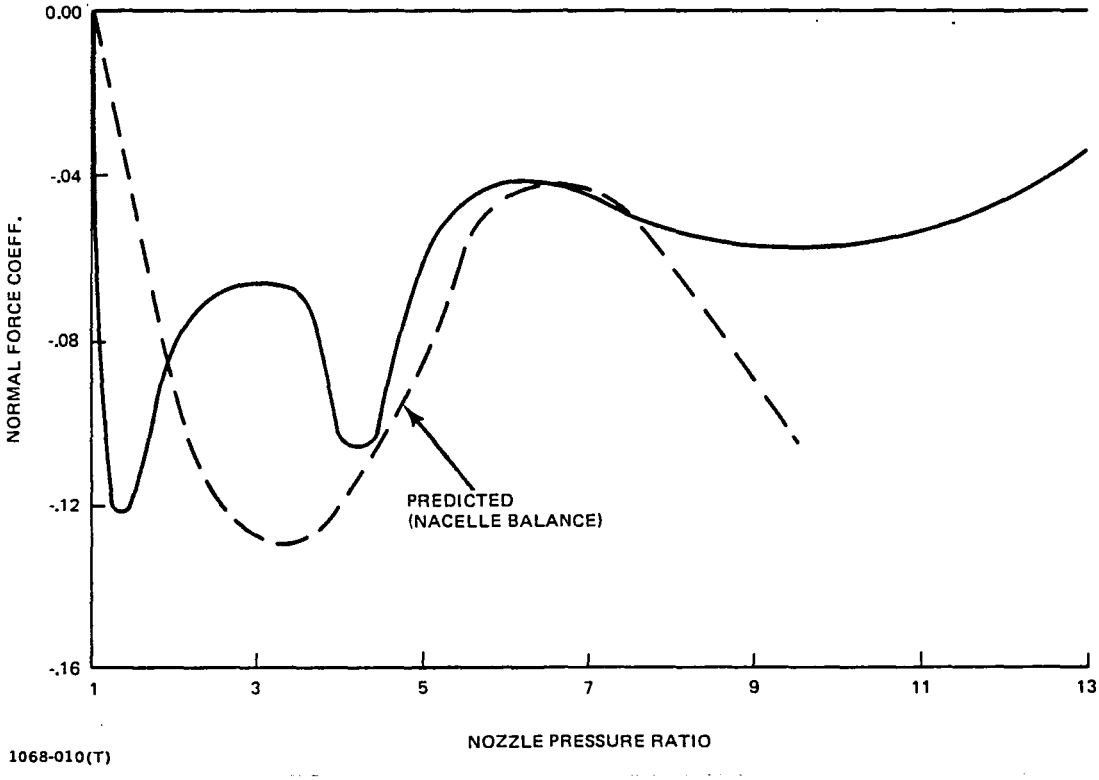

Figure 45 ADEN Cruise 0° Static Normal Force: Comparison with Prediction

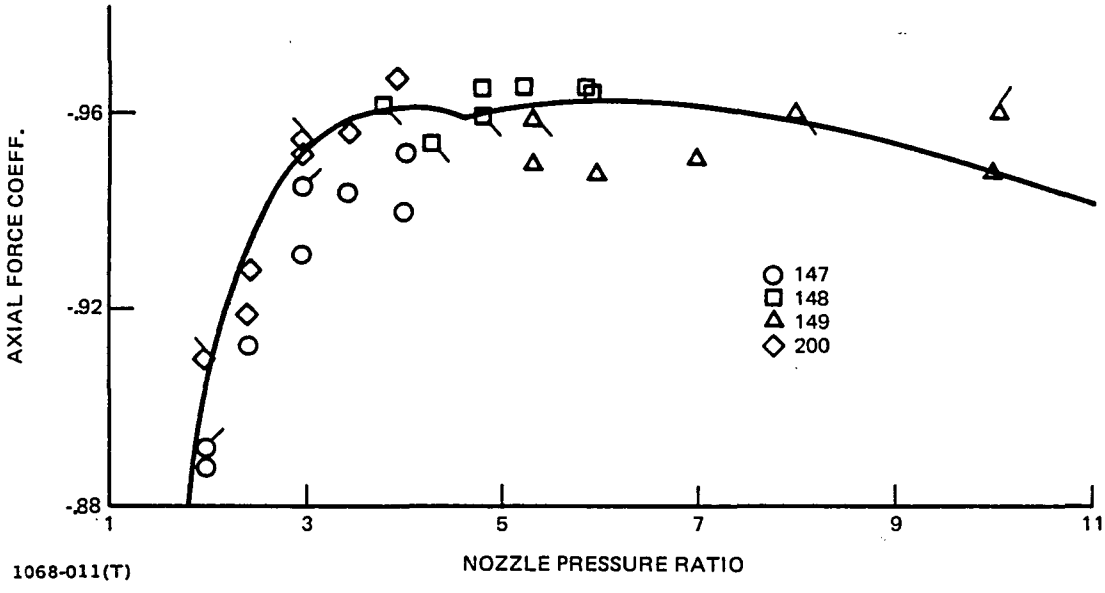

Figure 46 ADEN Combat 0°Main Balance Static Axial Force

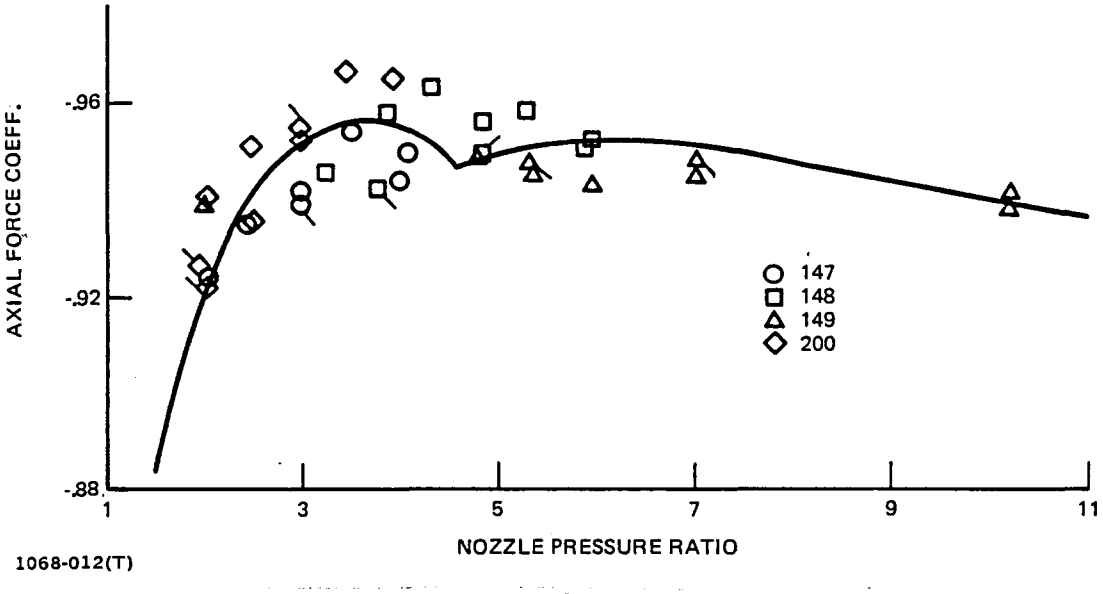

Figure 47 ADEN Combat 0° Nacelle Balance Static Axial Force

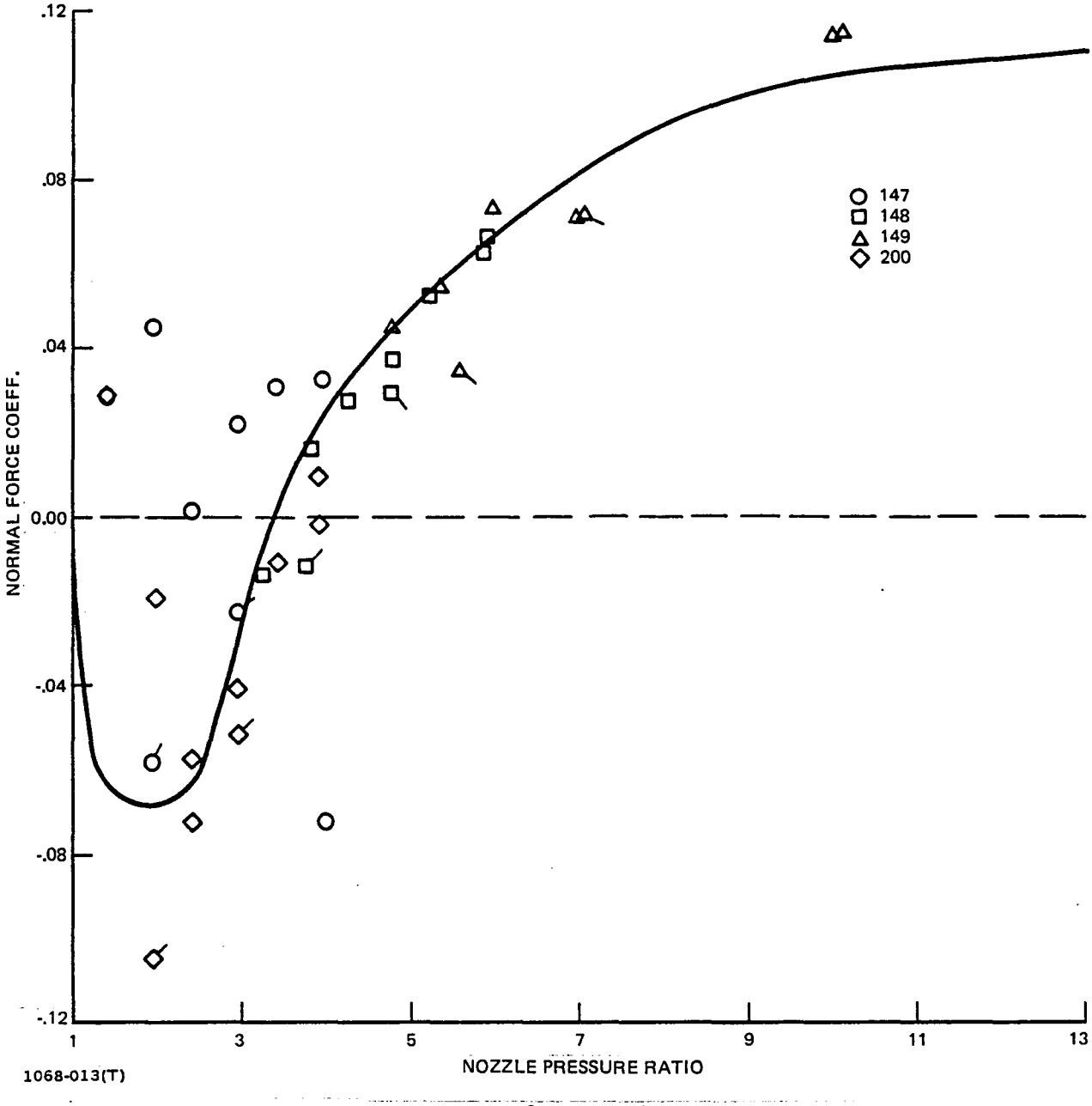

Figure 48 ADEN Combat 0° Main Balance Static Normal Force

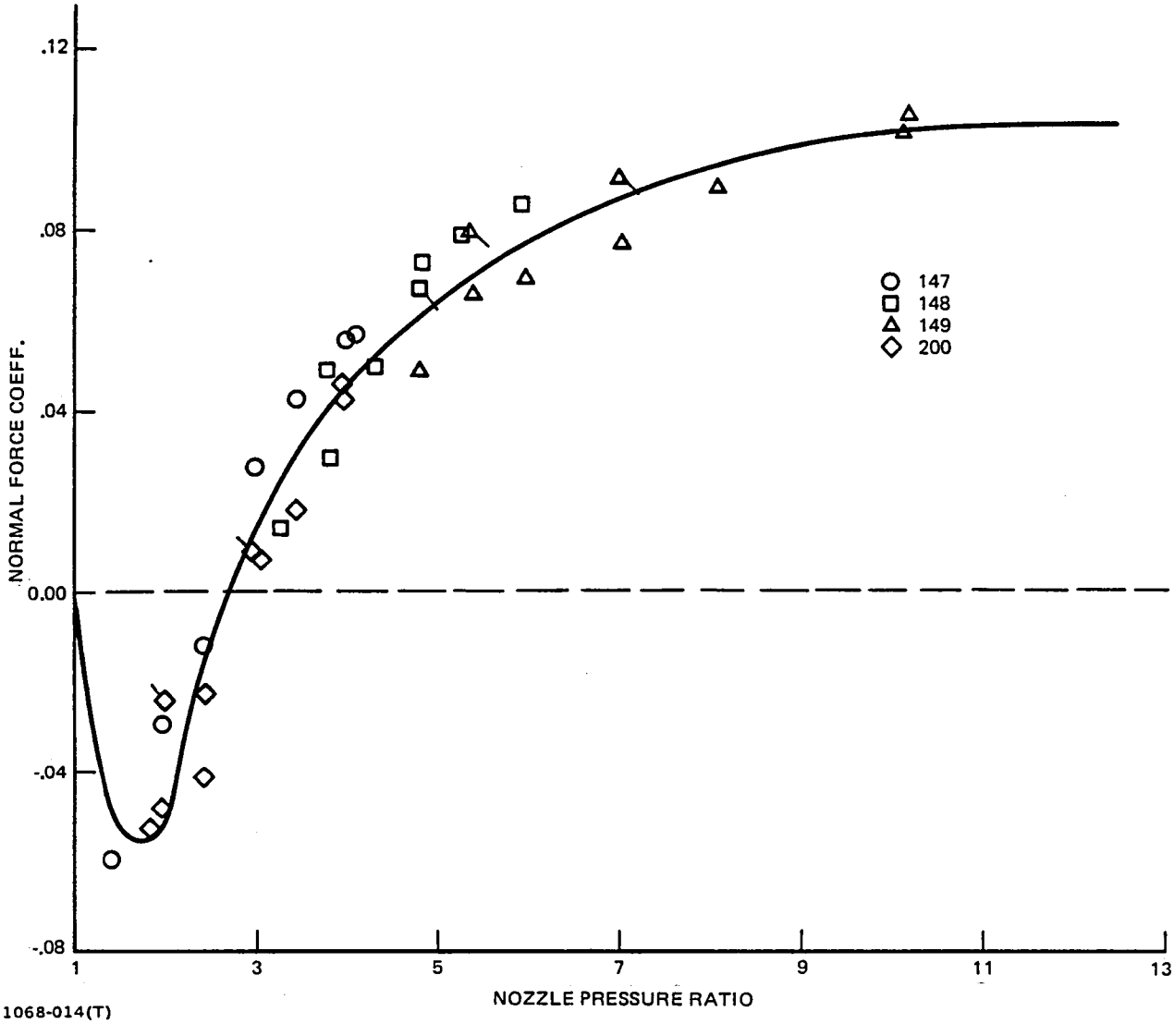

Figure 49 ADEN Combat 0° Nacelle Balance Static Normal Force

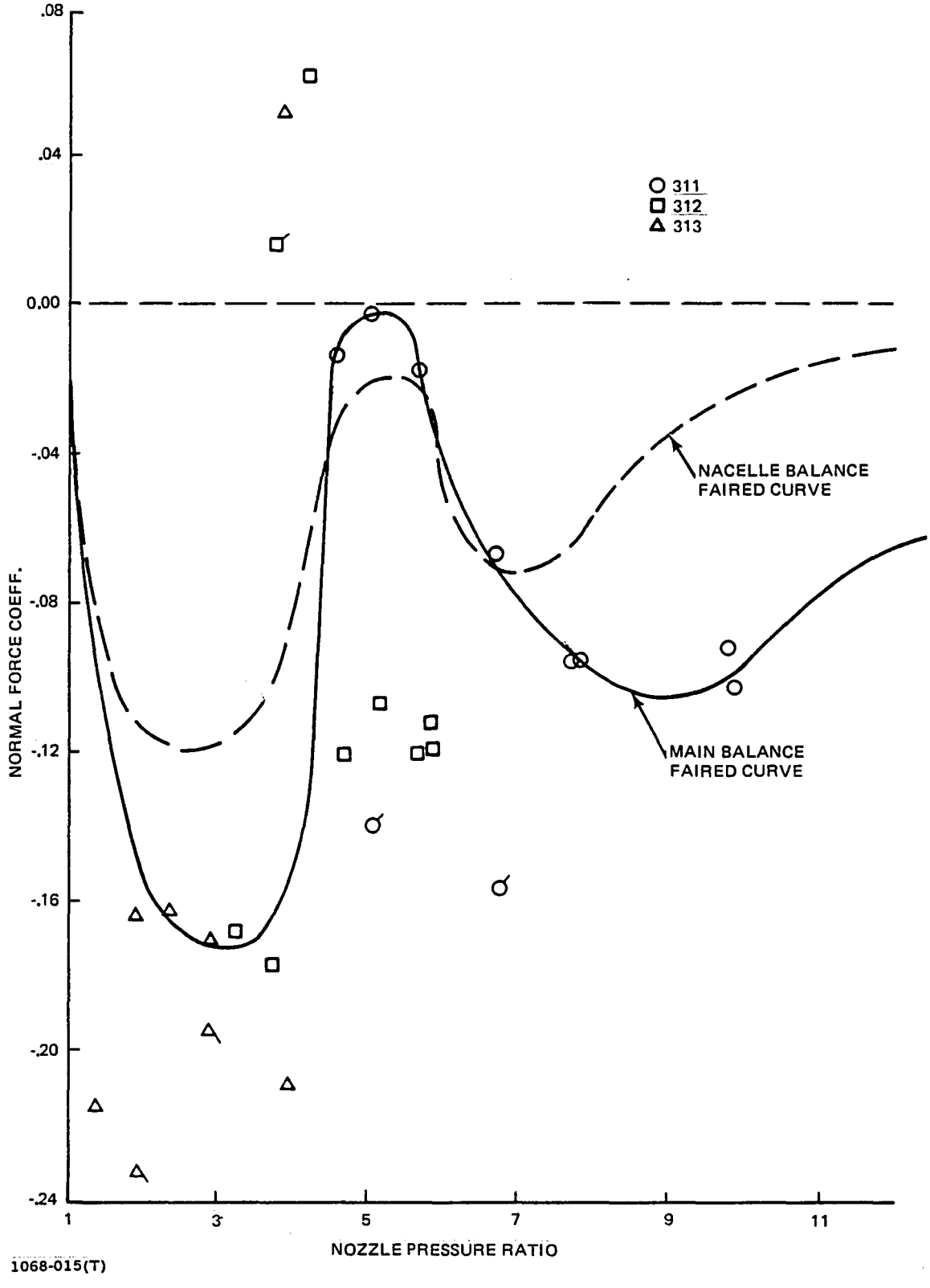

Figure 50 ADEN Dash Main Balance Static Normal Force

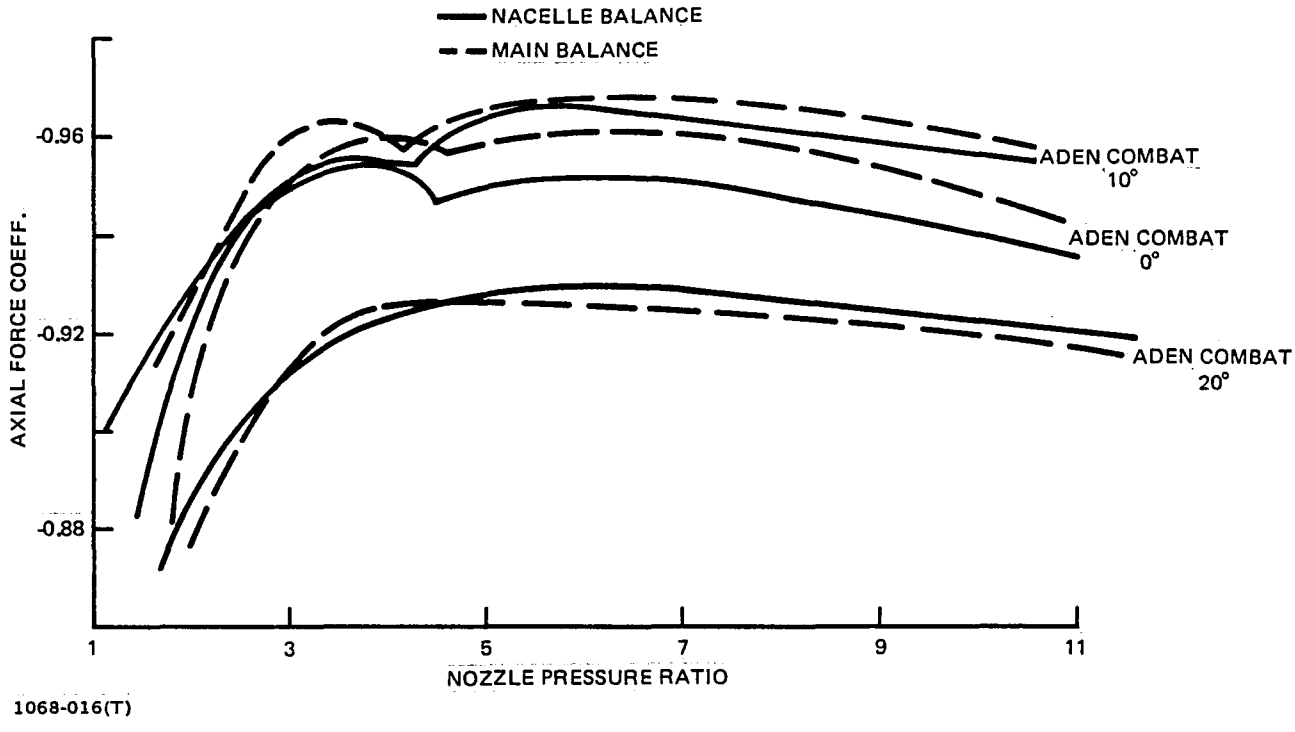

Figure 51 ADEN Combat 0°, 10°, 20° Static Axial Force: Balance Comparison

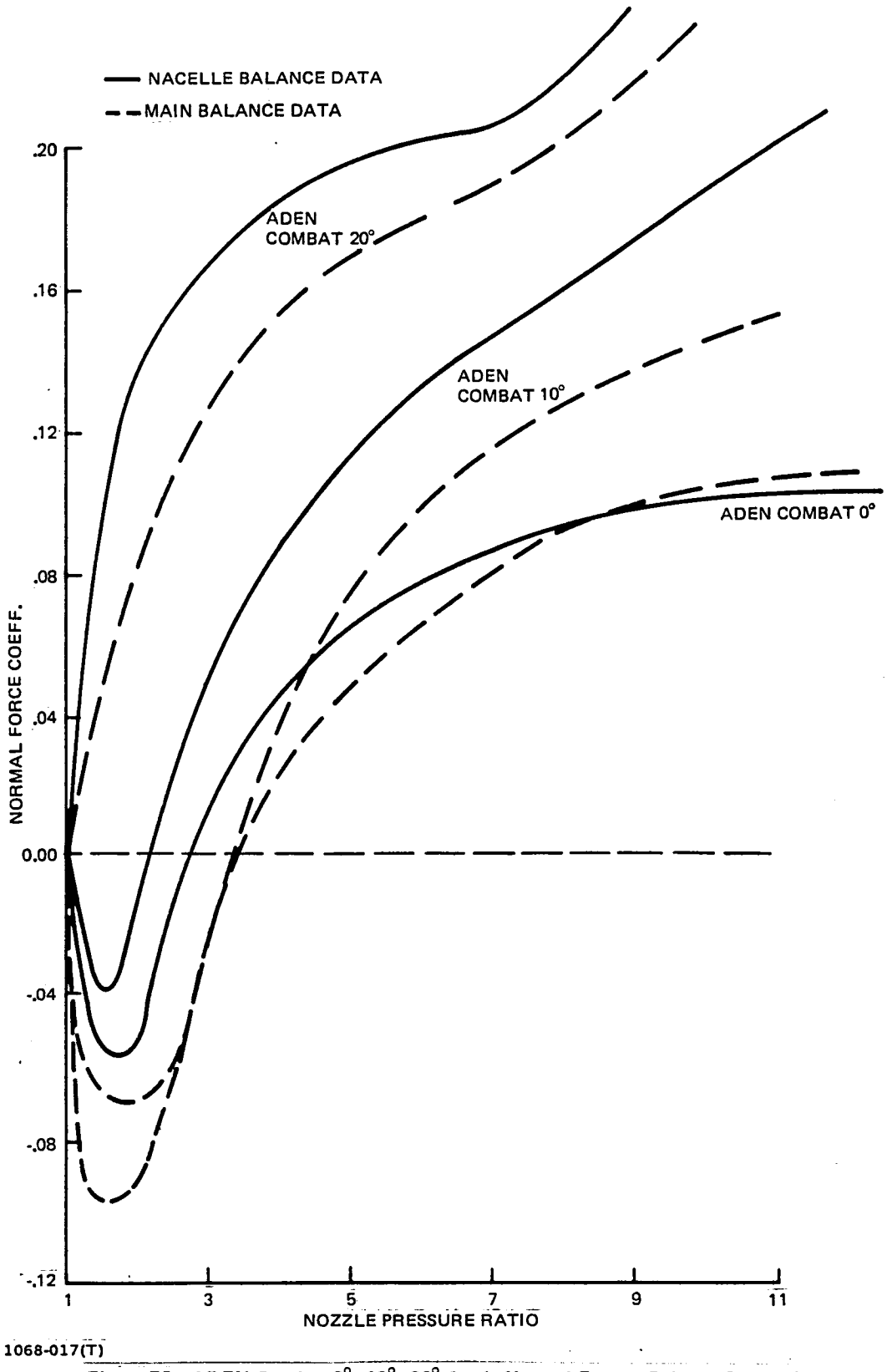

Figure 52 ADEN Combat 0°, 10°, 20° Static Normal Force: Balance Comparison

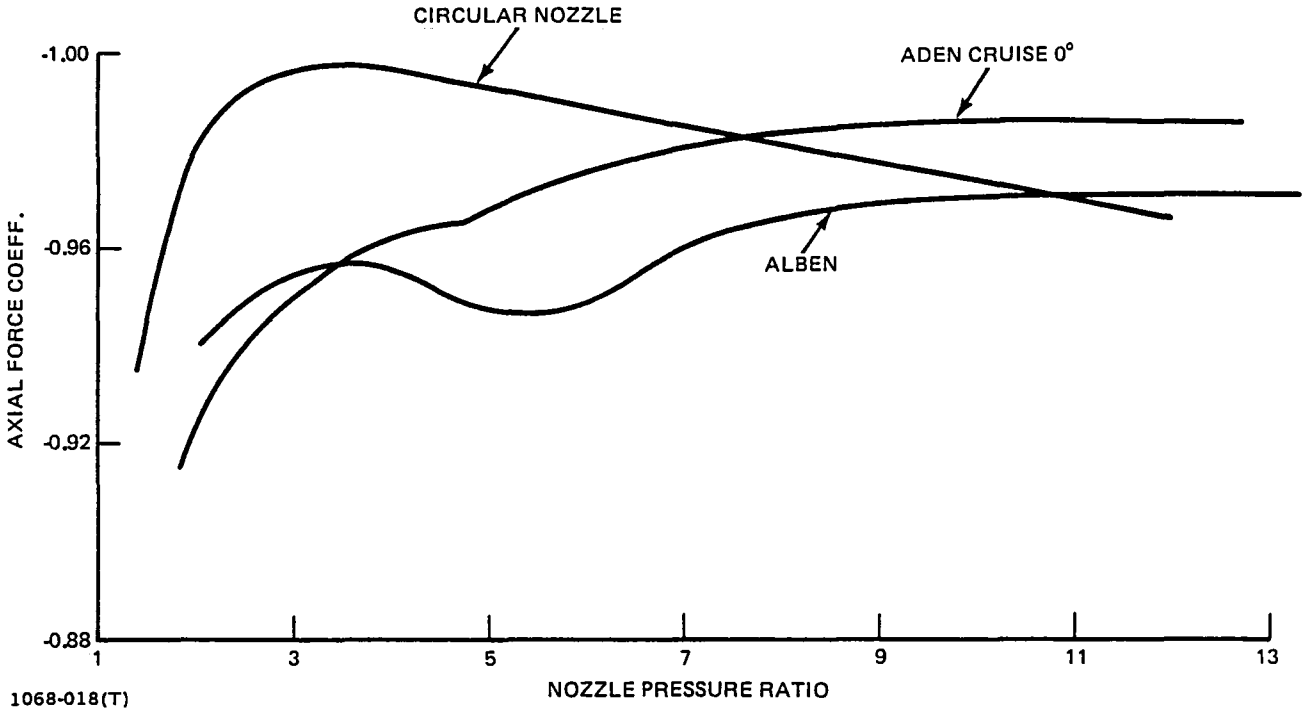

Figure 53 Effect of Unvectored Nozzle Type: Static Axial Force

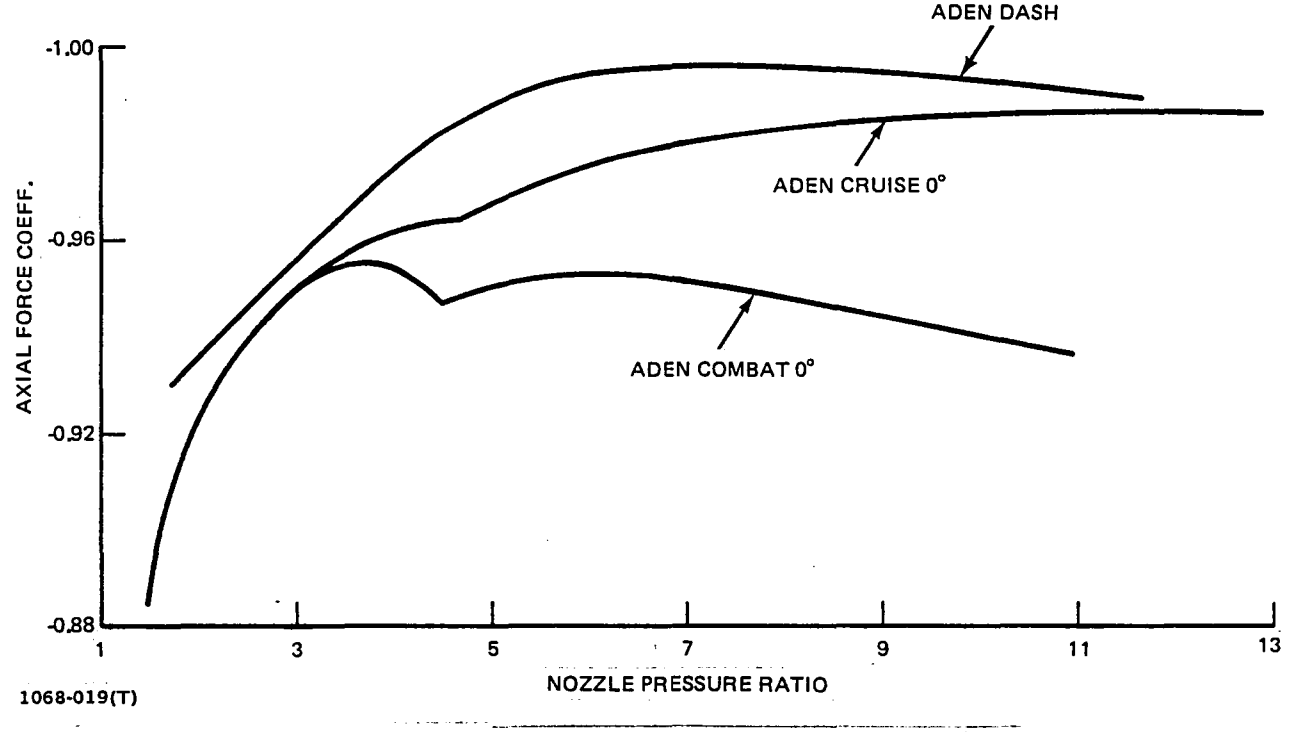

Figure 54 Effect of Jet Area Variation: Static Axial Force

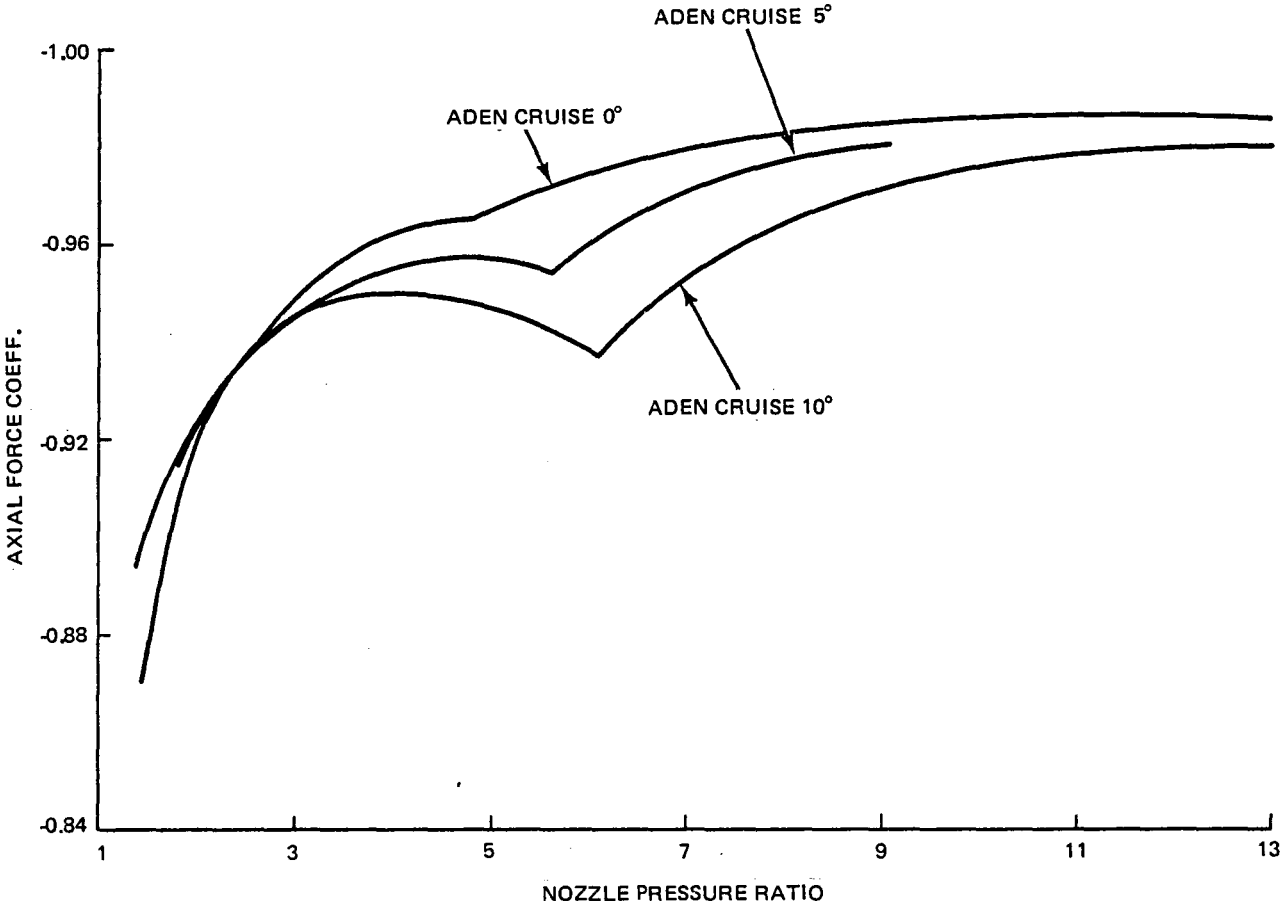

1068-020(T)

Figure 55 Effect of Cruise Nozzle Vectoring: Static Axial Force

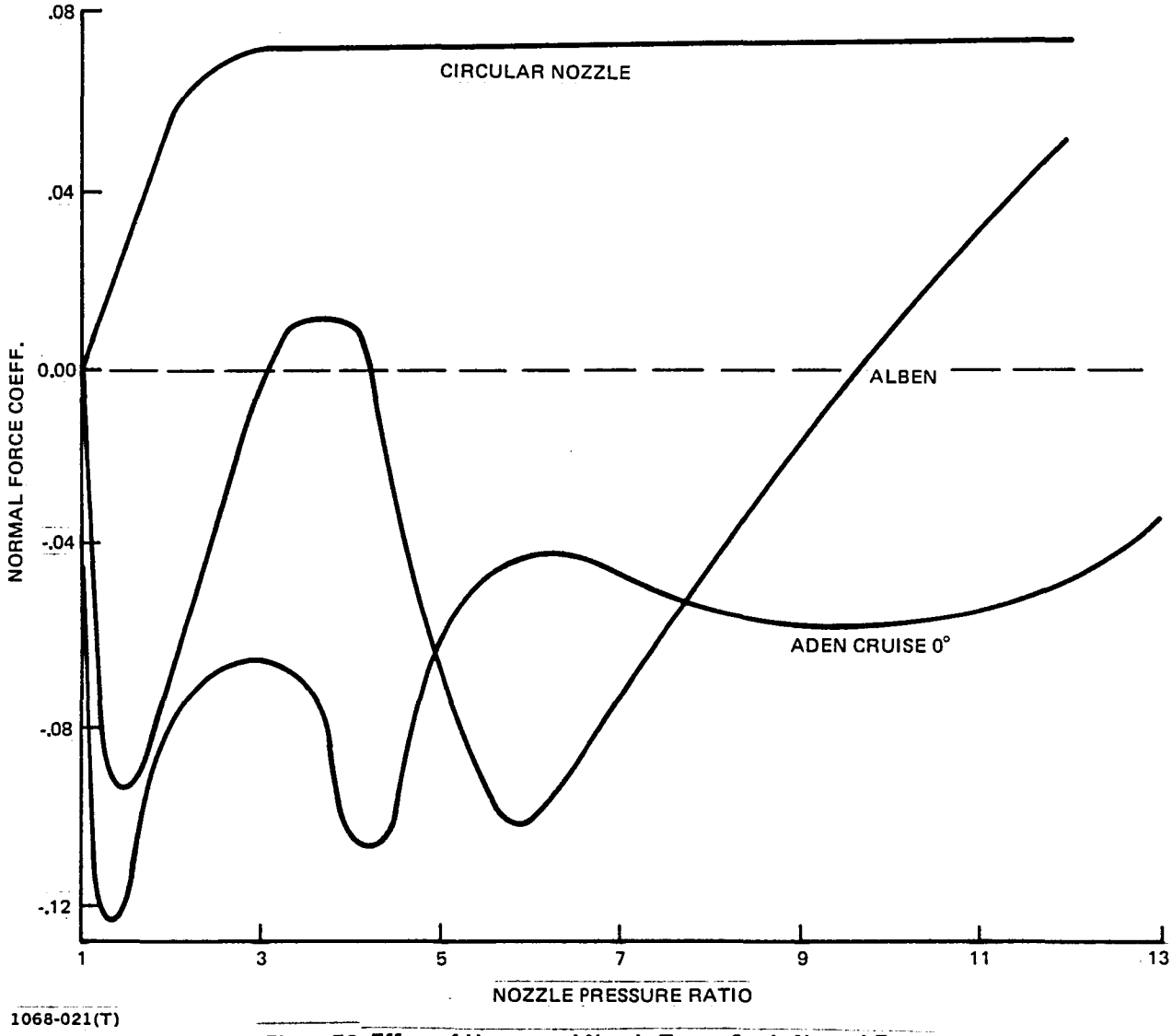

Figure 56 Effect of Unvectored Nozzle Type: Static Normal Force

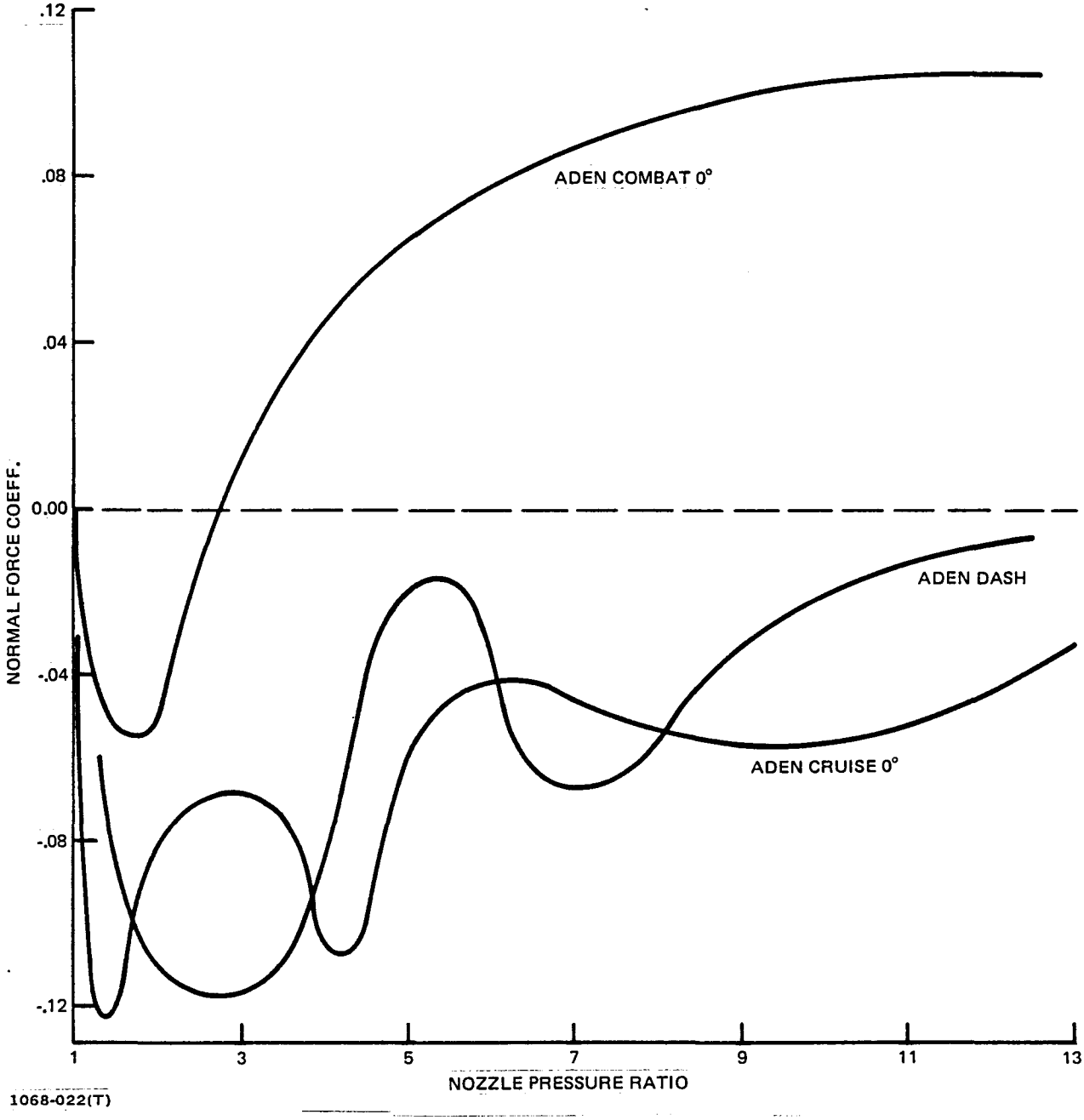

Figure 57 Effect of Jet Area Variation: Static Normal Force

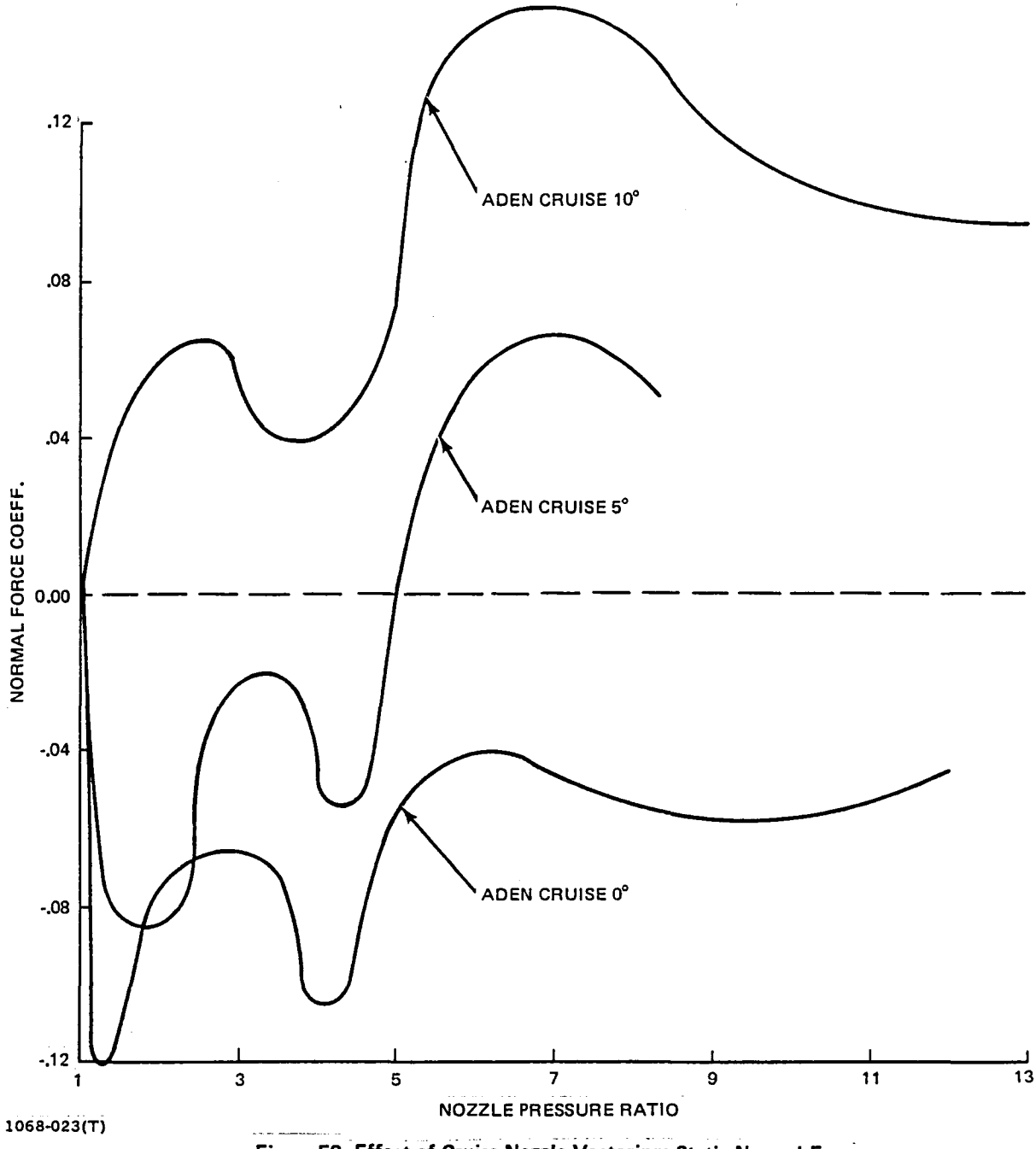

Figure 58 Effect of Cruise Nozzle Vectoring: Static Normal Force

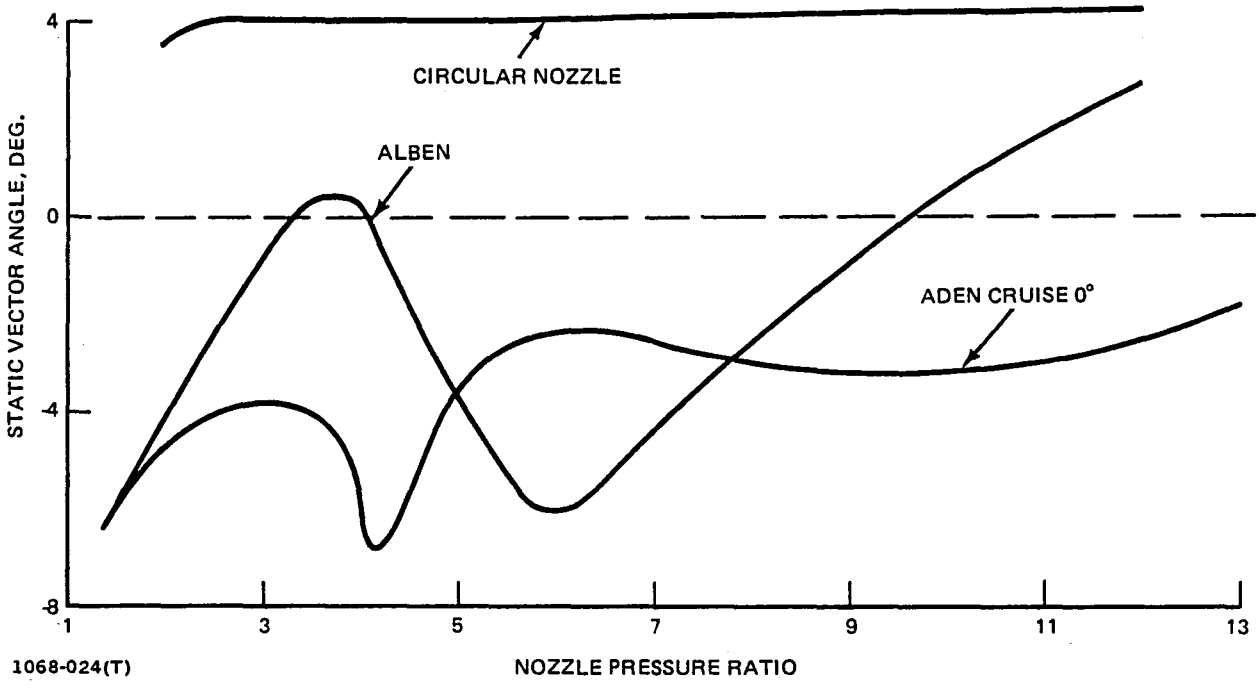

Figure 59 Effect of Unvectored Nozzle Type: Static Vector Angle

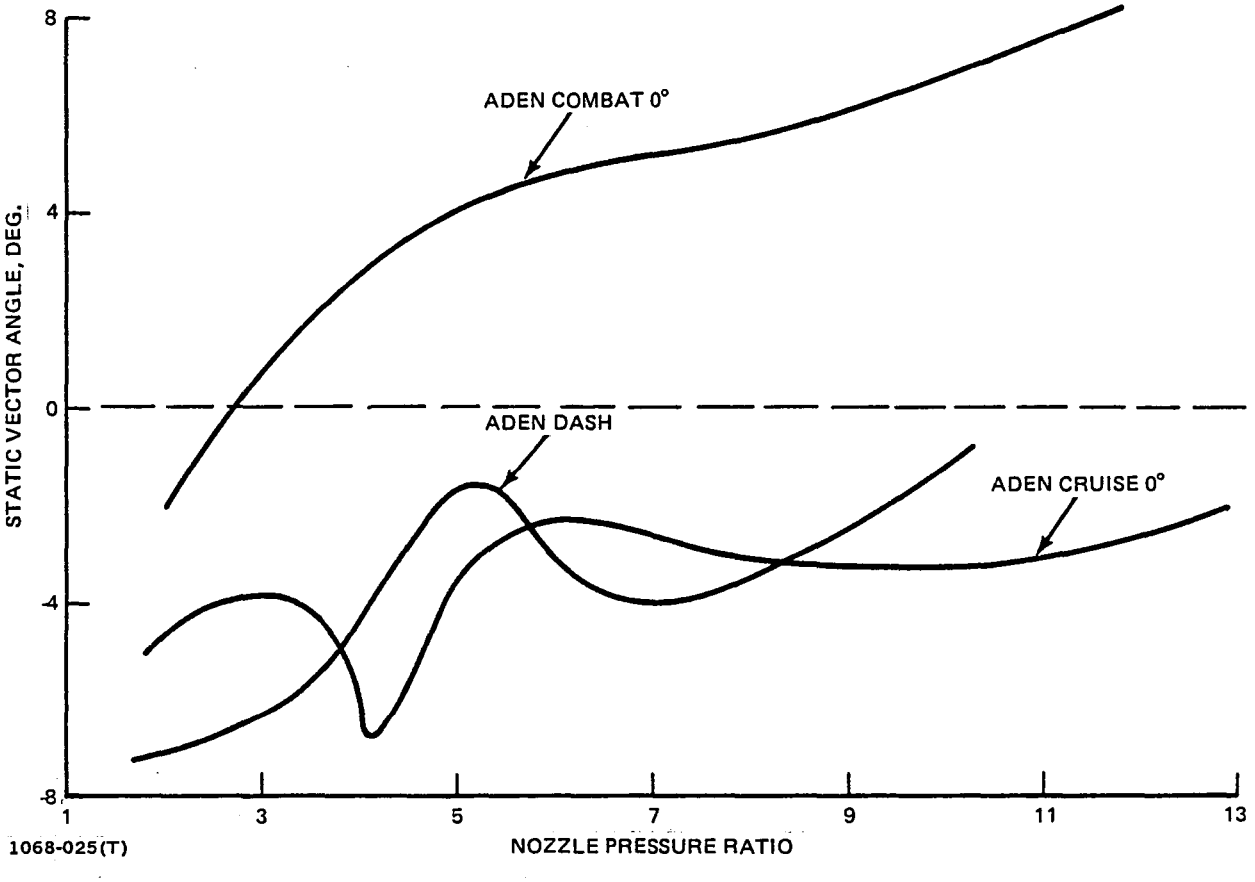

Figure 60 Effect of Jet Area Variation: Static Vector Angle

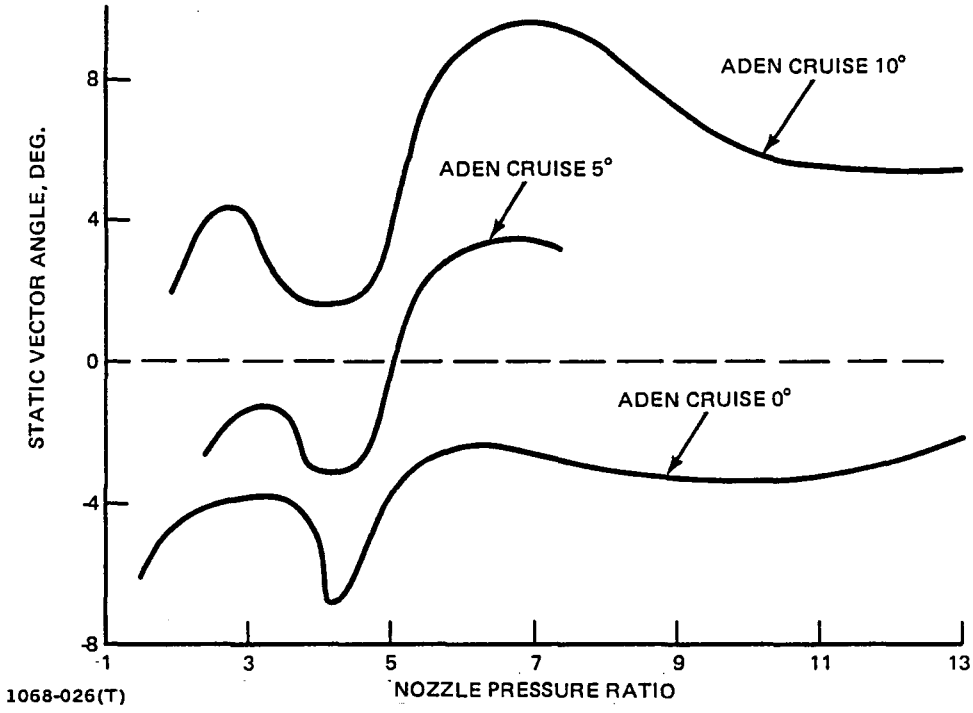

Figure 61 Effect of Cruise Nozzle Vectoring: Static Vector Angle

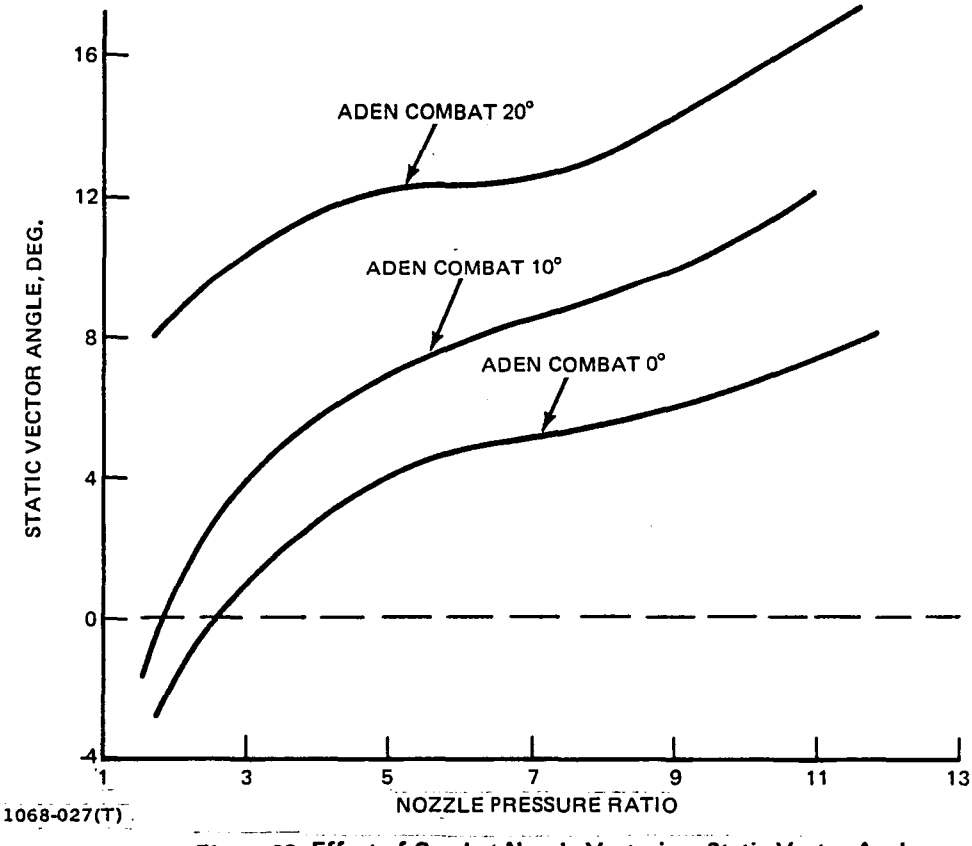

Figure 62 Effect of Combat Nozzle Vectoring: Static Vector Angle

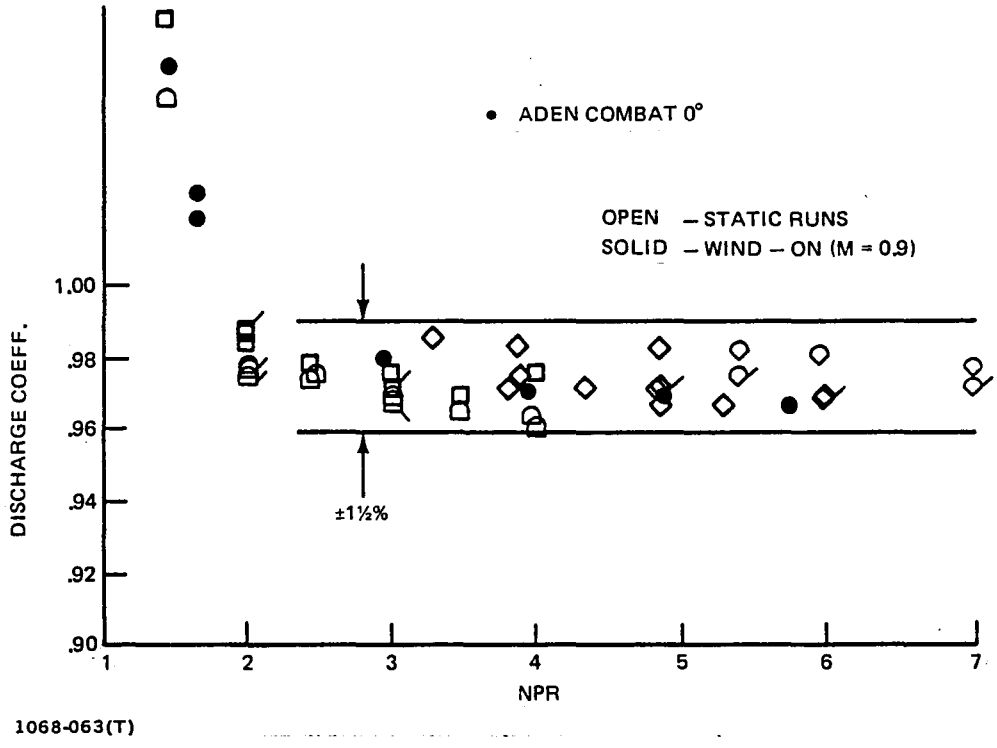

Figure 63 Static and Wind-on Discharge Coeff.

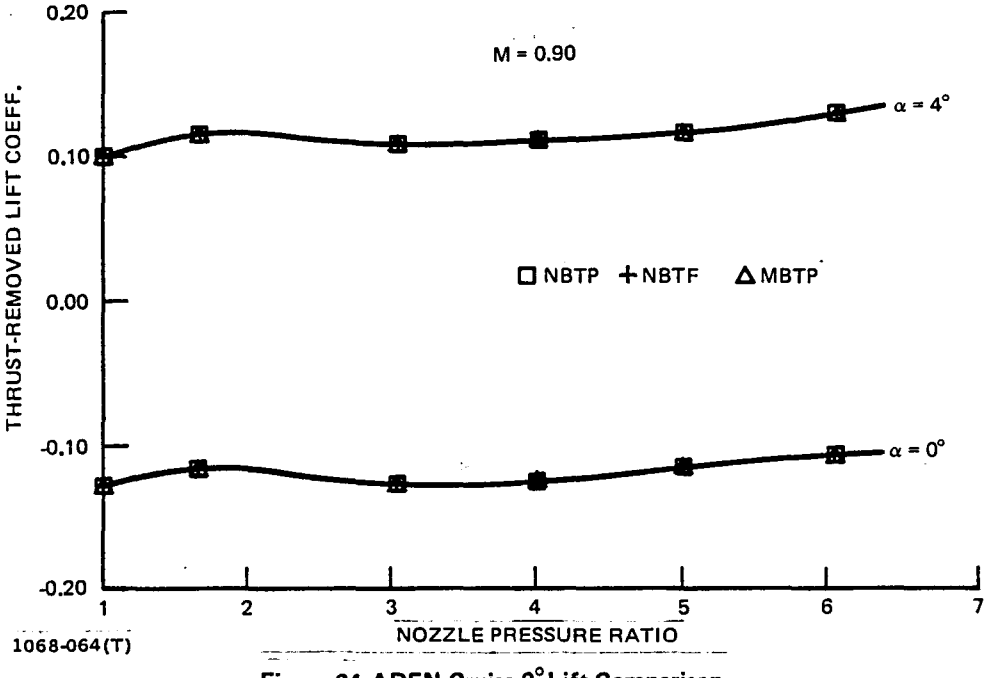

Figure 64 ADEN Cruise 0° Lift Comparison

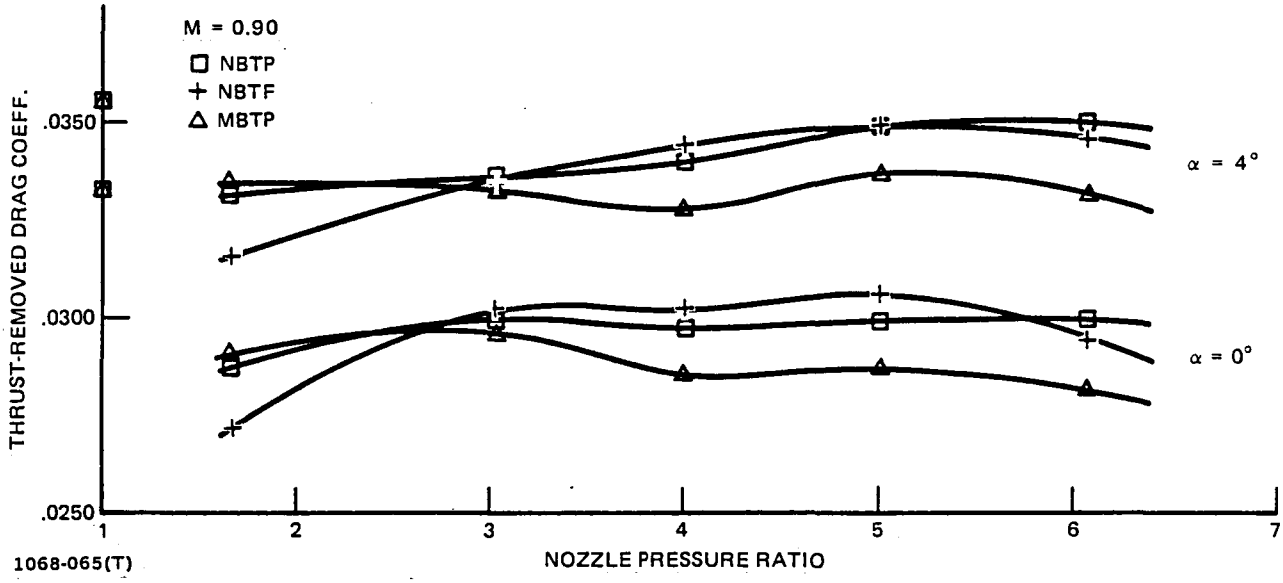

Figure 65 ADEN Cruise 0° Drag Comparison

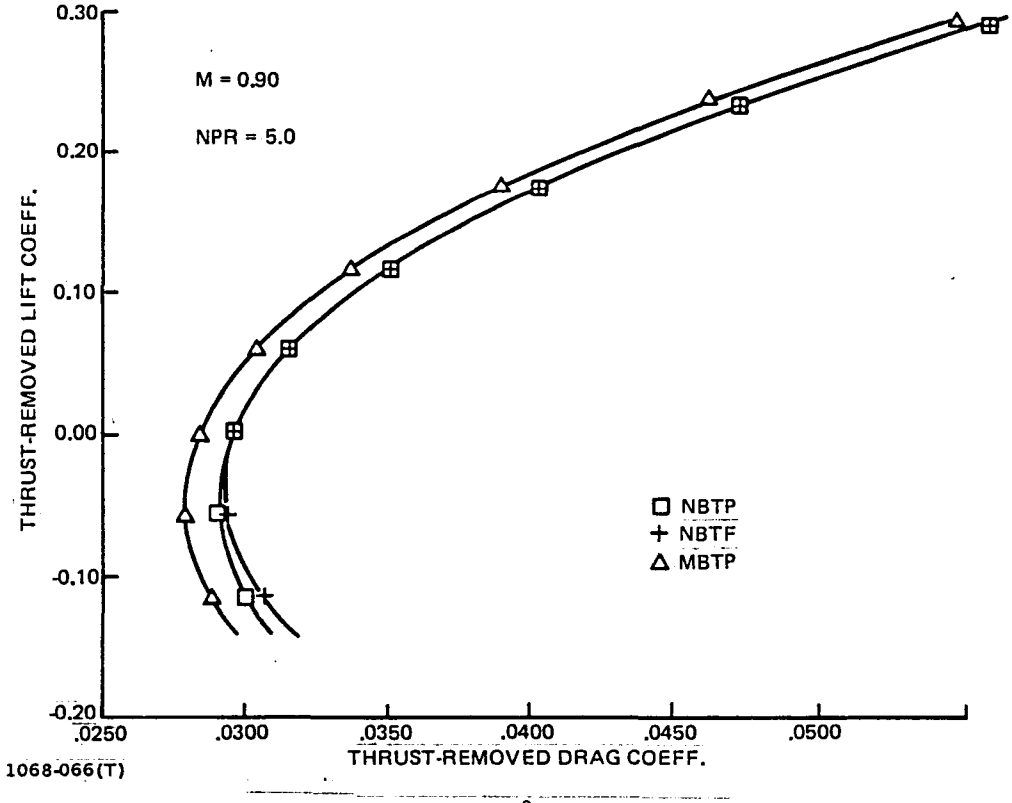

Figure 66 ADEN Cruise 0° Polar Comparison

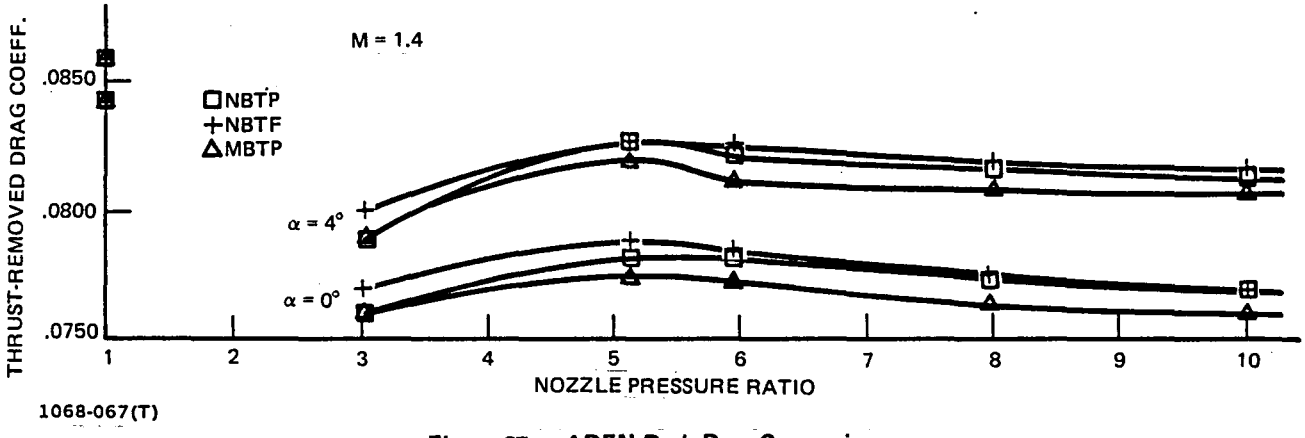

Figure 67 ADEN Dash Drag Comparison

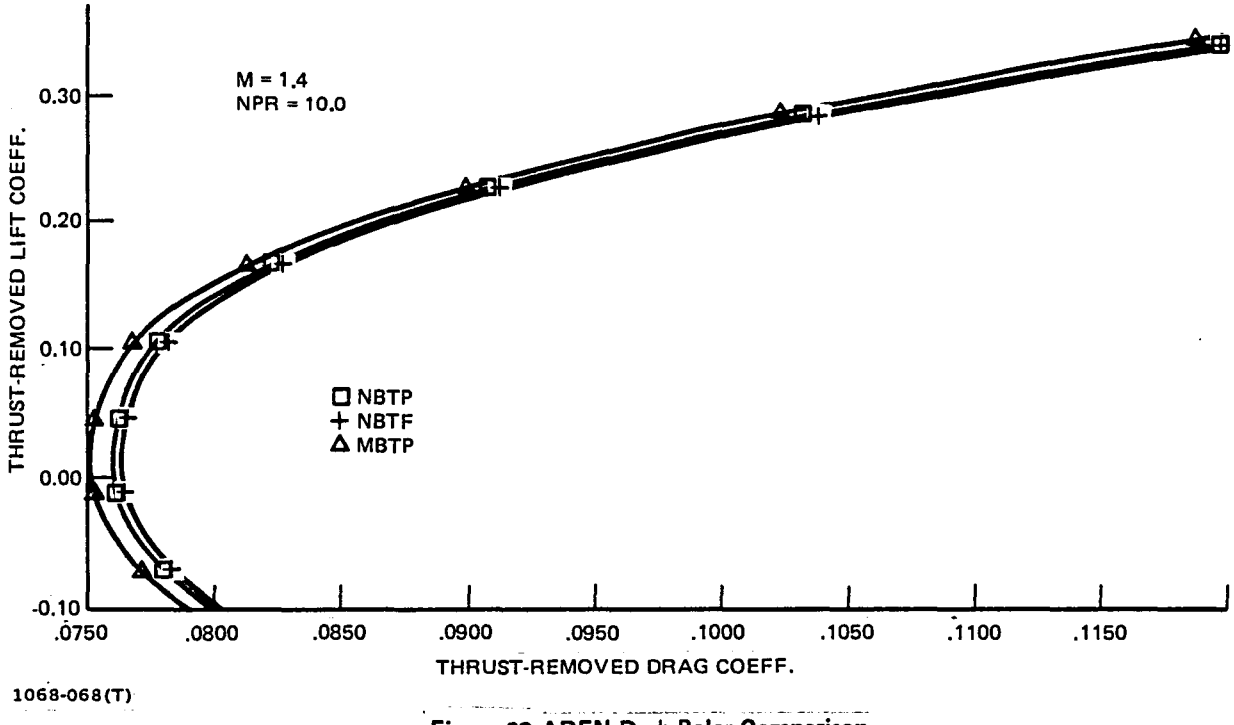

Figure 68 ADEN Dash Polar Comparison

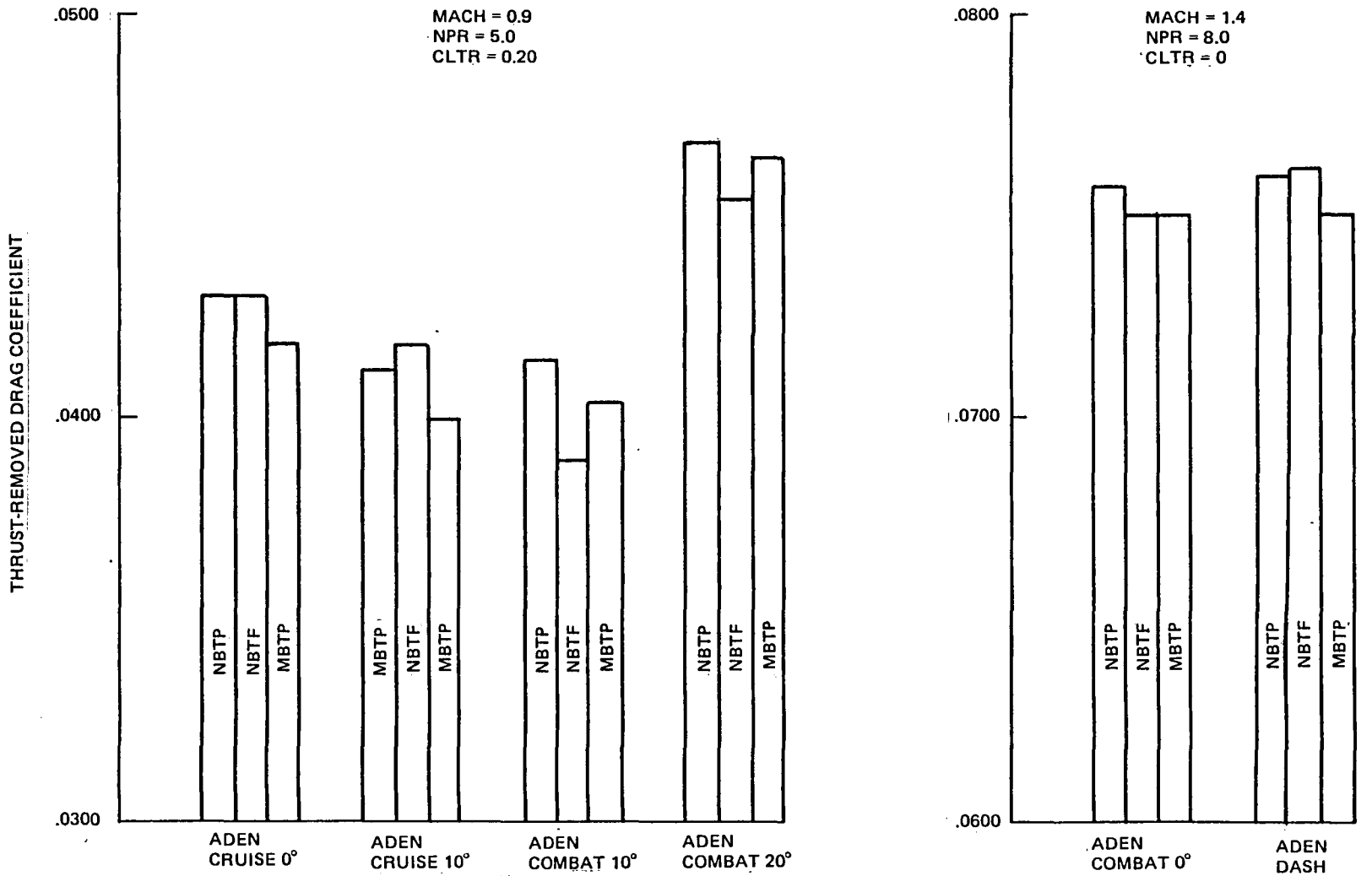

Figure 69 Comparison of Data Reduction Methods

1068-069(T)

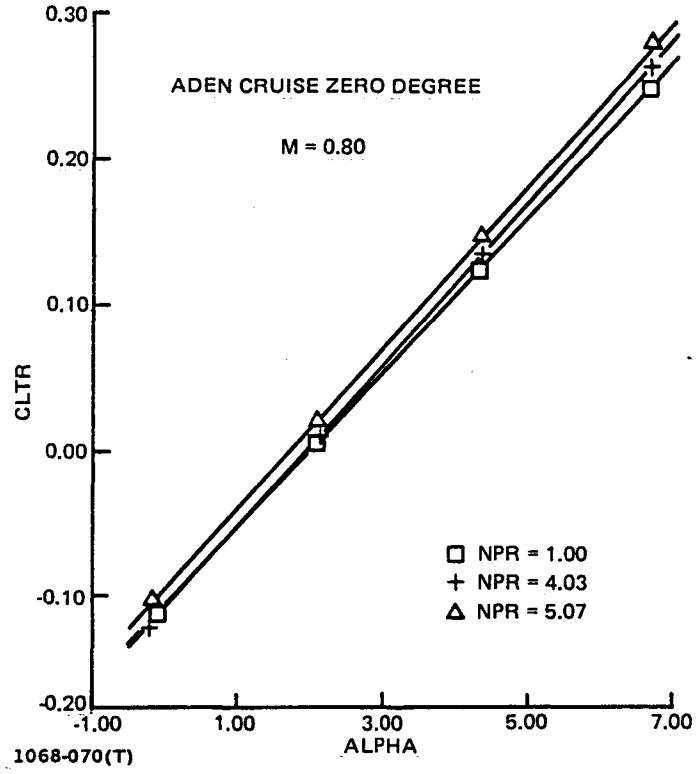

Figure 70 Thrust-Removed Lift Characteristic vs Angle-of-Attack

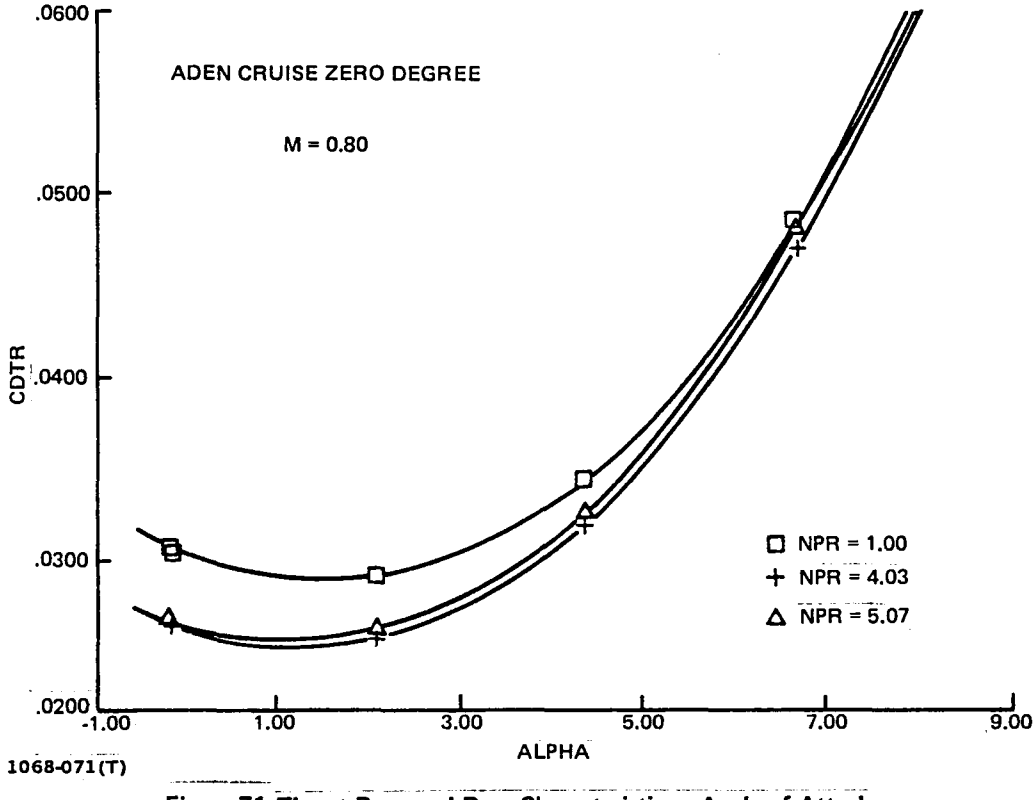

Figure 71 Thrust-Removed Drag Characteristic vs Angle-of-Attack

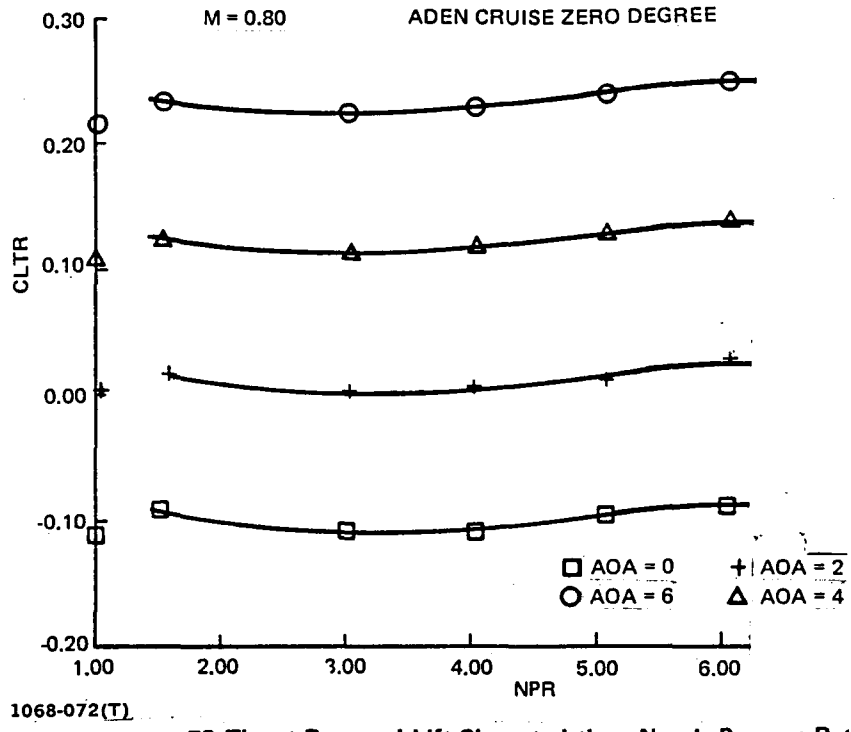

Figure 72 Thrust-Removed Lift Characteristic vs Nozzle Pressure Ratio

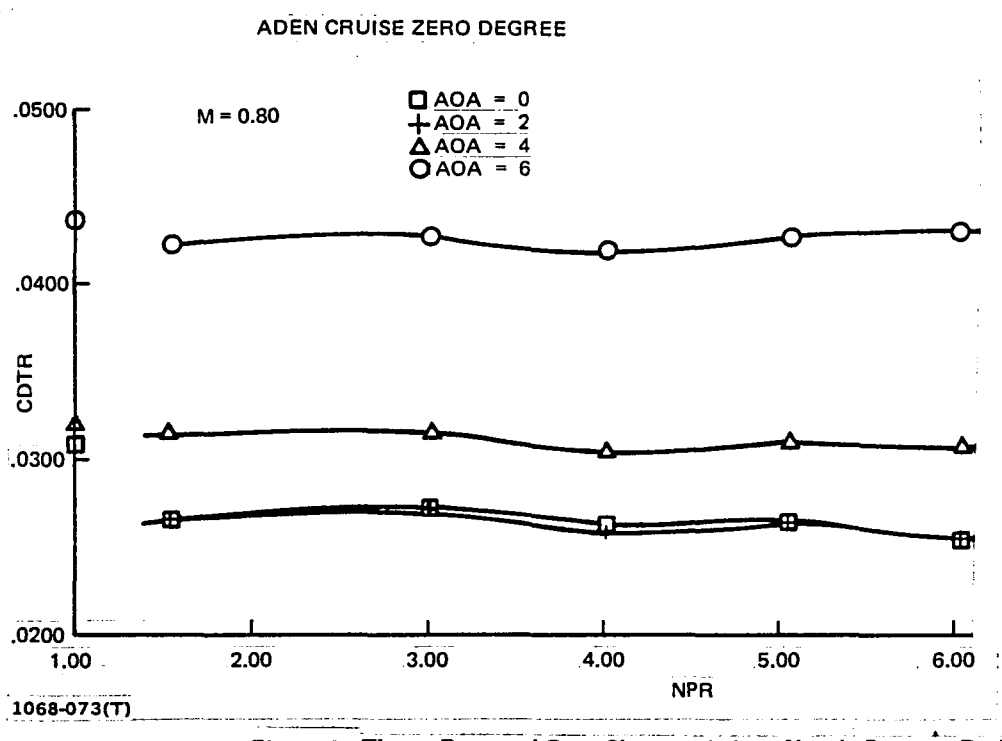

Figure 73 Thrust-Removed Drag Characteristic vs Nozzle Pressure Ratio

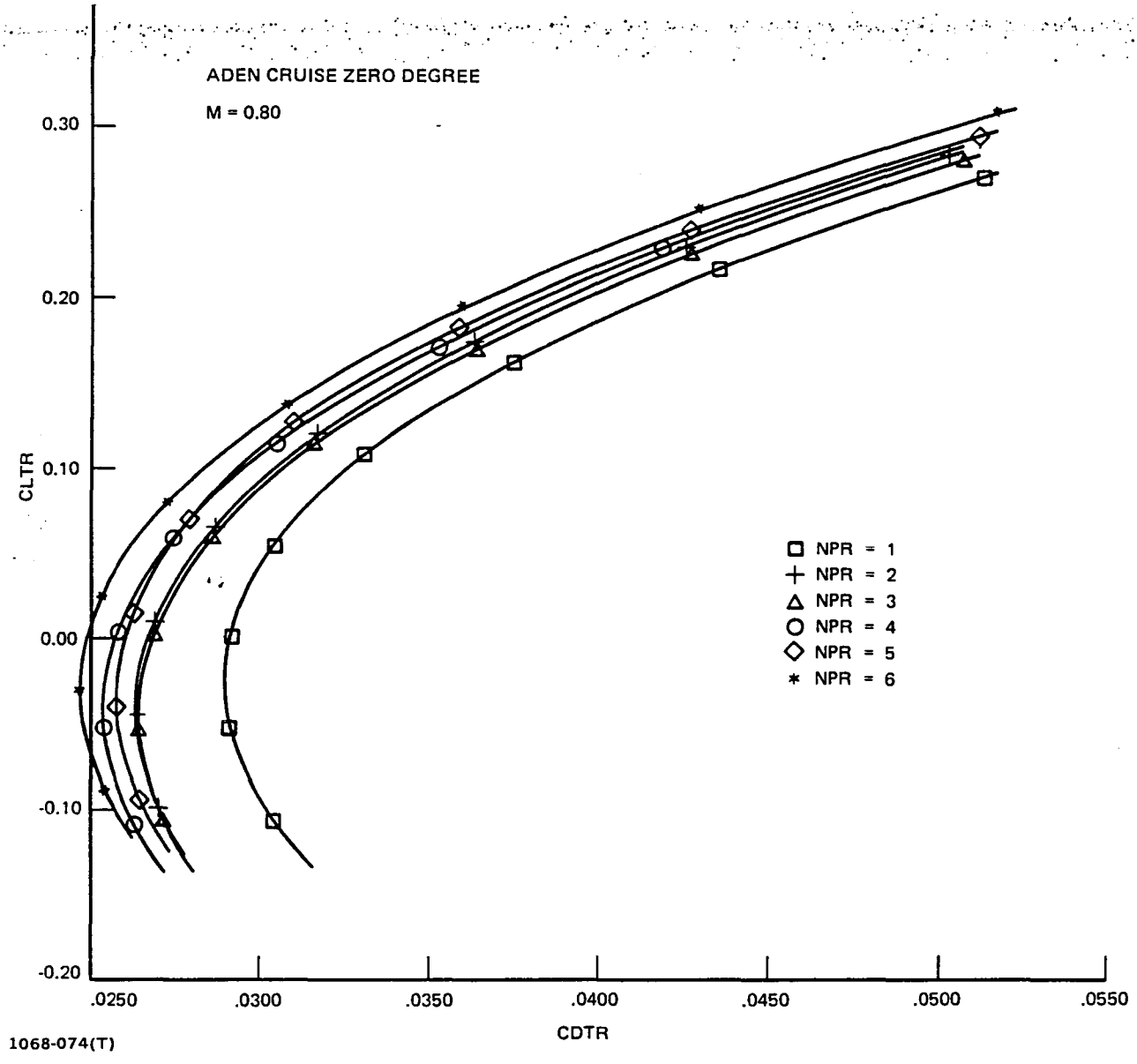

Figure 74 Thrust-Removed Drag Polar

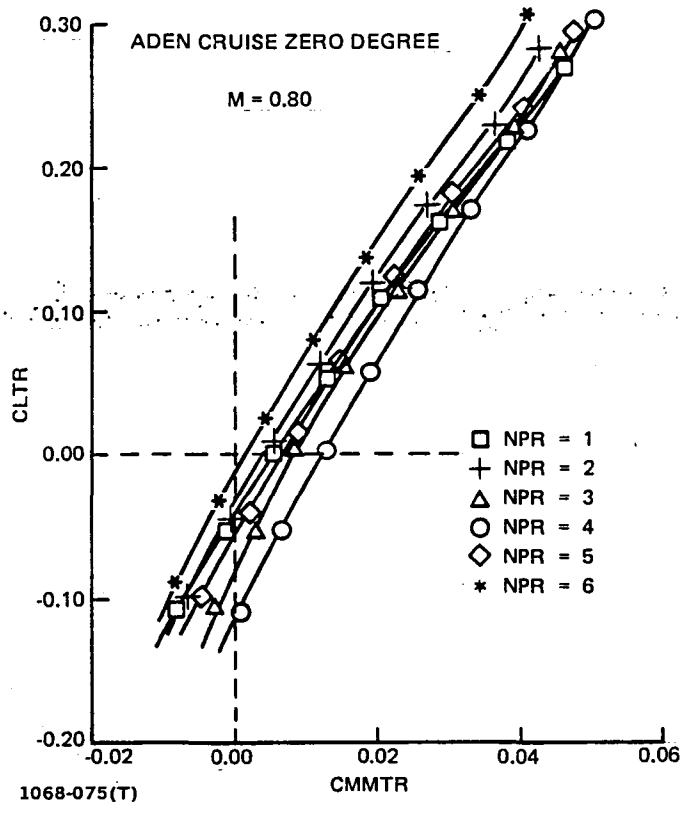

Figure 75 Thrust-Removed Pitching Moment vs Thrust-Removed Lift

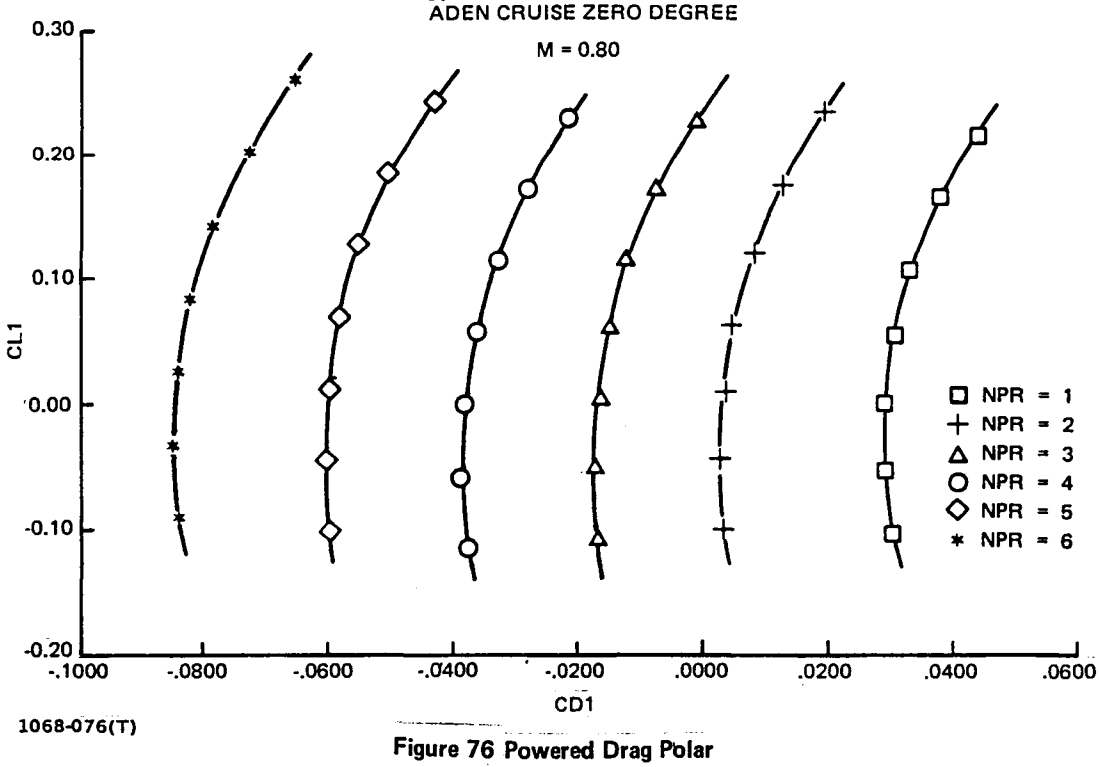

Figure 76 Powered Drag Polar

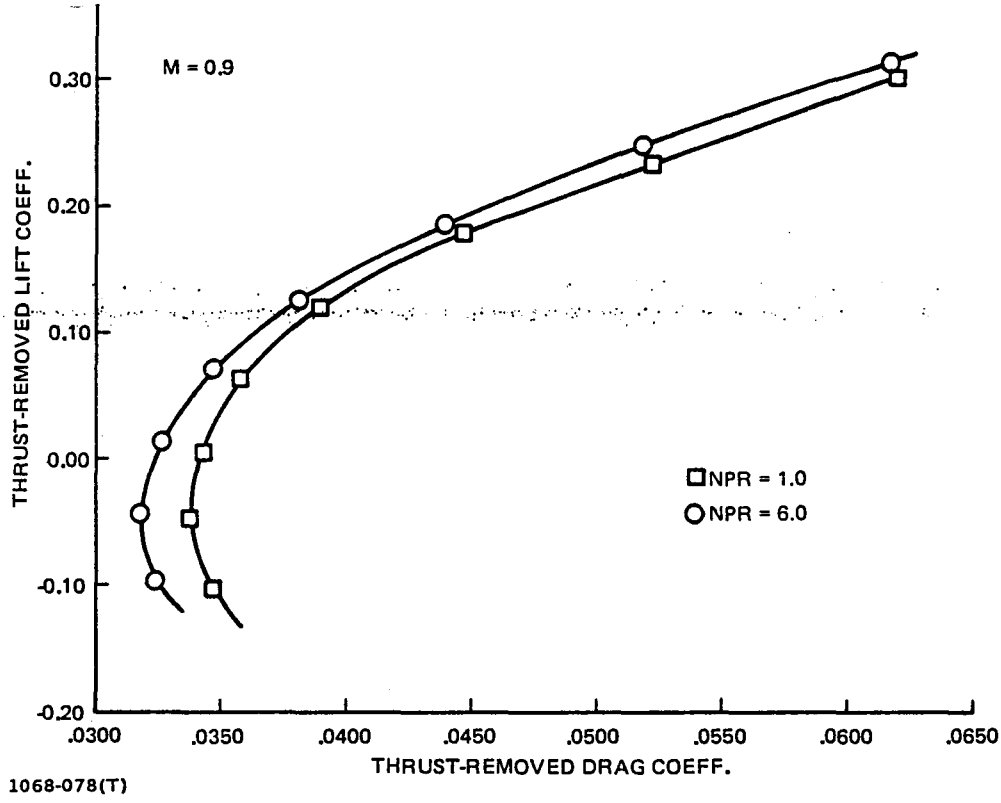

Figure 77 Circular Nozzle Power Effect on Drag Polar

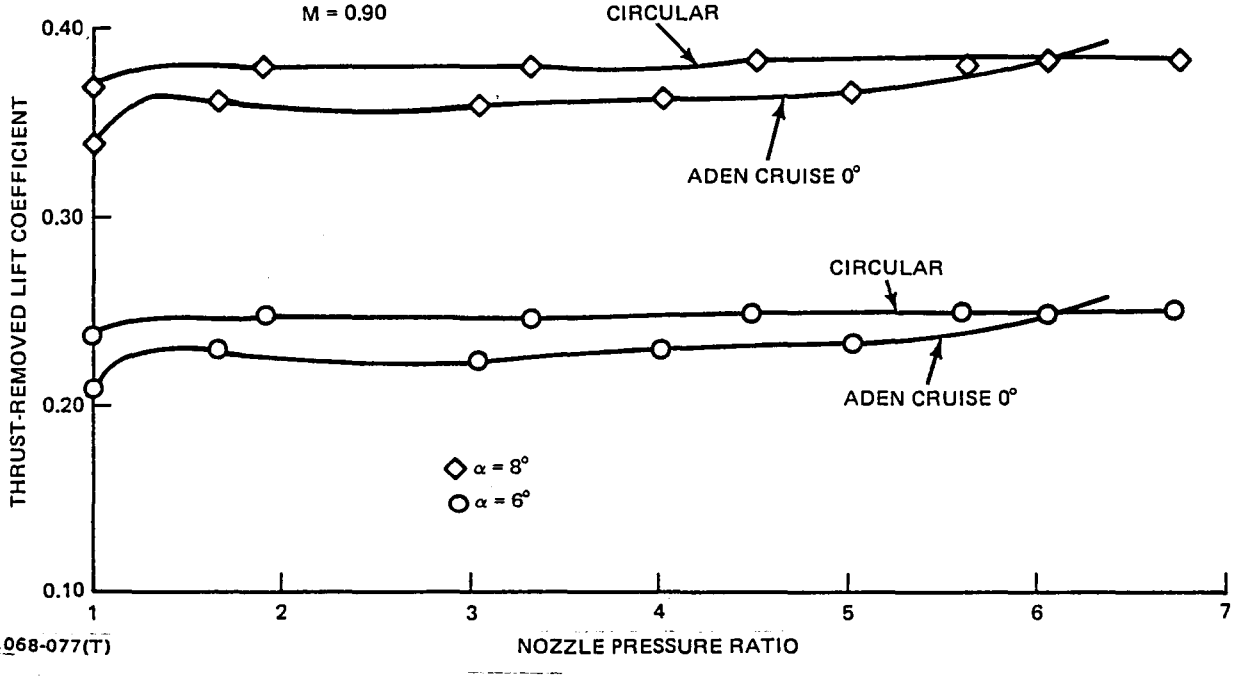

Figure 78 Lift Sensitivity to Power

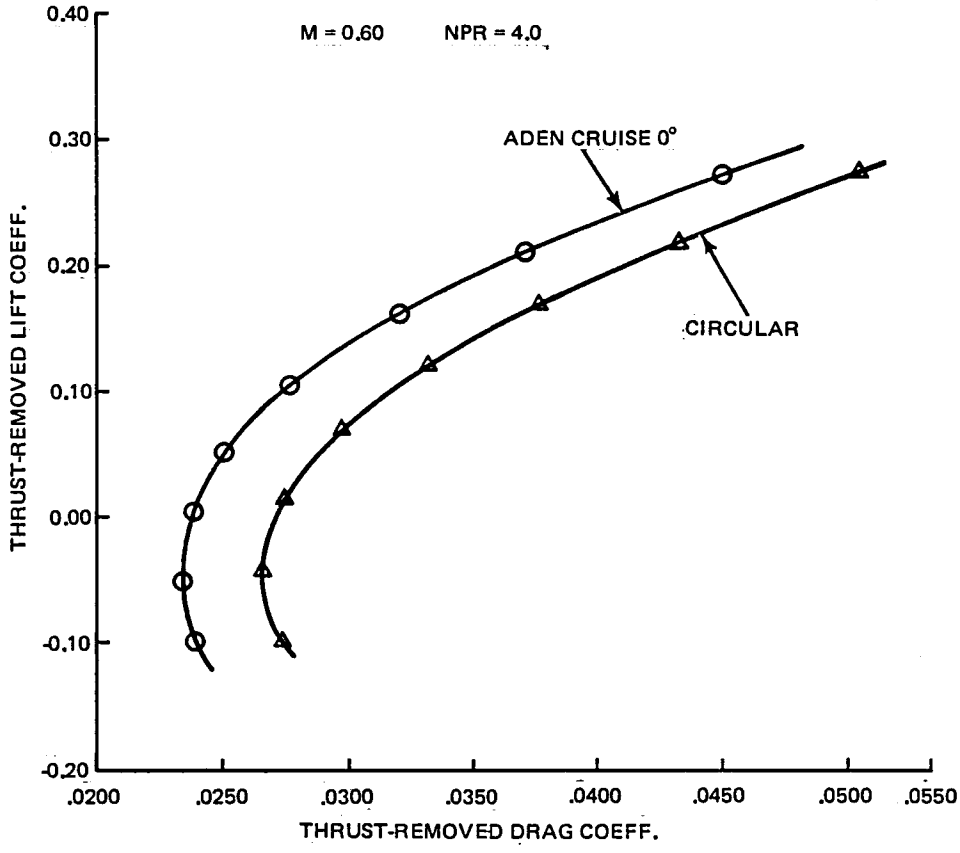

Figure 79 ADEN and Circular Nozzle Thrust-Removed Polar Comparison

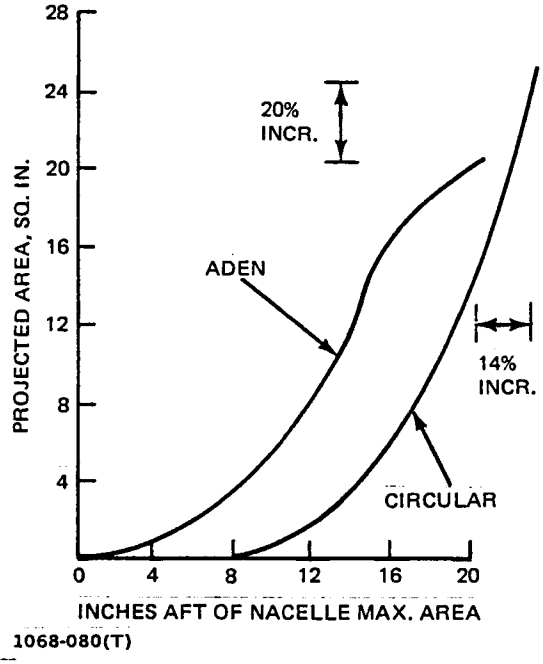

Figure 80 Projected Area Comparison — ADEN vs Circular Nozzle

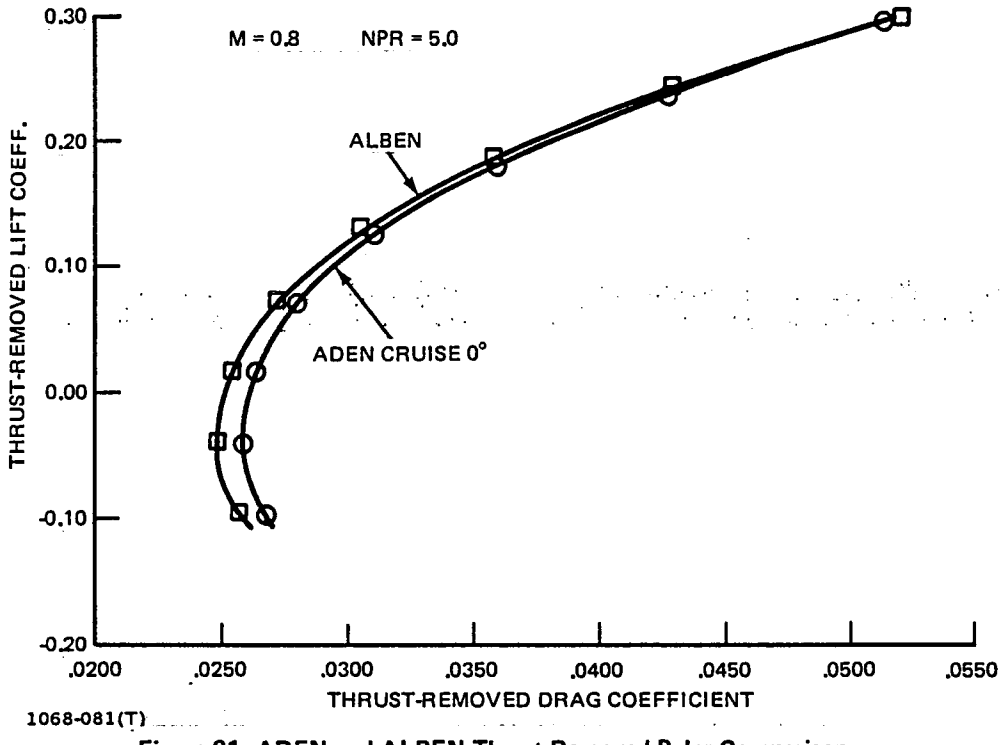

Figure 81 ADEN and ALBEN Thrust-Removed Polar Comparison

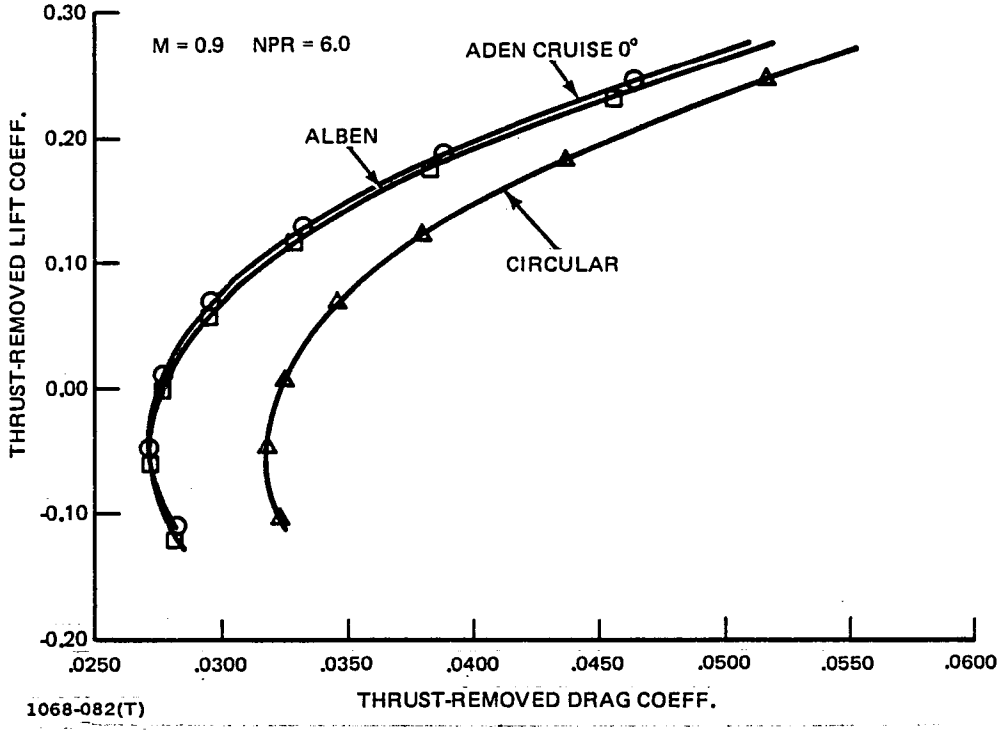

Figure 82 ADEN, ALBEN, and Circular Nozzle Thrust-Removed Polar Comparison

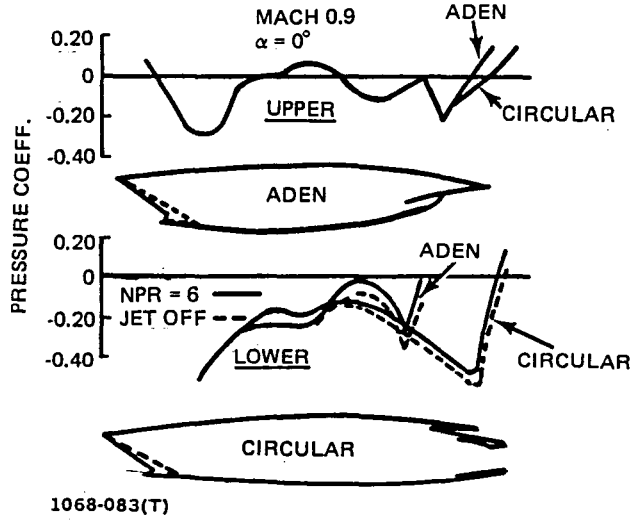

Figure 83 ADEN/Circular Nacelle/Nozzle Surface Pressure Distributions

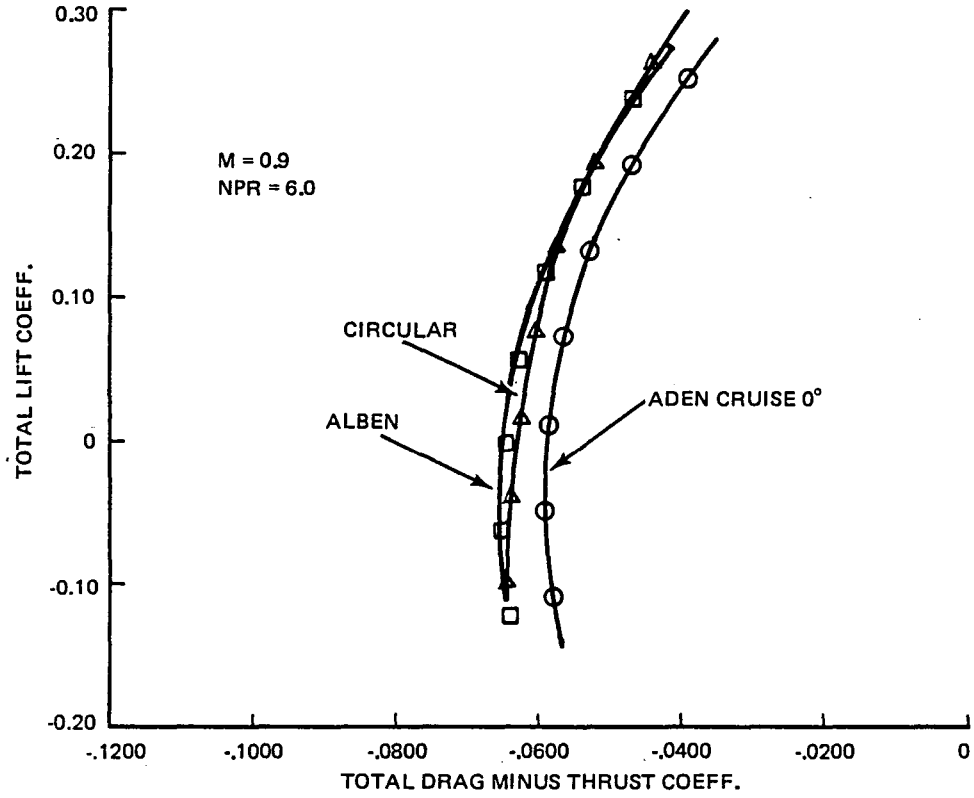

1068-084(T)

Figure 84 ADEN, ALBEN and Circular Powered Polar Comparison

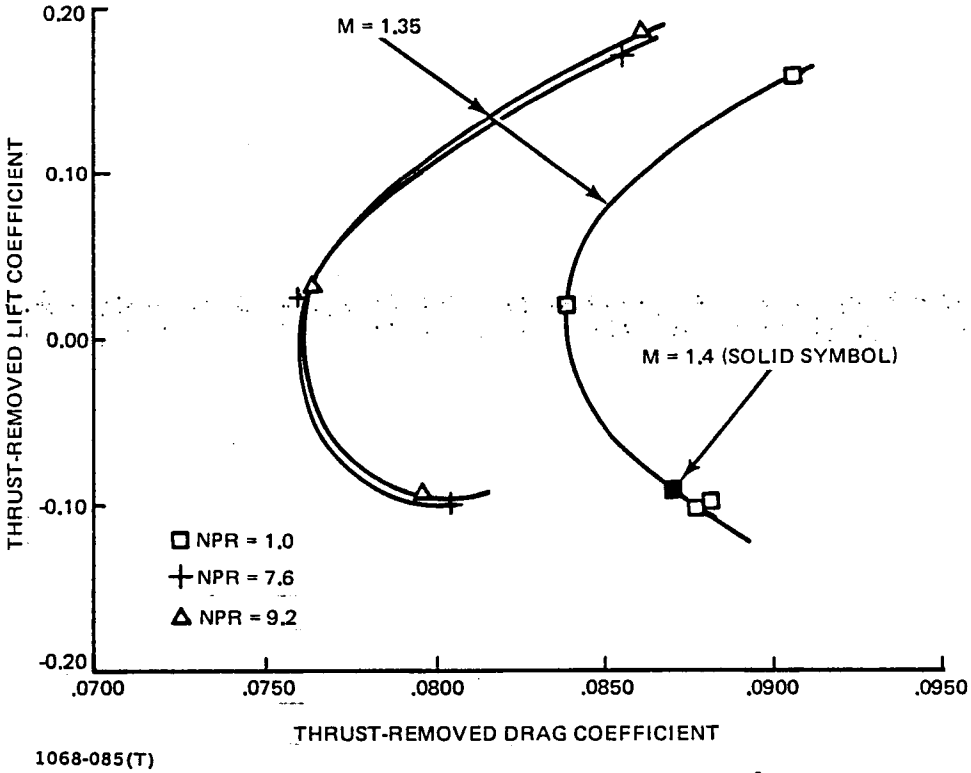

1068-085(T)

Figure 85 Effect of Mach Variation; ADEN Cruise 0°

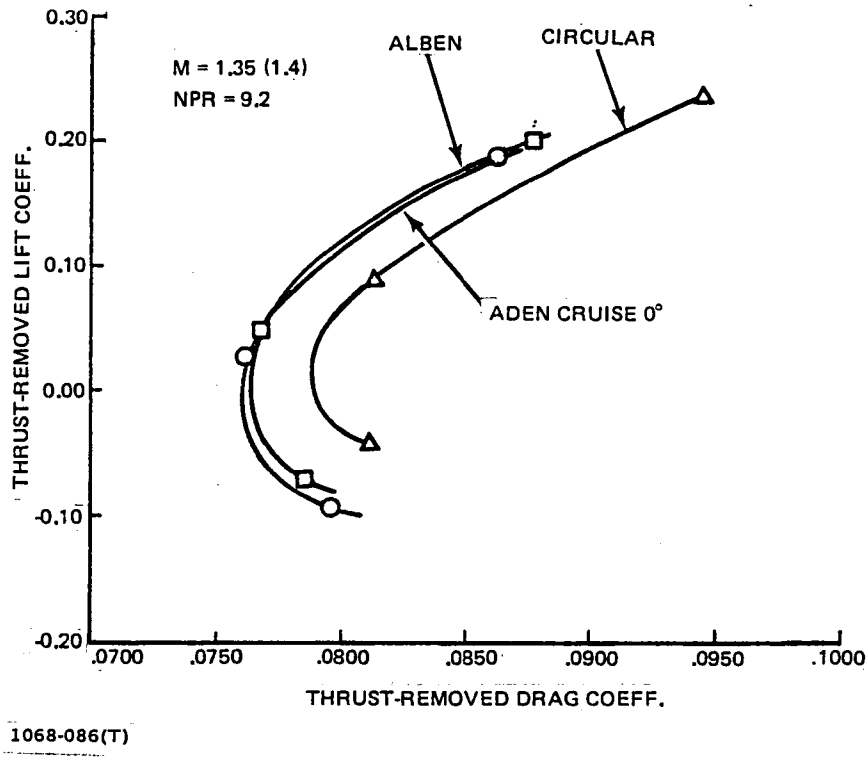

1068-086(T)

Figure 86 ADEN, ALBEN and Circular Nozzle Comparison at Supersonic Speeds

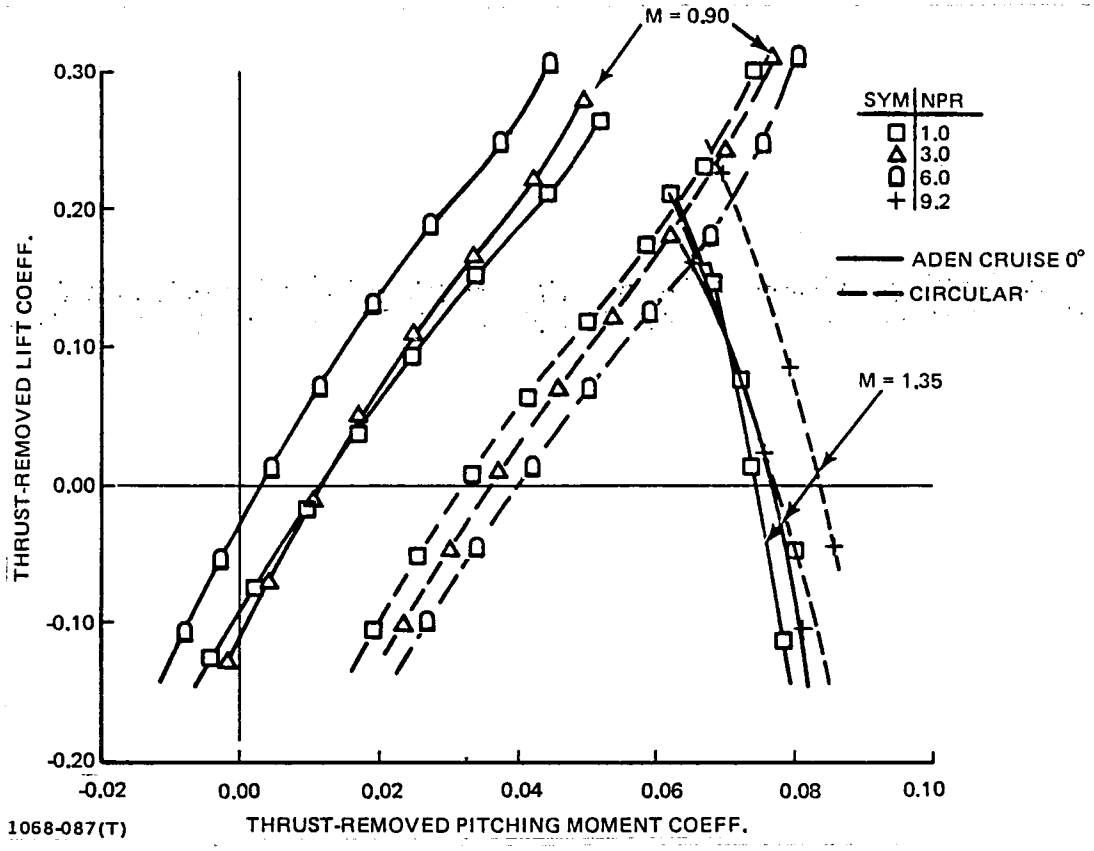

Figure 87 Effect of Nozzle Type and Power on Pitching Moment

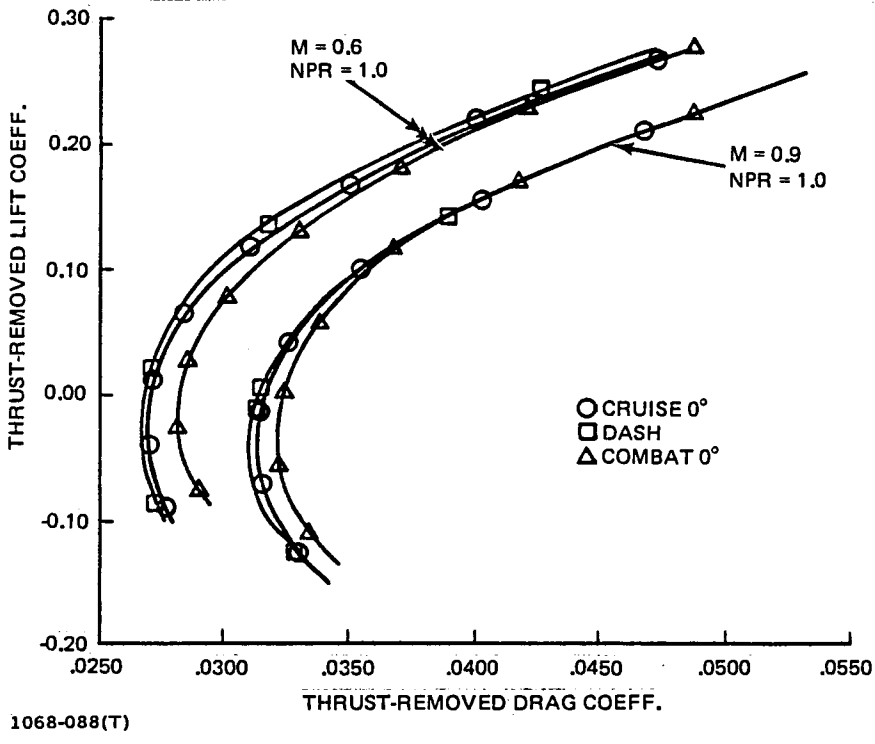

Figure 88 Effect of ADEN Jet Area Variation at Jet-Off Conditions

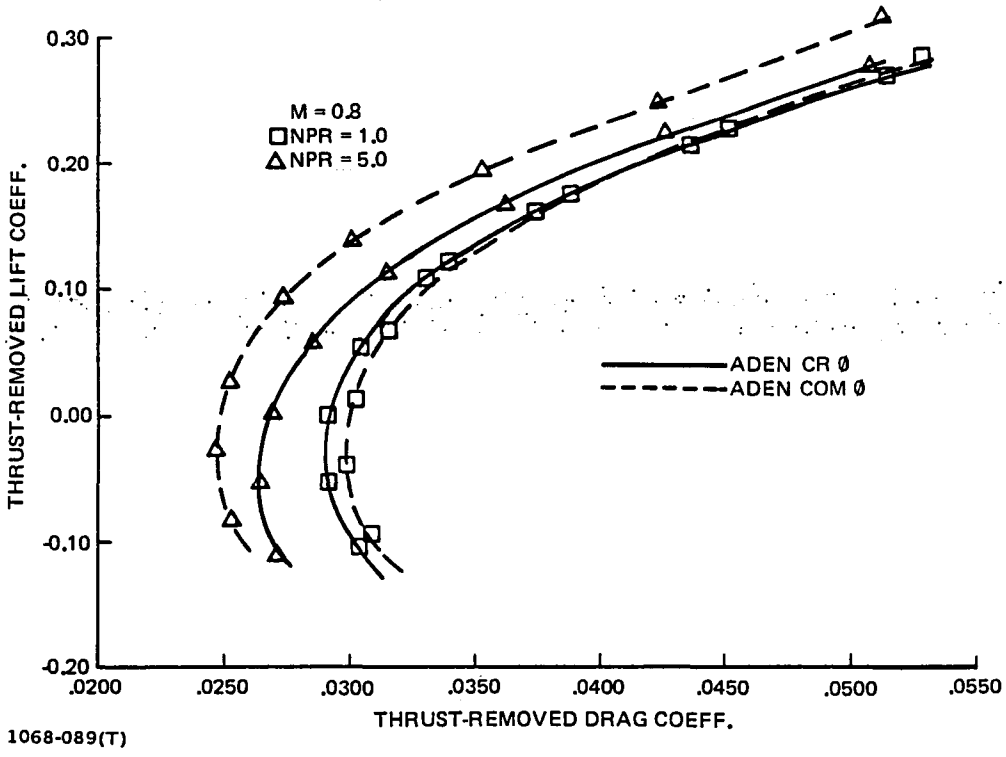

1068-089(T)

Figure 89 Effect of ADEN Jet Area Variation on Jet-Effects Increments

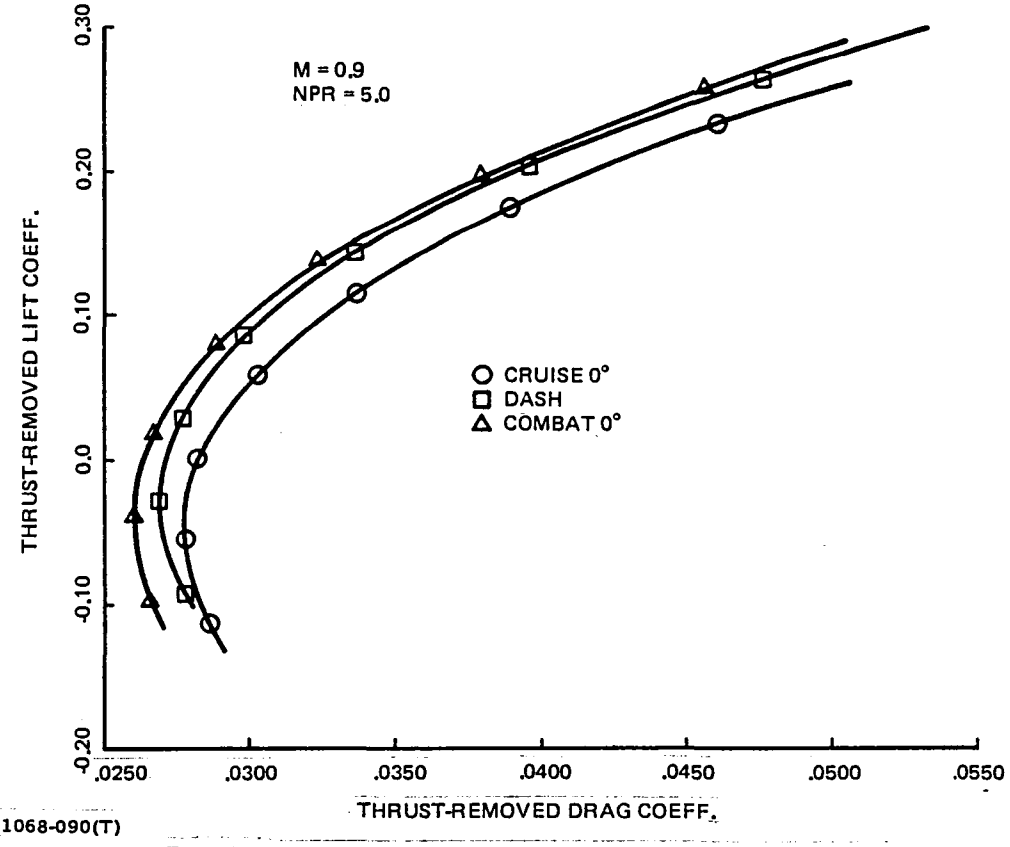

1068-090(T)

Figure 90 Effect of ADEN Jet Area Variation at Jet-On Conditions

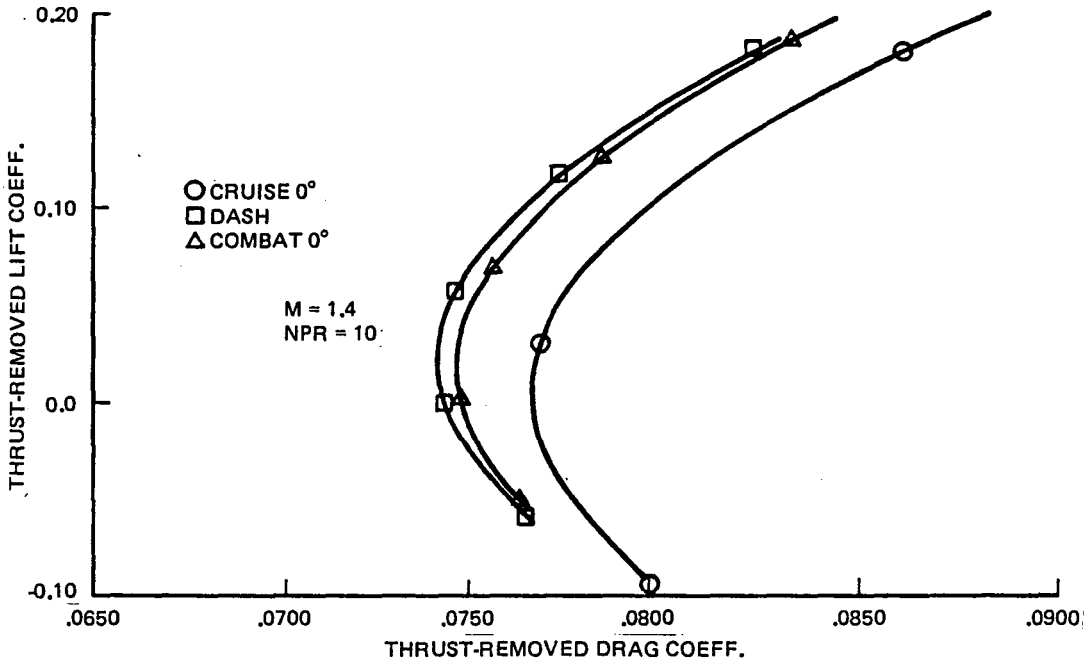

1068-091(T)

Figure 91 Effect of ADEN Jet Area Variation at Supersonic Conditions

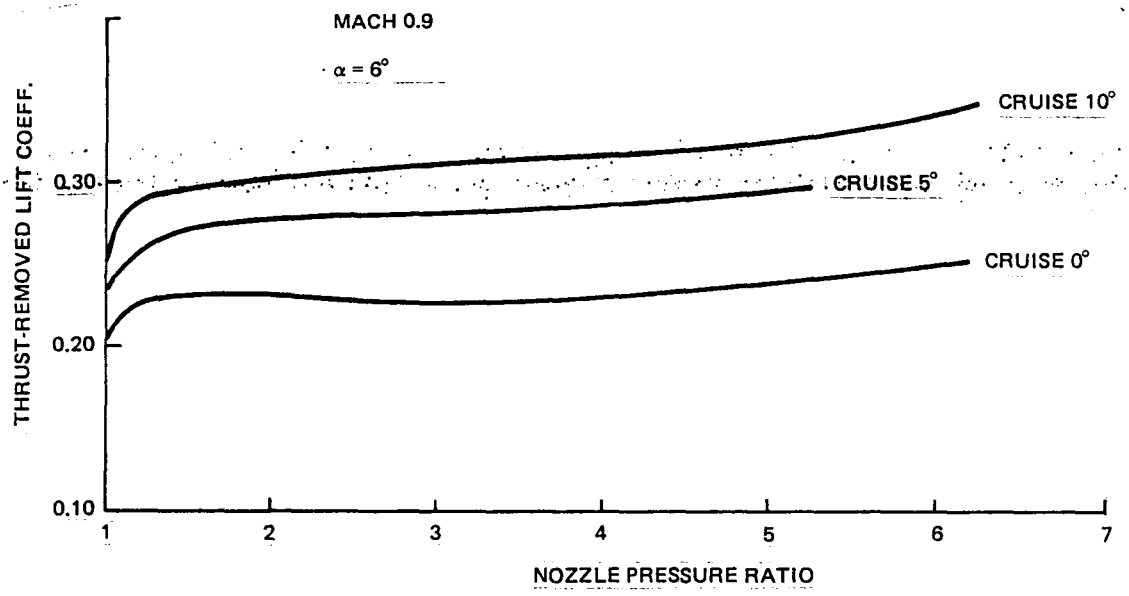

1068-092(T)

Figure 92 ADEN Cruise Vectoring Lift Comparison

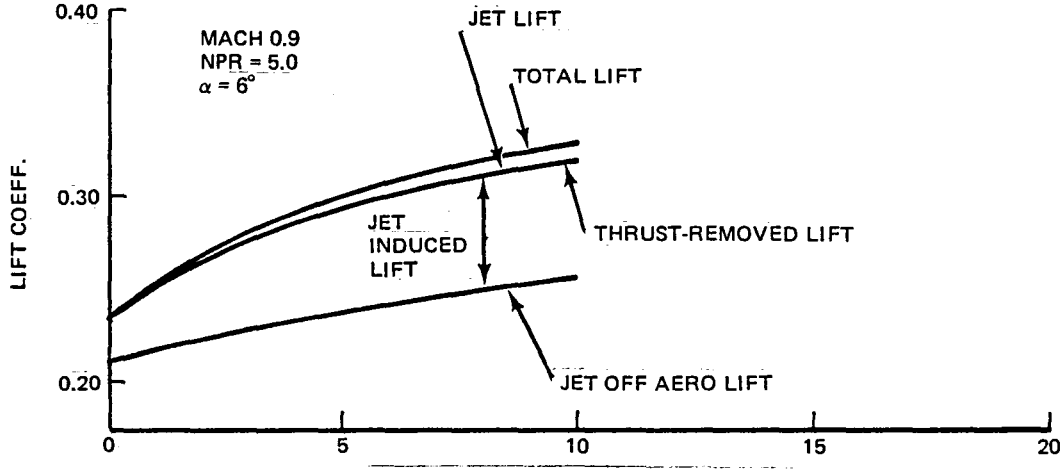

1068-093(T)

Figure 93 ADEN Cruise Lift Component Build-up

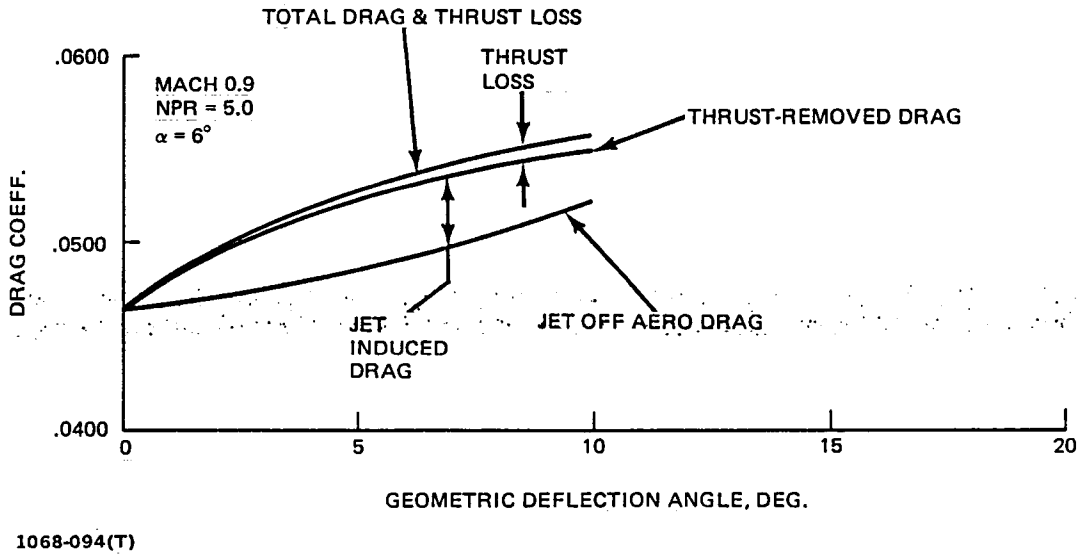

1068-094(T)

Figure 94 ADEN Cruise Drag Component Build-up

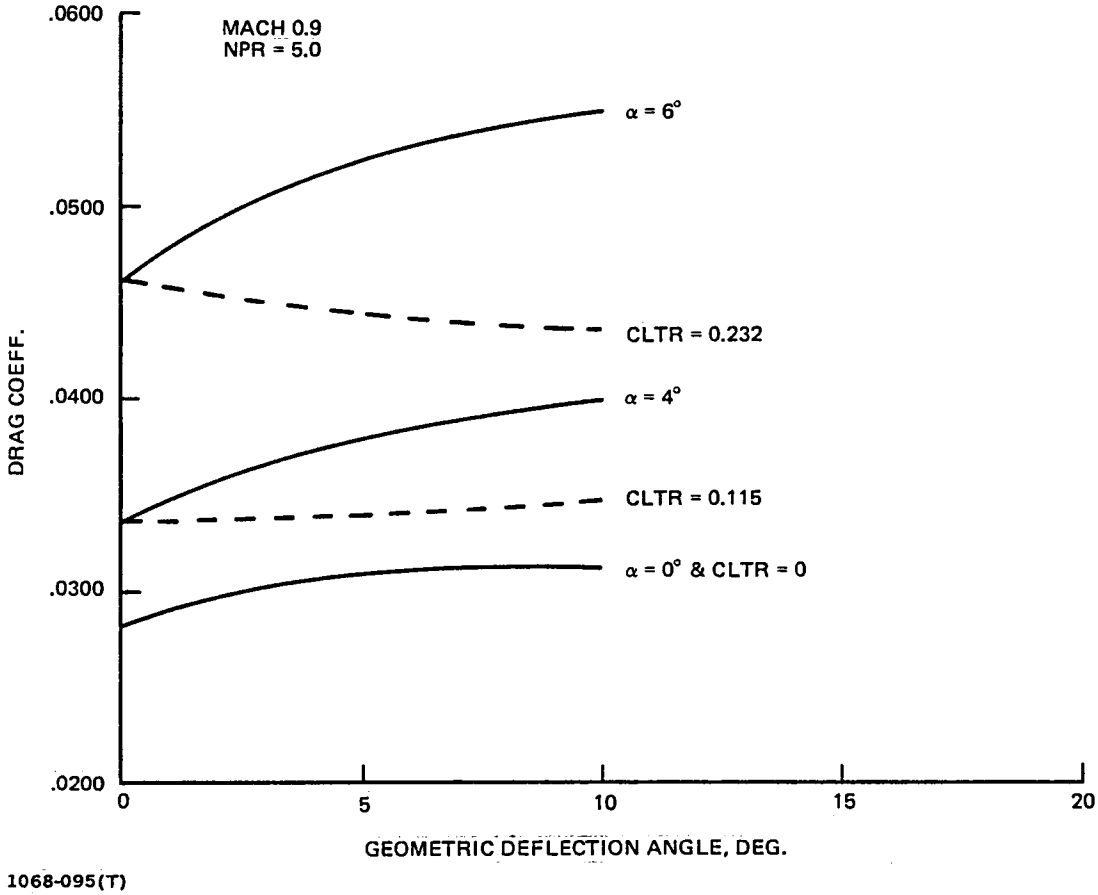

1068-095(T)

Figure 95 Effect of ADEN Cruise Vectoring on Drag

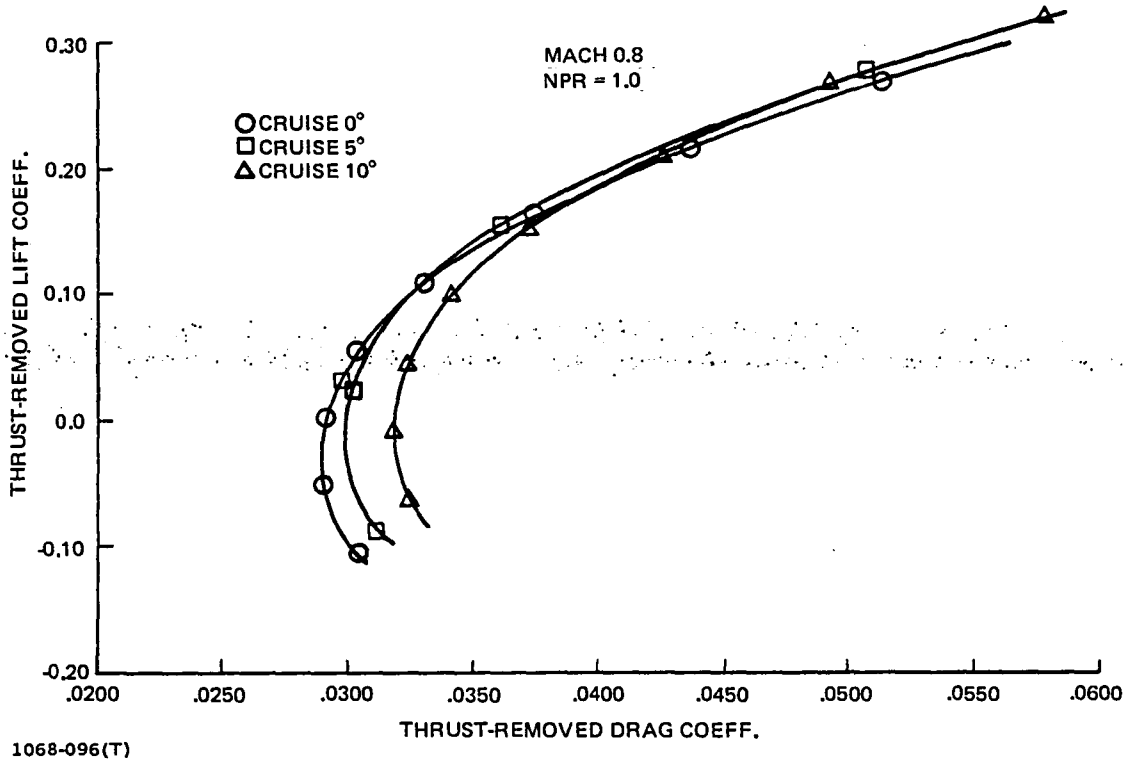

Figure 96 Effect of ADEN Cruise Vectoring at Jet-Off Conditions

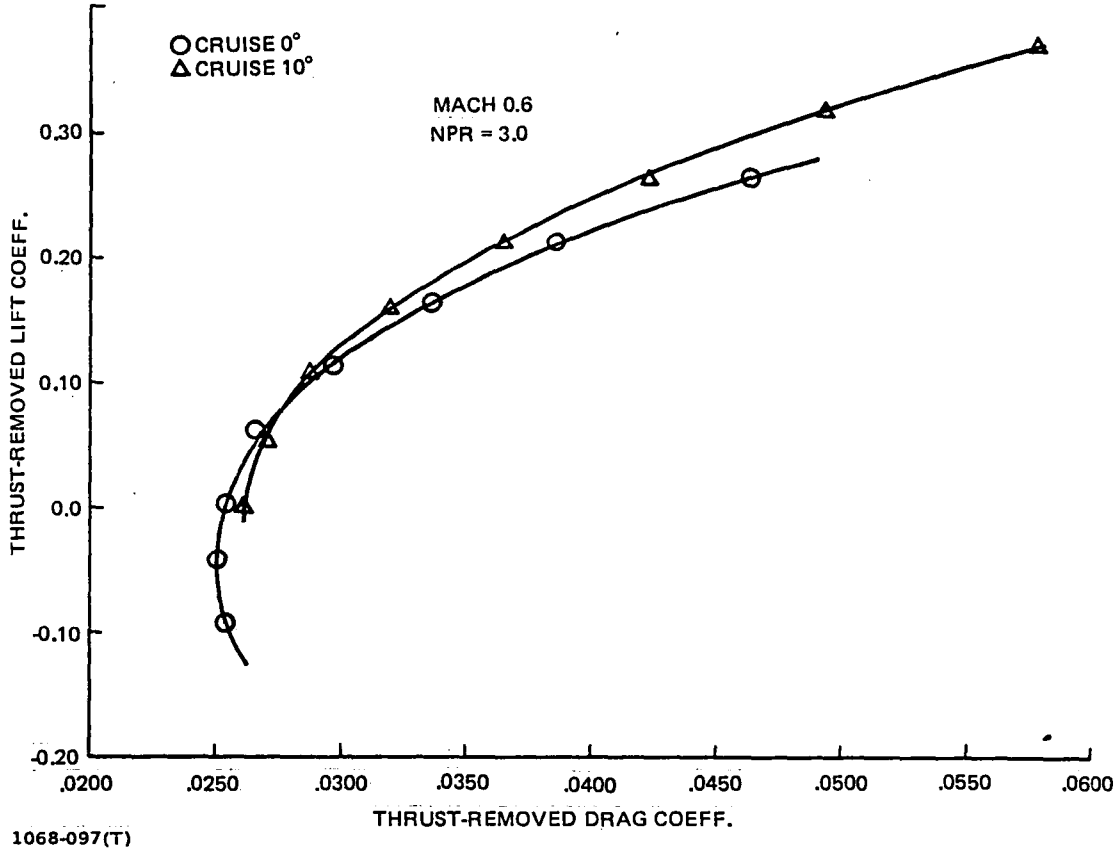

Figure 97 Effect of ADEN Cruise Vectoring at Mach 0.6

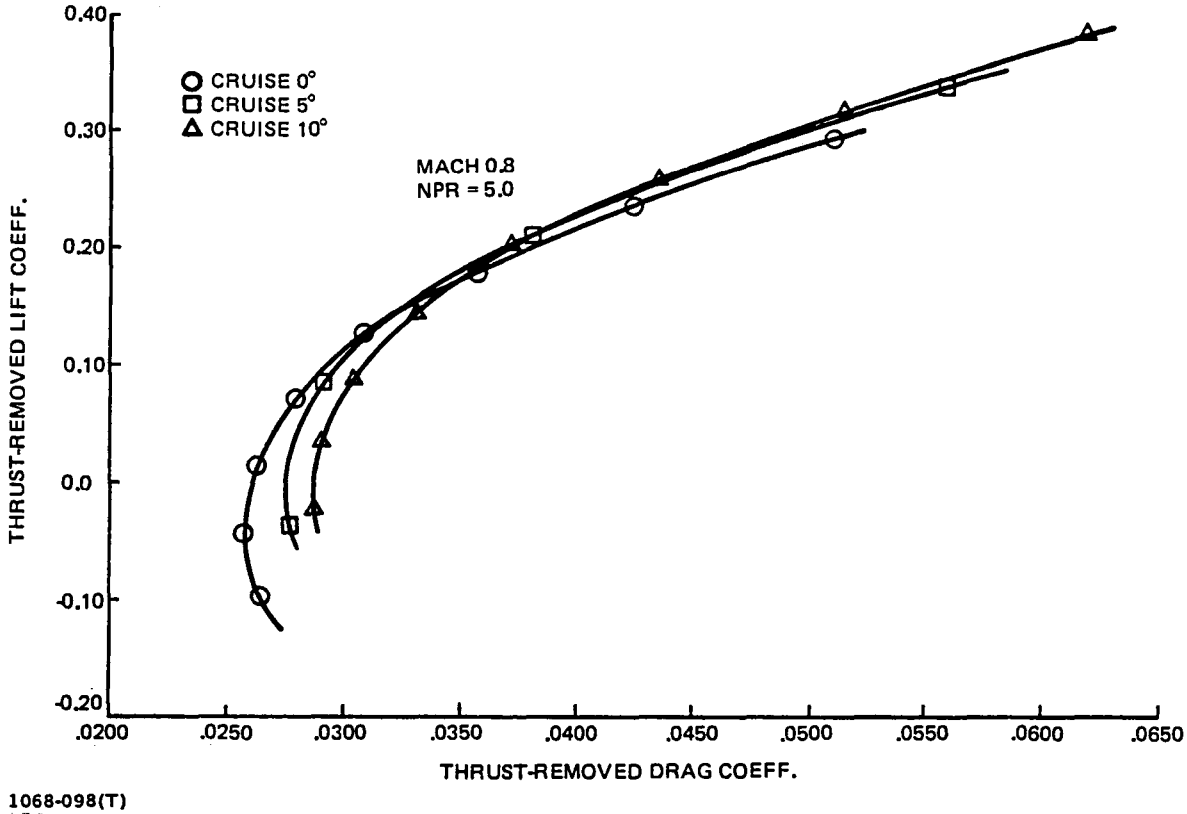

Figure 98 Effect of ADEN Cruise Vectoring at Mach 0.8

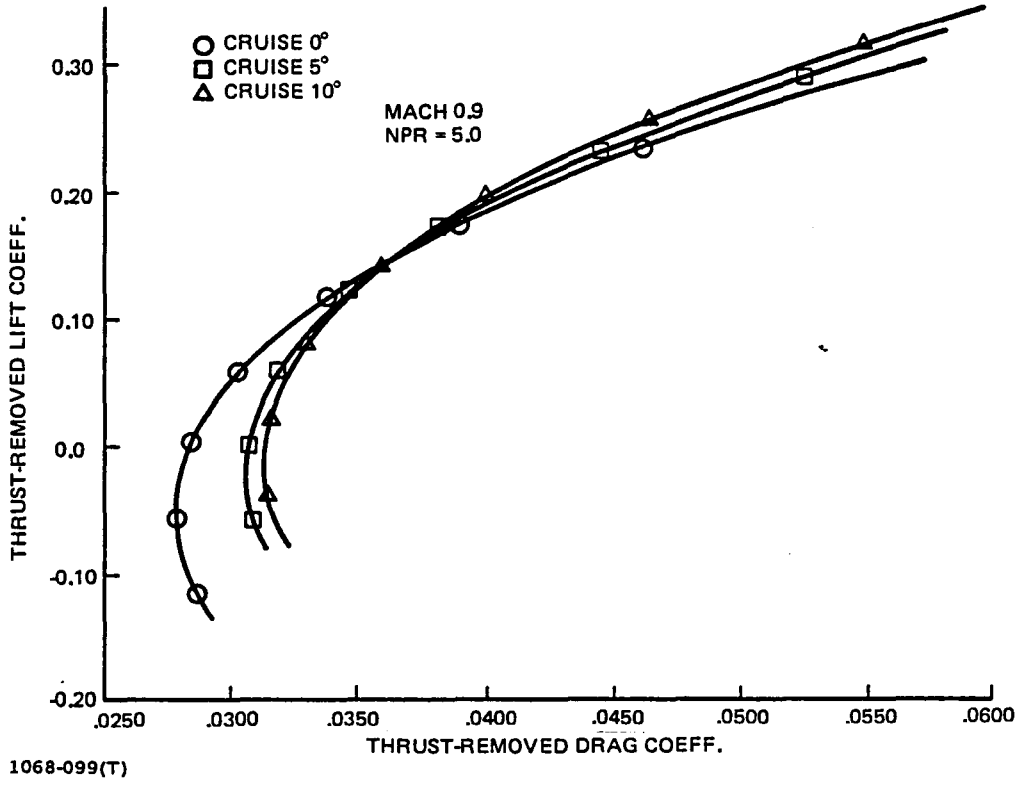

Figure 99 Effect of ADEN Cruise Vectoring at Mach 0.9

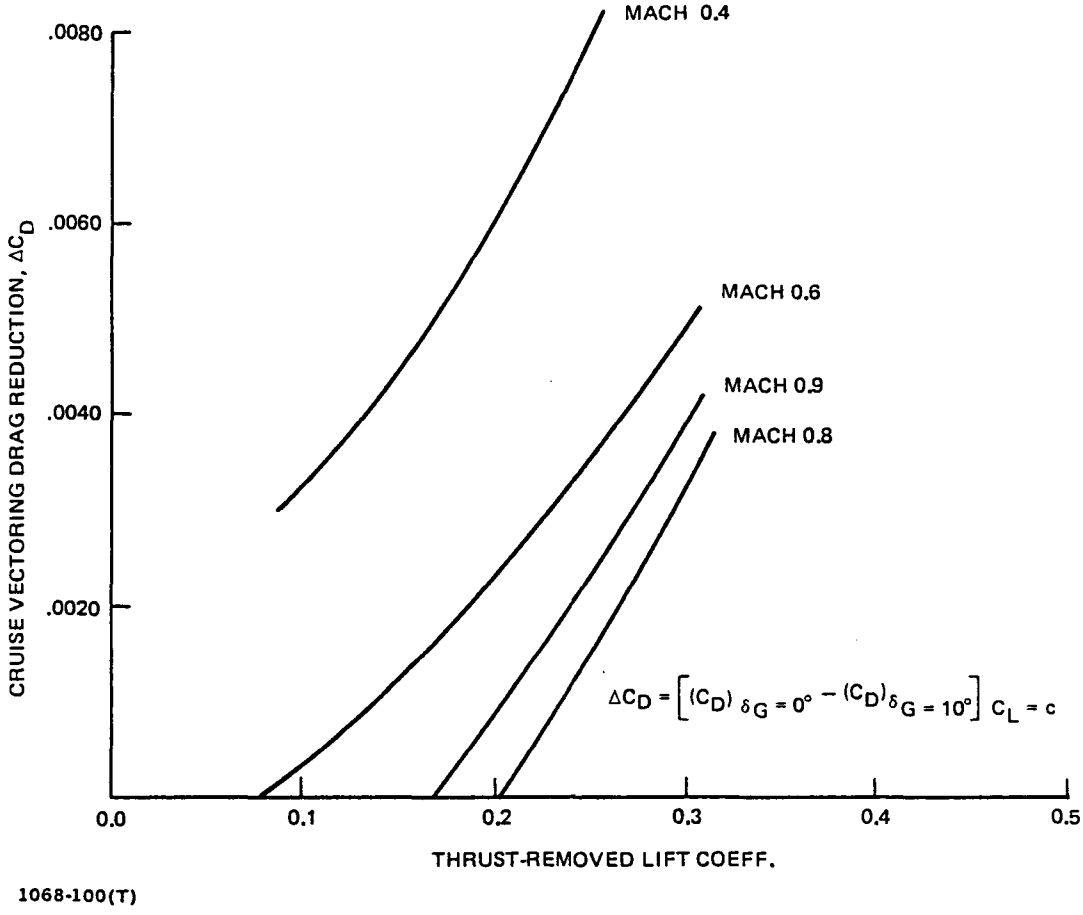

Figure 100 Effect of Lift and Mach on ADEN Vectoring Drag Reduction

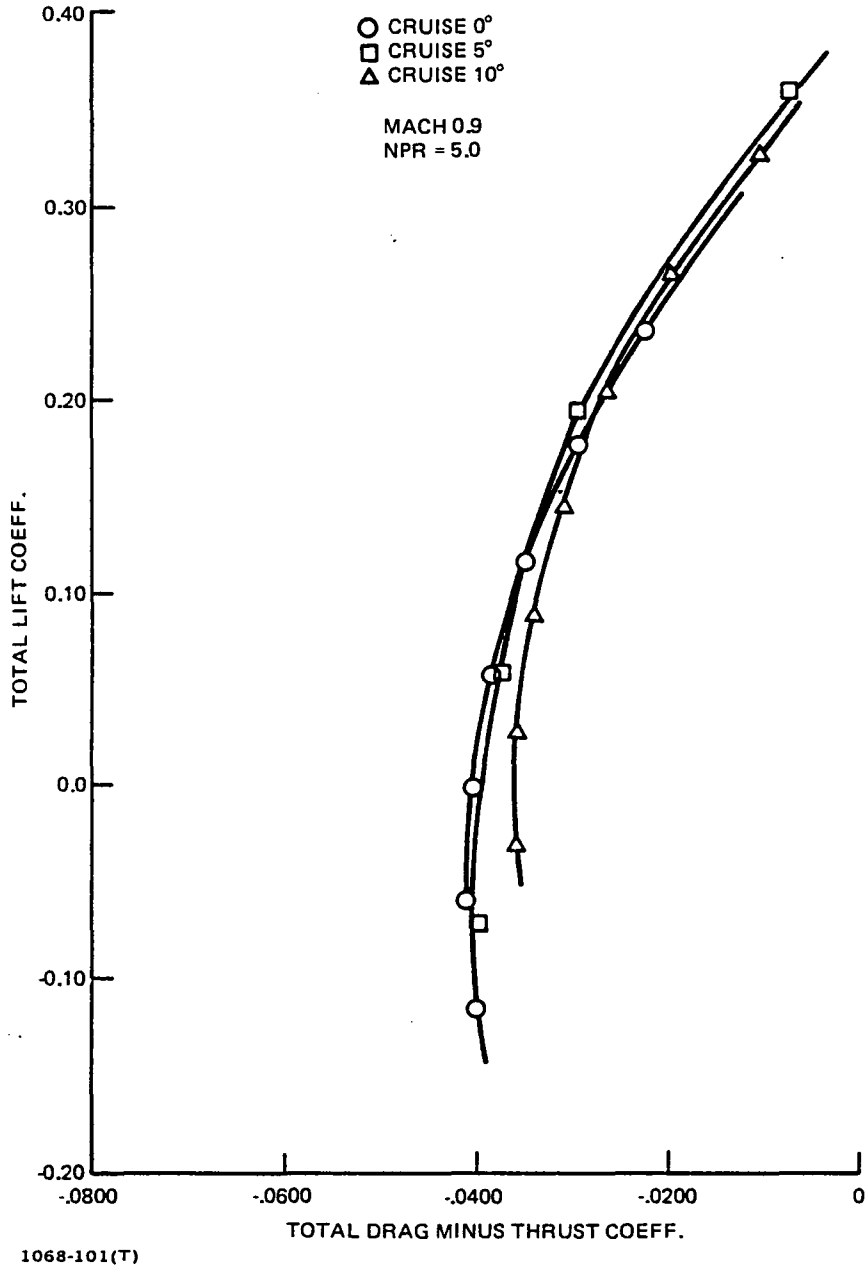

Figure 101 Effect of ADEN Cruise Vectoring on Powered Polar

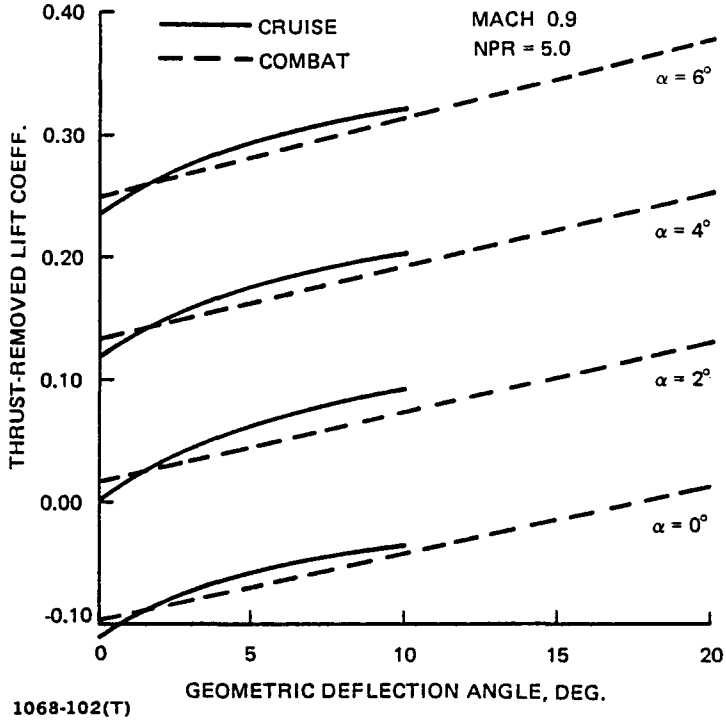

Figure 102 Effect of ADEN Vectoring on Lift

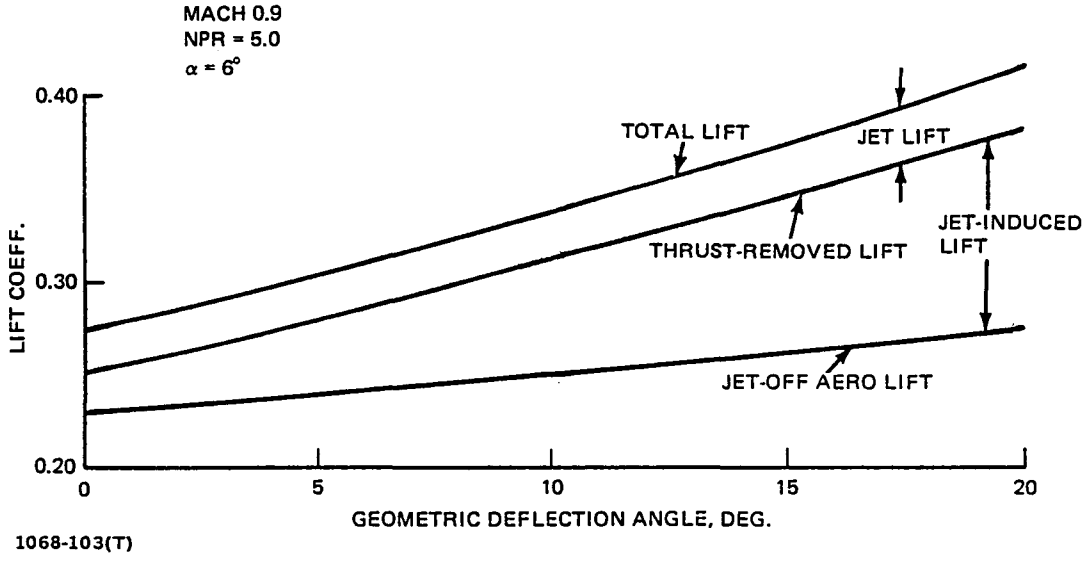

Figure 103 ADEN Combat Lift Component Build-up

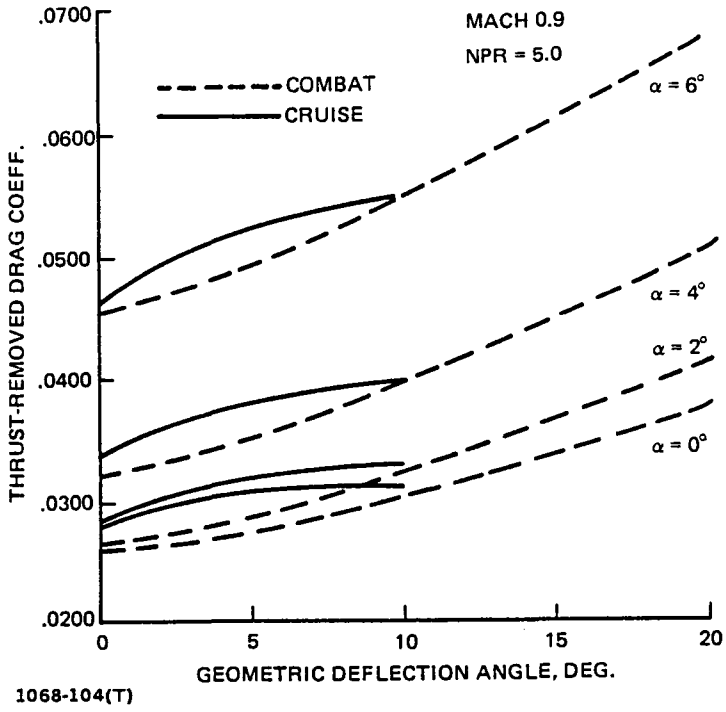

Figure 104 Effect of ADEN Vectoring on Drag

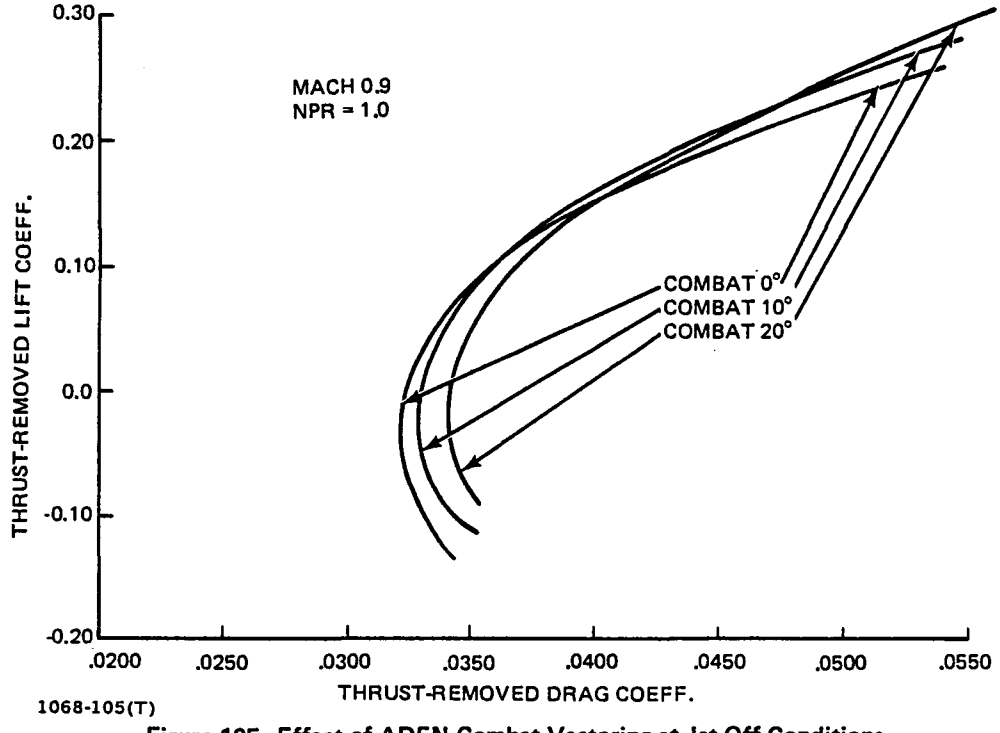

Figure 105 Effect of ADEN Combat Vectoring at Jet-Off Conditions

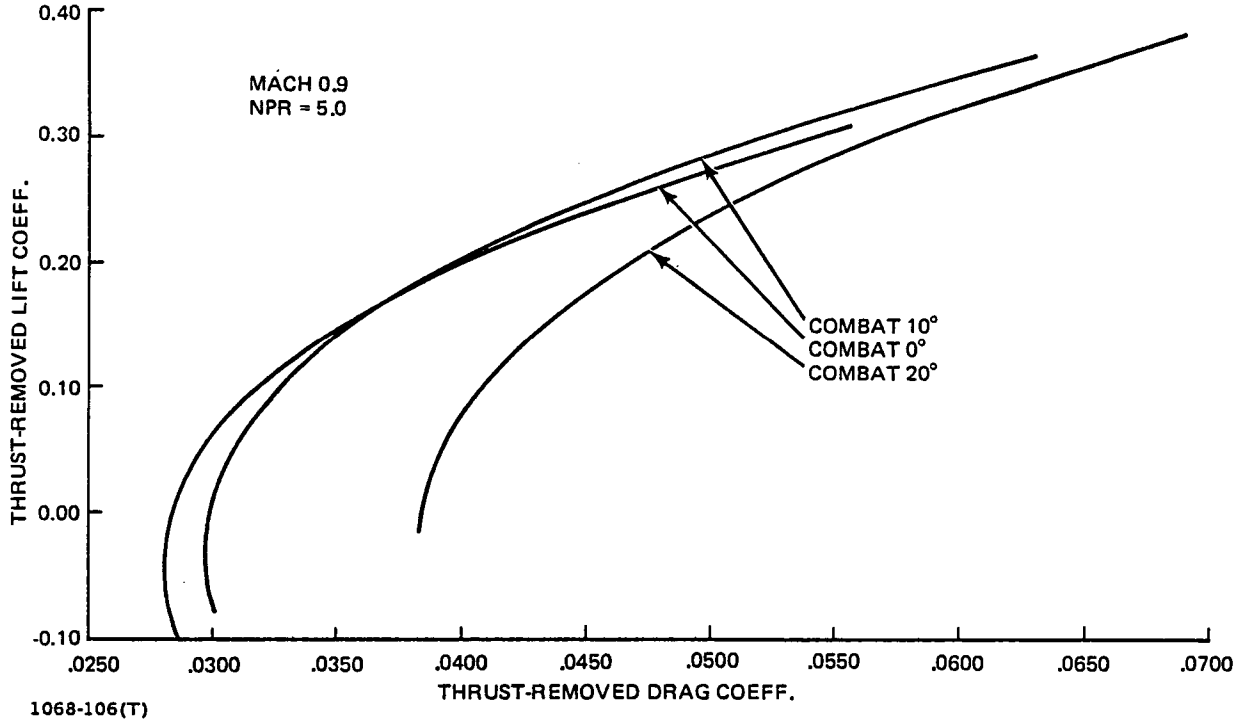

Figure 106 Effect of ADEN Combat Vectoring at Mach 0.9

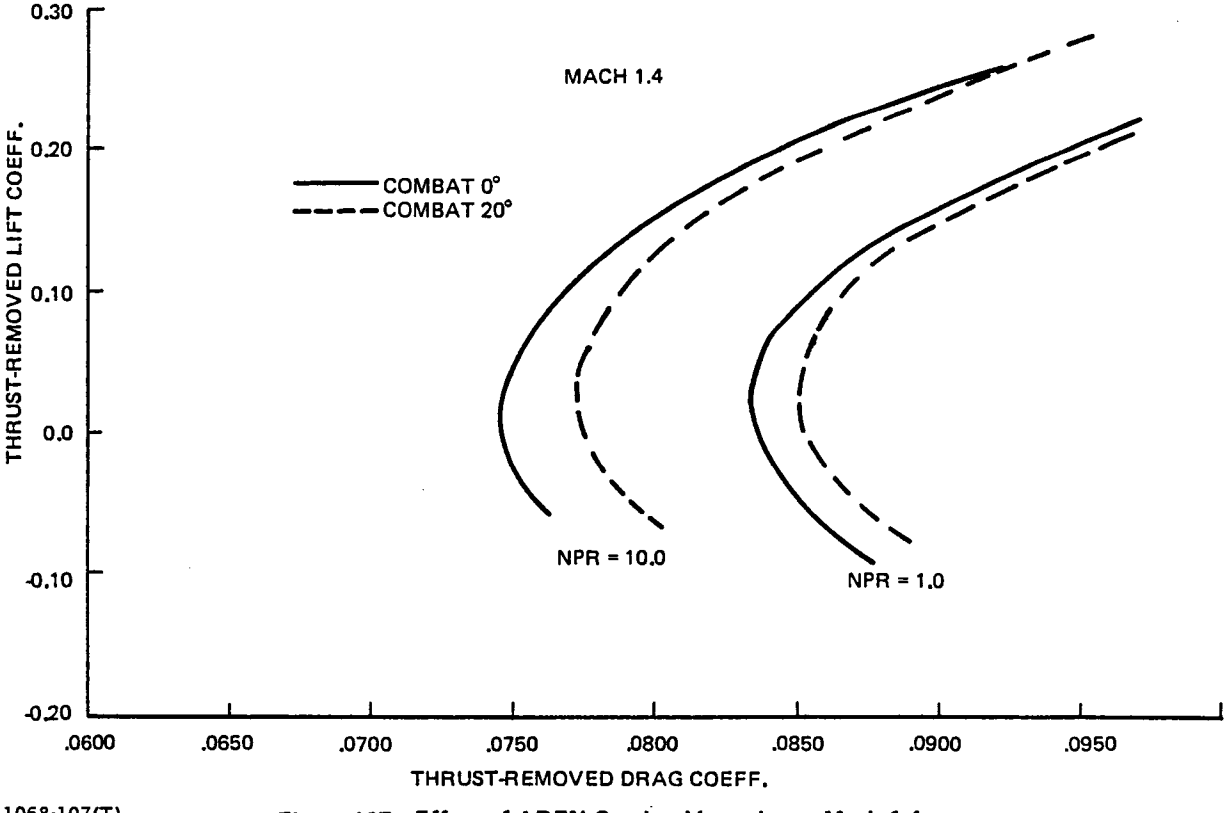

Figure 107 Effect of ADEN Combat Vectoring at Mach 1.4

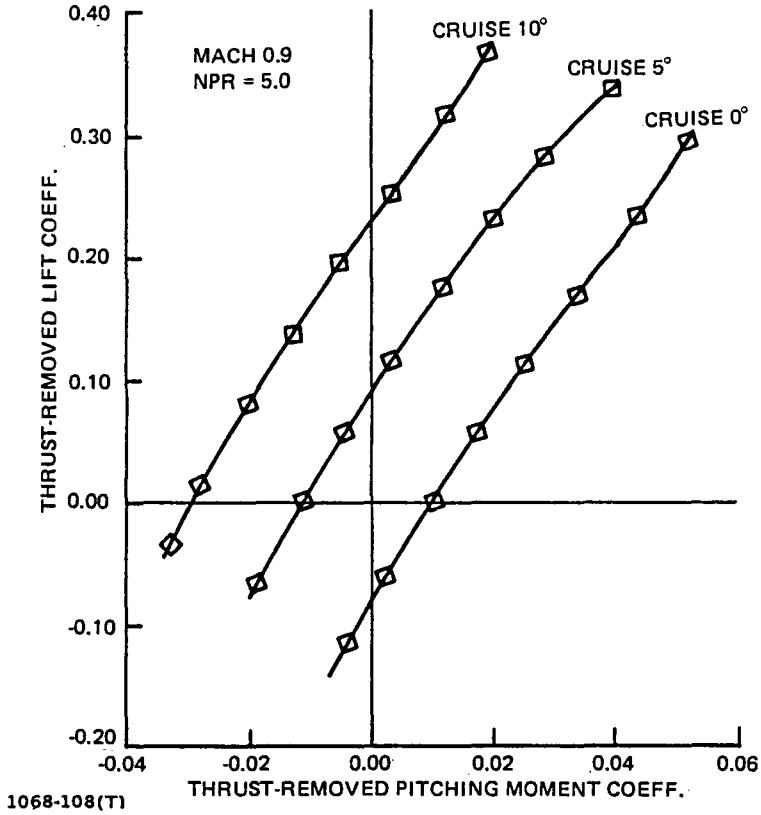

Figure 108 Effect of ADEN Cruise Vectoring on Pitching Moment

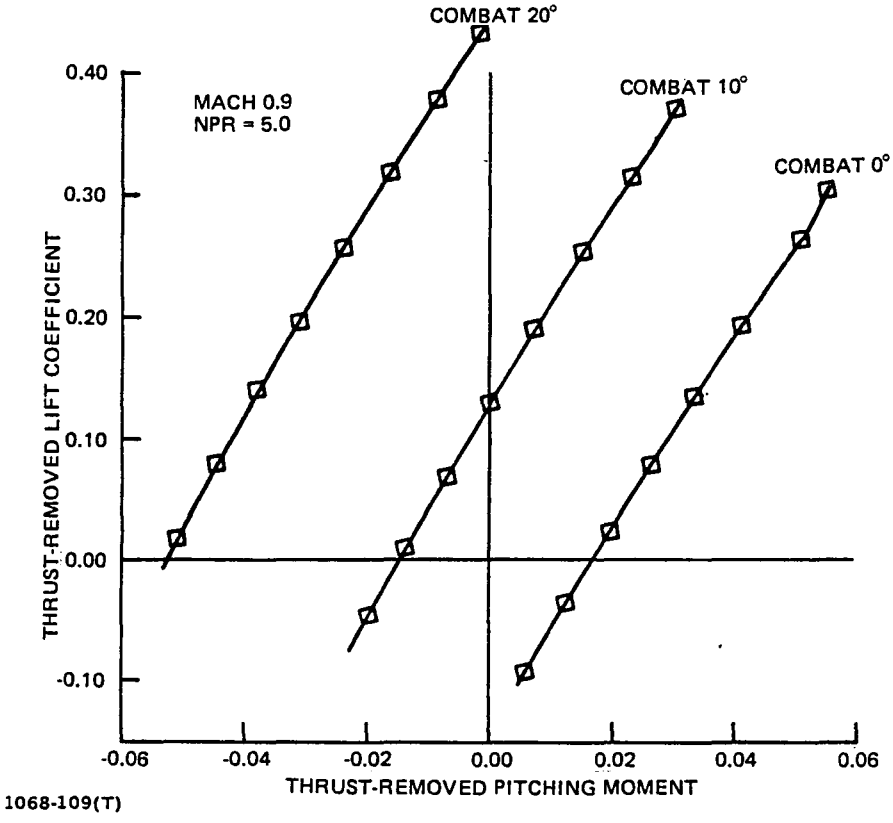

Figure 109 Effect of ADEN Combat Vectoring on Pitching Moment

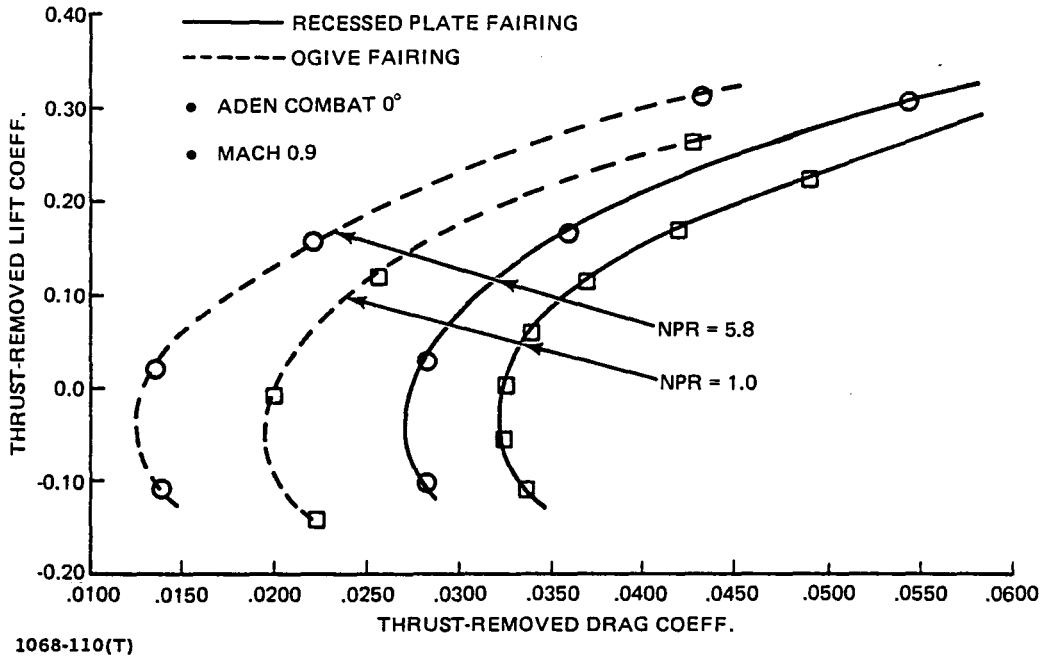

Figure 110 Effect of Inlet Fairing at Mach 0.9

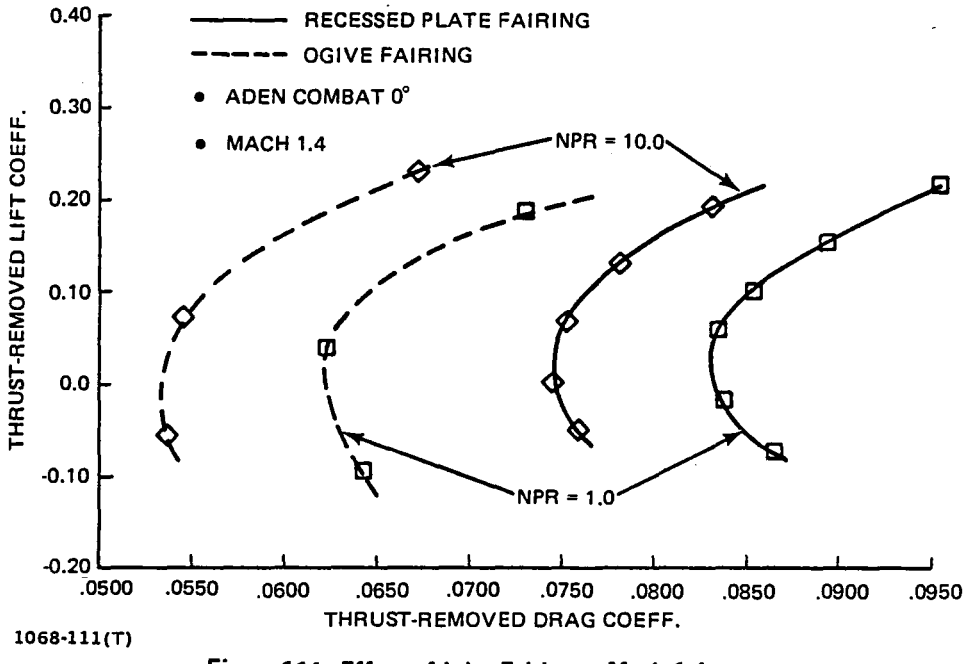

Figure 111 Effect of Inlet Fairing at Mach 1.4

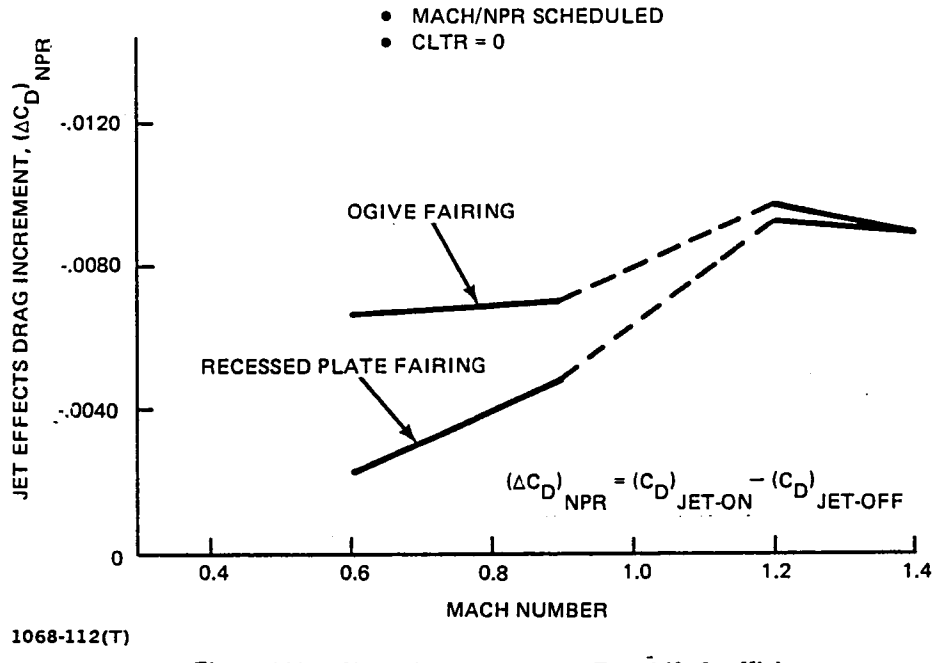

Figure 112 Effect of Inlet Fairing at Zero Lift Coefficient

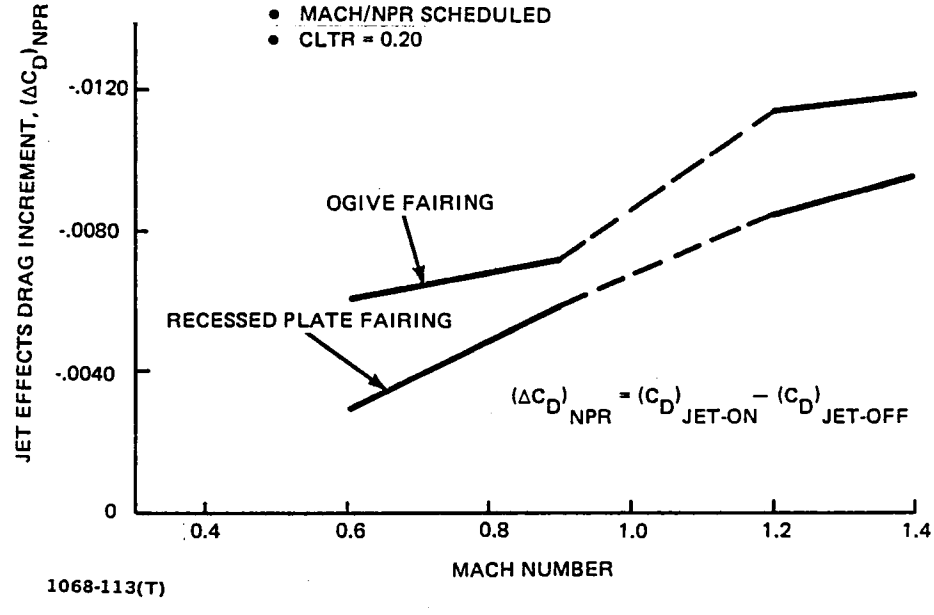

Figure 113 Effect of Inlet Fairing at 0.20 Lift Coefficient

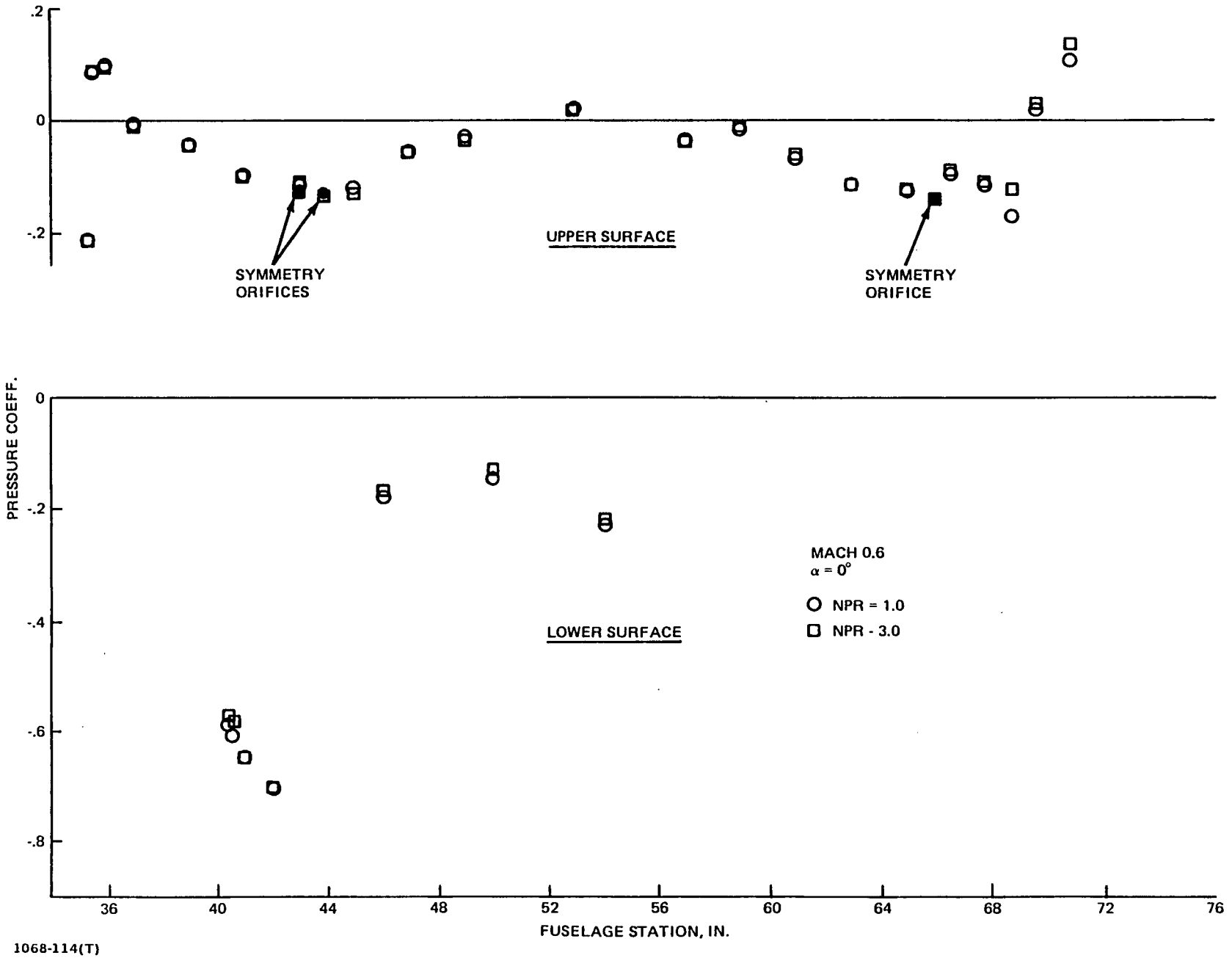

Figure 114 Jet Effects in Presence of Recessed Plate Fairing

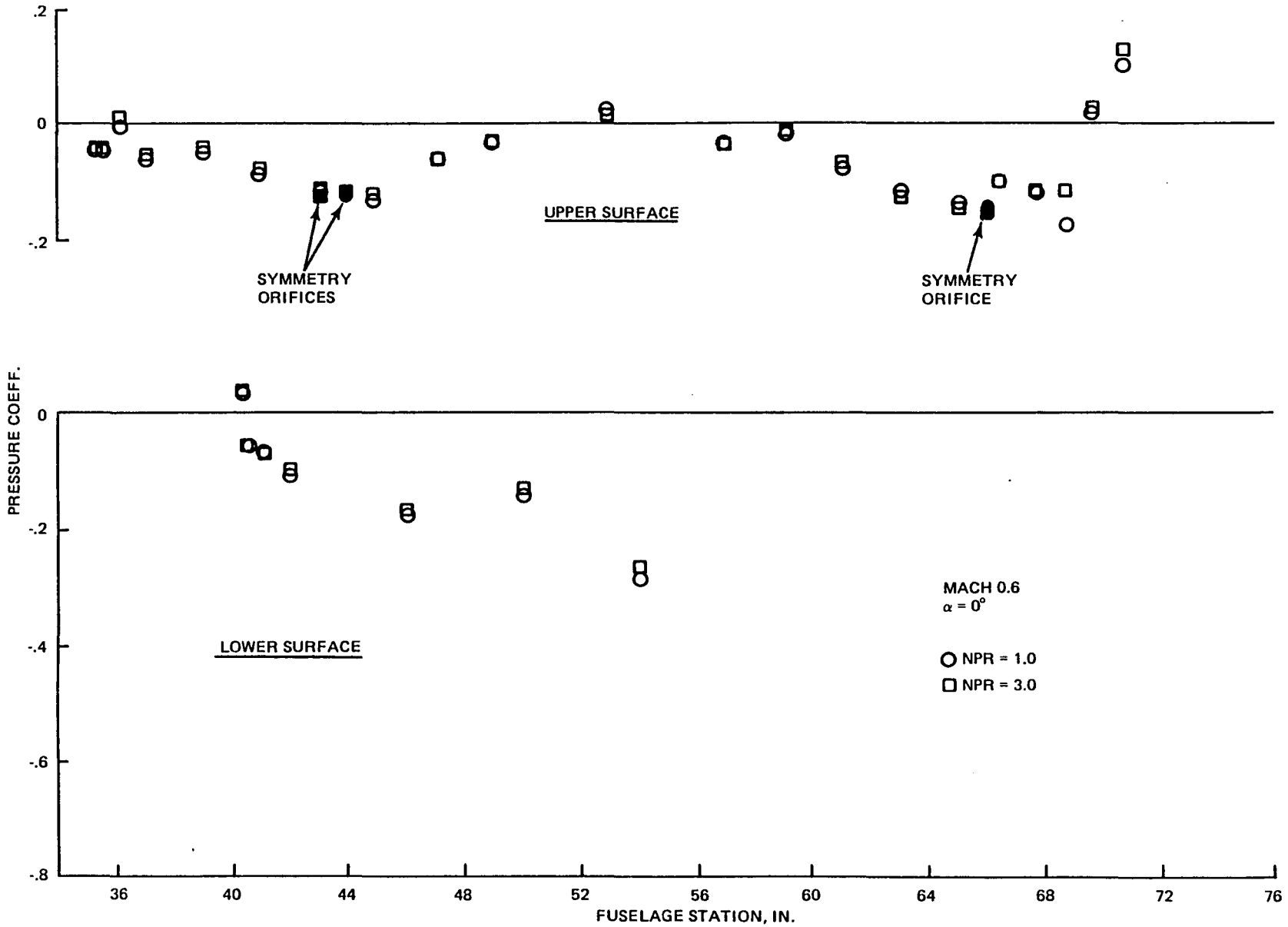

Figure 115 Jet Effects in Presence of Ogive Fairing

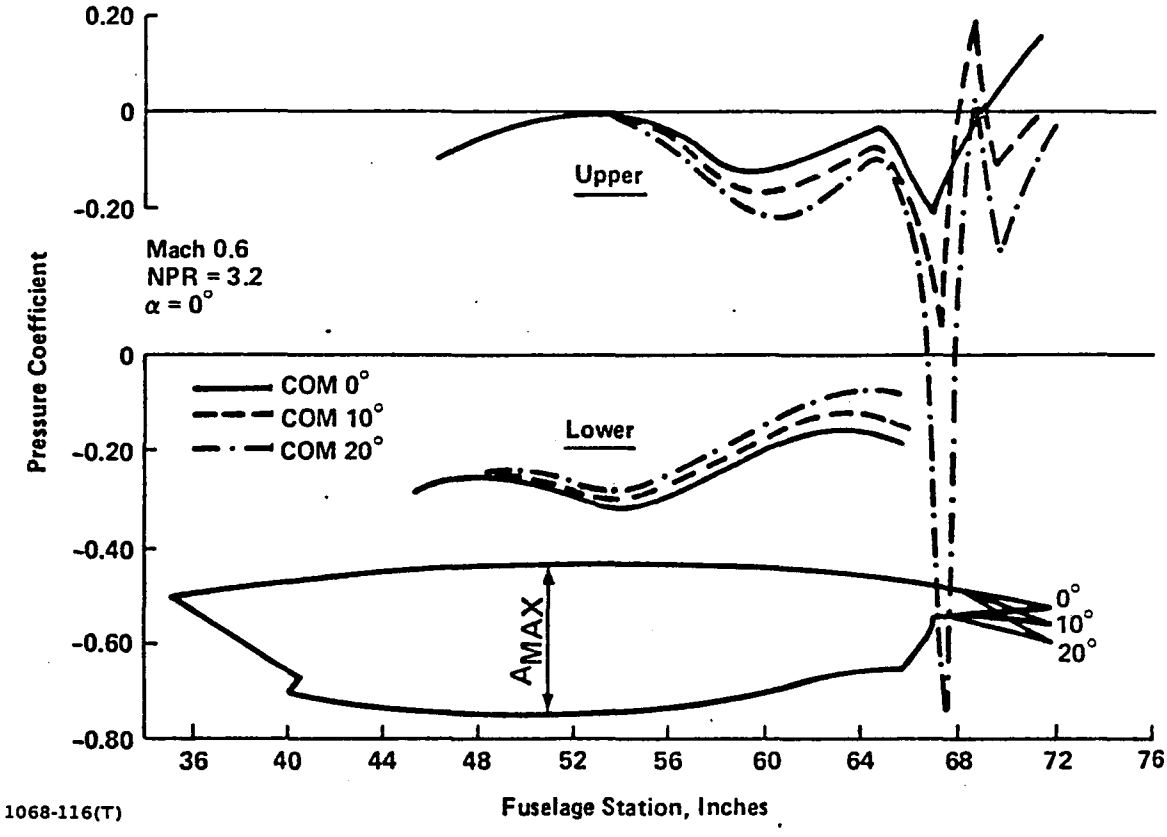

Figure 116 Effect of Vectoring on Nacelle Pressures – ADEN Combat Configurations

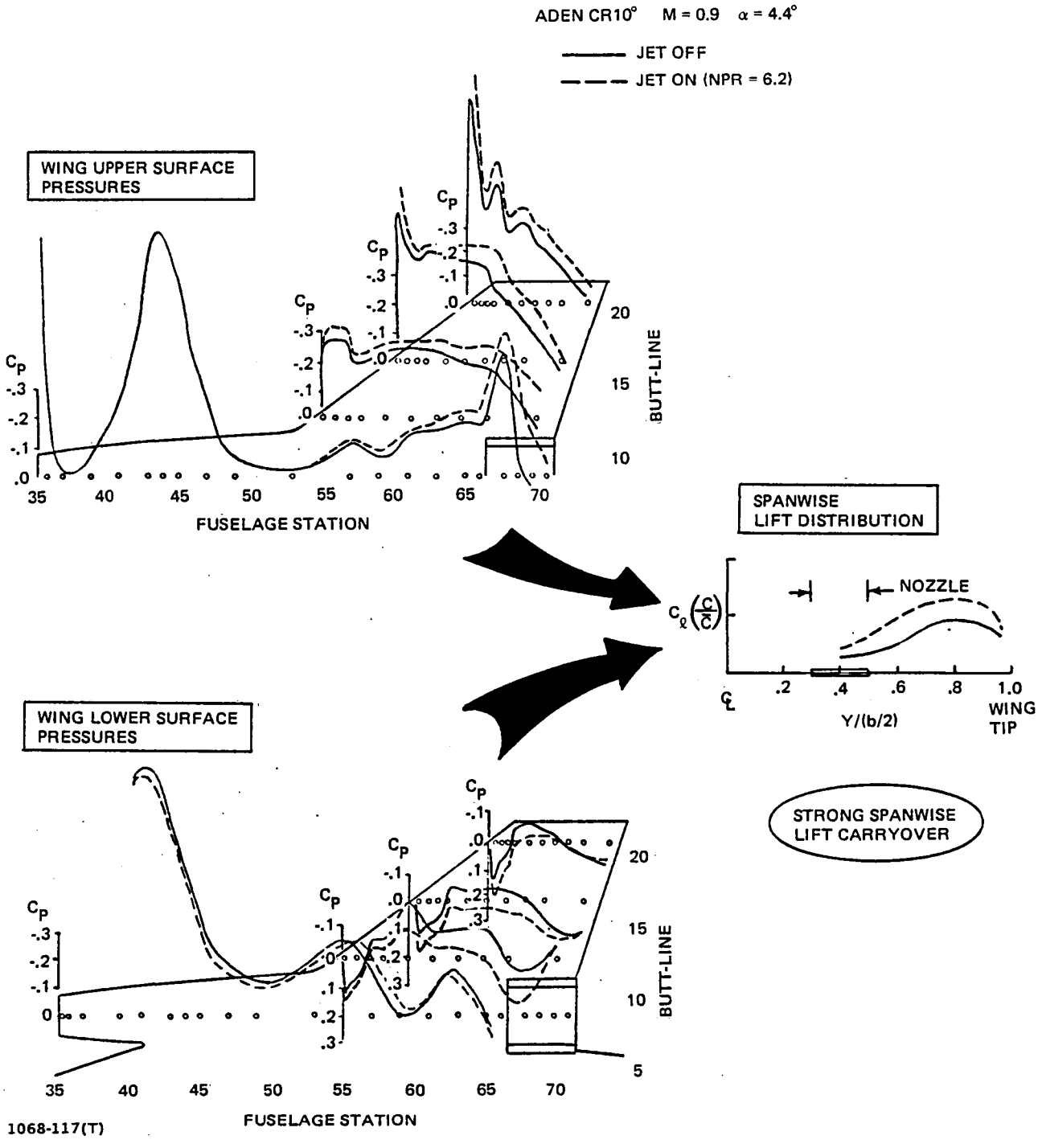

Figure 117 Thrust Vectoring Lift Enhancement Mechanisms

JET OFF (NPR = 1.0)

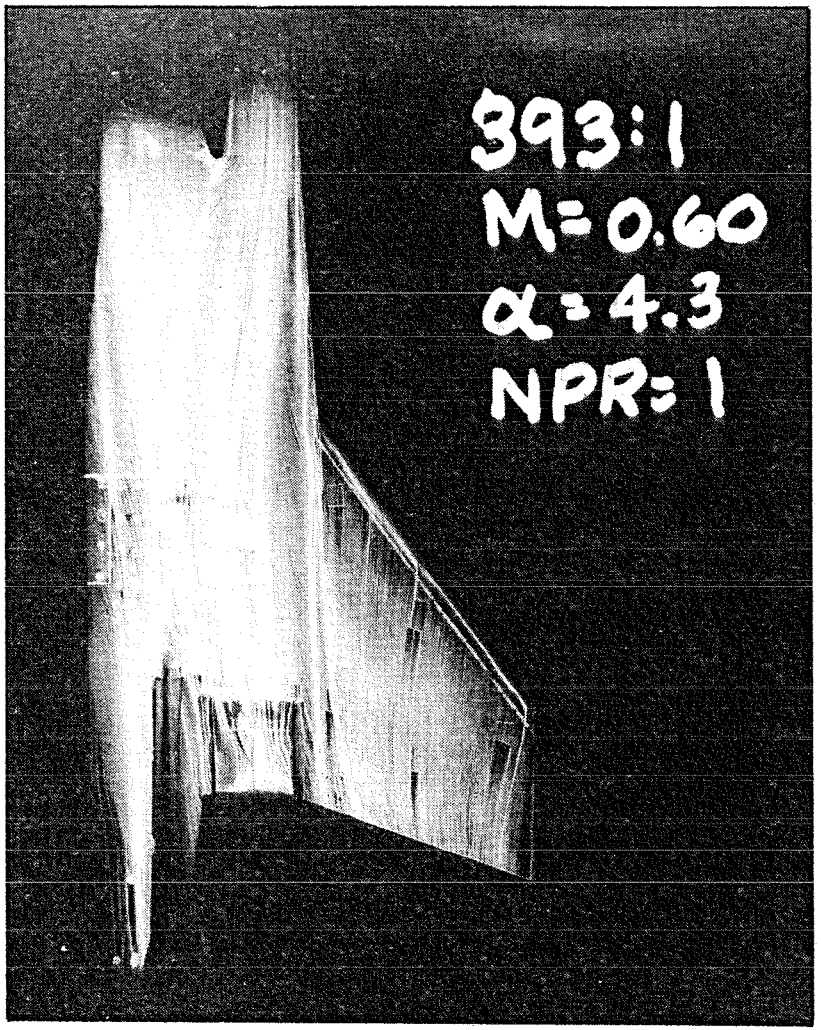

- SEPARATED FLOW OVER ADEN VEER
- STRONG WING TRAILING EDGE SPANWISE FLOW GRADIENT

JET ON (NPR = 5.4)

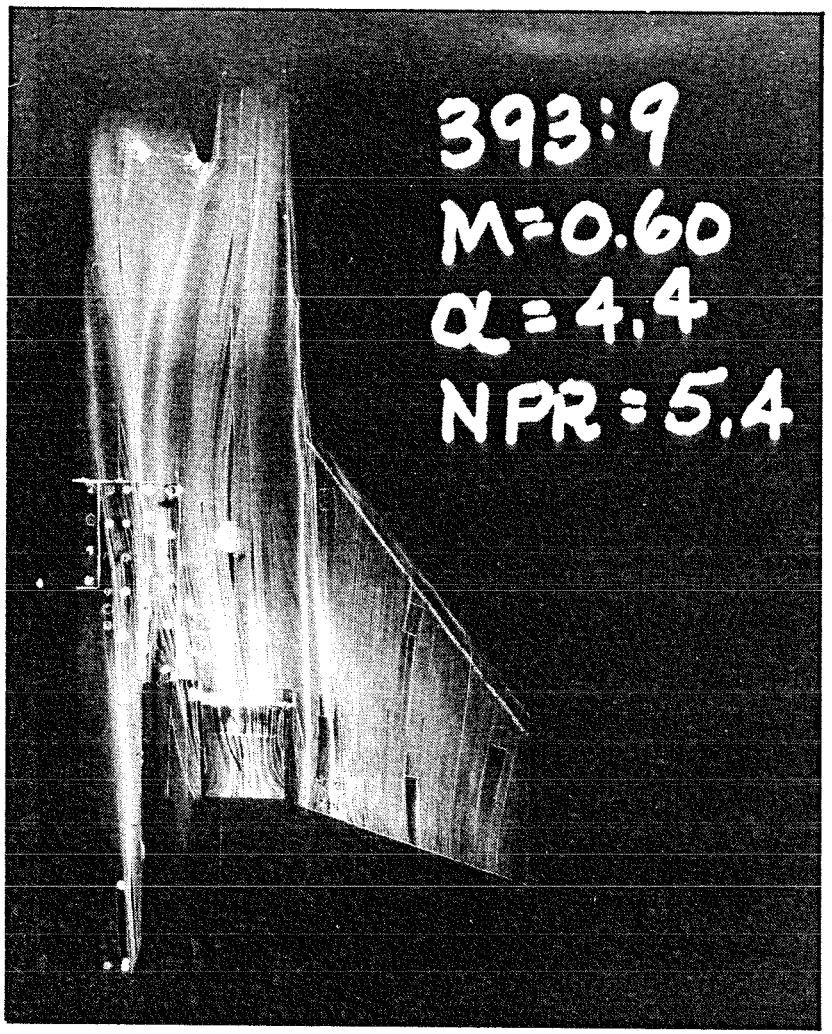

- REATTACHED FLOW OVER ADEN VEER
- WING TRAILING EDGE FLOW TURNED TO STREAMWISE DIRECTION

1068-118(T)

Figure 118 Oil Flow Results for ADEN Cruise 10°, M = 0.9, α = 4.5°

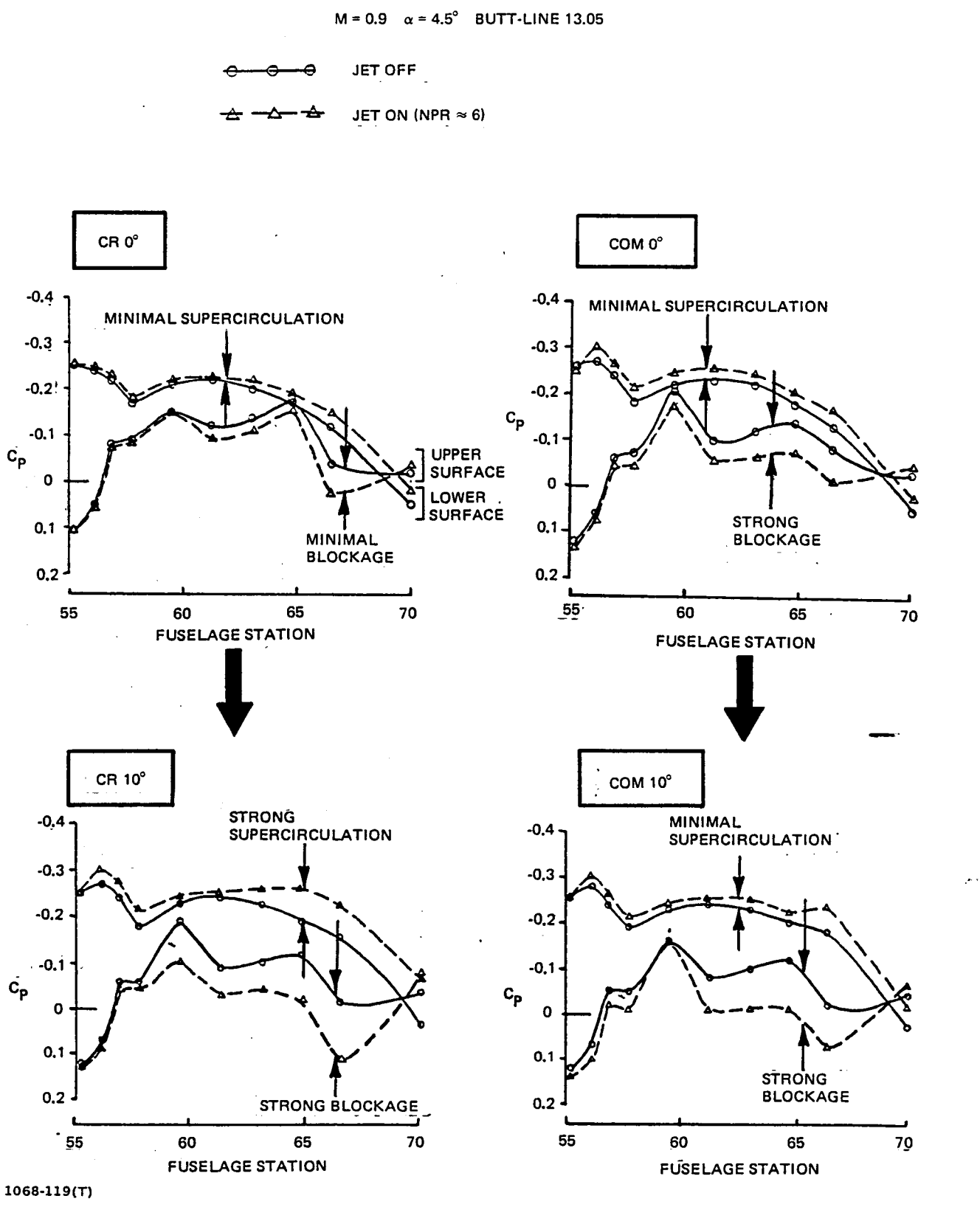

Figure 119 Pressure Distribution Comparison: ADEN Cruise/Combat

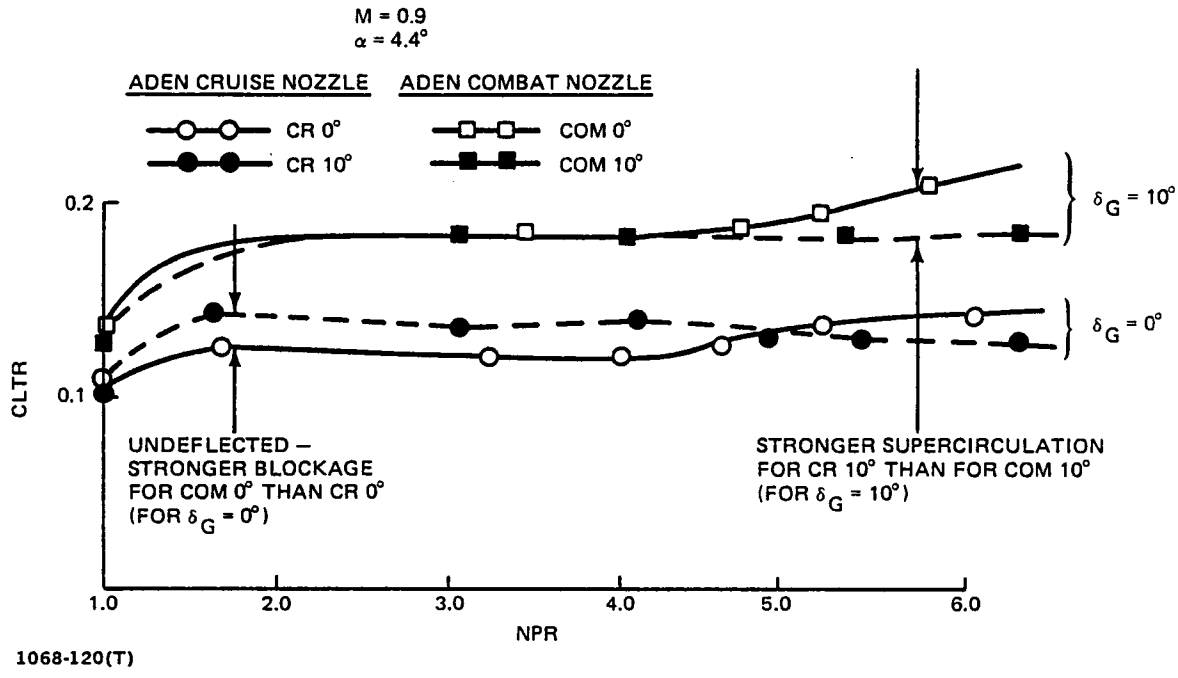

Figure 120 Thrust-Removed Lift Comparison: ADEN Cruise/Combat

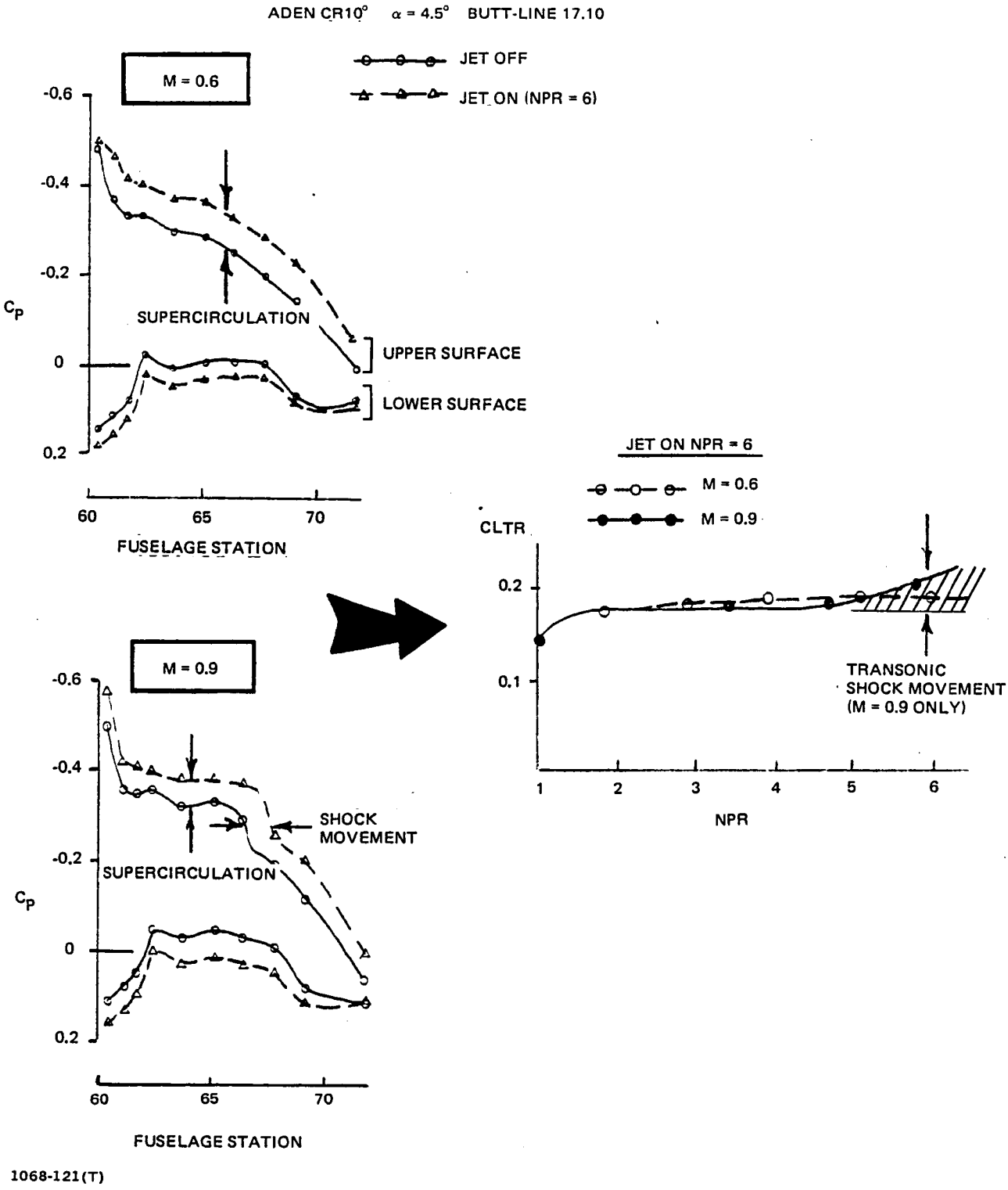

Figure 121 Transonic Shock Movement Effect on ADEN Cruise 10°

MACH	CR 0°		CR 10°		COM 0°		COM 10°	
	0.6	0.9	0.6	0.9	0.6	0.9	0.6	0.9
BLOCKAGE	1	1	2	2	2	2	2	2
SUPERCIRCULATION	1	1	2	2	1	1	1	1
SHOCK MOVEMENT	0	1	0	2	0	1	0	1

0 . . . . NO EFFECT
1 . . . . LIMITED EFFECT IF ANY
2 . . . . EFFECTIVE

1068-122(T)

Figure 122 Lift Enhancement Mechanism Comparison: ADEN Cruise/Combat

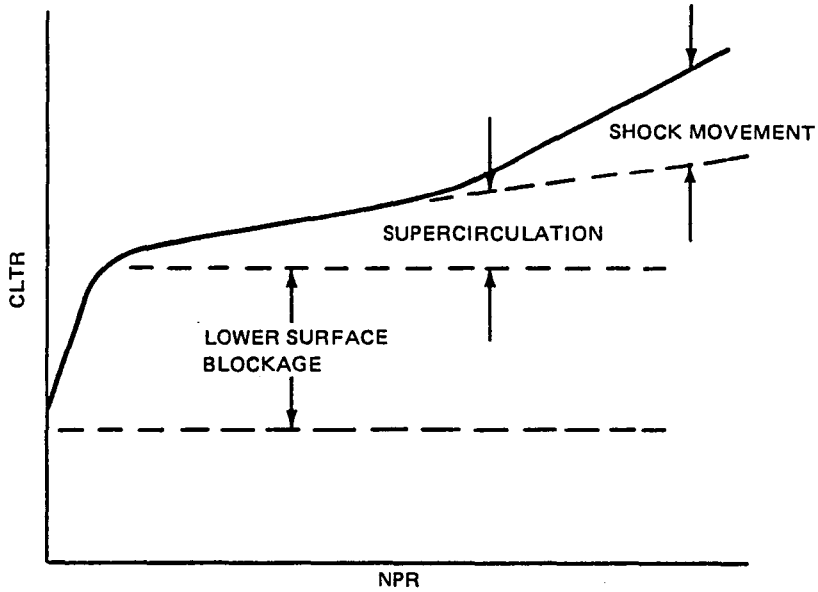

1068-123(T)

Figure 123 Lift Enhancement Mechanism Model

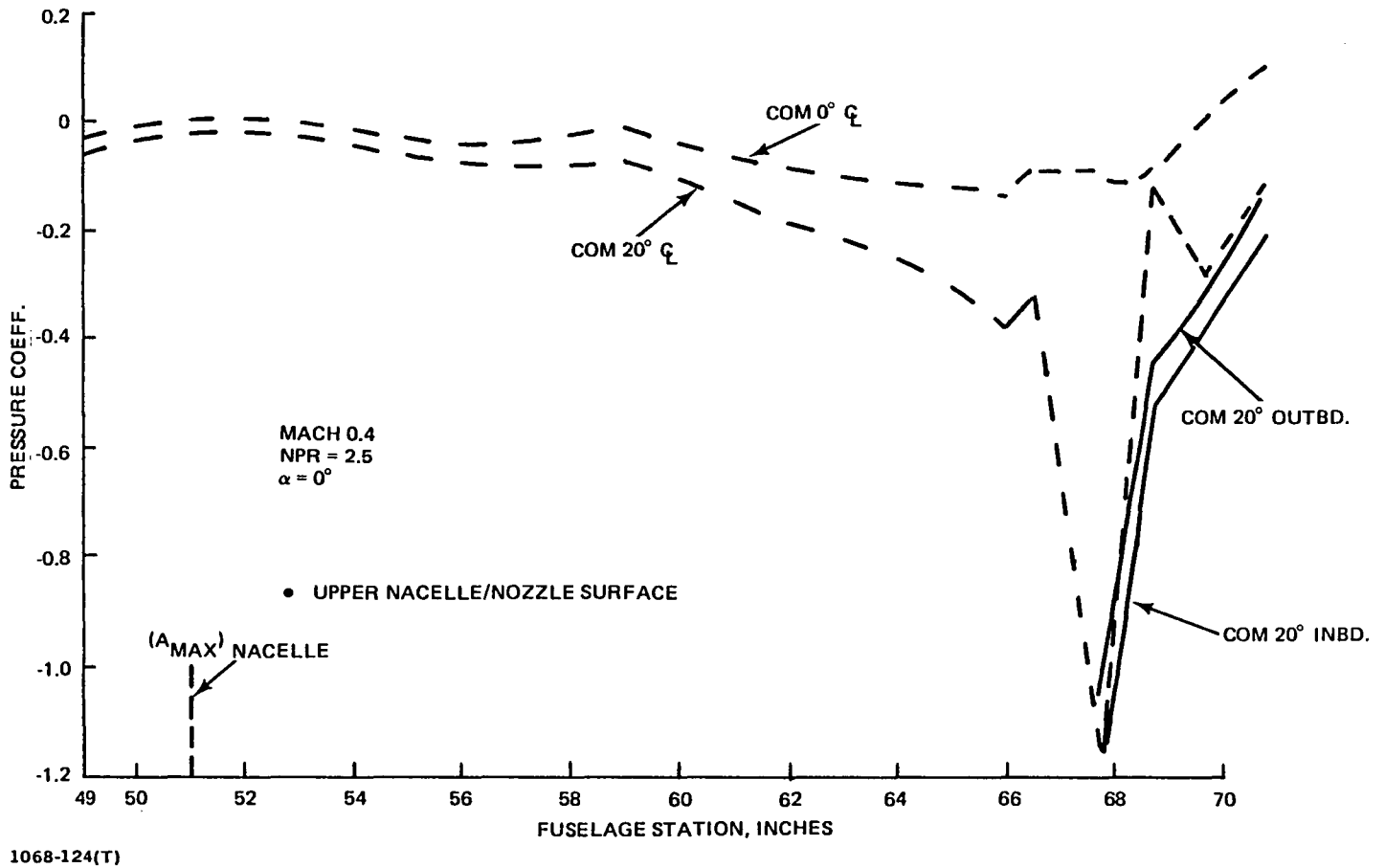

Figure 124 Effect of Span on VEER Pressures at Mach 0.4

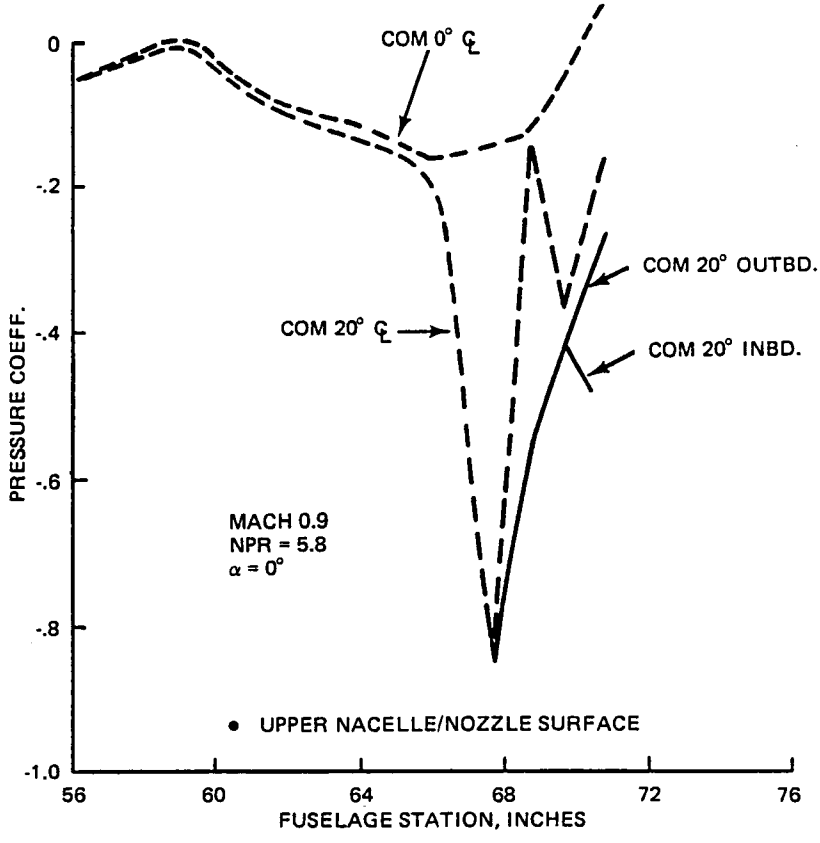

1068-125(T)

Figure 125 Effect of Span on VEER Pressures at Mach 0.9

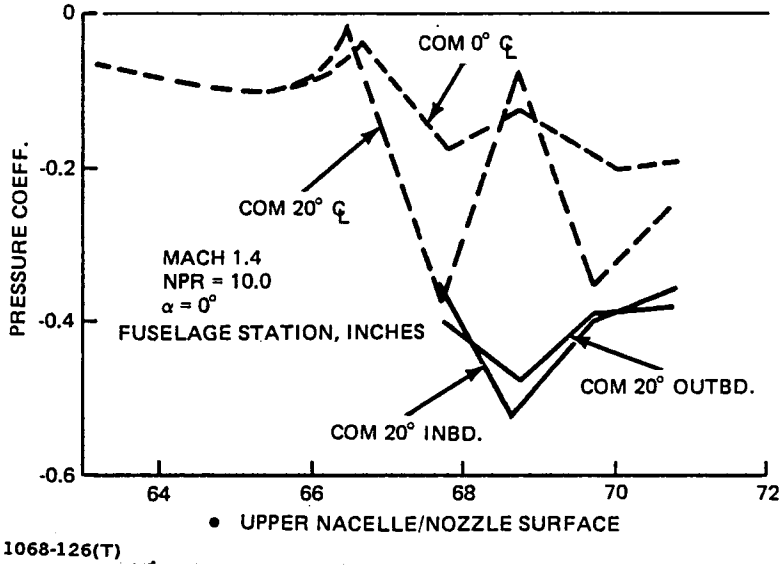

Figure 126 Effect of Span on VEER Pressures at Mach 1.4

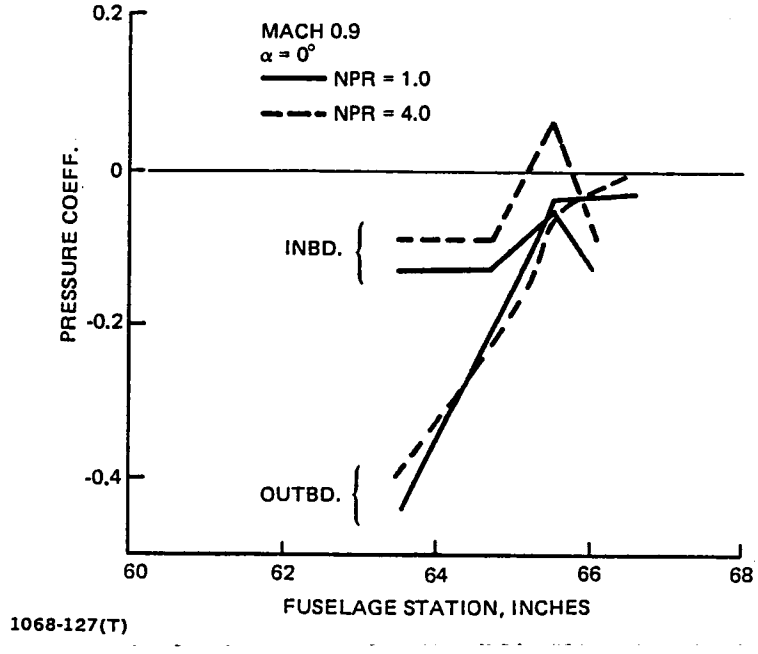

Figure 127 Effect of Pressure Ratio on ADEN Sidewall Pressures

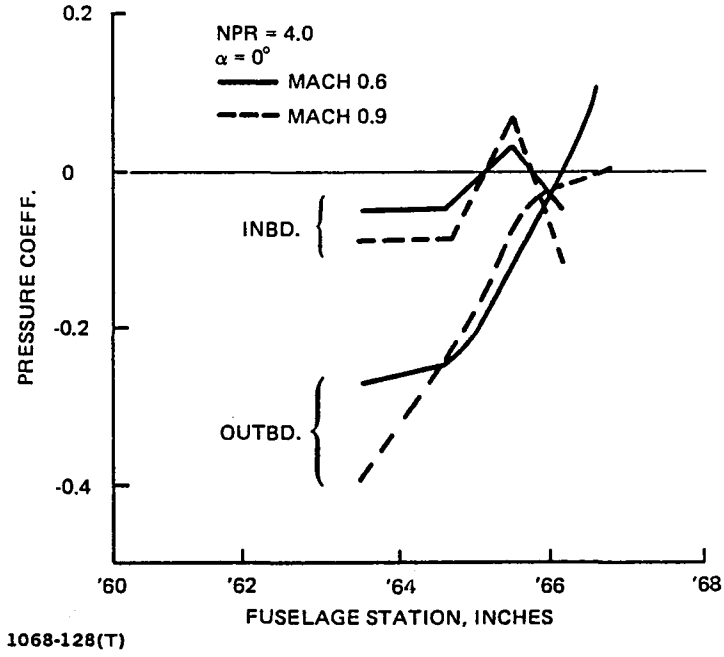

1068-128(T)

Figure 128 Effect of Mach on ADEN Sidewall Pressures

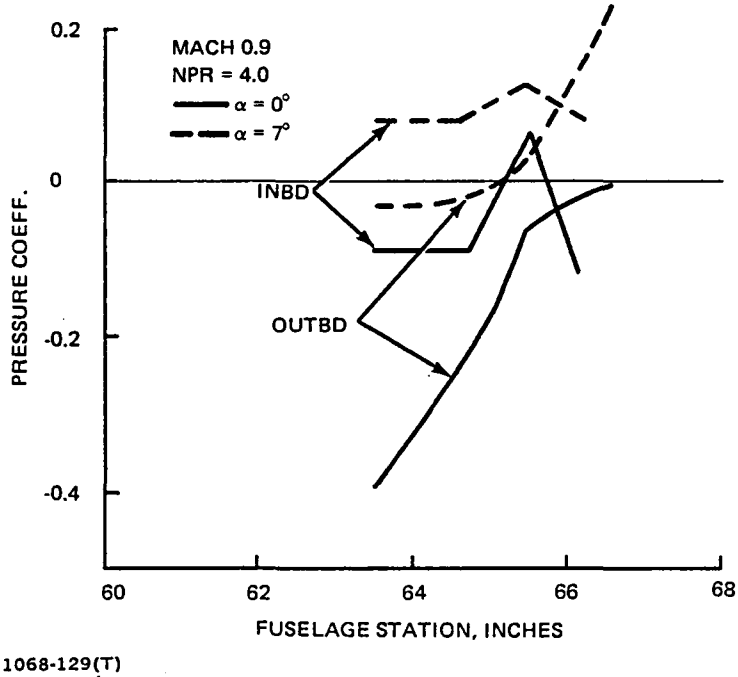

1068-129(T)

Figure 129 Effect of Attitude on ADEN Sidewall Pressures

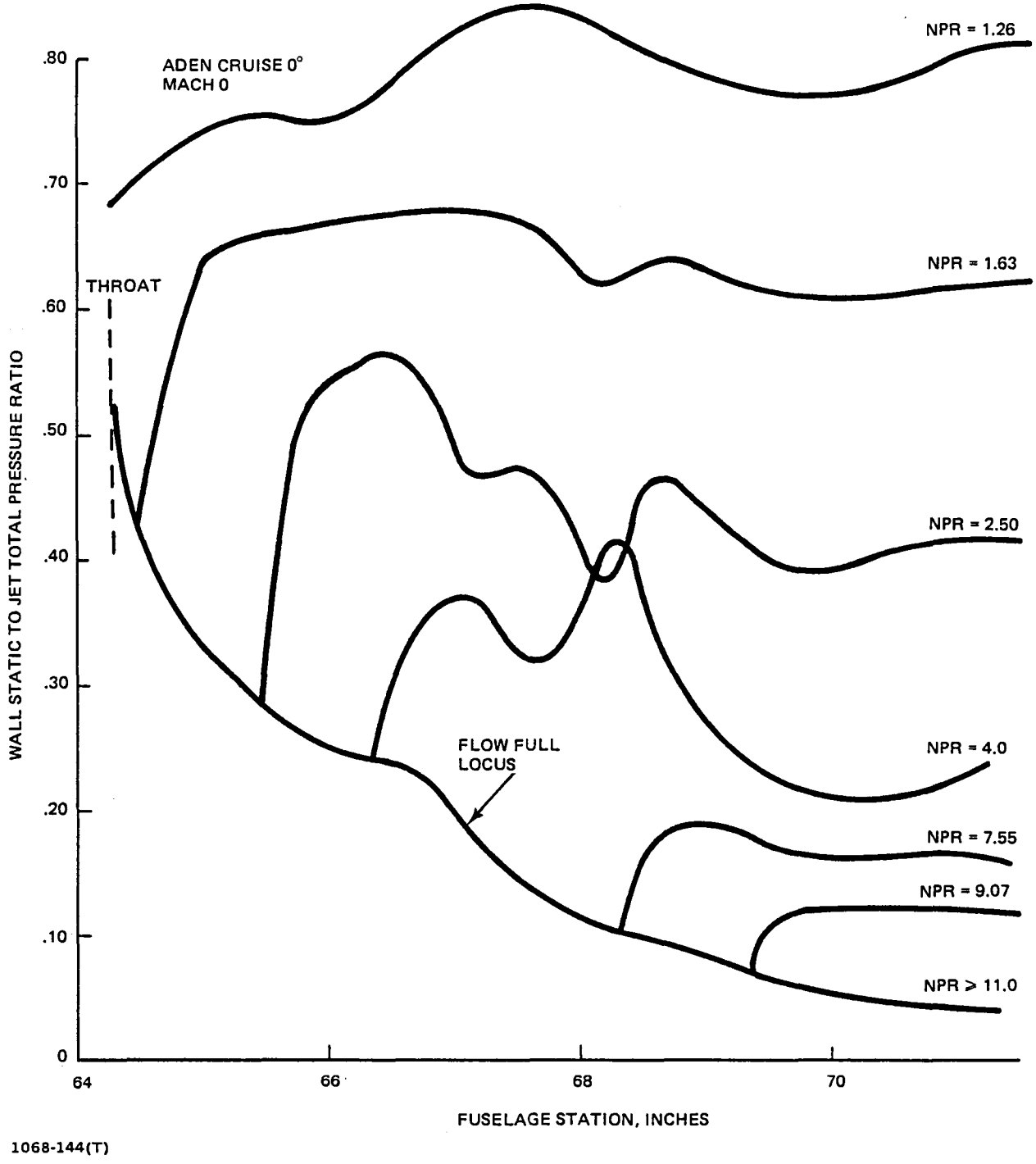

Figure 130 ADEN Cruise 0° VEER Internal Pressure Distribution

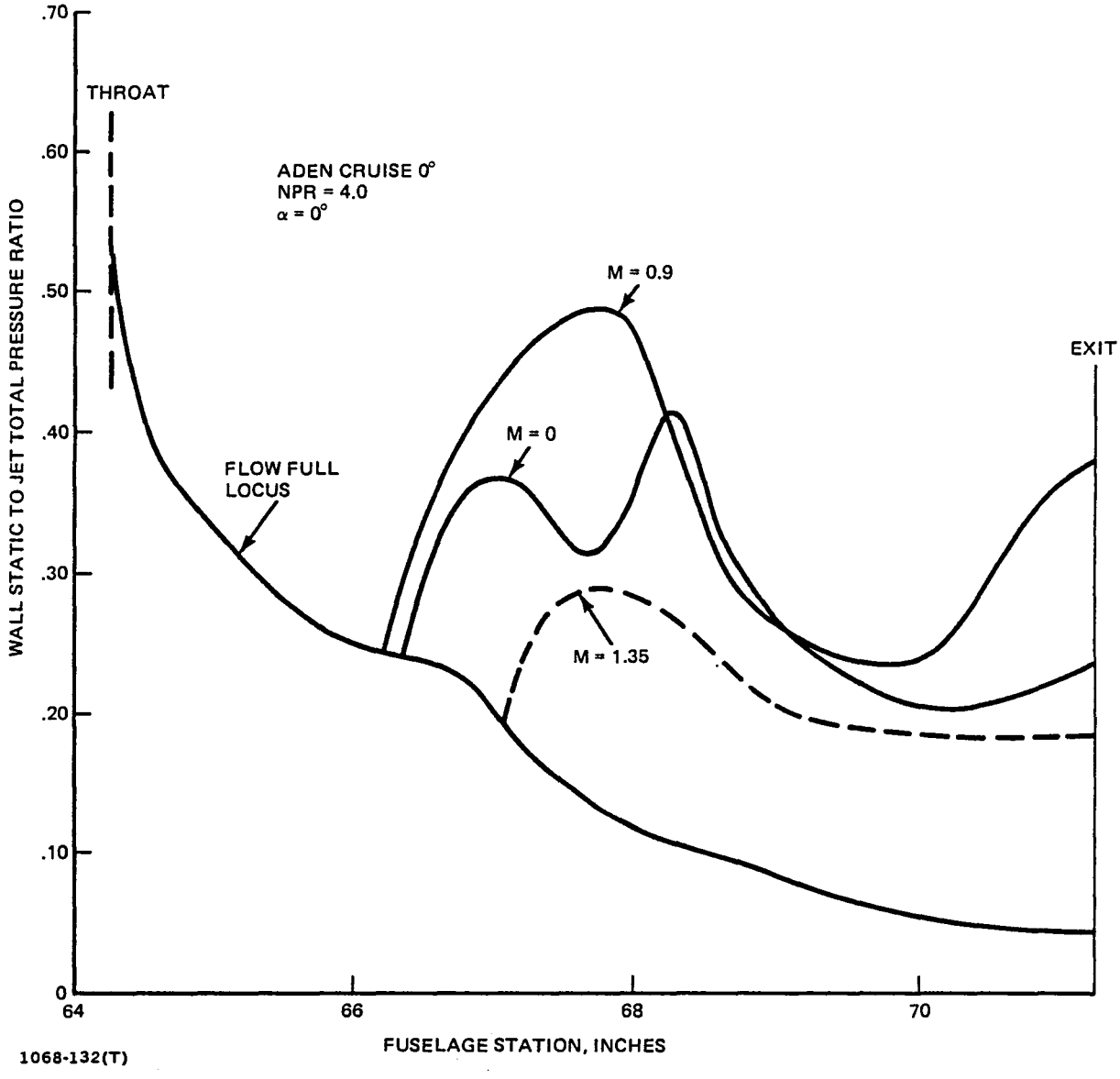

Figure 131 Effect of External Flow on ADEN Cruise 0° VEER Pressure Distribution

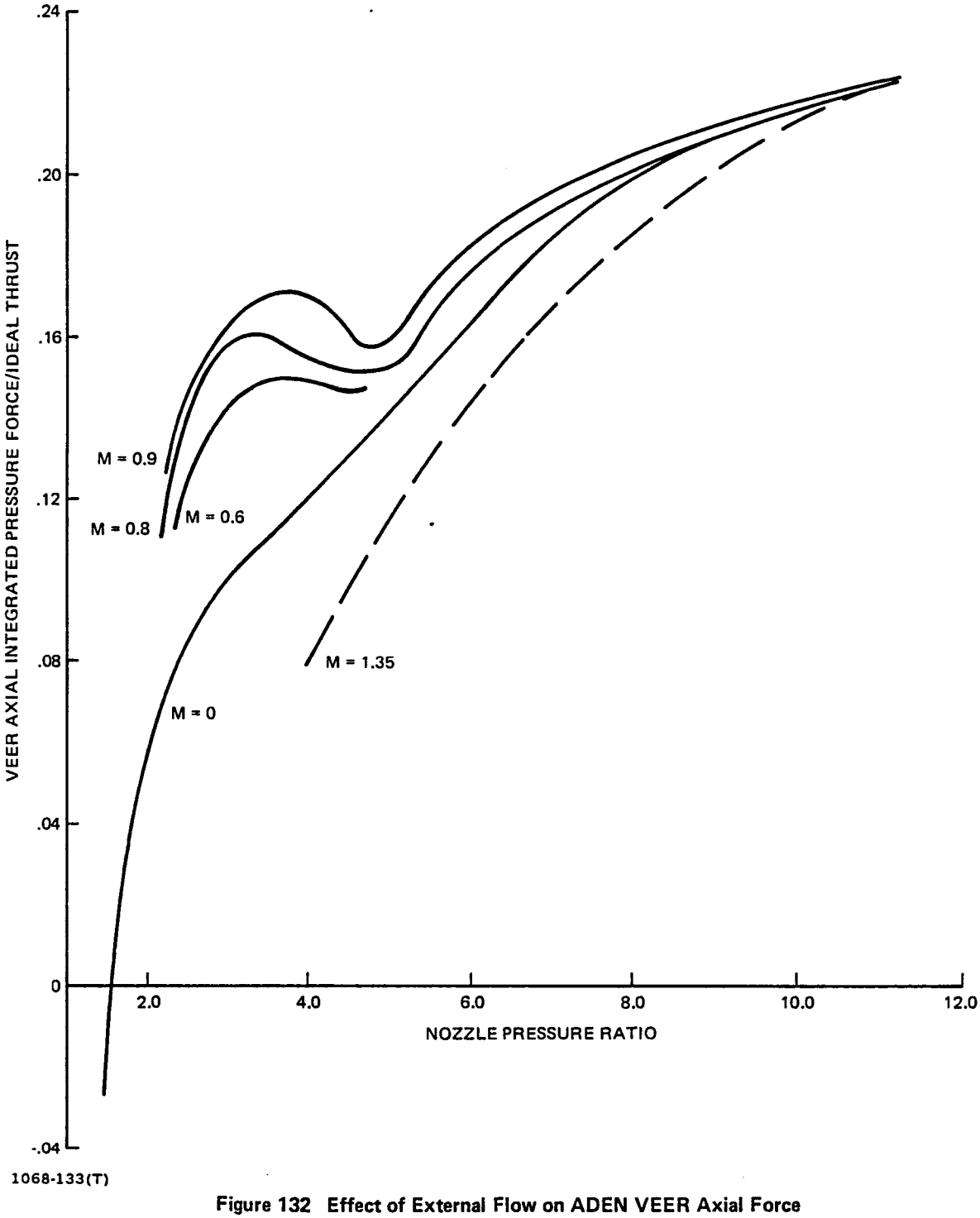

Figure 132 Effect of External Flow on ADEN VEER Axial Force

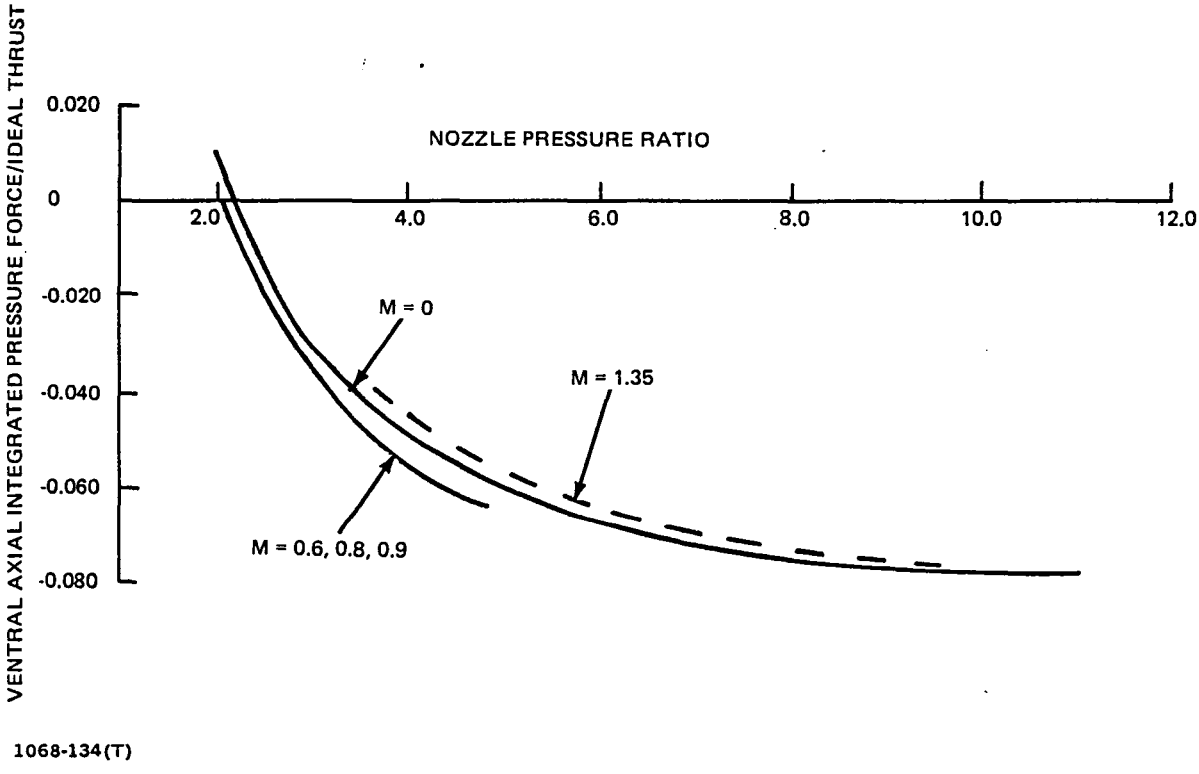

Figure 133 Effect of External Flow on ADEN Ventral Axial Force

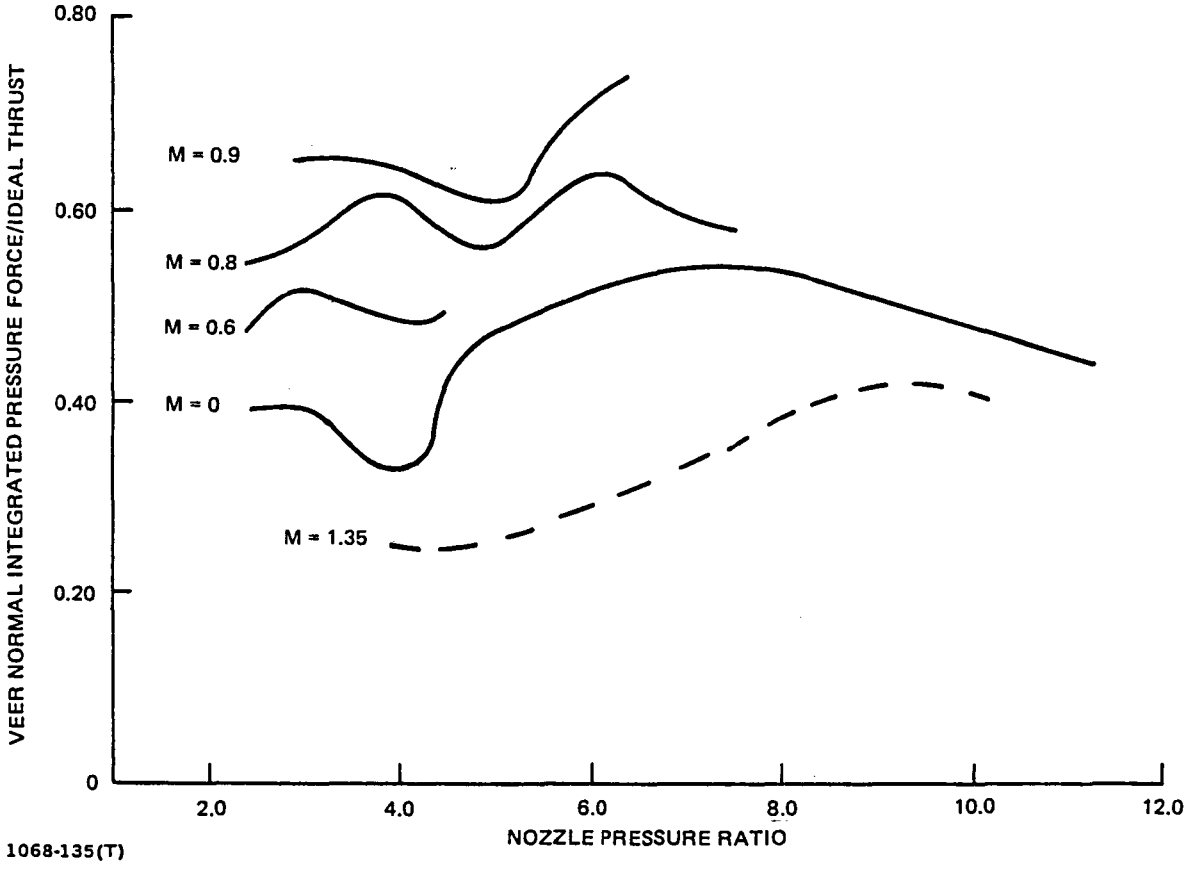

Figure 134 Effect of External Flow on ADEN VEER Normal Force

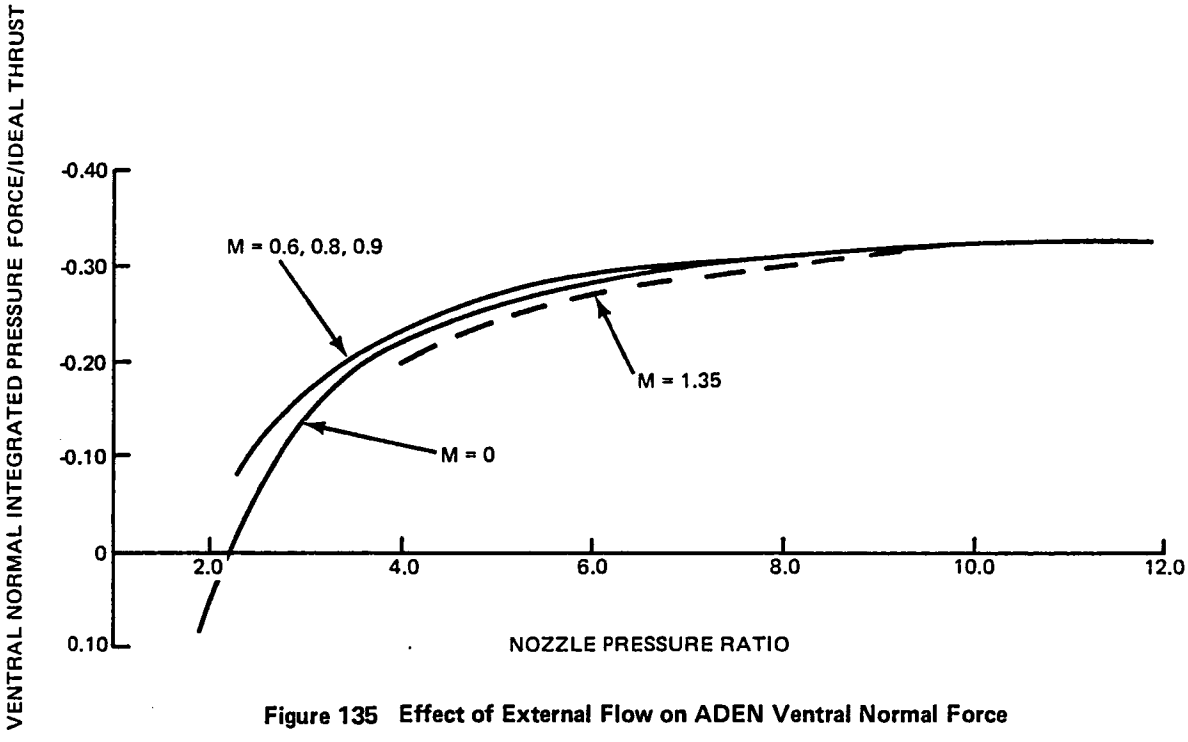

Figure 135 Effect of External Flow on ADEN Ventral Normal Force

1068-136(T)

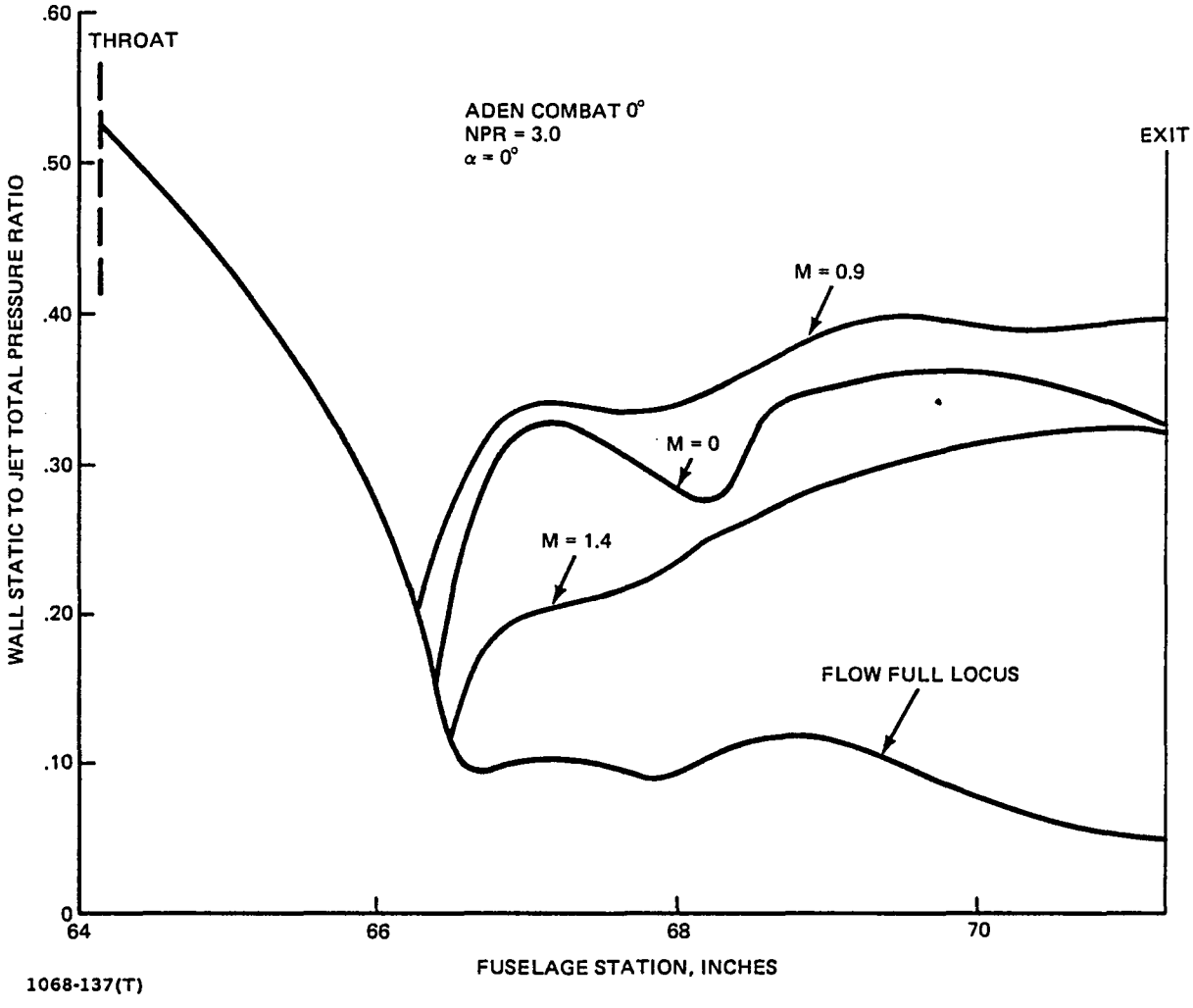

Figure 136 Effect of External Flow on ADEN Combat 0° VEER Pressure Distribution

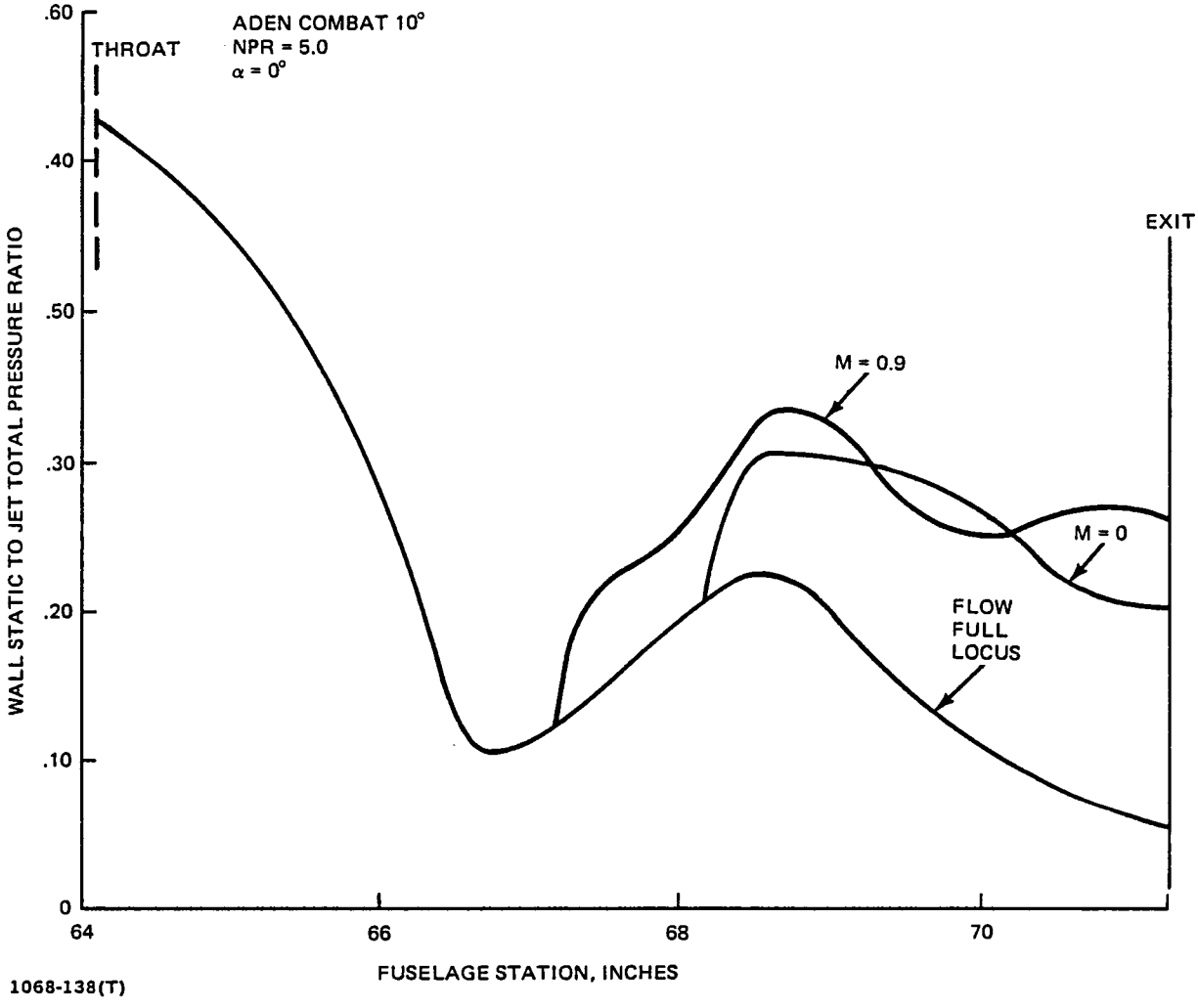

Figure 137 Effect of External Flow on ADEN Combat 10° VEER Pressure Distribution

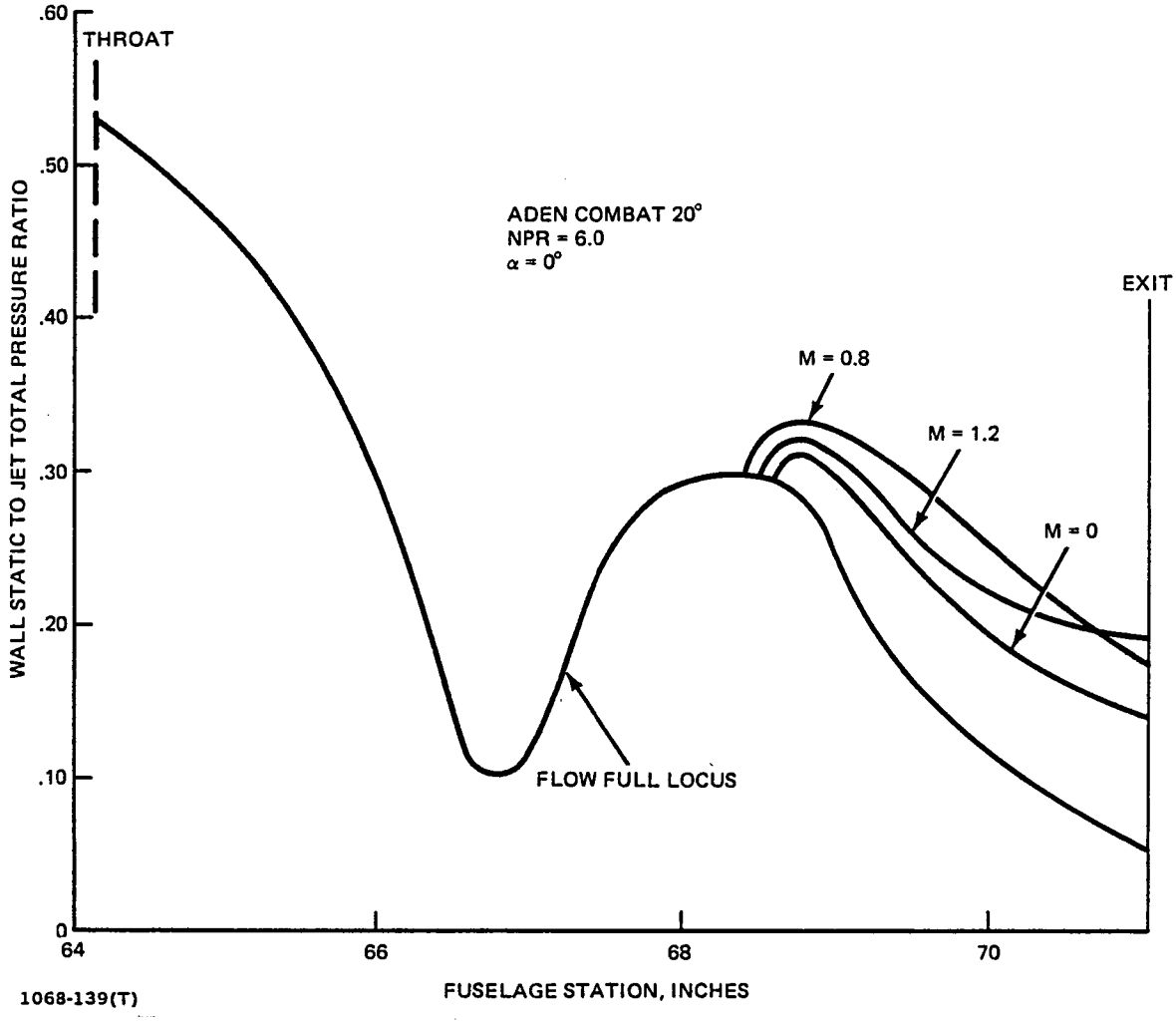

Figure 138. Effect of External Flow on ADEN Combat 20° VEER Pressure Distribution

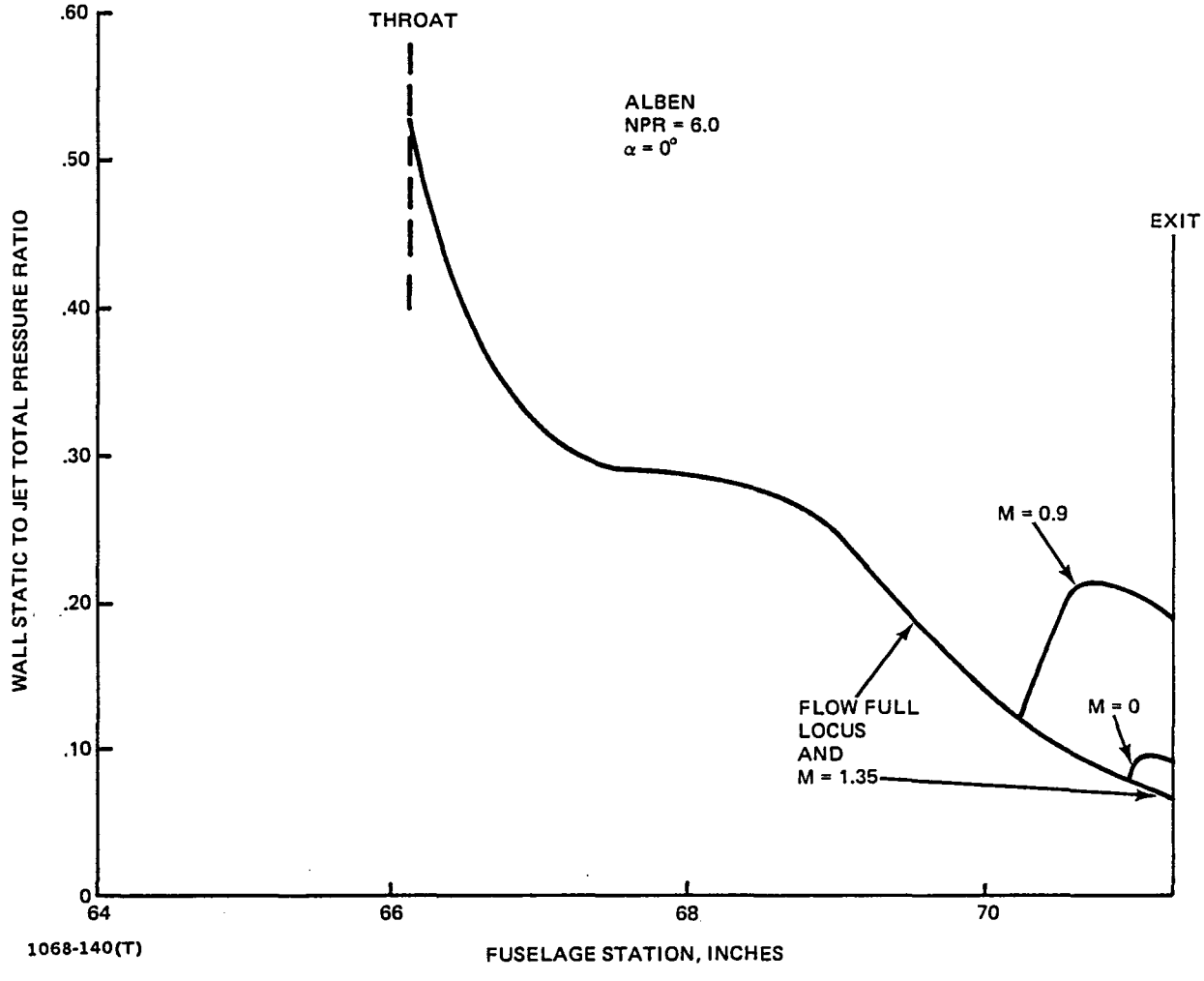

Figure 139 Effect of External Flow on ALBEN Expansion Ramp Pressure Distribution

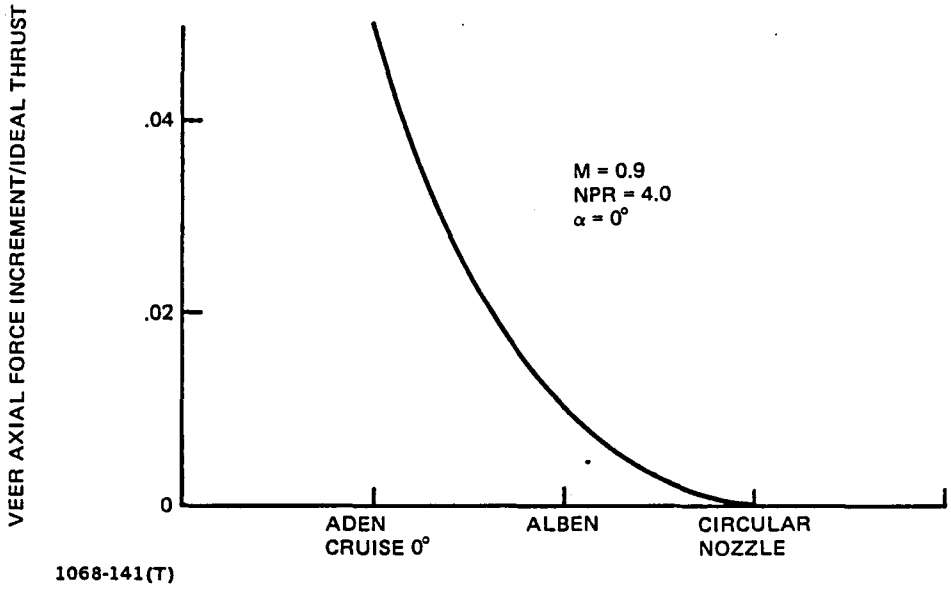

Figure 140 Effect of Nozzle Type on Wind-on/Wind-off VEER Axial Force Increment

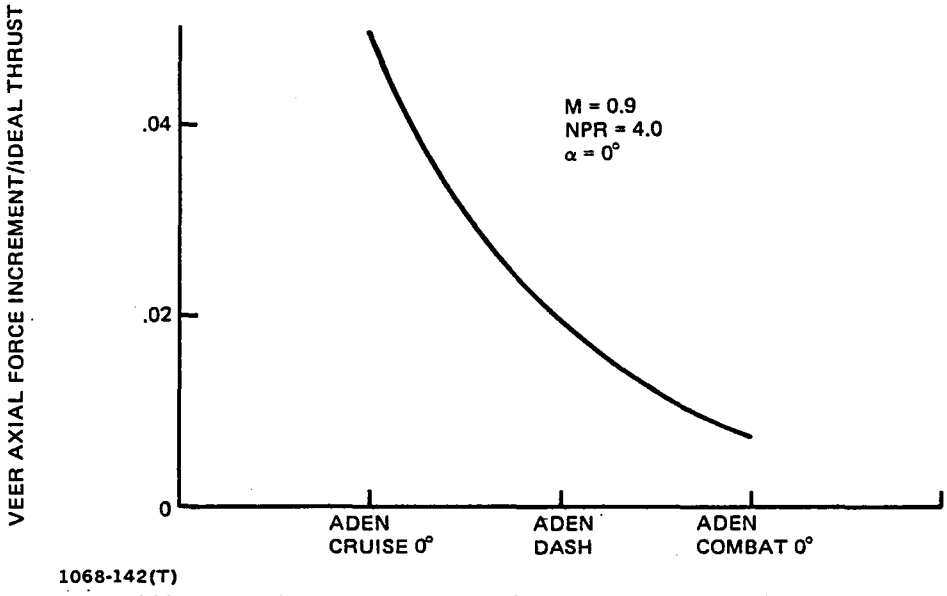

Figure 141 Effect of Jet Area on Wind-on/Wind-off VEER Axial Force Increment

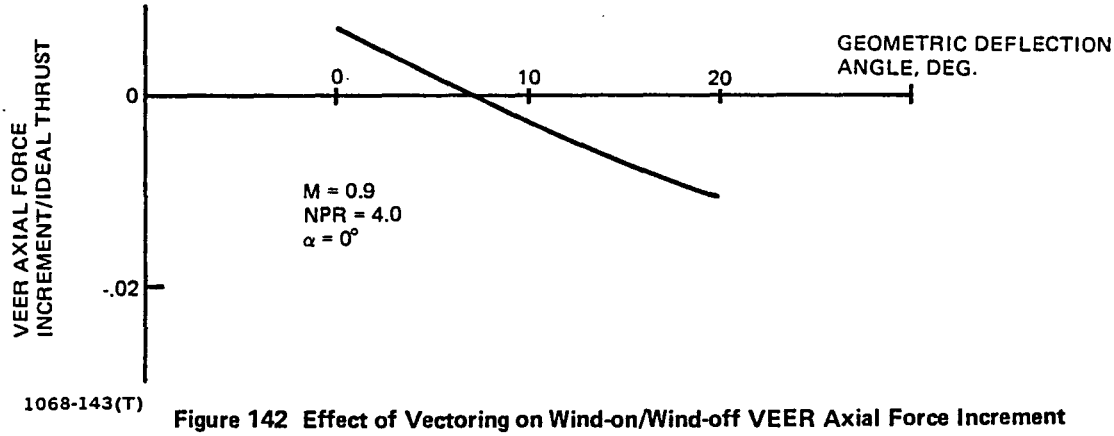

Figure 142 Effect of Vectoring on Wind-on/Wind-off VEER Axial Force Increment

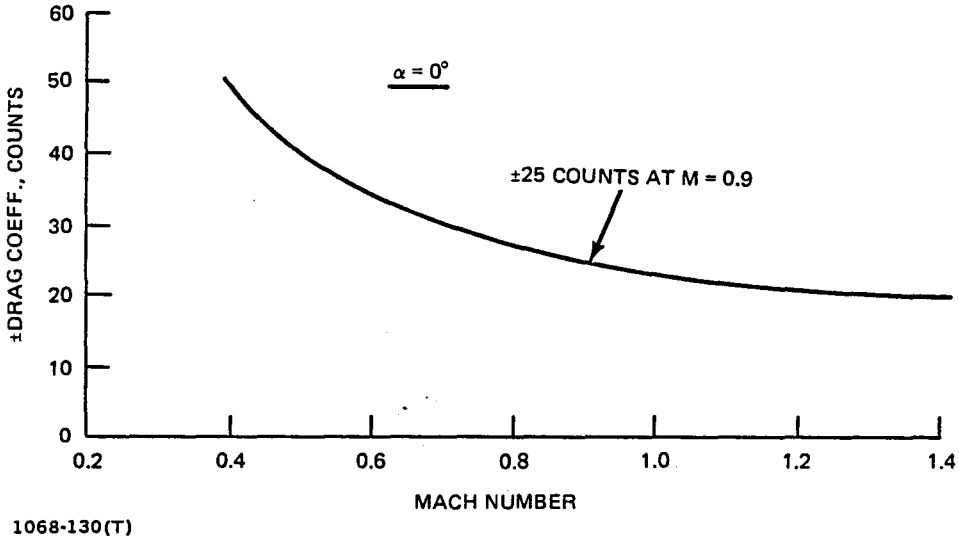

Figure 143 Effect of Theoretical Balance Uncertainty on Drag

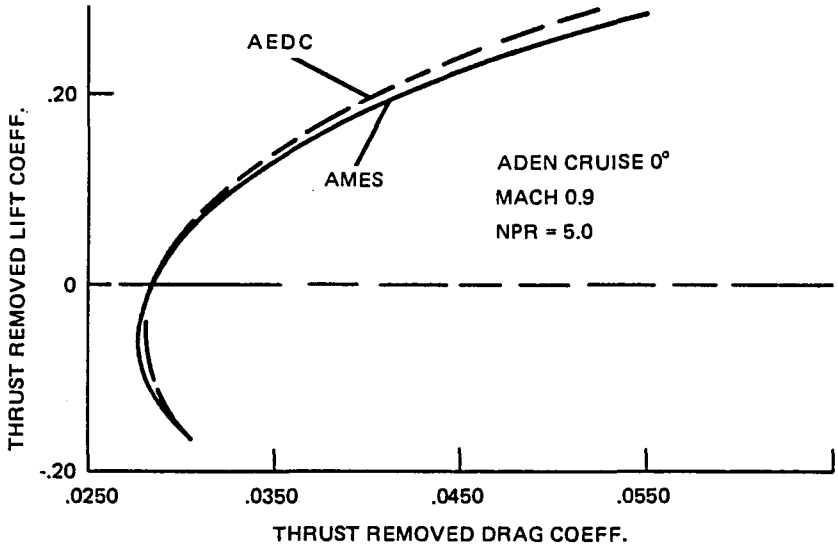

1068-131(T)

Figure 144 Facility Data Comparison

1. Report No.	2. Government Accession No.	3. Recipient's Catalog No.
NASA CR 166365		

4. Title and Subtitle	5. Report Date
AXISYMMETRIC & NON-AXISYMMETRIC EXHAUST JET INDUCED-EFFECTS ON A V/STOL VEHICLE DESIGN (Part II: Analysis of Results)	January 1982
	6. Performing Organization Code
7. Author(s) W. C. Schnell	8. Performing Organization Report No.
	10. Work Unit No.
9. Performing Organization Name and Address Grumman Aerospace Corp. Bethpage, NY	11. Contract or Grant No. NAS2-9887
	13. Type of Report and Period Covered Contractor Report
12. Sponsoring Agency Name and Address National Aeronautics and Space Administration Moffett Field, CA 94035	14. Sponsoring Agency Code

15. Supplementary Notes

Point of contact: D. B. Smeltzer, M.S. 227-2, NASA Ames Research Center
Moffett Field, CA 94035
Phone: FTS 448-5858, 415-965-5858

16. Abstract

A wind tunnel investigation, employing a 1/8 scale model in the NASA Ames 11-Foot Transonic Wind Tunnel (Mach 0.4-1.4), was conducted to determine the jet effects of several exhaust nozzles on the aeropropulsive performance of a V/STOL fighter design. The force and pressure data show that significant differences in aeropropulsion performance can be expected by varying the exhaust nozzle type, jet area and deflection angle on an underwing nacelle installation. At unvectored conditions, the single expansion ramp nozzles show large performance gains relative to a circular nozzle installation. Additionally, a further drag reduction is realized when the non-axisymmetric nozzle is vectored through a 10° deflection angle. The combined payoff of the vectored non-axisymmetric nozzle over the baseline circular nozzle installation is equivalent to 25 percent of zero lift drag.

17. Key Words (Suggested by Author(s))	18. Distribution Statement
Aerodynamics, Inlets, Propulsion	Unlimited Subject Category 02

19. Security Classif. (of this report)	20. Security Classif. (of this page)	21. No. of Pages	22. Price*
Unclassified	Unclassified		

*For sale by the National Technical Information Service, Springfield, Virginia 22161

End of Document